LBL-23698
c.2

# Lawrence Berkeley Laboratory
UNIVERSITY OF CALIFORNIA

## Materials & Chemical Sciences Division

RECEIVED
LAWRENCE
BERKELEY LABORATORY

AUG 21 1987

LIBRARY AND
DOCUMENTS SECTION

**THE ROLE OF LONG-RANGE FORCES IN THE FORMATION OF THIN LIQUID FILMS ON METALS**

J.R. Gyory* and R.H. Muller
(*Ph.D. Thesis)

June 1987

TWO-WEEK LOAN COPY
This is a Library Circulating Copy
which may be borrowed for two weeks.

LBL-23698
c.2

Prepared for the U.S. Department of Energy under Contract DE-AC03-76SF00098

## DISCLAIMER

This document was prepared as an account of work sponsored by the United States Government. While this document is believed to contain correct information, neither the United States Government nor any agency thereof, nor the Regents of the University of California, nor any of their employees, makes any warranty, express or implied, or assumes any legal responsibility for the accuracy, completeness, or usefulness of any information, apparatus, product, or process disclosed, or represents that its use would not infringe privately owned rights. Reference herein to any specific commercial product, process, or service by its trade name, trademark, manufacturer, or otherwise, does not necessarily constitute or imply its endorsement, recommendation, or favoring by the United States Government or any agency thereof, or the Regents of the University of California. The views and opinions of authors expressed herein do not necessarily state or reflect those of the United States Government or any agency thereof or the Regents of the University of California.

LBL-23698

# The Role of Long-Range Forces in the Formation of Thin Liquid Films on Metals

J. Richard Gyory
(Ph.D. Dissertation)

with

Rolf H. Muller

Department of Chemical Engineering
and Lawrence Berkeley Laboratory
University of California
Berkeley, California 94720

June 1987

This work was supported by the Director, Office of Energy Research, Office of Basic Research, and Materials Sciences Division of the US Department of Energy under contract No. DE-AC03-76SF00098.

# The Role of Long-Range Forces in the Formation of Thin Liquid Films on Metals

J. Richard Gyory

Department of Chemical Engineering
and Lawrence Berkeley Laboratory
University of California
Berkeley, California 94720

## ABSTRACT

White-light multiple beam interference is used to study the drainage of aqueous electrolytes (0.01 M to 3 M KOH, 0.01 M to 1 M $NaClO_4$, and 1 M and 67 wt % $H_3PO_4$) from vertically oriented optically smooth platinum and gold plates in a closed, isothermal system. The draining films are created by draining the bulk liquid from a cell in which the metal substrate is contained. A small amount of bulk liquid is left in contact with the bottom of the metal plate, providing a reference level and ensuring that the vapor phase is saturated.

For short times following the lowering of the bulk liquid level, the change in the film profile agrees with that expected from viscous drainage. However, at long times, the film profile deviates from that expected and eventually becomes independent of time at a thickness between 0.08 and 0.25 micrometers. These profiles are best represented by a function dependent on the inverse cube root of height. The thickness of the equilibrium film profiles

with increasing electrolyte concentration.

A model based on long range van der Waals interactions resulting in a repulsive force between the interfaces of the film is shown to predict the correct profile shape, and for dilute electrolytes, the correct film thickness. This model also predicts increasing film thickness for increasing electrolyte concentration. The strength of this interaction is characterized by the Hamaker constant which can be calculated from the dielectric functions evaluated at imaginary frequencies of the film and substrate. For metals, this function is generated from spectral absorption data, limiting behavior for low and high frequencies, and by use of the Kramers-Kronig transformation. Hamaker constants calculated from the dielectric functions generated in this manner agree well with those derived from film profiles for dilute electrolytes.

# Acknowledgements

I would like to express my gratitude to the many people who helped, guided and supported me in the completion of this work. I thank Dr. Rolf Muller for his faith and support and for giving me the freedom to explore new paths even though many of these did not directly lead to the completion of this work. I also thank my parents, John and Jane Gyory, for selflessly giving the trust and support that only loving parents can provide. Kathy Striebel and Mark Phillips deserve many thanks for being there when life was tough and providing many enjoyable diversions. Pam McKechnie shall receive a special thanks for understanding or at least accepting the craziness which accompanied the completion of this degree. May the resolution of her thesis be ever so more graceful than mine. I also extend my thanks to Mike Armstrong and Bob Crocker for helping with (or should I say doing?) the ellipsometric measurements and calculations. Also, I thank them for the many discussions that helped me formulate this work and the comradery that made it easier to complete. I would also like to thank Lee Johnson who's always quick with a joke, has the most complete set of supplies anywhere around, and is guardian to the kind of practical knowledge that keeps a laboratory running. Many thanks to Gina Whitney for graciously offering her expertise and the use of several of her computer files which were invaluable in the production of this thesis. Finally, the completion of this work would not have been possible without the tether to sanity provided by all my friends and colleagues.

This work was supported by the Director, Office of Energy Research, Office of Basic Research, and Materials Sciences Division of the US Department of Energy under contract No. DE-AC03-76SF00098.

# Table of Contents

Chapter 1 Introduction ..... 1

1.1 General Applications of Thin Liquid Films ..... 1

1.2 The Characteristics of Films Specific to this Study ..... 2

Chapter 2 Literature Review ..... 4

2.1 Introduction ..... 4

2.2 Lubrication ..... 4

2.3 Surface Stability of Flowing Films ..... 6

2.4 Drainage from a Flat Plate ..... 8

2.5 Marangoni Films ..... 10

2.6 Electrochemical Double Layers ..... 12

2.7 van der Waals Interactions Between Molecules ..... 13

2.8 Retarded London Interactions ..... 19

2.9 The Interaction of Macroscopic Bodies ..... 20

2.10 Stability of Colloidal and Surfactant Systems ..... 27

Chapter 3 Surface Tension, Transport, and Double Layers ..... 30

3.1 Introduction and General Observations ..... 30

3.2 Surface Tension ..... 32

3.3 Transport ..... 37

3.4 Double Layers ..... 41

Chapter 4 van der Waals Interactions in Thin Films ..... 51

4.1 Introduction ..... 51

4.2 Negative Hamaker Constants ..... 51

4.3 The Dielectric Function of Condensed Media ..... 58

4.4 The Calculation of Hamaker Constants ..... 70

4.5 The Effect of a Dissolved Salt ..... 76

4.6 Predicted Film Profiles ..... 83

4.7 Retarded Interactions Between Surfaces ..... 85

4.8 The Retarded Hamaker Constant ..... 86

Chapter 5 Experimental Technique, Setup, and Procedure ..... 92

5.1 Introduction ..... 92

5.2 White-Light Multiple-Beam Interference ..... 93

5.3 Ellipsometric Measurements ..... 106

5.4 The Optical Bench ..... 106

5.5 Liquid Film Cell, Substrates, and Electrolytes ..... 110

5.6 Surface Preparation and Procedure ..... 119

Chapter 6 Results and Discussion ..... 126

6.1 General Observations ..... 126

6.2 Transient Profiles ..... 128

6.3 Ellipsometric and Intensity Measurements ..... 134

6.4 Equilibrium Profiles ..... 147

6.5 The Effect of Specific Adsorption ..... 160

6.6 Tetradecane ..... 164

6.7 Summary of Conclusions ..... 165

Appendix A Notation ..... 168

Appendix B The Surface Profile of Minimum Total Energy ..... 174

Appendix C Program for the Calculation of the Hamaker Constant ..... 179

Bibliography ..... 195

# List of Figures

2-1 Volume Element for the Integration of Pairwise Interaction Energies ..... 22

3-1 Liquid Film Cell: Before and After Liquid Level Lowering ..... 31

3-2 Geometry for Minimum Energy Calculation ..... 33

3-3 Meniscus Profile Shape ..... 36

3-4 Geometry for Surface Tension Gradient Calculation ..... 40

3-5 Interacting Double Layers ..... 44

3-6 Film Profile Calculated from Interacting Double Layers ..... 49

4-1 Geometry for Calculation of Energy of Interaction for Two Arbitrary Bodies ..... 54

4-2 Dielectric Functions for Water, Tetradecane, and Gold ..... 63

4-3 Absorption Spectrum for Gold: Data from Palik (1985), Together With Least Squares Cubic Spline Fit ..... 67

4-4 Dielectric Function Minus One for Gold: Equation 4-12, Compared to that Calculated by the Method of Parsegian ..... 69

4-5 Frequency Dependent Part of the Dielectric Function for Platinum: Calculated from Equation 4-12 ..... 70

4-6 Percent of Total Hamaker Constant as a Function of Frequency for the Platinum / Water / Vapor System ..... 75

4-7 Relative Importance of Frequency

to the Total Hamaker Constant ..... 76

4-8 Frequency Dependent Part of the Dielectric Function

for Water and Tetradecane ..... 78

4-9 Frequency Dependent Part of the Dielectric Function

for Water and Various Aqueous Electrolytic Solutions ..... 80

4-10 Dependence of Hamaker Constant on Film and

Solid Dielectric Function ..... 82

4-11 Retarded Hamaker Constant as a Function of Film Thickness ..... 91

5-1 Schematic of Multiple Beam Interference ..... 94

5-2 Schematic Defining the Reflection of s- and p-

Linearly Polarized Light ..... 97

5-3 Reflection Coefficient and Phase Change Upon Reflection ..... 99

5-4 Definition of Complex Reflection Coefficients ..... 100

5-5 Difference in Optical Path After One Internal Reflection ..... 102

5-6 Color Series for a Dilute Aqueous Film on Platinum ..... 105

5-7 Schematic Diagram of Optical Bench for Thin Film Interference ..... 107

5-8 Photograph of the Optical Bench and Related Instruments ..... 109

5-9 Cross-section Schematic of Small Liquid Film Cell ..... 111

5-10 Cross-section Schematic of Large Liquid Film Cell ..... 112

5-11 Top View Schematic of Large Liquid Film Cell ..... 113

5-12 Photograph of Large Liquid Film Cell ..... 114

5-13 Schematic of Metallic Substrate Shapes ..... 117

5-14 Thin Liquid Cell and Associated Equipment ..... 120

5-15 Cyclic Voltammogram of 100 $cm^2$ Surface Area

Platinum Substrate ..... 122

5-16 Schematic of Filled and Drained Cell ..... 124

6-1 Film Profiles at Various Times for 1 M KOH on Platinum ..... 129

6-2 Film Profiles at Various Times for 1 M KOH on Gold ..... 130

6-3 Film Profiles at Various Times for 1 M $H_3PO_4$ on Platinum ..... 131

6-4 Film Thickness as a Function of Inverse Square Root of Time

for 1 M KOH on Platinum ..... 133

6-5 Film Thickness as a Function of Inverse Square Root of Time

for 3 M KOH on Platinum ..... 134

6-6 PSI as a Function of wavelength at (a) 9 cm and

(b) 7 cm Above the Bulk Liquid Level ..... 136

6-6 PSI as a Function of wavelength at (c) 5 cm and

(d) 7 cm Above the Bulk Liquid Level ..... 137

6-7 Sum of Squares Error as a Function of Thickness for

(a) 9 cm and (b) 7 cm Above the Bulk Liquid Level ..... 140

6-7 Sum of Squares Error as a Function of Thickness for

(c) 5 cm and (d) 3 cm Above the Bulk Liquid Level ..... 141

6-8 Comparison of Film Profile from Interference Colors to

that from Ellipsometric Parameters ..... 142

6-9 Film Profile for 67 weight % $H_3PO_4$ on Platinum

at 5 and 9 Days After Liquid Level was Lowered ..... 143

6-10 Normalized Reflected Light Intensity for 67 % $H_3PO_4$

on Platinum at (a) 9 cm and (b) 7 cm ..... 145

6-10 Normalized Reflected Light Intensity for 67 % $H_3PO_4$

on Platinum at (c) 5 cm and (d) 3 cm ..... 146

6-11 Equilibrium Profile for 1 M KOH on Platinum ..... 148

6-12 Equilibrium Profile for 1 M KOH on Gold ..... 149

6-13 Equilibrium Profile for 1 M $NaClO_4$ on Platinum ..... 150

6-14 Equilibrium Profile for 0.01 M KOH on Platinum ..... 151

6-15 Equilibrium Profile for 1 M $H_3PO_4$ on Platinum ..... 152

6-16 Equilibrium Film Thickness at 5 cm Dependence

on Film Electrolyte Concentration ..... 154

6-17 Equilibrium Film Profile for 1 M KOH on Platinum with Calculat-

ed Inverse $3^{rd}$ and Inverse $4^{th}$ Root Functions ..... 159

6-18 Film Profiles for 1 M KOH on Platinum Before

and After the Addition of 0.1 M KCl ..... 162

6-19 Film Profiles for 1 M $H^3PO^4$ on Platinum Before

and After the Addition of 0.1 M KCl ..... 163

# List of Tables

2-1 Contributions to the Total van der Waals Interaction Between Two Molecules in Vacuum ..... 14

2-2 Interaction Energies, U, for Various Geometries in Vacuum ..... 25

4-1 Definition of Terms for Equations 4-2 through 4-4 ..... 56

4-2 Parameter Values for Dielectric Functions of Water, Tetradecane, and Gold ..... 62

4-3 Calculated Hamaker Constants for Systems Derived from Gold, Platinum, Water, and Tetradecane ..... 73

4-4 Calculated Hamaker Constants for Systems Derived from Gold, Platinum, and Various Electrolytes ..... 81

6-1 Index of Refraction and Extinction Coefficient Data for Platinum in the Visible Range ..... 139

6-2 Value of the Exponent and Correlation Factor for a Power Law Fit of Film Thickness vs. Height ..... 153

6-3 Hamaker Constants Predicted from Film Profile Measurements with that Calculated from Theory ..... 157

# Chapter 1

# Introduction

## 1.1. General Applications of Thin Liquid Films

There are few areas in science which extend over as many and as varied fields as does the study of thin liquid films. The following examples, although not intended to be a complete list, will certainly provide some sense as to the ubiquitous nature of thin liquid films.

One of the earliest recorded intentional use of thin liquid films was for lubrication during the transport of the statue of Ti ca. 2400 B.C. However, animal fat and water were probably used long before that in door hinges, chariot wheels, potters wheels, etc. (Szeri, 1980). To this date, lubrication in the form of a thin layer of a liquid lubricant is a common means of preventing wear and the production of heat between two solids in relative motion. In extraction and distillation, thin liquid films reduce mass transfer resistances. Many technologies such as photographic film production depend on withdrawal coating, slide coating or spin coating of a liquid onto a solid substrate. Bonding of two dissimilar solids by an adhesive depends on the complete wetting of the solids by a thin liquid film of the adhesive. The stability of solid particles suspended in solution is controlled by the nature of the thin liquid film which separates neighboring particles. Electrochemical fuel cells require a three phase electrode, solid conductor/thin liquid electrolyte/gas phase reactant supply, for efficient operation. Also, corrosion of metals often occurs when a thin layer of electrolyte

provides a diffusion path for oxygen transport to the corrosion area and also removal of corrosion products by convection or diffusion. The thin liquid films important to each of these applications are not identical. They have differing thicknesses, flow characteristics and other properties.

## 1.2. The Characteristics of Films Specific to this Study

Thin liquid films can be divided into three categories: bulk films which behave much as a bulk liquid, adsorbed films which are limited to a few monolayers in thickness, and those films which do not display bulk liquid properties, but are too thick to be considered adsorbed. Generally speaking, bulk films will be greater than 1 $\mu$m in thickness and their formation and thinning characteristics will be controlled by inertial and capillary effects. Adsorbed films will be a fraction of a monolayer to perhaps several monolayers in thickness and will be controlled by the specific interaction between individual molecules of the film and specific adsorption sites on the surface of the substrate. The intermediate films will range between 10 nanometers and 1 $\mu$m in thickness and will be controlled by inertial and capillary forces and by intermolecular forces that are summed over the macroscopic thickness of these thin films. These categories are of our own choosing.

The origins of this study are in the field of electrochemistry. Work from this laboratory which directly influenced this study began with that by Bennion and Tobias (1966). Using silver and nickel segmented cylindrical electrodes, they showed that for the reduction of oxygen in KOH at a partially submerged electrode, a significant portion of the current flowed through an electrode

segment that was physically above the intrinsic meniscus. This indicated that there existed a thin liquid electrolyte film which extends above the intrinsic meniscus through which oxygen reduction could occur. During the same time period, Muller (1964 and 1966) measured the thickness of these films and found it to be on the order of 1-3 $\mu$m. He also found that these films extended several centimeters above the bulk solution. Turney (1971), Brown (1973), and Sand (1975) working with Muller perfected an optical technique which enables the determination of the thickness of transparent thin films by observing the interference colors resulting from the reflection of polarized white light from the film covered surface. This method is non-invasive and allows for the continuous monitoring of the film thickness at all points on the solid surface simultaneously. Their observation that thin liquid films draining from a vertically oriented planar metal surface can attain steady time-invariant profiles has prompted this work.

The purpose of this work is to determine the forces responsible for the existence of these time invariant films. The thickness of these films, as will be shown later, falls into the category we have termed intermediate films and it is the nature of these intermediate films that we shall study. More specifically, we will explore the interaction between the thin liquid film and the solid substrate and how this interaction determines the overall behavior of the thin film.

# Chapter 2

# Literature Review

## 2.1. Introduction

There is a voluminous literature pertaining to thin liquid films. A large part of this literature is concerned with physical phenomena that are not of direct concern to this thesis. Therefore, references considered in this chapter will include only those areas that are directly concerned with the work described in this study.

The literature reviewed will encompass flow in thin films including drainage under the influence of gravity and flow caused by surface tension gradients. Also, the review will include phenomena not directly leading to fluid flow. These include the electrochemical double layer and van der Waals interactions. Some of the relevant literature will not be covered in detail in this chapter; details omitted here will be covered along with the development of theory in chapters 3 and 4.

## 2.2. Lubrication

In general, the lubrication literature concerning thin liquid films can be grouped into two categories; 1) situations where reduction of friction is desired, and 2) situations where promotion of friction is desired. The geometry and physical conditions under which liquid lubricants are used for the reduction of friction vary widely. However, in almost all situations the liquid lubricant will itself

be flowing, either as the result of being pumped, or because it is entrained along the surfaces of the parts being lubricated. One of the more common situations involves the flow of a lubricant into a gap having a cross-section that decreases with distance. As a result, the hydrostatic pressure in the film increases and the film becomes capable of supporting a load (Ruddy and Summer-Smith, 1982). The main thrust of the scientific effort in lubrication theory is the prediction of how much load these films can support and under what conditions these films will fail. The load bearing capability and failure conditions for these films is highly dependent on the external pressure and temperature, geometry, lubricant viscosity, and hydrodynamic flow characteristics. Very good introductions to the specific problems encountered in lubrication and general approaches to determining operating conditions for varied geometries can be found in Gross, et al. (1980) and Szeri (1980).

Another common problem is the promotion of friction to prevent slippage. Perhaps the most common example is the performance of car tires on wet pavement. Here, the tire must come in solid contact with the pavement to maintain control and turning ability. Again, hydrodynamics and fluid viscosity play important roles in determining how quickly the fluid can flow out of the contact area (Moore, 1965).

In general it is safe to conclude that lubrication problems are, by their basic nature, dynamic. The lubrication literature contains little with respect to the interaction of system components in equilibrium. Therefore, it has limited application to the problem at hand.

## 2.3. Surface Stability of Flowing Films

A wealth of literature pertains to the problem of the surface stability of thin liquid films flowing under the influence of gravity down the surface of an inclined solid. Nusselt (1916), assuming that the inertial terms of the Navier-Stokes equation were approximately zero for these systems and that the only driving force for flow stemmed from gravity, presented the following equations to describe the flow of thin films along inclined solids:

$$\frac{d^2v}{dy^2} + \frac{g}{\nu_k} \sin \theta = 0 \tag{2-1}$$

$$\frac{dp}{dy} = \rho g \cos \theta \tag{2-2}$$

$$\frac{dp}{dz} = 0 \tag{2-3}$$

Here, v is the fluid velocity, g is the gravitational constant, $\nu_k$ is the kinematic viscosity of the fluid, $\theta$ is the angle the inclined plate makes with the horizontal, p is the pressure, $\rho$ is the liquid density, and y and z are the vertical and horizontal directions respectively. The solution to these equations results in laminar Poiseuille flow; a parabolic velocity profile with zero relative velocity at the solid/liquid interface and maximum velocity at the liquid/gas interface.

Since Nusselt many workers have noted the development of surface instabilities and waves. Reviews of the theory of predicting the onset of wave formation are numerous. Publications by Fulford (1964), Norman (1961), and Levich (1962) are representative of the available literature on this subject. However, at

this time I will mention the work and results of two individuals in particular.

Benjamin (1957) presented a linear stability analysis of the onset of surface waves. His analysis included the effects of surface tension. His work showed that for flow down a vertical plate at any finite value of the Reynolds number, $N_{Re}$, there is a disturbance wavelength whose amplitude undergoes unbounded growth.

$$N_{Re} = \frac{\bar{v}\,\bar{\delta}}{\nu_k} \tag{2-4}$$

In equation 2-4, $\bar{v}$ and $\bar{\delta}$ represent the average velocity and average film thickness respectively. Benjamin's own observations as well as those of others contradict this theoretical prediction. He surmises that this discrepancy is not serious because his predictions show that as the $N_{Re}$ approaches zero the wave number of the unstable disturbance goes to zero, *i.e.*, the wavelength approaches infinity. Yih (1963) presents a stability analysis of the same problem using a different expansion technique which predicts that flow down a vertical plate is stable to all wavelengths in the limit of $N_{Re} = 0$. However, as $N_{Re}$ is increased above zero, there should be some wavelength whose amplitude grows unbounded. Again this result is in conflict with observations which show for $N_{Re} \leq 5$ surface waves do not develop on films flowing on vertical surfaces (Shibuya, 1951; Yih, 1955; Binnie, 1957). For aqueous films draining from vertical surfaces, $N_{Re}$ is less than five for films of thickness less than 0.1 mm. This thickness exists within seconds of a plate being withdrawn from solution.

Despite all the effort put into these studies, the conditions and mathematical description of the phenomena responsible for surface instabilities in flowing thin liquid films are still not clearly and unambiguously determined. With the advent of numerical methods such as the finite-element and boundary-element techniques which can more easily handle non-linear moving boundary problems perhaps the stability regimes and conditions of these flowing films will eventually be fully described.

### 2.4. Drainage from a Flat Plate

When a solid object is withdrawn from a liquid bath, provided the liquid wets the solid, a thin liquid film adheres to the surface of the solid. The liquid in this film flows under the influence of gravity and will thin with time. The understanding of this process is important in several applications including dip-coating, slide coating, and any process involving the adherence of a liquid, such as a layer of wet paint, on a vertical surface. As seen from these examples, the liquid film can range from a simple Newtonian fluid to polymeric solutions or suspensions which exhibit complex fluid behavior.

Jeffreys (1930) first treated the problem of thin films draining from the inside walls of a vessel. Starting from equations 2-1, 2-2, and 2-3 and assuming the wall to be an infinitely wide flat plate, he solved for the film thickness, $\delta$, as a function of time, t, after liquid was drained from the vessel and distance, z, measured downward from the liquid film attachment point. His results are shown in equation 2-5 where $\mu$, $\rho$, and g are the fluid viscosity, fluid density, and the gravitational constant respectively.

$$\delta = \left( \frac{\mu z}{\rho g t} \right)^{1/2} \tag{2-5}$$

Satterly, et al. (1932, 1933) showed experimentally using Newtonian fluids made by mixing glycerin and water, that equation 2-5 was correct only for drain times greater than 500 seconds.

One effort to explain this discrepancy was made by Van Rossom (1958). He incorporated the velocity, $V_w$, at which the bulk liquid is lowered and the total length, L, of the draining liquid film.

$$\delta = \left( \frac{\mu V_w}{\rho g} \frac{z}{L} \right)^{1/2} \tag{2-6}$$

Although equation 2-6 did not greatly improve the agreement of experiments and theory at short times, Van Rossom did recognize the importance of the initial conditions present during the withdrawal of the solid from the liquid. Denson (1970) and Tallmadge and Lange (1971) discussed the importance of breaking the drainage process into two regimes. The first involved the initial generation of the film profile which occurs during the withdrawal of the bulk liquid. The second begins immediately following the cessation of withdrawal and is dominated purely by viscous and gravitational effects.

When capillary and inertial effects are considered during the initial withdrawal period, Groenveld (1970, 1971) and Tallmadge (1971a, 1971b) showed that the initial film profile can be divided into two sections. The first section, that closest to the film attachment point, $0 \leq z \leq z_o$, is characterized by a parabolic profile predicted by Jeffreys equation (eqn. 2-5). The second section

extends from a critical length, $z_o$, downward and is characterized by a uniform film thickness, $\delta_o$. The critical length is initially equal to $z_{oi}$ and increases with time until $z_o = L$, the full length of the film, at which point the entire film drains according to Jeffreys equation, eqn. 2-5. Tallmadge's equations may be expressed as follows;

$$\delta = \left( \frac{\mu z}{\rho g t} \right)^{1/2}, \quad \text{for} \quad z < z_o \tag{2-7}$$

$$\delta = \delta_o = \left( \frac{\mu V_w}{\rho g} \frac{z_{oi}}{L} \right)^{1/2}, \quad \text{for} \quad z \geq z_o, \tag{2-8}$$

where $z_{oi}$ is a function of the capillary number, $N_{Ca}$, and Reynolds number, $N_{Re}$. The capillary number is the ratio of viscous to capillary forces and is defined as;

$$N_{Ca} = \frac{\mu \bar{v}}{\gamma} \tag{2-9}$$

where $\gamma$ is the surface tension of the liquid. The functionality of $z_{oi}$ with $N_{Ca}$ and $N_{Re}$ can be determined experimentally over a wide range of conditions. This treatment has been shown to be valid also for various non-Newtonian fluids (Tallmadge, et al., 1980).

### 2.5. Marangoni Films

The Marangoni Effect has long been recognized as a phenomenon resulting in the transport of bulk liquid due to a surface tension gradient at a fluid/fluid interface (Fulford, 1964). This interface may be either between two liquids or between a liquid and a vapor. The surface tension gradients are caused by pre-

ferential evaporation of one species over another or by temperature gradients. At a three phase contact line such as a meniscus, the surface tension gradient can be great enough to lift bulk liquid above the upper limit of the intrinsic meniscus. When this occurs, these films generally become unstable and "tears" or rivulets will form returning liquid to the bulk. A common example of this phenomenon is the formation of tears on the insides of wine and liqueur glasses.

The Marangoni effect has been been found to be very important in absorption, distillation and cooling towers where local concentration differences and local thermal gradients can cause surface tension differences (Norman, 1961). The formation of surface instabilities on Marangoni films has been held responsible for both stirring of the film and increasing the surface area of the film; both these result in increased mass transfer rates over those for flat films (Brian, et al., 1967; Banarjee, et al., 1967; Emmert and Pigford, 1954). However, if these instabilities become too large, film breakup may follow and poor mass transfer rates will result (Norman and Soloman, 1959; Bond and Donald, 1967).

The stability of these films to changes in thickness across the width of the film can be modeled by imposing a standing cylindrical wave pattern oriented such that the troughs and peaks run in the vertical direction (Sternling and Scriven, 1959). Using a similar development, Ludviksson and Lightfoot (1968) determined the stability conditions for temperature induced surface tension gradients. Their conclusions were that films tended to be stable for either very large or very small thermally induced surface tension gradients. Films having large thermal conductivities tended to be more stable. And films observed in

model gas diffusion electrodes (Will, 1963; Bennion and Tobias, 1966; Muller, 1964, 1966) were unlikely to experience instabilities leading to vertically oriented cylindrical wave patterns.

Brian (1971) and Wang, Ludviksson and Lightfoot (1971) evaluated the stability of films caused by mass transfer-generated surface-tension gradients. According to the linear stability analysis used in these studies these films are unstable to some frequencies at all thicknesses and surface tension gradients. However, as in the case of horizontal waves on a flowing film, there is some question as to whether instabilities would be observed for small surface tension gradients imposed on very thin films.

## 2.6. Electrochemical Double Layers

It is well known that an effective surface charge at a solid/liquid interface will result in a surface potential at that interface. Furthermore, there will be a diffuse double layer extending from the interface into the liquid (Stern, 1924; Grahame, 1947). The physical consequence of this double layer is to cause a smooth transition of the electric potential from the potential at the surface to that in the bulk liquid. The reason why the double layer occurs may be directly attributed to the presence of mobile charged and/or polar molecules that are free to move in the presence of the surface potential at the solid/liquid interface.

The development of the theory of the electrochemical double layer at metal/electrolyte interfaces has evolved slowly. At the core of this development are the Gouy-Chapman theory, the use of Gibbs adsorption isotherms, and

allowing for specific adsorption of charged species on the surface. In general, barring specific adsorption, the electrical potential extending into the electrolyte from a metallic interface may be described as follows. The magnitude of the potential will decrease exponentially with distance from the metal/electrolyte interface from the value of the potential at the interface to the value in the bulk electrolyte which it approaches asymptotically. The distance at which the potential is 1/e times the potential at the interface is known as the Debye length; this length becomes smaller as the ionic strength of the electrolyte increases. For a mathematical description of the diffuse double layer, see section 3.4 of this thesis. For a complete development of the double layer theory, see virtually any physical chemistry or electrochemistry textbook a few of which are represented by Adamson (1982), Hiemenz (1977), Delahay (1965) and Bard and Faulkner (1980).

## 2.7. van der Waals Interactions Between Molecules

The van der Waals interaction between molecules results from the summation of three interactions. These interactions are electrical in nature and stem from the fact that molecules either have a dipole moment or may be induced to exhibit a dipole moment by the electric field generated by a neighboring molecule. The overall force resulting from these interactions will always cause an attractive force between any two molecules interacting through a vacuum. Table 2-1 lists the interaction potentials and the physical basis for each component of the total van der Waals interaction. The symbols used in table 2-1 are defined in appendix A at the end of this thesis.

Table 2-1: Contributions to the Total Van der Waals Interaction Between Two Molecules in Vacuum

| Contribution | Origin | Interaction Potential |
|---|---|---|
| Keesom | Permanent Dipole-Permanent Dipole | $U_K = \frac{-(\mu_1 \mu_2)^2}{3(4\pi\epsilon_o)^2 k_B T r^6}$ |
| Debye | Permanent Dipole-Induced Dipole | $U_D = \frac{-(\alpha_{o2}\mu_1^2 + \alpha_{o1}\mu_2^2)}{(4\pi\epsilon_o)^2 k_B T r^6}$ |
| London | Induced Dipole-Induced Dipole | $U_L = \frac{-3}{4} \frac{(\alpha_{o1}\alpha_{o2})^2}{(4\pi\epsilon_o)^2 r^6} \frac{I_1 I_2}{I_1 + I_2}$ |
| Retarded London | Induced Dipole-Induced Dipole | $U_{rL} = \frac{-23}{8\pi^2} \frac{h_P c \alpha_{o1}\alpha_{o2}}{(4\pi\epsilon_o)^2 r^7}$ |

In the literature, these interactions are referred to by the name of the researcher who first developed the power law describing their behavior. Thus, permanent dipole-permanent dipole interactions will be referred to as Keesom interactions, permanent dipole-induced dipole interactions will be termed Debye interactions, and induced dipole-induced dipole and the retarded induced dipole-induced dipole will collectively be called London interactions. The latter two are also referred to as dispersion interactions in the literature. There are many excellent reviews of the derivation and historical background of the interaction potentials presented in table 2-1. Most physical chemistry and surface chemistry textbooks prove to be very good sources for this information. A few of these are represented by Adamson (1982), Hiemenz (1977), and Israelachvili (1985).

The total van der Waals interaction between two atoms or molecules interacting through free space will be given by the sum of the Keesom, Debye, and London interaction energies. However, the free space condition will only apply in a relatively low pressure gaseous medium. McLachlan (1963a, 1963b) presented a more general version of the van der Waals theory which allows for the presence of a dielectric medium in which the interacting molecules reside. McLachlan's theory also accounts for the existence of more than one ionization potential for each of the interacting molecules. McLachlan's equation was developed using the Lifshitz field theory of dielectric media (Lifshitz, 1956). This theory accounts for the dielectric nature and the frequency dependence of the dielectric function of the intervening medium and the frequency dependence

of the polarizabilities of the interacting molecules. The total energy of interaction of two dissimilar molecules through a third medium is given by equation 2-10 (Israelachvili, 1985, p. 79),

$$U_t = \frac{-6\, k_B\, T}{(4\,\pi\,\epsilon_o)^2\, r^6} \sum_{n=0}^{\infty}{}' \frac{\alpha_{o1}(i\,\nu_n)\,\alpha_{o2}(i\,\nu_n)}{\epsilon_3'(i\,\nu_n)} \tag{2-10}$$

where $k_B$ is Boltzman's constant, T is the absolute temperature, $\epsilon_o$ is the electric permittivity of free space, r is the distance of separation between the two molecules, n is a counter which determines the discrete frequency $\nu_n$ (see equation 2-12) $\alpha_{o1}(i\,\nu_n)$ and $\alpha_{o2}(i\,\nu_n)$ are the polarizabilities of molecules 1 and 2, and $\epsilon_3'(i\,\nu_n)$ is the real part of the complex dielectric function of the intervening medium evaluated at imaginary frequencies.

$$\hat{\epsilon} = \epsilon' + i\,\epsilon'' \tag{2-11}$$

The frequency $\nu_n$ is given by:

$$\nu_n = \frac{2\,\pi\,k_B\,T}{h_P}\,n\,, \quad \text{where} \quad n = 0,1,2,\ldots\infty \tag{2-12}$$

where $h_P$ is Plank's constant. The prime following the summation sign in equation 2-10 indicates that the n=0 term of the summation is to be multiplied by 1/2.

To achieve a better understanding of equation 2-10 we must first realize that, as Von Hippel (1958) showed, the electronic polarization of a molecule can be estimated at any frequency if an average rotational relaxation frequency, $\nu_{rot}$, and the ionization frequency, $\nu_I$, are known. In terms of these variables, the fre-

quency dependence of the polarizability of a polar molecule in free space is given by:

$$\alpha(\nu_n) = \left( \frac{\mu^2}{3\, k_B\, T\, (1 - \frac{i\, \nu_n}{\nu_{rot}})} \right) + \left( \frac{\alpha_o}{1 - (\frac{\nu_n}{\nu_I})^2} \right) \tag{2-13}$$

Using this definition of the electronic polarizability it can be shown (Israelachvili, 1985, pp. 76-7) that for n=0, equation 2-10 reduces to the sum of the Keesom and Debye potentials multiplied by the inverse dielectric constant of the medium. Furthermore, the sum of the $n > 0$ terms can be converted to an integral and assuming only one ionization potential for each species, the value of this integral is identically equal to the London potential, see table 2-1, multiplied by the inverse dielectric constant of the medium. From this it is evident that equation 2-10, for the simple case of a single ionization potential for each species, reduces to the sum of the Keesom, Debye, and London interaction potentials.

The above development can be extended to apply not only to molecules interacting through a medium, but also to macromolecules or very small particles (McLachlan, 1965). McLachlan showed that the important quantity in this situation is the excess polarizability, $\alpha_1(\nu)$, of the small particle. This can be calculated for spherical particles of radius $a_1$ and is a function of the dielectric function of both the particle and surrounding medium, as is shown in equation 2-14.

$$\alpha_1(\nu) = 4\,\pi\,\epsilon_o\,\epsilon_3' \left( \frac{\epsilon_1'(\nu) - \epsilon_3'(\nu)}{\epsilon_1'(\nu) + 2\,\epsilon_3'(\nu)} \right) a_1^{\,3} \tag{2-14}$$

On the substitution of 2-14 into 2-10 and after the conversion of the summation to an integral the total van der Waals interaction energy is given by:

$$U_t = -\frac{3\,h_P\,a_1^3\,a_2^3}{\pi\,r^6} \int_0^\infty F_1(i\nu)\,F_2(i\nu)\,d\nu \tag{2-15}$$

where

$$F_1(i\nu) = \left( \frac{\epsilon_1'(i\nu) - \epsilon_3'(i\nu)}{\epsilon_1'(i\nu) + 2\,\epsilon_3'(i\nu)} \right) \tag{2-16}$$

and

$$F_2(i\nu) = \left( \frac{\epsilon_2'(i\nu) - \epsilon_3'(i\nu)}{\epsilon_2'(i\nu) + 2\,\epsilon_3'(i\nu)} \right) \tag{2-17}$$

Equations 2-15, 2-16 and 2-17 show that if two interacting particles are identical the total energy of interaction, $U_t$, will always be negative, hence the particles will attract one another. However, if the two particles are different and if the real part of the dielectric function of the medium, $\epsilon_3'$, is intermediate between the real part of the dielectric functions of the two particles, *i.e.*, $\epsilon_1' > \epsilon_3' > \epsilon_2'$, then $F_1$ and $F_2$ will have opposite signs. Therefore, the total interaction energy will be positive, hence the particles will repel one another. This possibility was first recognized by Hamaker (1937) when he was considering the total energy of interaction between macroscopic bodies which will be covered in more detail in section 2.9 and in chapter 4.

## 2.8. Retarded London Interactions

The physical basis for induced-dipole/induced-dipole interactions between two molecules may be summarized as follows. The electric field generated by the orbiting electrons in molecule 1 induce a dipole in molecule 2. The resulting electric field from the induced dipole of molecule 2 will in turn induce a dipole in molecule 1, thus an electrostatic attraction results. Since electromagnetic fields cannot travel faster than the speed of light, and if molecules 1 and 2 are separated by a large enough distance, the position of the orbiting electrons in molecule 1 may change appreciably by the time the electric field generated by molecule 2 returns. Under these circumstances, the resulting interaction will be less than that predicted by the London interaction potential given in table 2-1.

Casimir and Polder (1948) modified the London potential using a fourth order perturbation method; their result is that listed in table 2-1 as the retarded London potential. The energy of interaction for two molecules where retardation effects are important is shown to depend on the inverse seventh power of the distance of separation. This power law does, as was expected, fall off more quickly than the inverse sixth power of separation distance exhibited by Keesom, Debye, and London potentials.

The Lifshitz theory is ideal for analyzing the overall retardation effect. This theory generalizes all the local spontaneous electric field fluctuations resulting from a quantum mechanical analysis of condensed media into an electromagnetic field which extends over the entire system. It is then possible to frequency analyze the time-varying field. The strength of the field for a given frequency

directly depends on the response of the material to an imposed field of that frequency. In other words, the dielectric susceptibility, $\epsilon(\nu)$ determines what frequencies are transmitted and which are attenuated. The total interaction is then determined by summing the systems response over all frequencies. The advantage to this method is that the response of the entire system is determined at each frequency and then summed, rather than finding each molecular pair interaction and suming over all interactions. Thus the response of the system at one frequency does not depend on any other frequency whereas molecular pair interactions will depend on neighboring molecular pair interactions.

The exact method of applying Lifshitz theory is beyond the scope of this thesis. The derivation of the full distance of separation dependent and temperature dependent interaction potential may be found in Dzyaloshinskii, et al. (1961) or Mahanty and Ninham (1976). Retardation effects as they apply to this work will be treated in more detail in chapter 4 of this thesis.

## 2.9. The Interaction of Macroscopic Bodies

Before proceeding further, it will be useful to define a variable C. This is done to simplify several of the equation that will appear in the next few pages. The total energy of interaction, $U_t$, has already been shown to be the sum of the Keesom, Debye, and London interaction potentials which are all functions of the inverse sixth power of the distance of separation of two interacting molecules. Therefore, we may define the variable C as follows;

$$U_t = U_K + U_D + U_L = -\frac{C}{r^6} \tag{2-18}$$

Therefore, referring to table 2-1,

$$C = \frac{1}{(4\pi\epsilon_o)^2}\left(\frac{(\mu_1\mu_2)^2}{3k_BT} + \alpha_{o2}\mu_1^2 + \alpha_{o1}\mu_2^2 - \frac{3}{4}(\alpha_{o1}\alpha_{o2})^2\frac{I_1I_2}{I_1+I_2}\right). \tag{2-19}$$

It is seen that the variable C contains all necessary information to calculate the interaction energy of two molecules across a vacuum except the distance of separation.

The van der Waals interactions between surfaces may be obtained by summing all the individual molecular interactions of the two bodies. This is known as pairwise additivity of the interaction energy and involves a very important assumption: according to which each interaction may be summed as if it were totally independent of all other interactions. For example, consider a single molecule interacting with a semi-infinite planar surface comprised of another material a distance D away; see figure 2-1. The total interaction of this molecule with the planar solid can be estimated as the sum of the interaction energy between the individual molecule and each molecule of the planar solid. Assuming the planar surface to be a continuum of atomic number density $N_\rho$, the sum of all individual interaction energies may be replaced by the integral in equation 2-20;

$$U_t = -2\pi C N_\rho \int_D^\infty \int_0^\infty \frac{x}{(\sqrt{z^2+x^2})^6}\, dx\, dz\,. \tag{2-20}$$

On evaluation of this integral, we find that the interaction energy of a molecule

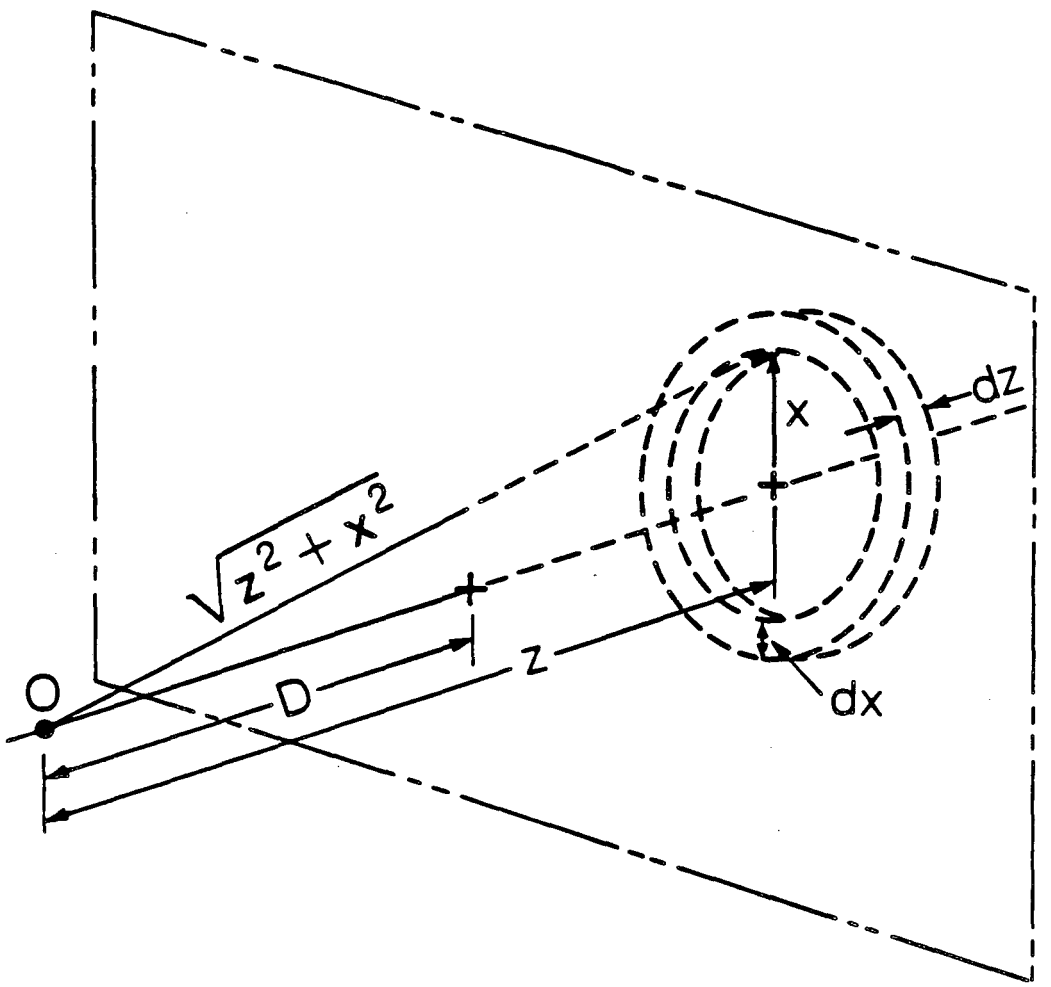


XBL 876-9703

**Figure 2-1:** Volume element for the integration of pairwise interaction energies between a molecule at point O a distance D from a semi-infinite medium.

with a planar surface through a vacuum, $U_{Molec.-Surf.}$, is given by;

$$U_{Molec.-Surf.} = \frac{-\pi C N_\rho}{6 D^3} . \tag{2-21}$$

Through a similar treatment we find that the interaction through a vacuum of two identical planar solids, $U_{Surf.-Surf.}$ is given (Hiemenz, 1977, pp. 411-2) by:

$$U_{Surf.-Surf.} = \frac{-\pi C N_\rho^2}{12 D^2} \tag{2-22}$$

From these two examples, we see that by knowing the value of the variable C, the energy of interaction of molecules 1 and 2 or large bodies made up of molecules 1 and 2 may be found simply by accounting for the effects of geometry.

Hamaker (1937) was the first to realize that the effects of geometry could be separated from the physical-property-dependent contribution to the total interaction energy: he showed that it is possible to tabulate a variable, A, that is particular to each binary system. Then, to calculate the total energy of interaction of two bodies interacting through a vacuum the variable A is used in an equation which describes the effect of that particular geometry. The variable A is now known as the Hamaker constant.

$$A = \pi^2 C N_\rho^2 \tag{2-23}$$

Table 2-2 is a list of several geometries and their interaction energies in terms of the Hamaker constant A. Once again, the great advantage to using Hamaker constants is that the Keesom, Debye, and London interactions are accounted for

in A and once A is determined for a particular interaction, only adjustments for geometry must be made to calculate the total interaction energy.

So far only the interaction of two bodies through a vacuum has been considered. Since the Hamaker constant accounts only for the physical properties of the interacting system, it may be modified to account for the presence of an intervening dielectric medium. As long as the functionality with distance of separation is not changed while accounting for the an intervening dielectric, the effects of geometry on the total interaction energy will remain independent of the physical properties of the system. Therefore, the equations shown in table 2-2 will still apply when the intervening space between two interacting bodies is occupied by a third dielectric medium (Israelachvili, 1985).

It was already shown that McLachlan, using the Lifshitz field theory, was able to account for the existence of a dielectric medium between two interacting molecules. Through a similar development, the Hamaker constant may be modified using the Lifshitz field theory so that it accounts for a third dielectric medium. This theory not only accounts for an intervening dielectric medium, but also for the non-additivity of pairwise interactions due to the influence of other nearby atoms. This is accomplished through a complicated use of Greens functions and will not be reproduced here as Parsegian (1975), Richmond (1975), and Mahanty and Ninham (1976) present excellent derivations of equation 2-24, 2-25 and 2-26.

Table 2-2: Interaction Energies, U, for Various Geometries in Vacuum

| Geometry | Physical Picture | Power Law |
|---|---|---|
| Two Spheres | 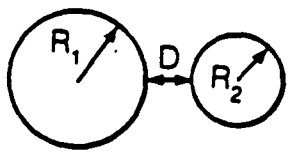 | $U = \frac{-A}{6D} \frac{R_1 R_2}{R_1 + R_2}$ |
| Colinear Cylinders | 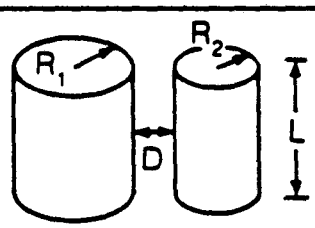 | $U = \frac{-\sqrt{2}\,A\,L}{24\,D^{3/2}} \left(\frac{R_1 R_2}{R_1 + R_2}\right)^{1/2}$ |
| Crossed Cylinders | 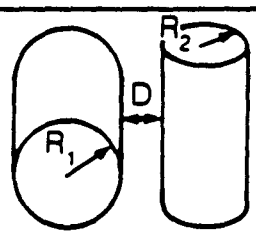 | $U = \frac{-A\sqrt{R_1 R_2}}{6D}$ |
| Sphere and Planar Surface | 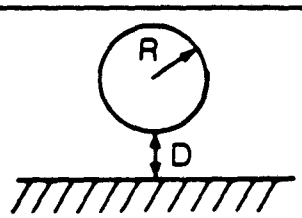 | $U = \frac{-A\,R}{6D}$ |
| Two Planar Surfaces | 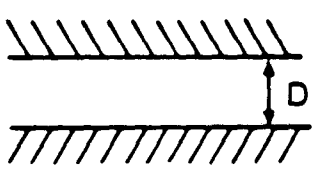 | $U = \frac{-A}{12\,\pi\,D^2}$ |

XBL 876-9698

$$A_{132} = \frac{3\,k_B\,T}{2} \sum_{n=0}^{\infty}{}' \sum_{j=1}^{\infty} \frac{1}{j} \left( G_1(i\nu\sum n)\, G_2(i\nu_n) \right)^j \tag{2-24}$$

where

$$G_1(i\nu_n) = \frac{\epsilon_1'(i\nu_n) - \epsilon_3'(i\nu_n)}{\epsilon_1'(i\nu_n) + \epsilon_3'(i\nu_n)} \tag{2-25}$$

and

$$G_2(i\nu_n) = \frac{\epsilon_2'(i\nu_n) - \epsilon_3'(i\nu_n)}{\epsilon_2'(i\nu_n) + \epsilon_3'(i\nu_n)} \tag{2-26}$$

In equation 2-24, $A_{132}$ represents the Hamaker constant of species 1 interacting with species 2 through medium 3, $\epsilon_1'$, $\epsilon_2'$, and $\epsilon_3'$, represent the dielectric functions of species 1, species 2, and medium 3 respectively, and $\nu_n$ is given by equation 2-12. Equation 2-24 makes it possible to calculate the Hamaker constant for any system where the dielectric function evaluated at imaginary frequencies, $i\nu_n$, is known for each of the three components.

Tabulations of the dielectric function evaluated at imaginary frequencies are difficult to find in the literature. However, the absorption spectra and the index of refraction for several materials are tabulated over a large range of frequencies (Palik, 1985). Using this information and the Kramers-Kronig transformation, shown in equation 2-27, it is possible to construct the desired functions.

$$\epsilon'(i\nu) = 1 + \frac{2}{\pi} \int_0^{\infty} \frac{\omega\,\epsilon''(\omega)}{\omega^2 + \nu^2}\, d\omega \tag{2-27}$$

The Kramers-Kronig transformation uses linear causality and Cauchy's theorem to relate the real and imaginary parts of the dielectric function. For a

discussion of the Kramers-Kronig transformation, see most any electrodynamics or optics textbook, *e.g.*, Jackson (1975), Landau and Lifshitz (1980), Abeles (1972), or Wooten (1972).

## 2.10. Stability of Colloidal and Surfactant Systems

The physical reasons for the stability of colloidal systems was for many years poorly understood. However, in the 1940's, Derjagin and Landau (1941) and Verwey and Overbeek (1948) independently realized the importance of both van der Waals interactions and double layers in explaining the stability of these systems. Their theory, called the DLVO theory, showed that the attractive force between colloidal particles due to van der Waals interactions could be opposed by the repulsive force resulting from overlapping double layers. These opposing forces provide stability to the system. The DLVO theory has made it possible to predict many properties of colloidal systems including particle size effects, salting effects, and coagulation kinetics.

Another important concept in the stability of colloidal and other thin film systems is the disjoining pressure of a thin film. The disjoining pressure, first proposed by Derjagin and Kussakov (1939a, 1939b), is defined as the pressure inside a thin film that is required to provide mechanical equilibrium against forces acting to cause the film to thin. More recently, Derjagin and Churaev (1978) and Teletzke (1983), define the disjoining pressure, $\Pi$, as the force/area required to maintain a thin film of thickness h between two flat plates. A more formal definition of $\Pi$ is given by:

$$\Pi = P_n - P_o \tag{2-28}$$

where $P_n$ is the normal component of pressure acting from within on the surface of the film and $P_o$ is the bulk Laplacian pressure within the film. When the disjoining pressure is negative, sometimes referred to as conjoinig pressure, the surfaces of the thin film attract one another. Conversely, when the disjoining pressure is positive the surfaces of the thin film repel one another.

The disjoining pressure may be calculated from the derivative of the total energy of interaction of two surfaces with distance of separation.

$$\Pi = -\frac{dU_{Surf.-Surf.}}{dx} \tag{2-29}$$

If the interaction energy decreases with decreasing distance of separation, a net attraction will be experienced by the surfaces and the disjoining pressure will be negative. Conversely, if the interaction energy increases with decreasing distance of separation, a net repulsion will be experienced and the disjoining pressure will be positive.

Many efforts have been made to directly measure the repulsive or attractive force between two surfaces (Israelachvili and Tabor, 1973). The most successful of these utilizes molecularly smooth mica cylinders. The cylinders are brought into close proximity and the force between them is measured by very sensitive springs. The distance of separation is measured by multiple beam interferometry to within $\pm 0.1$nm. The force of interaction between mica plates has been measured in air and various liquid systems for distances of separation ranging from 2-130 nm. (Tabor and Winterton, 1969; Israelachvili and Tabor, 1972;

Coakley and Tabor, 1978). Their results show that even in the most non-ideal systems, theory agreed with experiment to within 30%.

The disjoining pressure of a thin film is a direct consequence of the surfaces of the thin film being in close proximity to one another. Several effects combine to produce the disjoining pressure. These are van der Waals interactions, electrostatic effects resulting from charged interfaces and diffuse double layers, and steric effects. Generally speaking, steric effects are only important in films of a few molecular layers in thickness, however, in contrast van der Waals and electrostatic effects can be important over a much larger distance, $>1000$ Å (Hough and White, 1980; Adamson, 1982; Israelachvili, 1985). Together, the DLVO theory and the disjoining pressure have been shown to explain many related phenomena such as the stability of soap bubbles, soap films, and coalescence and film rupture of other thin film systems (Overbeek, 1960; Marrucci, 1969; Ruckenstein and Jain, 1974; Williams and Davis, 1982; Sharma and Ruckenstein, 1986).

# Chapter 3

# Surface Tension, Transport, and Double Layers

## 3.1. Introduction and General Observations

One may wonder what ties surface tension, transport and double layers together and warrants these appearing in the same chapter. The answer lies not in their similarities, but in their differences. An understanding of these phenomena and how each affects thin liquid films is crucial to determining their importance to the films of concern in this study. To provide a basis on which to determine the importance of each of these affects, a description of general observations made by myself and previous workers will be presented. The exact details of the present experimental method, observational technique, and a complete description of the observations are presented in chapter 6.

When the aqueous solution covering a large clean metallic plate is lowered and replaced with pure nitrogen saturated with water vapor (see figure 3-1) a thin film of solution remains on the surface of the plate. This liquid drains viscously over the next several hours according to Jeffreys' equation (eqn 2-5). However, at long times the drainage of these films stops altogether and they achieve a steady time-invariant profile. These steady profiles have been observed to remain unchanged for up to two months at which time the experiment was terminated. The time-invariant profiles have thicknesses between 0.1 and 0.5 $\mu$m. These observations should be kept in mind during the following

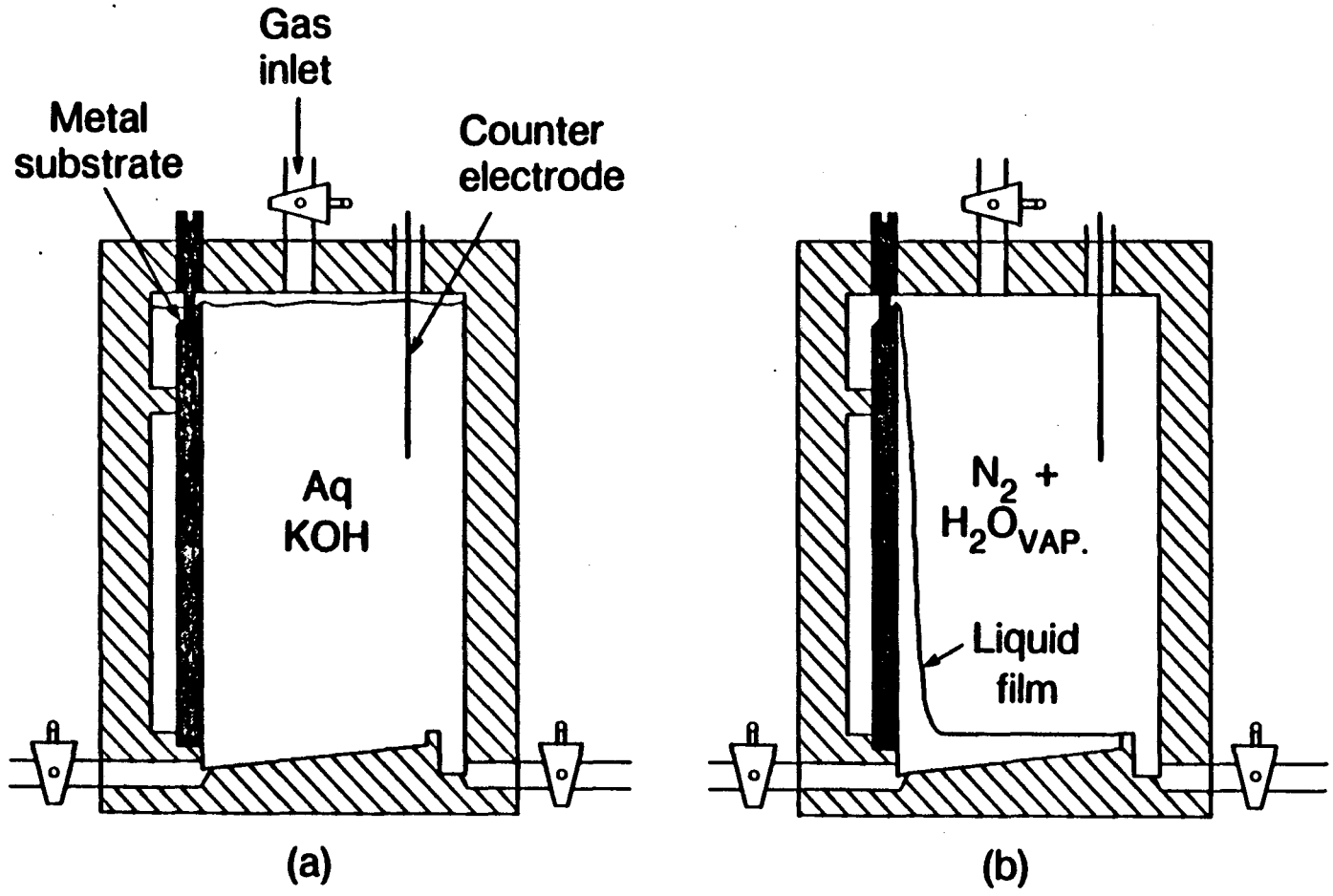


XBL 8611-9959 A

**Figure 3-1:** Schematic of the liquid film cell before and after the liquid level is lowered: (a) filled, (b) drained. KOH is shown as the liquid phase.

discussion of the effects of surface tension, transport and double layers.

### 3.2. Surface Tension

A quick calculation reveals that: given a 0.5 $\mu$m film extending 10 cm above the bulk liquid level, the mass of this film is only 0.5 mg/cm of width. Integrating to find the potential energy required to lift this film shows that only 2.45 ergs/cm of width is required. This represents a small energy expenditure, however, the crucial factor is not the energy expended but that the stress at the liquid/vapor interface should not exceed the liquid/vapor surface tension. If this were to occur, the surface would no longer be capable of supporting the weight of the liquid film. The surface would extend, creating new surface area, resulting in a flow of liquid back to the bulk which thins the film and reduces its total weight within the limits that surface tension is capable of supporting. To determine the total weight the interface must support, the shape of the liquid/vapor interface must be found.

One means of accomplishing this is to determine the interfacial shape which minimizes the total energy. In this problem we have two processes which cause an increase in the energy of the system. These are the increase in potential energy due to the lifting of the film, and the increase in surface energy due to the increased surface area as opposed to not having a film at all. These two energy terms are written in equations 3-1 and 3-2, see figure 3-2 for a description of the geometry.

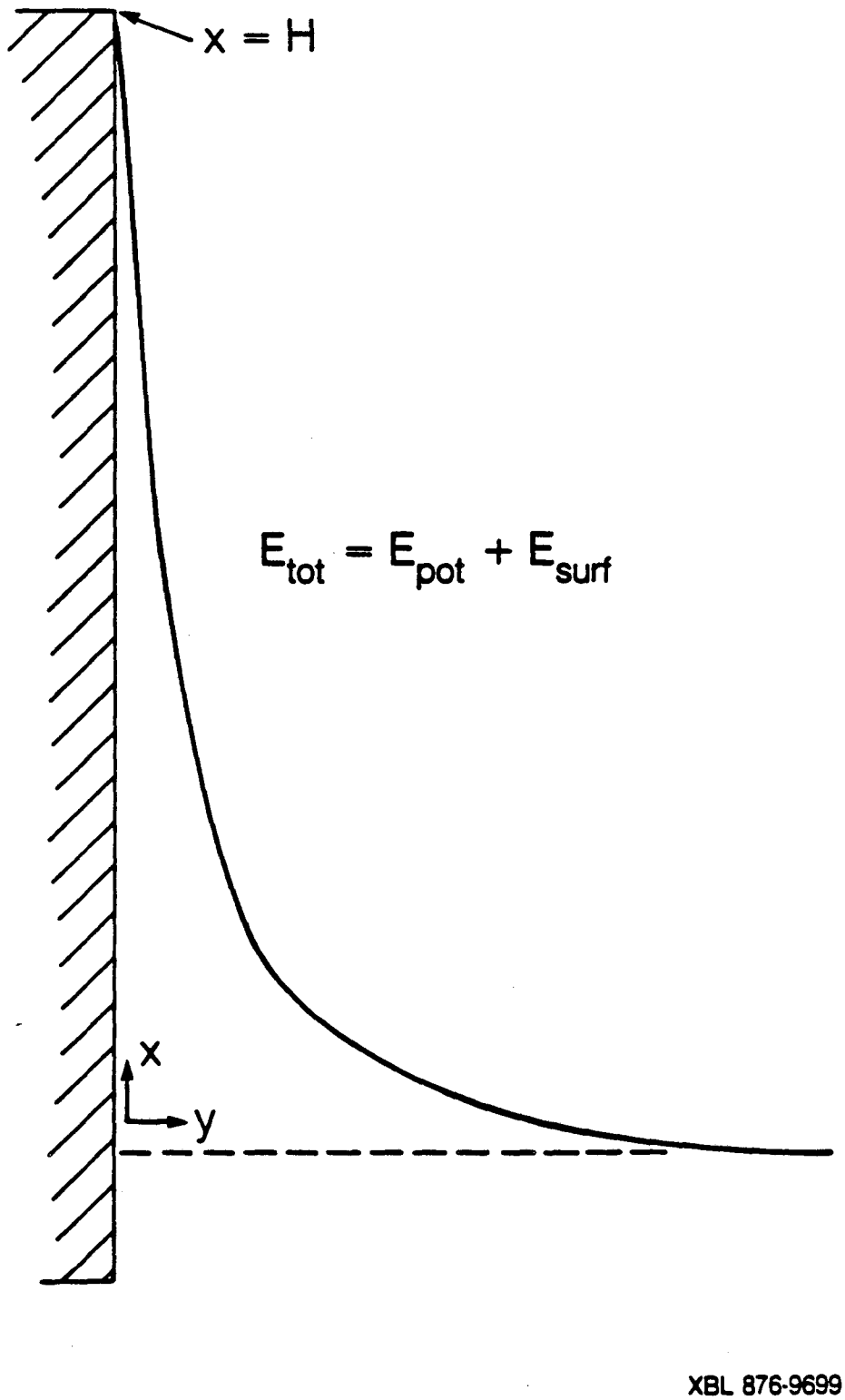


**Figure 3-2:** Definition of coordinates for the calculation of the profile of a film of height, H, which minimizes the total surface and potential energy.

$$E_{pot} = \rho g w \int_0^H y x \, dx \tag{3-1}$$

$$E_{surf} = \gamma w \int_0^H \sqrt{1 + y'^2} \, dx \tag{3-2}$$

In these equations, $\rho$ is the liquid density, g the gravitational constant, w the width of the film, H is the total height the film rises above the bulk liquid level, $\gamma$ is the liquid/vapor surface tension, and $y'$ is the derivative of y with respect to x. The total energy is the sum of equations 3-3 and 3-4. The equilibrium shape will be given by the function, $y = F(x)$, that gives the minimum total energy.

The calculus of variations was used to determine y (details of applying the method to this problem may be found in appendix B). After applying the method, integrating once and using the boundary condition; as $x \rightarrow 0$, $y' \rightarrow -\infty$, the following equation results;

$$y' = \frac{B x^2 - 1}{(2B)^{1/2} x (1 - \frac{B}{2} x^2)^{1/2}} \tag{3-3}$$

where B is the following group of parameters.

$$B = \frac{\rho g}{2 \gamma} \tag{3-4}$$

Before solving for the shape of the interface, valuable information may be obtained from the form of the slope given by equation 3-3.

Referring to figure 3-2, it is obvious that in the chosen coordinate system, the slope of the liquid/vapor interface must always be non-positive. At $x = 0$, y is a very large number, and as x increases, y must decrease. It is physically

impossible for y, the film thickness, to increase as x increases as that would result in a film that becomes thicker with increasing distance above the bulk liquid level, an inherently unstable configuration. Therefore, the slope, $y'$, must always be less than or equal to zero. Applying this condition to equation 3-3, we find that;

$$\frac{\rho g}{2\gamma} x^2 - 1 \leq 0 \tag{3-5}$$

or, solving for the maximum value for x;

$$x_{max} = H = \left(\frac{2\gamma}{\rho g}\right)^{1/2} \tag{3-6}$$

For pure water having a surface tension of 72 ergs/cm$^2$ and a density equal to 1, H = 0.38 cm. Equation 3-6 gives the physical limit to the height which surface tension alone will allow a liquid to attain when it wets a solid with a contact angle of zero degrees. Therefore, assuming that surface tension is the only source of support available to a water film we know that at x = 0.38 cm., y = 0. This point can be used as a boundary condition for the solution of equation 3-3. The solution is shown in figure 3-3. It was obtained numerically using a fourth order Runge-Kutta method. The calculated profile shown is identical to that of water wetting a solid with a contact angle of zero degrees and may be compared with experimental profiles found in Hartland and Hartley (1976) or with calculated results using the method of Bashforth and Adams (1883). The method of Bashforth and Adams, the standard commonly used even today, is cumbersome, requiring the the calculation of a shape parameter and the curvature of the film

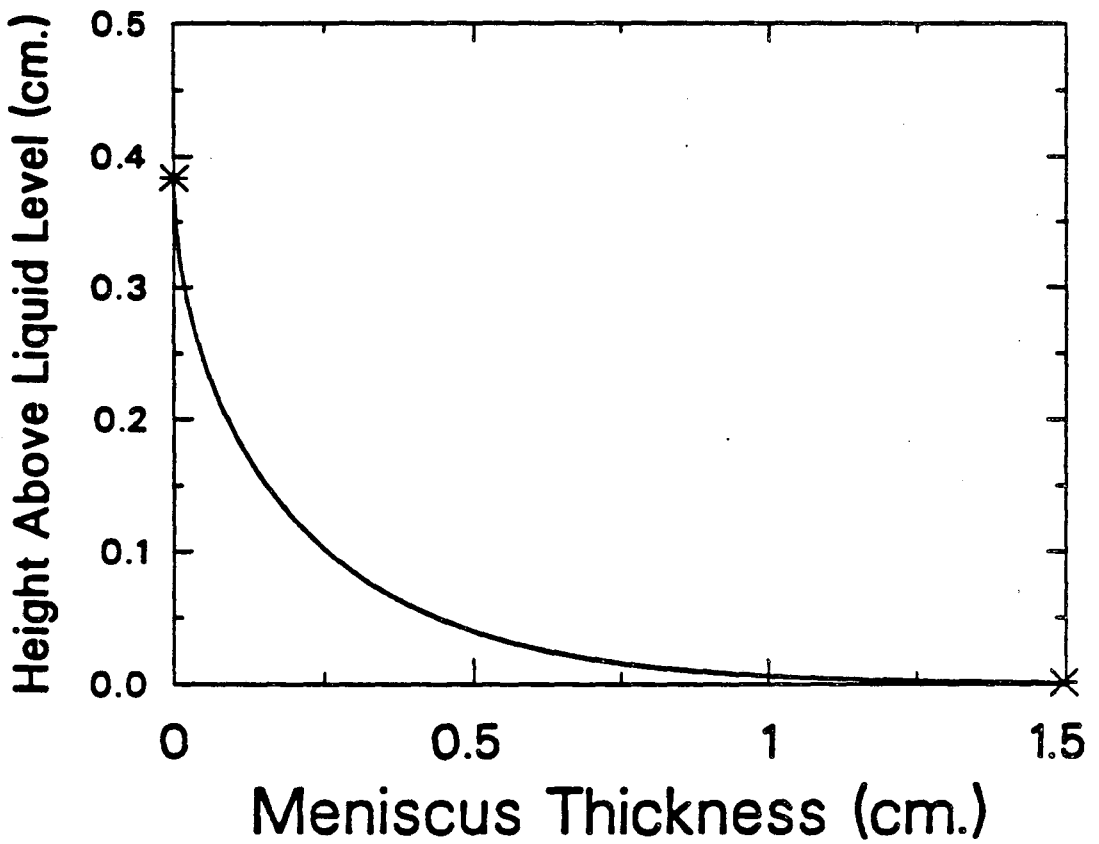


XBL 867-2724

**Figure 3-3:** The shape of the meniscus for water, $\gamma = 72$ dynes/cm, $\rho = 1.0$ gm/cm$^3$, wetting a solid with a 0° contact angle.

at the three phase contact line. A series of curves must be generated and the best fit is then chosen, or an iterative technique is used until the contact angle and total extent of the curve match observations. The minimum energy method described here works for any system exhibiting any contact angle. It is very easy to use requiring only the value of the contact angle. The fourth order Runge-Kutta integration technique is a simple well behaved initial value integration technique that is inexpensive to use. For complete details see appendix B.

The fact that surface tension is only capable of explaining the intrinsic meniscus is not particularly surprising. Bashforth and Adams (1883) verified this when they showed that the meniscus can be predicted solely from energetic considerations, as was done here. However, we have learned two important items. The height of meniscus rise of any fluid wetting a vertically oriented planar solid with a zero contact angle is given by equation 3-6. Any film that exists more than a distance H above the bulk liquid level must be influenced by forces other than those of gravity and capillarity effects.

### 3.3. Transport

A thin draining liquid film could be maintained by a continuous supply of liquid. This would result in a dynamic situation which would reach a steady time-invariant profile when the rate of supply equals the rate of drainage. The driving force for this supply could be a vapor pressure difference between the bulk liquid and the surface of the film. The vapor pressure difference would cause evaporation at the bulk liquid surface and condensation on the film surface. The problem then is to estimate the vapor pressure difference required to

maintain a film of the observed thickness.

The flow, Q, within a uniformly thick film may be found by solving equations 2-1, 2-2, and 2-3 for the velocity profile and then integrating the velocity profile over the thickness of the film.

$$Q = \frac{\rho g w \delta^3}{3 \mu} \tag{3-7}$$

For a dynamic steady state to occur the flow rate in the film, and the flux, flow per area, through the gas phase must be equal. Assuming a linear vapor pressure profile from the bulk liquid to the film, the flux, $\Phi$ is given by;

$$\Phi = \frac{D^* M_w \Delta P}{L R T} \tag{3-8}$$

where $D^*$ is the diffusion coefficient of vapor through the gas phase, $M_w$ is the molecular weight of the vapor, $\Delta P$ is the vapor pressure difference from the bulk surface to the film surface, L is the length over which diffusion takes place, and R is the gas constant. Assuming a 10 cm. square surface, a 10 cm. diffusion length, and using physical properties for water, the $\Delta P$ is estimated to be 0.1 mm Hg.

A reason for a vapor pressure difference to exist between the bulk liquid and the film surface is, *e.g.*, a temperature difference between these surfaces. From vapor pressure data for water, it can be determined that a 0.1 °C temperature difference between the surfaces is required. Although not a large difference, it is difficult to imagine how this temperature gradient could be maintained in a closed system. The transport process of evaporating from the bulk and

condensing on the film surface would inherently transfer heat simultaneously with mass. The direction of heat transfer would cause a cooling of the bulk surface and a heating of the film surface. This process directly counters that needed to maintain the film surface cooler than the bulk to maintain the vapor pressure difference needed for the transport of vapor from the bulk to the film.

Another means to supply liquid to a draining film is with an imposed surface tension gradient which pulls liquid up along the vapor/liquid interface in the same way a Marangoni film lifts liquid above the intrinsic meniscus. A steady state film resulting from such a surface tension gradient would exhibit a flow in the upward direction at the liquid/vapor interface and a flow of equal volume downward in the interior of the film, as shown in the inset in figure 3-4. A decision as to the reality of such a situation may be made if the surface tension gradient required to maintain a given film thickness can be determined.

Once again, the flow rate within the thin film may be determined by solving equations 2-1, 2-2 and 2-3. Now however, the boundary condition at the liquid/vapor interface is no longer given by zero stress at this interface. The new boundary condition is that the stress is given by the surface tension gradient at that interface,

$$\text{at} \quad x = 0, \qquad \tau_{xh} = -\frac{d\gamma}{dh} . \tag{3-9}$$

After solving for the velocity profile, integrating to find the flow rate and setting the flow rate equal to zero, we find that to achieve a steady state profile the gradient of the surface tension is given by equation 3-10.

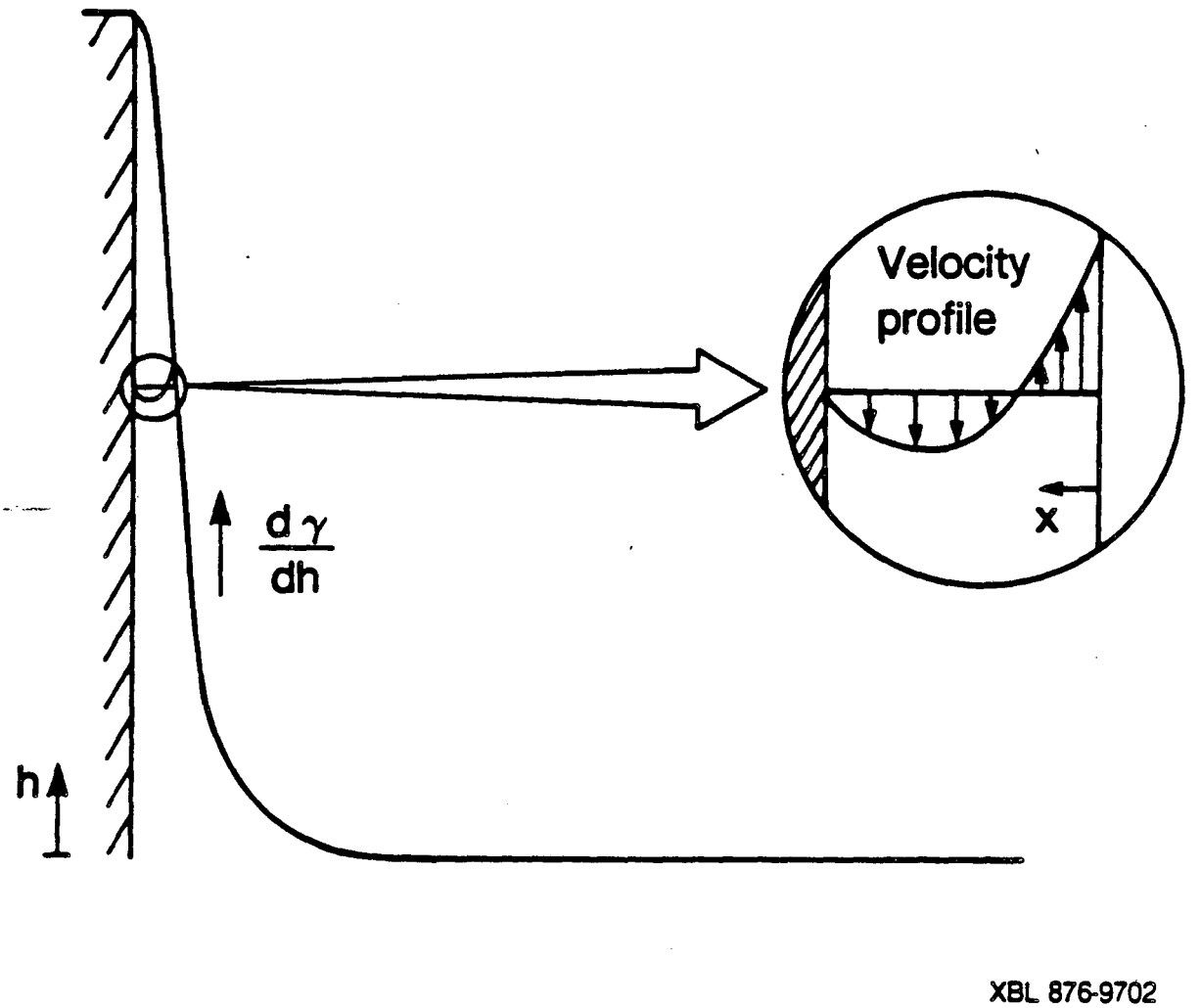


**Figure 3-4:** Geometry and velocity profile within the film for flow driven by a surface tension gradient $d\gamma/dh$.

$$\frac{d\gamma}{dh} = \frac{2\rho g \delta}{3} \tag{3-10}$$

For a 0.5 $\mu$m thick film the required surface tension gradient equals 0.0327 ergs/cm$^3$. If the film is an aqueous KOH solution the surface tension of the film will increase with increasing KOH concentration. If the bulk solution is at a concentration of 1 N, to maintain a film extending 10 cm. above the bulk liquid level the concentration at the top of the film would need to be 1.19 N. It is well known that dissolving an inorganic salt in water results in the suppression of the vapor pressure of water. Therefore, if this situation were to arise there would be an immediate transport of water vapor through the gas phase to reduce the concentration difference between the bulk and the film. However, if there were also a temperature difference between the film and the bulk liquid, perhaps the situation could be stabilized. Unfortunately, this would require the top of the film to be nearly 4 °C colder than the bulk liquid, a highly improbable situation in a closed system.

It is clear that any transport mechanism proposed to stabilize these supermeniscus films will tend to diminish the gradient upon which it depends for a driving force. Therefore, to maintain these driving forces, a continual input or removal of energy is required. This is simply not possible in the closed-isothermal system used in this study.

### 3.4. Double Layers

The presence of a diffuse double layer at electrode/electrolyte interfaces was discussed in section 2.5. The presence of a diffuse double layer is not restricted

to interfaces having an imposed potential. As the result of the specific adsorption of ionic species, a surface can exhibit a diffuse double layer without being polarized. By the same mechanism, liquid/liquid and liquid/vapor interfaces can also exhibit diffuse double layers (Llopis, 1976). Since the surfaces of a thin film are in close proximity, the double layers at the two surfaces may interact. If the double layers result from surface charges of the same sign, the surfaces will repel one another, if they result from surface charges of opposite sign they will attract one another. This section will evaluate the shape of a liquid vapor interface resulting from the interaction of surfaces having surface charges of the same sign.

Given a system such as platinum/aqueous KOH/nitrogen saturated with water vapor, two double layers will form. At the platinum electrolyte interface, hydroxide ions will be adsorbed on the surface of the platinum. Hydrated hydroxide ions are smaller than hydrated potassium ions and will be able to get physically closer to the platinum surface than will the hydrated cation. The plane defined by the point of closest approach of the hydrated anions is called the inner Helmholtz plane, IHP. The plane lying just outside the IHP defined by the closest approach of hydrated cations to the platinum surface is called the outer Helmholz plane, OHP. Since only negatively charged species or neutral solvent molecules lie within the OHP, the potential at the OHP will be negative. Outside the OHP lies the diffuse double layer in which the potential changes roughly exponentially from the value at the OHP to the value in the bulk solution, as will soon be defined.

At the electrolyte/vapor interface, hydroxide ions, because of their small size, will be able to get closer to the interface than will hydrated potassium ions. This causes an effective separation of charge at the interface and an apparent negative surface charge on the liquid/vapor interface. If the metal/liquid and liquid/vapor surfaces are close enough together, the diffuse portions of both double layers, that portion lying outside the OHP, may interact with each other. A sketch of how this might occur appears in figure 3-5.

For a supermeniscus film to exist in equilibrium the pressure inside and external to the film must be equal. Because the liquid/vapor interface is nearly flat for these films, the total pressure inside these films must be equal to the pressure in the vapor phase, the atmospheric pressure. The capillary pressure, $P_{Ca}$, within the thin film will be equal to the atmospheric pressure at the bottom of the meniscus and decrease linearly with distance above the bulk liquid level. The purpose of this section is to evaluate the importance of double layer interactions. Therefore, the disjoining pressure, $\Pi$, will be assumed to be comprised of only the pressure resulting from the overlapping of two diffuse double layers. Also, since the total pressure within the thin film must equal atmospheric pressure in order for the film to be stable, the sum of $\Pi$ and $P_{Ca}$ will equal 1 atmosphere.

$$P_{Ca} = 1 - \rho g h \tag{3-11}$$

$$\Pi = P_{DL} = 1 - P_{Ca} = \rho g h \tag{3-12}$$

Therefore at any height, h, the magnitude of the pressure caused by the interac-

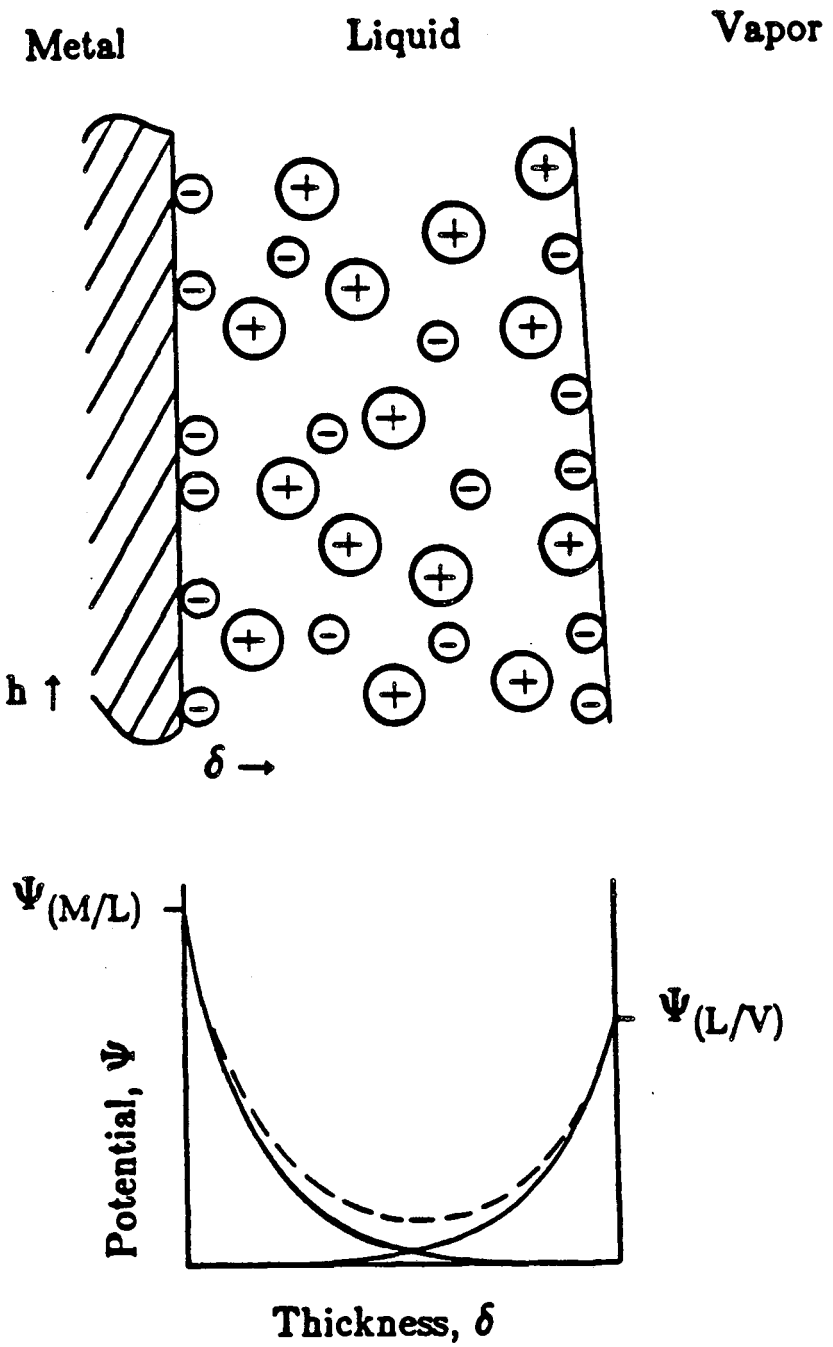


XBL 869-3351

**Figure 3-5:** Schematic representation of the distribution of ionic species within a film in which the diffuse portions of the double layers (solid lines) at the two interfaces are overlapping. The potential distribution within the film resulting from such an interaction is also shown (dashed lines).

tion of two overlapping diffuse double layers, $P_{DL}$, is given by equation 3-12.

The force per unit area between two interacting double layers in a symmetrical electrolyte was derived by Langmuir (1938) and is given by:

$$P_{DL} = 2\,[c]\,k_B\,T\,(\cosh y_m - 1) \tag{3-13}$$

where [c] is the concentration of the electrolyte, and $y_m$ is the dimensionless minimum potential between the surfaces (see equation 3-15). The minimum potential, $y_m$, is a function of the potential at the OHP of each interface, the electrolyte concentration, and the distance of separation of the interfaces. Knowing these parameters, $y_m$ may be found using the tables calculated by Devereux and de Bruyn (1964). However, with two assumptions it is possible to directly calculate $y_m$.

Verwey and Overbeek (1948 ch. 2) showed that if we are interested only in knowing the potential far from the interface, the dimensionless potential is approximately given by;

$$y = y_1\,e^{-\xi} \tag{3-14}$$

where $y_1$ is the dimensionless potential at the OHP and $\xi$ is the dimensionless distance from the OHP. The potential and distance are non-dimensionalized in the following manner;

$$y = \frac{v_a\,e_-\,\Psi}{k_B\,T} \tag{3-15}$$

$$\xi = \kappa x , \quad \text{where} \quad \kappa^2 = \frac{8 \pi [c] v_a^2 e_-^2}{\epsilon_o k_B T} \tag{3-16}$$

$v_a$ is the valence of the symmetrical electrolyte, $e_-$ is the charge on an electron, $\Psi$ is the electrical potential, and $1/\kappa$ is the Debye length.

The second assumption is that for small interactions, the total potential in the region of overlapping double layers is approximately equal to the sum of the potentials derived from the individual double layers. With these assumptions the following expression may be derived;

$$y_m = 8 ( \Gamma_1 \Gamma_2 e^{\xi_\delta} )^{1/2} \tag{3-17}$$

$$\Gamma_1 = \frac{e^{y_1/2} - 1}{e^{y_1/2} + 1} \tag{3-18}$$

$$\Gamma_2 = \frac{e^{y_2/2} - 1}{e^{y_2/2} + 1} \tag{3-19}$$

where $y_1$ and $y_2$ are the dimensionless potentials at the OHP of each interface and $\xi_\delta$ is the dimensionless distance of separation between the interfaces. Working from equation 3-12 to 3-17, we may now calculate consecutively the disjoining pressure as a function of height, the minimum potential as a function of disjoining pressure, and the distance of separation as a function of minimum potential. Therefore, it is possible to find the thickness of the thin film at any given height.

Now, it is only necessary to determine the potential at the OHP for each of the interfaces to make use of the above equations. This is not so difficult for the

liquid/vapor interface as there are many estimates made from deflection of droplets or jets of electrolyte passing through electric fields (Llopis, 1976). From the review by Llopis the potential at the OHP of a liquid/vapor interface will lie between -0.2 and -1.0 volts, with respect to a standard hydrogen electrode, depending on the ionic strength and salt in the electrolyte. For these calculations, a value of -1.0 volts will be used as an upper limit on the value of the liquid/vapor surface potential.

The potential at the OHP of a metal/liquid interface is not as clearly determined. Few measurements have been made largely because of the difficulties associated with maintaining a contaminant free surface (Delahay, 1965; Bard and Faulkner, 1980). However, the potentials of zero charge for several electrolytes on different metals have been estimated from differential capacitance measurements or maximum hardness tests (Delahay, 1965, ch. 6). The potential of zero charge is defined as that potential where there is no surface charge at the interface, hence the potential at the OHP may be assumed also to be zero. As the potential of the metal is changed from the potential of zero charge to zero potential, anions will begin to adsorb on the surface causing the potential at the OHP to become negative. If we assume that the potential on the metal and the potential at the OHP are linearly related with a slope of one, then when the potential on the metal equals zero, the potential at the OHP will be equal to the potential of zero charge. Essentially, this is the same as assuming the surface and OHP behave as a parallel plate capacitor. In other words if x volts are required such that no charged species adsorb onto the surface, at zero imposed

voltage, the potential at the OHP will be x volts. From tables of potentials of zero charge appearing in Newman (1973), Bard and Faulkner (1980), and Delahay (1965) a value of -0.2 volts was chosen as an estimate of the potential at the OHP of a typical metal/electrolyte interface.

Figure 3-1 shows the calculated liquid/vapor interface profile for various electrolyte concentrations. The three profiles shown are all less than 600 Å in thickness. The most notable feature of these profiles is their dependence on electrolyte concentration. The thickest profile is for the most dilute electrolyte. This is perfectly reasonable because the Debye length, $1/\kappa$, is a measure of the extent of the diffuse double layer, and the Debye length is proportional to the inverse square root of the electrolyte concentration. Curve 4 in figure 3-6 illustrates the effect of substantially increasing the voltage between the interfaces. The fact that so little effect is observed when the surface potential is increased justifies the assumptions made in the beginning. The reason such a small increase in film thickness is observed is that the minimum potential is very small. Therefore, each of the double layers has decayed to a very small value and the point at which the minimum potential occurs is several Debye lengths from the interfaces. Both the assumptions made hold only at large distances in comparison to the thickness of the double layer and this is indeed the situation. Also, the fact that the potential at the OHP has little influence on the calculated profile shows that it is unnecessary to try to determine the potential at the OHP to any more accuracy than has been done.

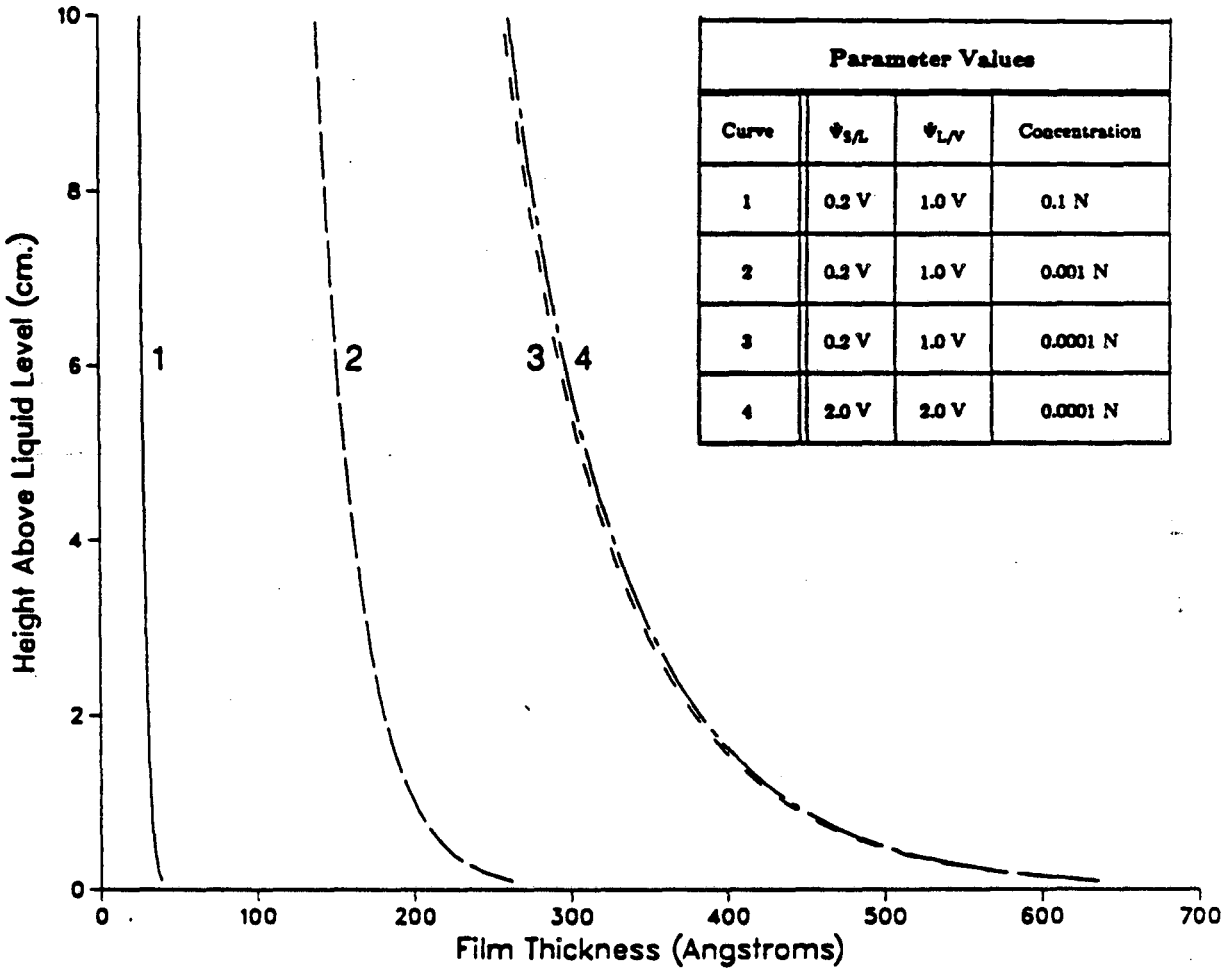


| Parameter Values | | | |
|---|---|---|---|
| Curve | $\Psi_{S/L}$ | $\Psi_{L/V}$ | Concentration |
| 1 | 0.2 V | 1.0 V | 0.1 N |
| 2 | 0.2 V | 1.0 V | 0.001 N |
| 3 | 0.2 V | 1.0 V | 0.0001 N |
| 4 | 2.0 V | 2.0 V | 0.0001 N |

XBL 876-9700

**Figure 3-6:** Equilibrium film profile derived from the interaction of two plane parallel double layers. Parameter values for each curve are listed in the inset.

The following conclusions can be drawn from this section. (1.) The profile of a film stabilized by interfacial repulsion caused by the overlap of two diffuse double layers may be calculated using equations 3-12 to 3-17. (2.) The calculated profiles for reasonable values of the potential at the outer Helmhotz plane are shown to be on the order of 20 to 350 Å thick. (3.) The thickness of these films is weakly dependent on the voltage at the outer Helmholtz plane. (4.) The thickness is highly dependent on the electrolyte concentration of these films, and it is predicted to decrease with increasing concentration.

# Chapter 4

# van der Waals Interactions in Thin Films

## 4.1. Introduction

The origin of van der Waals interactions was discussed in sections 2.6 and 2.7. In this chapter, we will specifically apply these interactions to thin electrolyte films on metal surfaces. The meaning and source of repulsive forces between interfaces will be discussed. The construction of dielectric functions from electromagnetic absorption and index of refraction data will be included here as will the use of these dielectric functions to calculate the Hamaker constant of three- phase systems.

Retardation effects will also be considered and an equation will be derived for the form of the retarded Hamaker constant. The retarded Hamaker constant is not only dependent on the physical properties of the matter that makes up the system, but also on the separation distance of the interacting bodies. Limiting values for the retarded Hamaker constant will be determined, and its dependence on the distance of separation will be described. Finally, predictions of film profiles resulting from van der Waals interactions will be presented for comparison to measured data in later chapters.

## 4.2. Negative Hamaker Constants

For all the systems discussed in section 2.7 (see table 2-2) the total energy of interaction is inversely proportional to some power of the distance of

separation of the interacting bodies.

$$U_t = -\frac{A\,K}{D^n} \tag{4-1}$$

In equation 4-1, A is the Hamaker constant, K is a group of positive valued parameters that depend on the geometry, D is the separation distance between the bodies, and n is a positive number greater than or equal to one. Clearly, as the distance of separation decreases, the magnitude of the energy of interaction will increase. If the Hamaker constant is positive, the energy of interaction will be negative. Therefore, a decrease in the distance of separation will lead to a decrease in the total system energy and thus an attraction between the interfaces. Conversely, if the Hamaker constant is negative, the energy of interaction will be positive. Therefore, a decrease in the distance of separation will lead to an increase in the overall energy and thus a repulsive interaction between the surfaces.

As was stated earlier, van der Waals interactions between molecules in a vacuum are always attractive. With this being the case, the question must arise; is it possible to sum an inherently attractive interaction and find an apparent repulsive force between two surfaces? The answer is unequivocally yes, as long as the molecules are interacting through a third medium. This possibility was first alluded to at the end of section 2.6. The conditions necessary to exhibit an apparent repulsive interaction are as follows:

1) There must be three unique phases involved, therefore, any two bodies interacting through a vacuum will always attract one another. Also, any two

identical phases interacting through a third will always attract one another.

2) The energy of interaction of at least one of the bodies with the medium separating them must be stronger than the interaction energy of the bodies with one another.

Hamaker (1937) first argued in favor of negative values of the Hamaker constant in his original paper on the subject. Derjagin and Kussakov (1939a) presented a similar argument in support of repulsive forces between surfaces. The following will be an argument using elements of both Hamaker and Derjagin and Kussakov. It is presented to provide an understanding of the origin of repulsive forces from an interaction which on the intermolecular level is purely attractive.

To show how this repulsive force might arise, we will consider the energy of interaction of two bodies immersed in a surrounding medium. Let A and B represent bodies 1 and 2. Let A and B be immersed in an infinite medium, C. Furthermore, let A′ represent a region of the medium C which has the same shape and volume as A, but contains the medium C. Likewise, let B′ represent a region of the medium C which has the same shape and volume as B, but contains the medium C. Initially, as shown in figure 4-1(a), bodies A and B are completely immersed in the surrounding medium, C, and are separated by a very large distance. B′ is positioned a small distance from A, and A′ is positioned a small distance from B. The total energy for the system shown in figure 4-1(a) may be written as follows;

$$E_{tot} = E_A + E_{B'} + E_{AB'} + E_{AC} + E_{B'C} + E_B + E_{A'} + E_{BA'} + E_{BC} + E_{A'C} \tag{4-2}$$

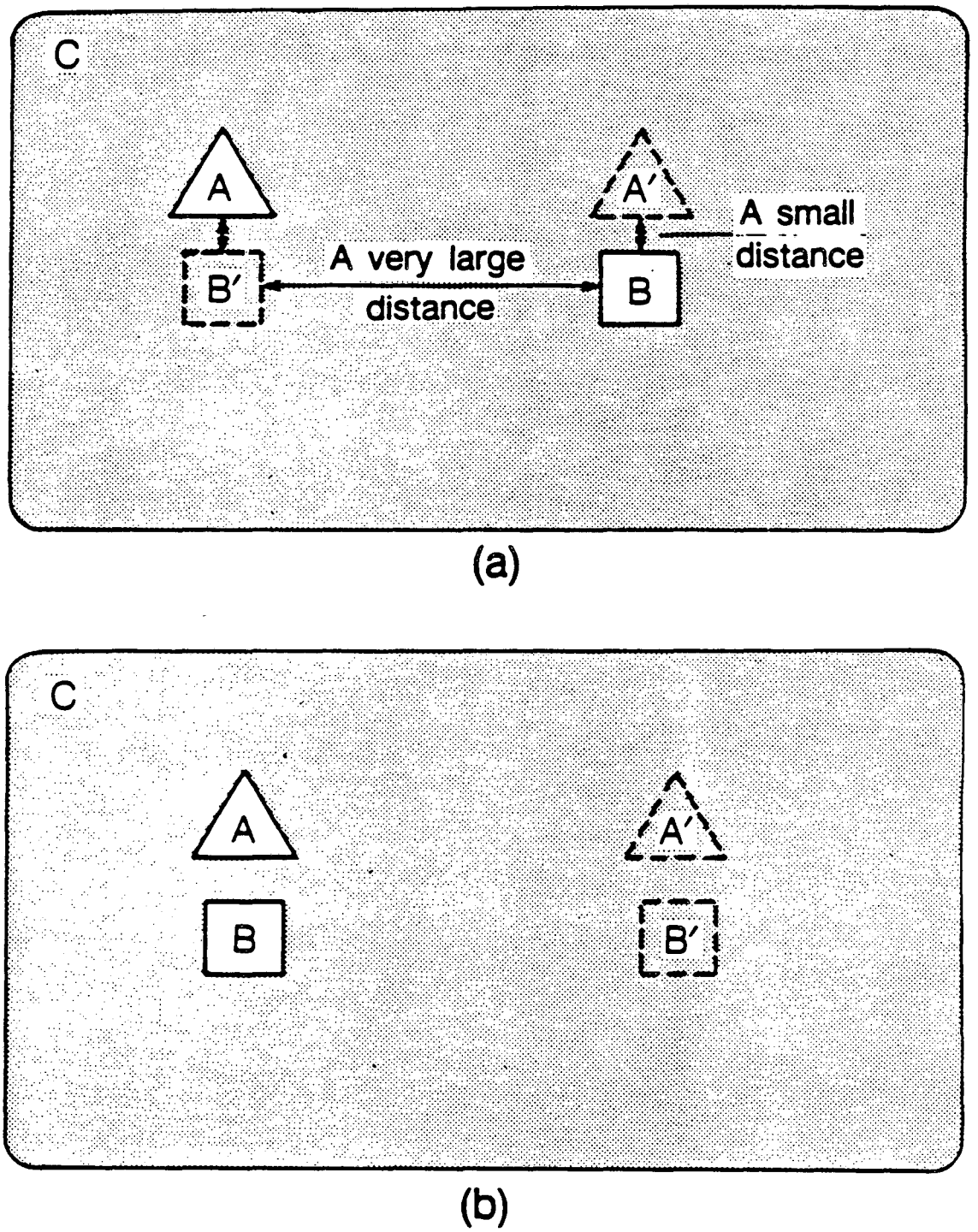


XBL 876-9697

**Figure 4-1:** Schematic of the geometry change when body B is moved from infinity (represented by (a)) to within a small distance of body A (represented by (b)). A′ and B′ represents regions oof the surrounding medium C which have the same shape and volume as bodies A and B.

The terms used in equation 4-2 are defined in table 4-1. Note it is assumed that each term appearing in table 4-1 results in a reduction of the total system energy and therefore each term will have a negative value. All the terms in table 4-1 are relative to a consistent but arbitrary reference state the exact conditions of which are not important since the final result will be given as the difference between two energy states.

We would like to compare the energy given by equation 4-2 with the system energy when B is very close to A, represented by figure 4-1(b). To evaluate this energy, B must be moved within a small distance of A. When B is thus moved a corresponding volume of the surrounding medium, B′, is displaced. The net result of changing the system from that represented by figure 4-1(a) to that represented by figure 4-1(b) is that bodies B and B′ exchange position. Again, using the definitions in table 4-1, the total energy of the system shown in figure 4-1(b) may be written as,

$$E_{tot} = E_A + E_B + E_{AB} + E_{AC} + E_{BC} + E_{A'} + E_{B'} + E_{A'B'} + E_{A'C} + E_{B'C} \tag{4-3}$$

The change in energy from having A and B separated by an infinite distance to having A and B in close proximity may now be found by subtracting equation 4-2 from 4-3 resulting in 4-4.

$$\Delta E_{tot} = E_{AB} + E_{A'B'} - E_{AB'} - E_{BA'} \tag{4-4}$$

By definition, each energy term of equation 4-4 is less than 0. Therefore, the change in energy from infinite separation to a small separation will be

Table 4-1: Definition of Terms for Equations 4-2 through 4-4

| Term | Definition |
|---|---|
| $E_A$ | Internal energy of body A |
| $E_B$ | Internal energy of body B |
| $E_{A'}$ | Internal energy of body A′ |
| $E_{B'}$ | Internal energy of body B′ |
| $E_{AC}$ | Energy of interaction between body A and the surrounding medium, C |
| $E_{BC}$ | Energy of interaction between body B and the surrounding medium, C |
| $E_{A'C}$ | Energy of interaction between body A′ and the surrounding medium, C |
| $E_{B'C}$ | Energy of interaction between body B′ and the surrounding medium, C |
| $E_{AB}$ | Energy of interaction between bodies A and B |
| $E_{AB'}$ | Energy of interaction between bodies A and B′ |
| $E_{BA'}$ | Energy of interaction between bodies B and A′ |
| $E_{A'B'}$ | Energy of interaction between bodies A′ and B′ |

negative if the magnitudes of $E_{AB}$ and $E_{A'B'}$ are larger than $E_{AB'}$ and $E_{BA'}$. This leads to an attractive force between bodies A and B. However, if the magnitudes of $E_{AB}$ and $E_{A'B'}$ are smaller than $E_{AB'}$ and $E_{BA'}$ the change in energy will be positive and an apparent repulsive force between bodies A and B will result. Another way of stating this result is that bringing bodies A and B from infinity into close proximity is energetically favorable only if the interaction between the two bodies and the solvent with itself is stronger than the interaction of each body with the solvent. Conversely, It is not energetically favorable to bring bodies A and B in close proximity if they interact strongly with the surrounding medium and weakly with one another.

The one implicit assumption made in the above development is that the interactions of bodies A and B with the surrounding medium are not affected by bringing A and B in close proximity. This model is not strictly true since any electronic structure changes caused by bringing A and B in close proximity must change the overall interaction of A and B with the solvent. For systems where the bodies interact strongly with the solvent, and weakly with one another, Hamaker argued that this effect would be small.

Fortunately, we have another means of theoretically verifying the existence of negative Hamaker constants. This method, based on the Lifshitz theory, does account for all electronic structure changes and treats the system as a whole rather than summing individual interaction energies. Therefore, it does not suffer from the deficiencies of the arguments put forth independently by Hamaker and by Derjagin and Kussakov. Equations 2-24 through 2-26 which

describe the Hamaker constant derived with the Lifshitz field theory demonstrate the possibility of negative Hamaker constants. In equations 2-24 through 2-26, the subscripts 1, 2, and 3 are interchangeable with bodies A, B, and the intervening medium C in that order. We see that if two bodies, 1 and 2, are interacting through an intervening medium 3 and if the dielectric function of the medium is intermediate between that of 1 and 2, *i.e.*, $\epsilon_1 > \epsilon_3 > \epsilon_2$, the following is evident: the ratio given in equation 2-25 is positive; the ratio given in equation 2-26 is negative; the product of these equations and therefore equation 2-24 will be negative. This leads to an overall increase in the energy of the system when bodies 1 and 2 are brought together and hence an effective repulsion will be observed between them.

### 4.3. The Dielectric Function of Condensed Media

Before undertaking the calculation of Hamaker constants using equations 2-24 through 2-25, an understanding of the dielectric functions of each of the three phases involved in the system must be obtained. The dielectric function formally relates the propagation of electromagnetic waves in a medium to that in a vacuum. Conversely, another means of explaining the physical consequence of the dielectric function is that it is a measure of the response of the electrons in a material to imposed electromagnetic radiation. The dielectric function can be calculated by measuring the complex index of refraction and the two are related by equation 4-5.

$$\hat{\epsilon} = \epsilon' + i\epsilon'' = \hat{n}^2 = (n + ik)^2 \tag{4-5}$$

In the above equation, $\hat{n}$ is the complex index of refraction, n is the real part of the refractive index, and k is the imaginary part of the refractive index which is often called the extinction coefficient. These quantities are frequency dependent for practically all materials, *e.g.*, water has strong absorption peaks, $k > 0$, in the infrared and ultraviolet regions of the spectrum, but is transparent, $k = 0$, in the visible range. Therefore, n and k must be measured over a wide range of frequencies in order to completely determine the behavior of $\hat{\epsilon}$.

Unfortunately the quantity required for the calculation of the Hamaker constant is the real part of the dielectric function evaluated at imaginary frequencies, $\epsilon'(i\nu)$. This quantity has no direct physical significance and arises during the mathematical evaluation of the free energy of these systems. Specifically, $\epsilon'(i\nu)$ results from a change of variable made to facilitate the evaluation of Greens functions within the Lifshitz theory, Lifshitz (1956). Fortunately the Kramers-Kronig transformation, see equation 2-27, which relates the real and imaginary parts of the dielectric function, may be used to find $\epsilon'(i\nu)$. On the substitution of imaginary frequencies into equation 2-27 we find that

$$\epsilon'(i\nu) = 1 + \frac{2}{\pi} \int_0^\infty \frac{\omega\, \epsilon''(\omega)}{\omega^2 + \nu^2}\, d\omega \ . \tag{4-6}$$

Thus, if the absorption spectrum, $\epsilon''(\omega)$, of a material is known over all frequencies then the desired quantity, $\epsilon'(i\nu)$, may be constructed from equation 4-6.

Electromagnetic radiation propagates through rarified media with very little attenuation or phase change. Therefore, for the purpose of this work, the

dielectric function of gaseous and vapor phases will be assumed to be identical to that of vacuum. Since there is no electromagnetic absorption in a vacuum, $\epsilon''$ will be zero at all frequencies, and therefore, the integral in equation 4-6 will also be zero. Hence, it will be assumed that for gaseous and vapor phases the real part of the dielectric function evaluated at imaginary frequencies will be identically equal to 1 at all frequencies.

For dielectric media such as water, hydrocarbons, or silica glass, there are certain similarities in the behavior of the function $\epsilon'(i\nu)$ (Hough and White, 1980). At zero frequency, $\nu = 0$, $\epsilon'(i\nu)$ is equal to the static dielectric constant for that media. As the frequency increases, $\epsilon'(i\nu)$ decreases monotonically. In the limit of very large frequency, $\nu \rightarrow \infty$, $\epsilon'(i\nu)$ approaches 1. Summarizing, $\epsilon'(i\nu)$ is equal to the static dielectric function at zero frequency, $\epsilon'(i\nu)$ equals one at infinite frequency, and $\epsilon'(i\nu)$ is only permitted to decrease as frequency increases (Dyzaloshinskii, et al., 1961; Hough and White, 1980; Israelachvili, 1985).

Few materials exist where the absorption spectrum, $\epsilon''(\nu)$, has been measured over a large enough frequency range to permit the direct use of equation 4-6 to calculate $\epsilon'(i\nu)$. However, alternate methods are available for the construction of the desired quantity. These generally involve the appropriate use of the strength of tabulated absorption peaks and the frequency at which they occur in an equation designed to be self consistent with the Kramers-Kronig transformation (Hough and White, 1980; Israelachvili, 1985, pp. 144-7). One method is that developed by Parsegian (1975). His method asserts that the

complex dielectric function may be constructed using the following equation;

$$\hat{\epsilon}(\nu) = \sum_j \frac{f_j - i\,\nu\,h_j}{\omega_j^2 - \nu^2 - i\,\nu\,g_j} \quad , \tag{4-7}$$

where $f_j$, $h_j$, $\omega_j$, and $g_j$ are fitted from either absorption peaks in the case of liquids, or from reflectance and transmittance data in the case of solids (Parsegian and Weiss, 1981). The desired quantity, $\epsilon'(i\nu)$, may be found from equation 4-7 by substituting the imaginary frequency $i\nu$ for the real frequency $\nu$. Values of the parameters $f_j$, $h_j$, $\omega_j$, and $g_j$ for water, tetradecane, and gold from Parsegian and Weiss (1981) appear in table 4-2 and the real part of the dielectric function evaluated at imaginary frequencies for these materials are presented graphically in figure 4-2.

When index of refraction and extinction coefficient data are available, these are rarely tabulated for more than a few decades of frequency ranging from $10^{13}$ to $10^{18}$ inverse seconds. For metals, it is then possible to use limiting functions to estimate absorption for frequencies less than $10^{13}$ and greater than $10^{18}$ inverse seconds. The Drude equation, eq. 4-8, expresses the complex dielectric function for an ideal conductor with one Lorenzian absorption (Wooten, 1972):

$$\hat{\epsilon}(\omega) = 1 - \frac{\omega_p^2}{\omega\,(\,\omega + i/\tau\,)} \tag{4-8}$$

Here, $\omega_p^2$ is the plasma frequency for the conduction electrons, and $\tau$ is the relaxation time for the Lorentzian oscillator. The plasma frequency is given by the following group of parameters;

Table 4-2: Parameter Values for use with Eqn. 4-7

| Data for use with Eqn. 4-7, Parsegian and Weiss (1981) | | | | | |
|---|---|---|---|---|---|
| Water | | | Tetradecane | | |
| $f_j$ (ev$^2$) | $\omega_j$ (ev) | $g_j$ (ev) | $f_j$ (ev$^2$) | $\omega_j$ (ev) | $g_j$ (ev) |
| $6.3 \times 10^{-4}$ | $2.1 \times 10^{-2}$ | $1.5 \times 10^{-2}$ | 6.61 | 8.44 | 0.36 |
| $3.5 \times 10^{-3}$ | $6.9 \times 10^{-2}$ | $3.8 \times 10^{-2}$ | 9.94 | 8.97 | 0.55 |
| $1.3 \times 10^{-3}$ | $9.2 \times 10^{-2}$ | $2.8 \times 10^{-2}$ | 13.79 | 9.70 | 0.74 |
| $5.7 \times 10^{-3}$ | $2.0 \times 10^{-1}$ | $2.5 \times 10^{-2}$ | 16.54 | 10.54 | 0.91 |
| $1.4 \times 10^{-2}$ | $4.2 \times 10^{-2}$ | $5.6 \times 10^{-2}$ | 17.48 | 11.58 | 1.14 |
| 2.7 | 8.3 | 0.51 | 19.66 | 12.92 | 1.44 |
| 5.7 | 10.0 | 0.88 | 21.21 | 14.58 | 1.77 |
| 12.0 | 11.4 | 1.54 | 22.30 | 16.56 | 2.11 |
| 26.3 | 13.0 | 2.05 | 22.23 | 18.97 | 2.50 |
| 33.8 | 14.9 | 2.96 | 19.22 | 22.03 | 2.68 |
| 92.8 | 18.5 | 6.26 | | | |
| Gold | | | | | |
| $f_j$ (ev$^2$) | $\omega_j$ (ev) | $g_j$ (ev) | | | |
| 40.11 | - | - | | | |
| 59.61 | 3.87 | 2.62 | | | |
| 122.55 | 8.37 | 6.41 | | | |
| 1031.19 | 23.46 | 27.57 | | | |

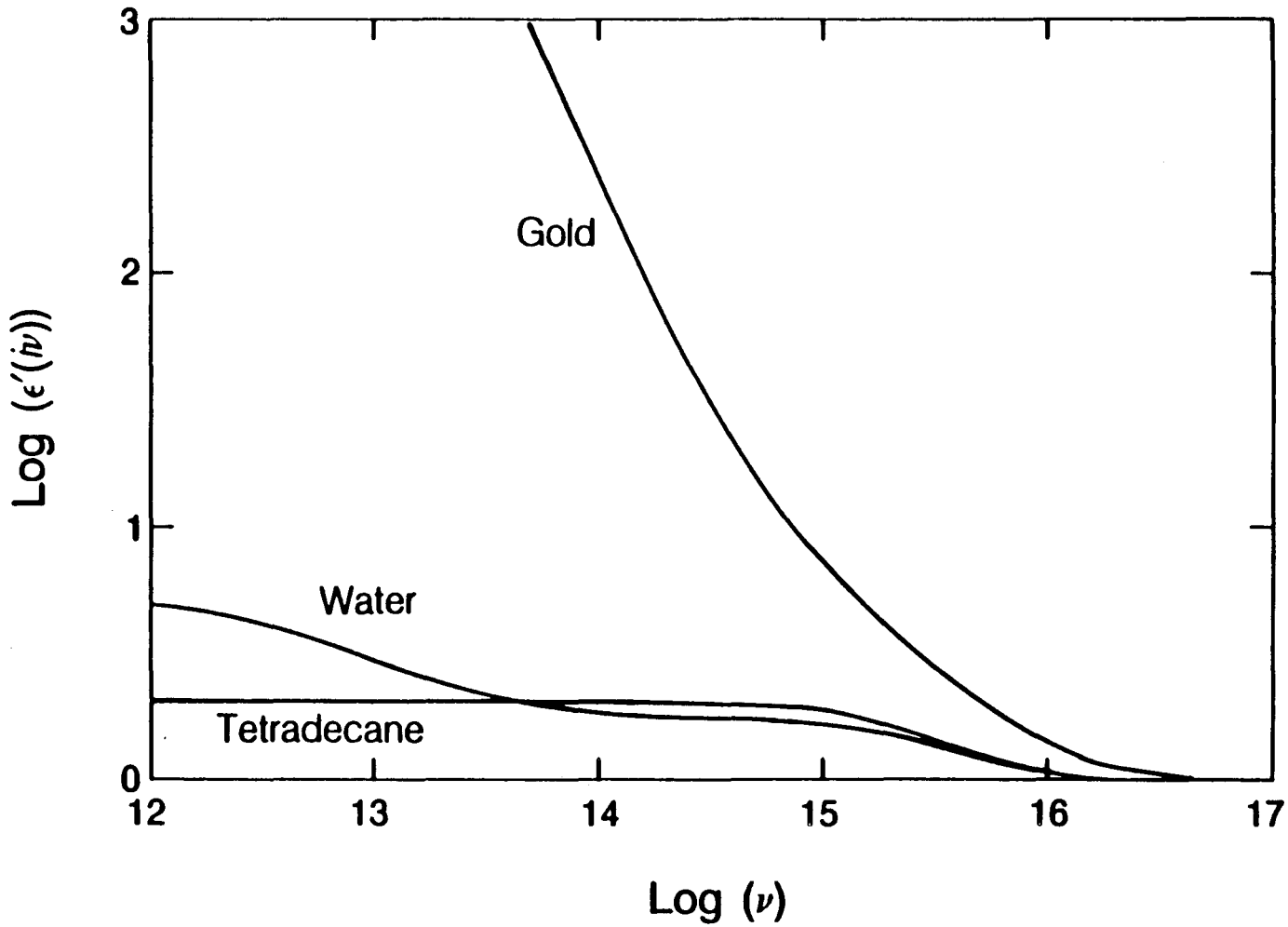


XBL 8611-4776

**Figure 4-2:** Dielectric functions evaluated at imaginary frequencies for gold, water, and tetradecane as calculated by the method and data of Parsegian and Weiss (1981).

$$\omega_p^2 = \frac{N_{ce}\, e_-^2}{\epsilon_o\, m_e} \tag{4-9}$$

where $N_{ce}$ is the number density of conduction electrons, $e_-$ is the charge on an electron, and $m_e$ is the mass of an electron. The low and high frequency limits for the imaginary part of the dielectric function may be found by taking the limits of this equation as frequency approaches zero and infinity respectively. In so doing the low frequency limit known as the absorbing region because the absorption coefficient is large, is given by;

$$\epsilon''(\omega) = \frac{\tau\, \omega_p^2}{\omega} \tag{4-10}$$

and is valid for the frequency range $0 < \tau\omega < 1$. The high frequency limit, also known as the transparent region because the absorption coefficient is very small, is given by;

$$\epsilon''(\omega) = \frac{\omega_p^2}{\tau\, \omega^3} \tag{4-11}$$

This limiting equation is valid for frequencies larger than the plasma frequency, $\omega_p$. More information pertaining to these limiting equations may be found in Jackson (1975), Abeles (1972), Landau and Lifshitz (1980) or Wooten (1972).

Real metals are not ideal conductors with one Lorentzian absorption, but will display several absorption frequencies. The limiting behavior of the dielectric function for real metals will be described by Equations 4-10 and 4-11 except that $\tau$ will not be the same in both equations (Wooten, 1972). Therefore, given data over a large enough frequency range, such that the conditions of validity

for each limiting equation are met, it is possible to find a $\tau_l$ so that equation 4-10 matches the low end of the data and to find a $\tau_h$ such that equation 4-11 matches the high end.

Now that the absorption spectrum is determined for all positive frequencies, it is possible to use equation 4-6 to find $\epsilon'(i\nu)$. The integral from zero to infinity may be broken into three parts: the first from zero to the lowest frequency for which there are data, $\omega_l$, can be solved analytically using equation 4-10: the second from $\omega_l$ to the highest frequency for which there are data, $\omega_h$, must be integrated numerically: and the third from $\omega_h$ to infinity can be solved analytically using equation 4-11. After completing the analytical integrations, the real part of the dielectric function evaluated at imaginary frequencies is given by;

$$\epsilon'(i\nu) = 1 + \frac{2\,\tau_l\,\omega_p^2}{\nu}\tan^{-1}\left(\frac{\omega_l}{\nu}\right) + \frac{2}{\pi}\int_{\omega_l}^{\omega_h}\frac{\omega\,\epsilon''(\omega)}{\omega^2+\nu^2}\,d\omega + \frac{2\,\omega_p^2}{\pi\,\tau_h}\left(\frac{1}{\omega_h\,\nu^2} + \frac{\tan^{-1}\left(\frac{\omega_h}{\nu}\right) - \frac{\pi}{2}}{\nu^3}\right) \tag{4-12}$$

Palik (1985) has tabulated index of refraction and extinction coefficient data for several materials including platinum and gold. The frequency range of these data are from $10^{13}$ to a little less than $10^{19}$ inverse seconds. The absorption spectrum for these materials may be calculated from index of refraction and extinction coefficient data using the relation given in equation 4-5. Specifically,

$$\epsilon''(\omega) = 2\,n(\omega)\,k(\omega) \tag{4-13}$$

Once the absorption spectrum is determined, equation 4-12 may be used to evaluate the real part of the dielectric function evaluated at imaginary frequencies.

The absorption spectra for gold and platinum were calculated from the data tabulated by Palik. These were then fitted using a least squares cubic spline with internal knots specified by the user. The internal knots are points where the determined function is to fit the data exactly. At all other points, cubic splines determined by the knots are spliced such that the sum of the squares of the error is minimized. Internal knots may be added or moved at will so that a smooth fit of the data is obtained. The use of internal knots minimizes unnecessary fluctuations of the fitted function which may result if all data points were used in a spline fit. Also, this method requires less computational time than does a complete spline fit. The data calculated from Palik (1985) and the fitted function for gold are shown together in figure 4-3. The internal knots specified for the fit displayed in figure 4-3 are shown in the table inset in figure 4-3.

The plasma frequency for gold is calculated using equation 4-9 and is found to be $1.67 \times 10^{16}$ inverse seconds. The low frequency and high frequency absorption data may now be used to determine $\tau_l$ and $\tau_h$ by matching values calculated using equations 4-10 and 4-11 to the data. The values determined for $\tau_l$ and $\tau_h$ are $3.16 \times 10^{-16}$ and $1.51 \times 10^{-18}$ seconds respectively. Now that all required parameters are determined, the real part of the dielectric function evaluated at imaginary frequencies, $\epsilon'(i\nu)$, may be calculated using equation

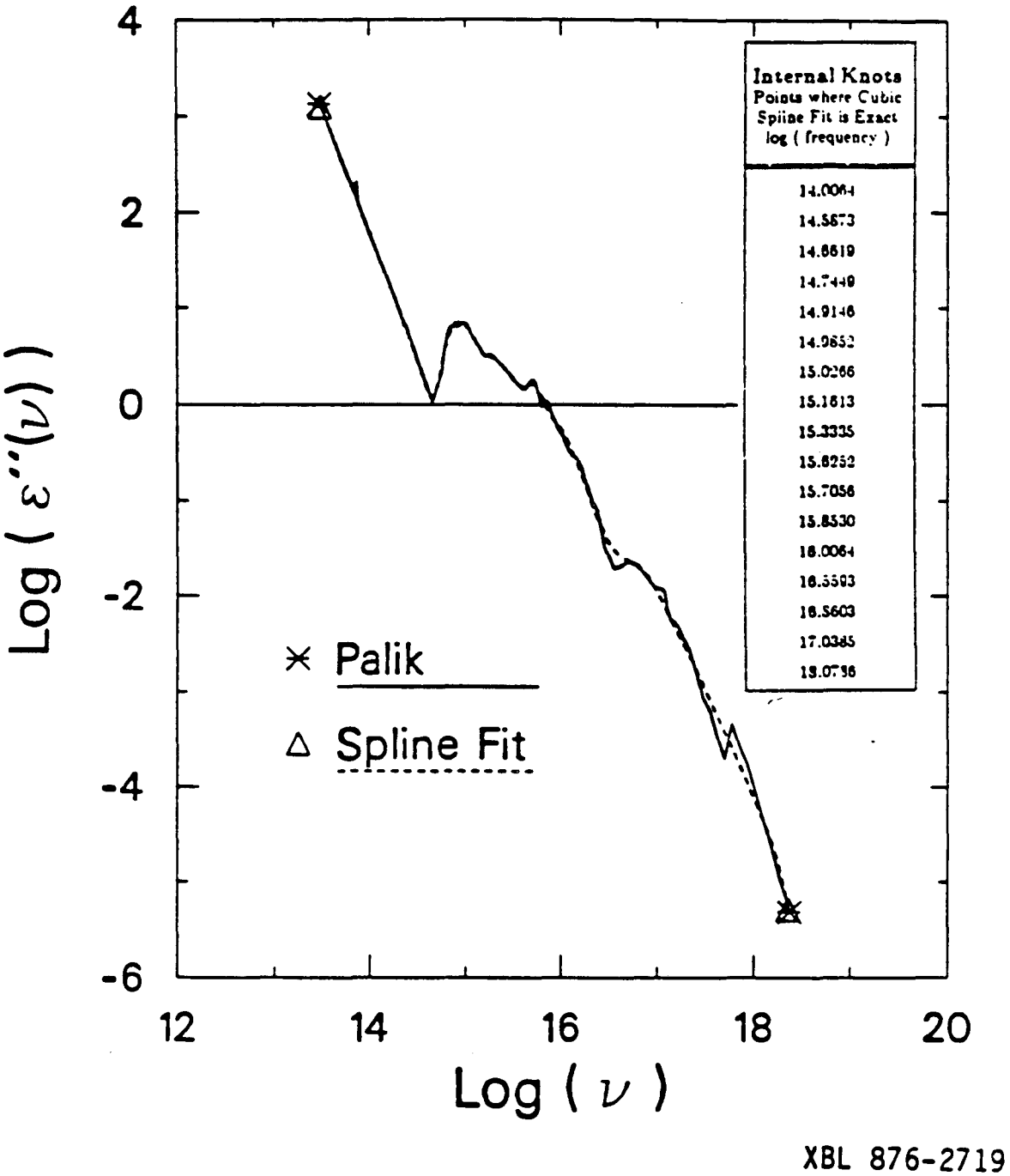


**Figure 4-3:** Absorption spectrum for gold: data (solid curve) form Palik (1985), together with the least squares cubic spline fit (dashed curve). The internal knots, points where the fit is exact, are listed in the inset.

4-12. The numerical integration was carried out using a quadrature method as described by Patterson (1968). Figure 4-4 is a log-log plot of $\epsilon'(i\nu) - 1$ against frequency as calculated for gold from equation 4-12. One is subtracted from the ordinate and a log-log plot is made in order to better show the frequency dependence of $\epsilon'(i\nu)$. The real part of the dielectric function for gold calculated from the data and by the method of Parsegian and Weiss (1981) in addition to that calculated using the Kramers-Kronig transformation, eqn. 4-12, are shown in figure 4-4. Comparing the curves shown in figure 4-4, it may be summarized that the methods give similar results. The functionality of the two curves are nearly identical, however, that calculated using equation 4-12 gives somewhat higher values than Parsegians data and method. This may result either from inherent inaccuracies in the fitting of the parameters used in Parsegian's method, or the discrepancy may result from differences in the optical data used by each method. The real part of the dielectric function for platinum as calculated from data found in Palik (1985) using equation 4-12 is shown in figure 4-5. The values of $\omega_p$, $\tau_l$, and $\tau_h$ used in the calculation of the curve in figure 4-5 are listed in the table inset in figure 4-5.

### 4.4. The Calculation of Hamaker Constants

At this point, all the critical ground work has been laid for the calculation of Hamaker constants for three-phase systems. For ease of reference, the equation describing the Hamaker constant introduced in chapter 2 will be repeated here.

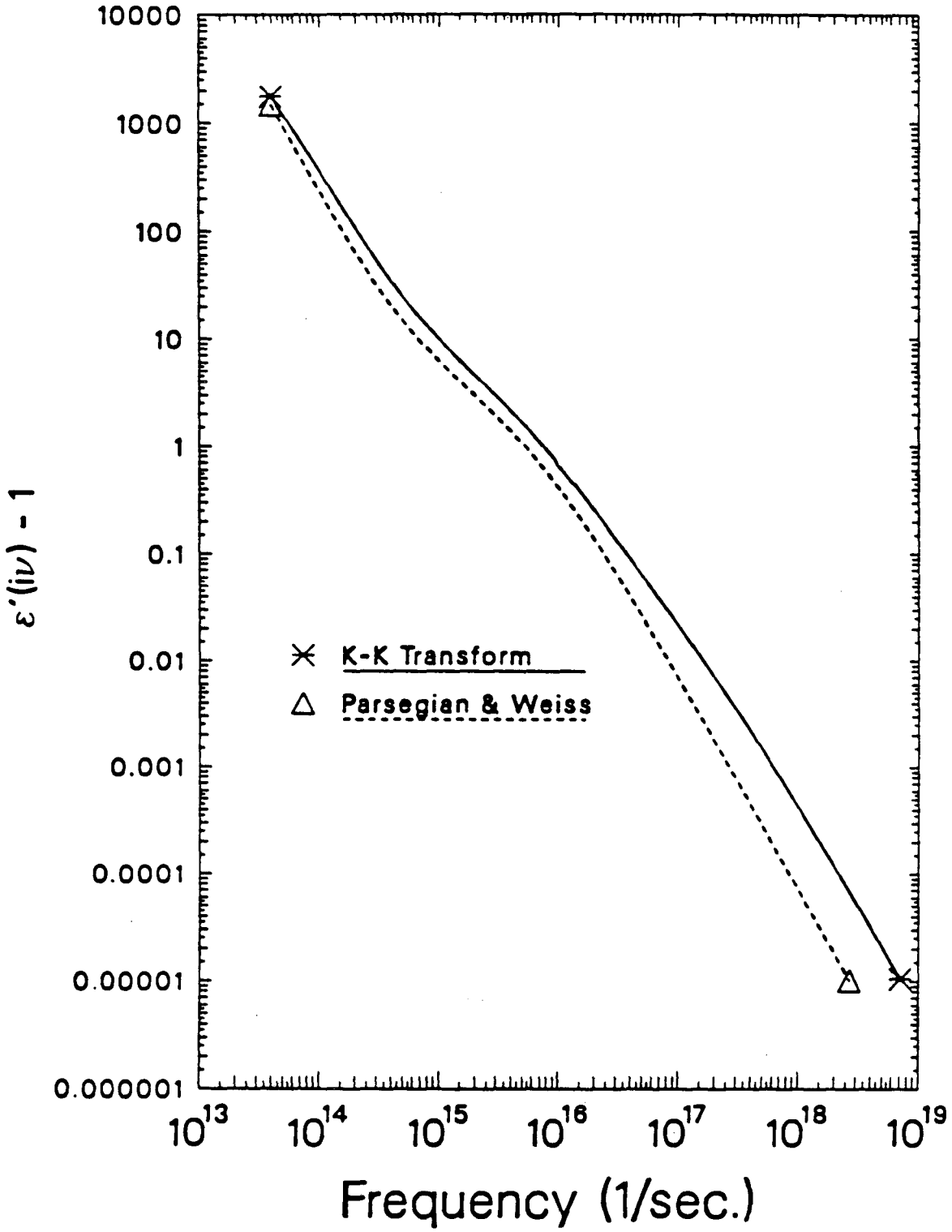


XBL 876-2726

**Figure 4-4:** Real part of the dielectric function evaluated at imaginary frequencies minus one, $\epsilon'(i\nu) - 1$, for gold: calculated from equation 4-12, together with that calculated by the method of Parsegian.

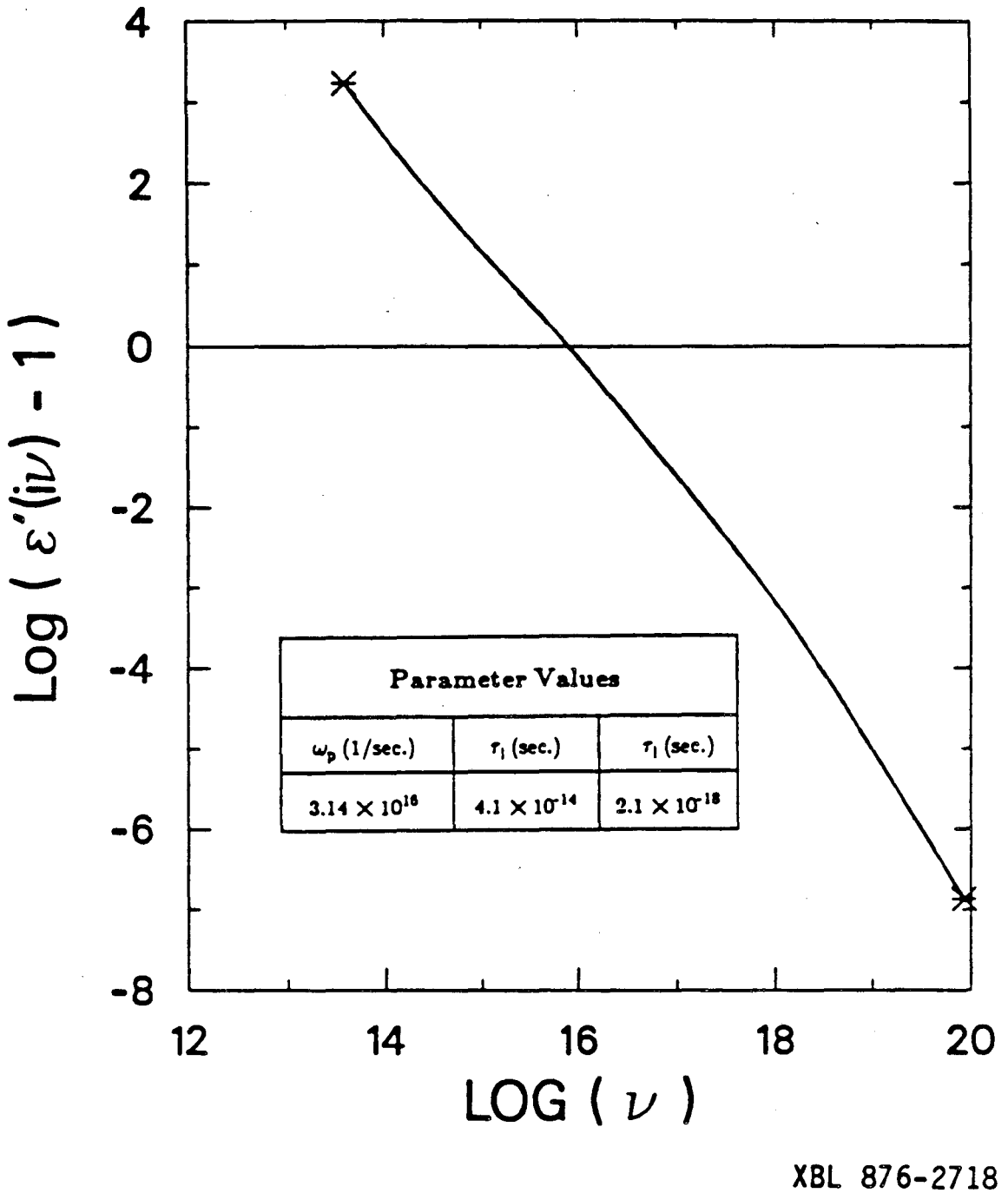


**Figure 4-5:** Real part of the dielectric function evaluated at imaginary frequencies minus one, $\epsilon'(i\nu) - 1$, for platinum as calculated from equation 4-12.

$$A_{132} = \frac{3\,k_B\,T}{2} \sum_{n=0}^{\infty} \sum_{j=1}^{\infty} \frac{1}{j^3} \left\{ G_1(i\nu_n)\, G_2(i\nu_n) \right\}^j \tag{4-14}$$

$$G_1(i\nu_n) = \frac{\epsilon'_1(i\nu_n) - \epsilon'_3(i\nu_n)}{\epsilon'_1(i\nu_n) + \epsilon'_3(i\nu_n)} \tag{4-15}$$

$$G_2(i\nu_n) = \frac{\epsilon'_2(i\nu_n) - \epsilon'_3(i\nu_n)}{\epsilon'_2(i\nu_n) + \epsilon'_3(i\nu_n)} \tag{4-16}$$

$$\nu_n = \frac{2\,\pi\,k_B\,T}{h_P}\,n\ , \quad \text{where} \quad n = 0,1,2,\cdots,\infty \tag{4-17}$$

As a reminder, $A_{132}$ refers to the Hamaker constant of body 1 interacting with body 2 across medium 3. Likewise, $\epsilon'_1$, $\epsilon'_2$, and $\epsilon'_3$ refer to the dielectric functions of bodies 1 and 2 and medium 3 respectively. Since the remainder of this work will be concerned specifically with metal/liquid film/vapor systems, the following designations will be assumed. The metallic phase dielectric function will always be $\epsilon'_1$. The liquid film, being the intermediate phase, will always be $\epsilon'_3$. Finally, the vapor phase will be designated $\epsilon'_2$ and the value of $\epsilon'_2$ will be assumed identically equal to 1 at all frequencies. Therefore $G_2$ may be written as;

$$G_2(i\nu) = \frac{1 - \epsilon'_3(i\nu_n)}{1 + \epsilon'_3(i\nu_n)}\ . \tag{4-18}$$

At this point, it is a simple matter to use the dielectric functions for gold, platinum, water, and tetradecane determined in the last section, in conjunction with equations 4-14 through 4-17 to calculate the appropriate Hamaker constant. This has been done for systems made up of these materials, and the

Hamaker constants appear in table 4-3. Hamaker constants calculated by others using various methods also appear in table 4-3 along with the reference. The following trends may be summarized from table 4-3. Interactions through vacuum are slightly stronger than interactions through water. Interactions involving tetradecane are slightly stronger than those involving water. Likewise, interactions involving platinum are slightly stronger than those involving gold.

Aside from the calculation of Hamaker constants, interesting properties of equation 4-14 may be observed. These properties are the subject of the remainder of this section. The frequency $\nu_n$ increases linearly with the counter n. When n = 0, the frequency is of course 0, and as discussed in the last section, the dielectric functions will be equal to the DC or static dielectric permittivity for the metal and liquid film. For metals, the dielectric function approaches infinity as the frequency approaches zero. Even though the dielectric function for metals becomes infinite, equation 4-14 remains finite. This becomes obvious when equation 4-15 is examined a bit more closely. $G_1$ is the ratio of the difference between $\epsilon_1$ and $\epsilon_3$ to the sum of these two quantities. Since $\epsilon_3$ is finite at $\nu = 0$ as $\epsilon_1$ approaches infinity the ratio represented by $G_1$ will approach 1. Therefore, the n = 0 term of equation 4-14 will be finite.

The next frequency, $\nu_1$, (n = 1), for which the dielectric function is evaluated is found according to equation 4-18 at room temperature to be equal to $3.96 \times 10^{13}$ inverse seconds. Each subsequent frequency, $\nu_2, \nu_3, \cdots, \nu_\infty$, will be separated from the previous by $3.96 \times 10^{13}$. Therefore, each subsequent decade of frequency will have more and more importance since there will be a

Table 4-3: Calculated Hamaker Constants

| Hamaker Constant; Calculated | | |
|---|---|---|
| System | A | ref. |
| Water / Vacuum / Water | $4.0 \times 10^{-13}$ ergs | #1 |
| | $3.7 \times 10^{-13}$ ergs | #2 |
| Tetradecane / Vacuum / Tetradecane | $5.3 \times 10^{-13}$ ergs | #1 |
| | $5.1 \times 10^{-13}$ ergs | #2 |
| | $5.4 \times 10^{-13}$ ergs | #4 |
| Tetradecane / Water / Tetradecane | $4.5 \times 10^{-14}$ ergs | #1 |
| | $5.0 \times 10^{-14}$ ergs | #2 |
| | $5.6 \times 10^{-14}$ ergs | #3 |
| | $4.4 \times 10^{-14}$ ergs | #5 |
| Gold / Vacuum / Gold | $4.4 \times 10^{-12}$ ergs | #1 |
| | $4.6 \times 10^{-12}$ ergs | #2 |
| | $4.0 \times 10^{-12}$ ergs | #3 |
| Gold / Water / Gold | $4.1 \times 10^{-12}$ ergs | #1 |
| | $4.1 \times 10^{-12}$ ergs | #2 |
| | $3 - 4 \times 10^{-12}$ ergs | #5 |
| Gold / Water / Vacuum | $-1.2 \times 10^{-12}$ ergs | #1 |
| Platinum / Water / Vacuum | $-1.3 \times 10^{-12}$ ergs | #1 |

#1 Equation 4-14 #2 Parsegian and Weiss (1981)

#3 Visser (1972) #4 Hough and White (1980)

#5 Israelachvili (1985)

larger number of frequencies at which $G_1$ and $G_2$ are evaluated and summed in equation 4-14.

Although the number of contributors increase with frequency, the magnitudes of $G_1$ and $G_2$ decrease with increasing frequency. As stated in the previous section, as frequency increases, $\epsilon'(i\nu)$ approaches 1. Therefore, the ratios represented by $G_1$ and $G_2$ will approach zero as frequency increases. Considering both these effects, we would expect that the Hamaker constant will increase rapidly as terms of the summation over n are evaluated. However, at sufficiently large frequency, we expect that the contribution of each term will become small and the total Hamaker constant will reach a limiting value. This behavior is demonstrated graphically in figures 4-6 and 4-7.

These figures demonstrate the relative importance of frequency to the total Hamaker constant. It is readily seen that beyond the middle of the $16^{th}$ decade of frequency there is no significant contribution to the Hamaker constant. Therefore, an upper limit may be established on the number of terms necessary to evaluate when using equation 4-14. The upper limit of n, the number of terms beyond which no significant contribution to the Hamaker constant is made, is approximately 800.

### 4.5. The Effect of a Dissolved Salt

The absorption spectra of pure liquids, over a large enough frequency range to permit the calculation of Hamaker constants, are difficult to locate. As for data concerning liquids with dissolved salts, it is just not available. Therefore,

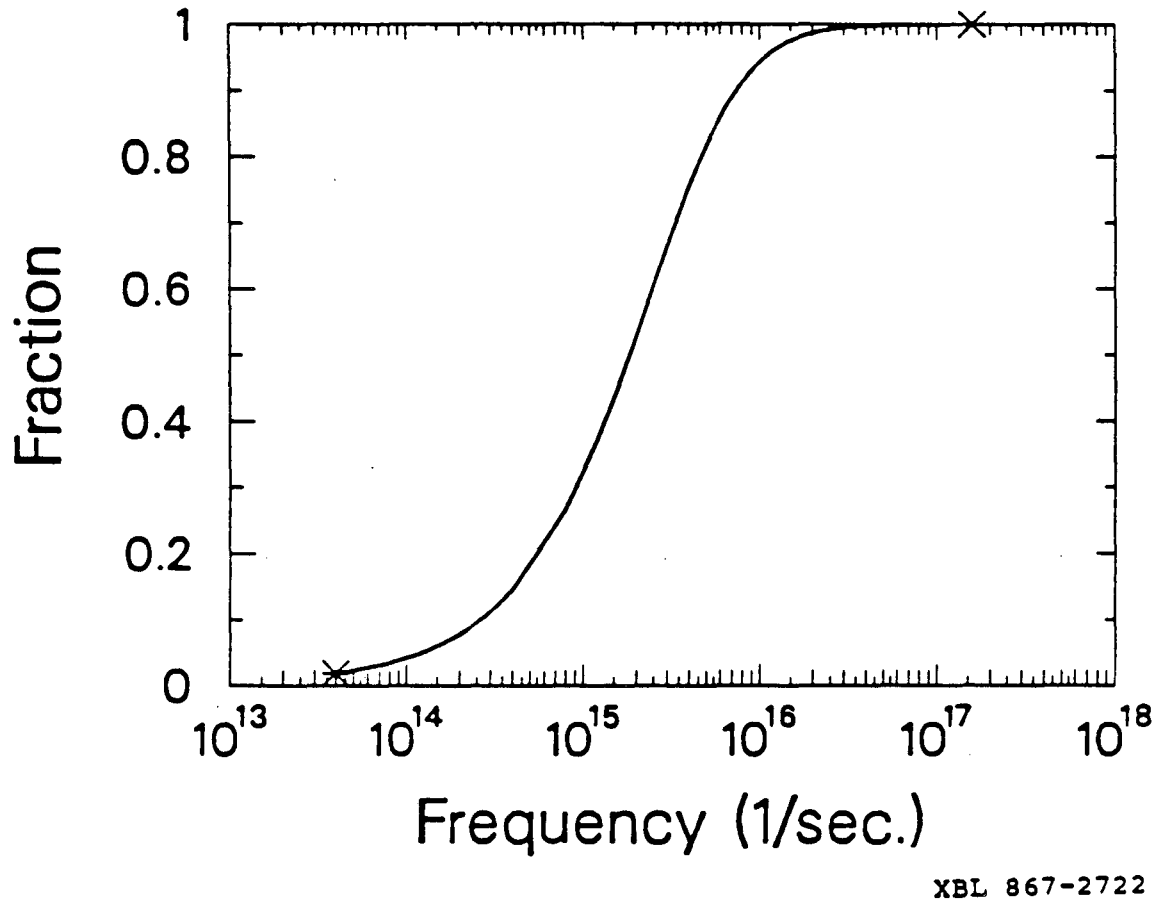


**Figure 4-6:** Ratio of the running sum of equation 4-14 to the final sum as the contributions of increasing frequencies are included for the platinum / water / vapor system.

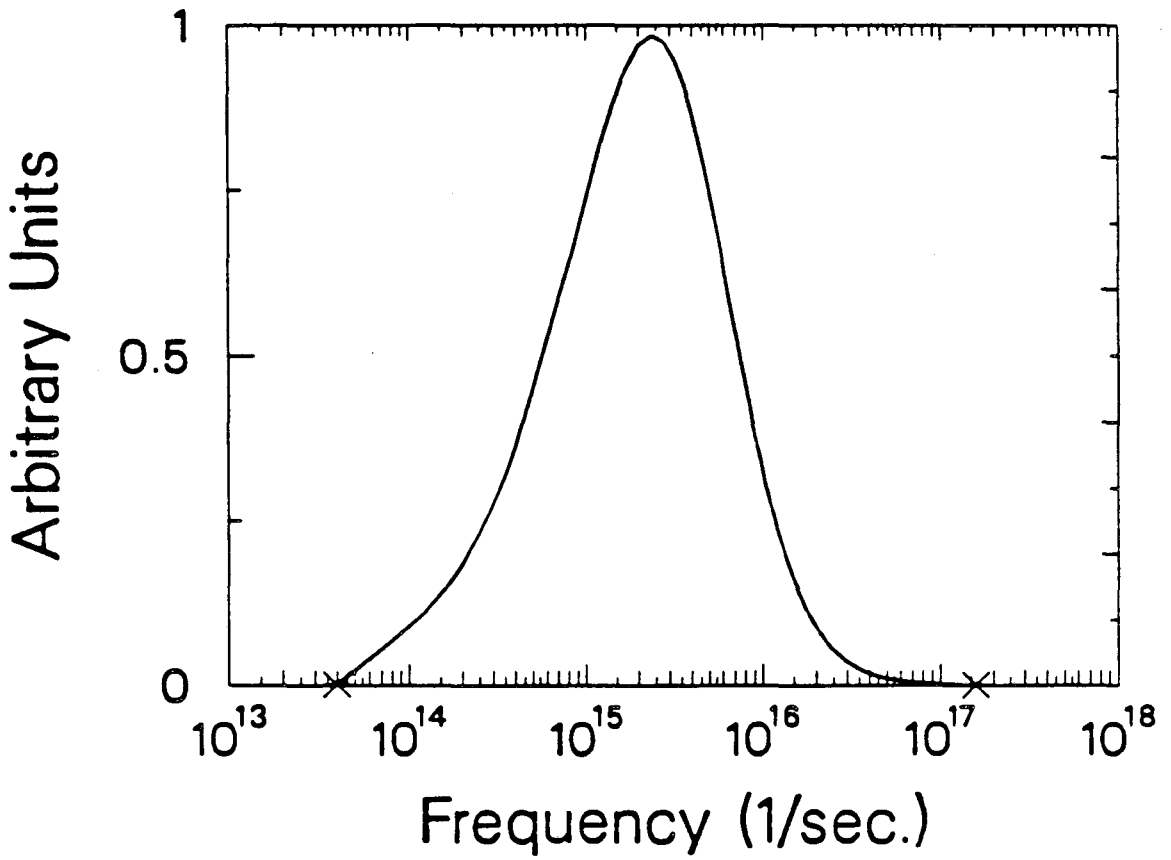


XBL 867-2723

**Figure 4-7:** Relative importance of frquency to the total Hamaker constant for the platinum/ water / vapor system.

some approximations will have to be made to predict the Hamaker constants of liquids with dissolved salts.

In section 4.3, it was pointed out that $\epsilon'(i\nu)$ had similar features for all dielectrics. These features are that $\epsilon'(i\nu)$ equals the dielectric constant of the dielectric at $\nu = 0$, $\epsilon'(i\nu)$ approaches one as $\nu$ approaches infinity, and $\epsilon'(i\nu)$ is only permitted to decrease as $\nu$ increases. A log-log plot of $\epsilon'(i\nu) - 1$ against frequency for pure water and tetradecane, shown in figure 4-8, shows nearly linear behavior for both liquids at high frequency, and both exhibit the same limiting slope.

Data that are available for most electrolytic solutions are the dielectric constant, and the index of refraction for frequencies in the visible range. For transparent electrolytes, $\epsilon''$ may be assumed to be vanishingly small. Therefore, $\epsilon'(i\nu)$ may be assumed to be equal to the square of the index of refraction in the visible region, $3.8 \times 10^{14} < \nu < 7.5 \times 10^{14}$ inverse seconds.

With this information, and the fact that $\epsilon'(i\nu) - 1$ is a featureless function of frequency, we may surmise the following about $\epsilon'(i\nu)$ for a dissolved salt in water: the dielectric constant of the electrolyte may be used for $\nu = 0$. Since all dielectrics exhibit similar behavior, there is no reason to believe the slope of the log-log plot should change. Therefore, the entire curve for the pure solvent is raised or lowered such that $\epsilon'(i\nu)$ matches that calculated from the index of refraction of the electrolyte in the visible region. Log-log plots for water and for several aqueous electrolytes constructed in the manner described, are shown in figure 4-9. We see that the dissolved salt does not considerably affect the

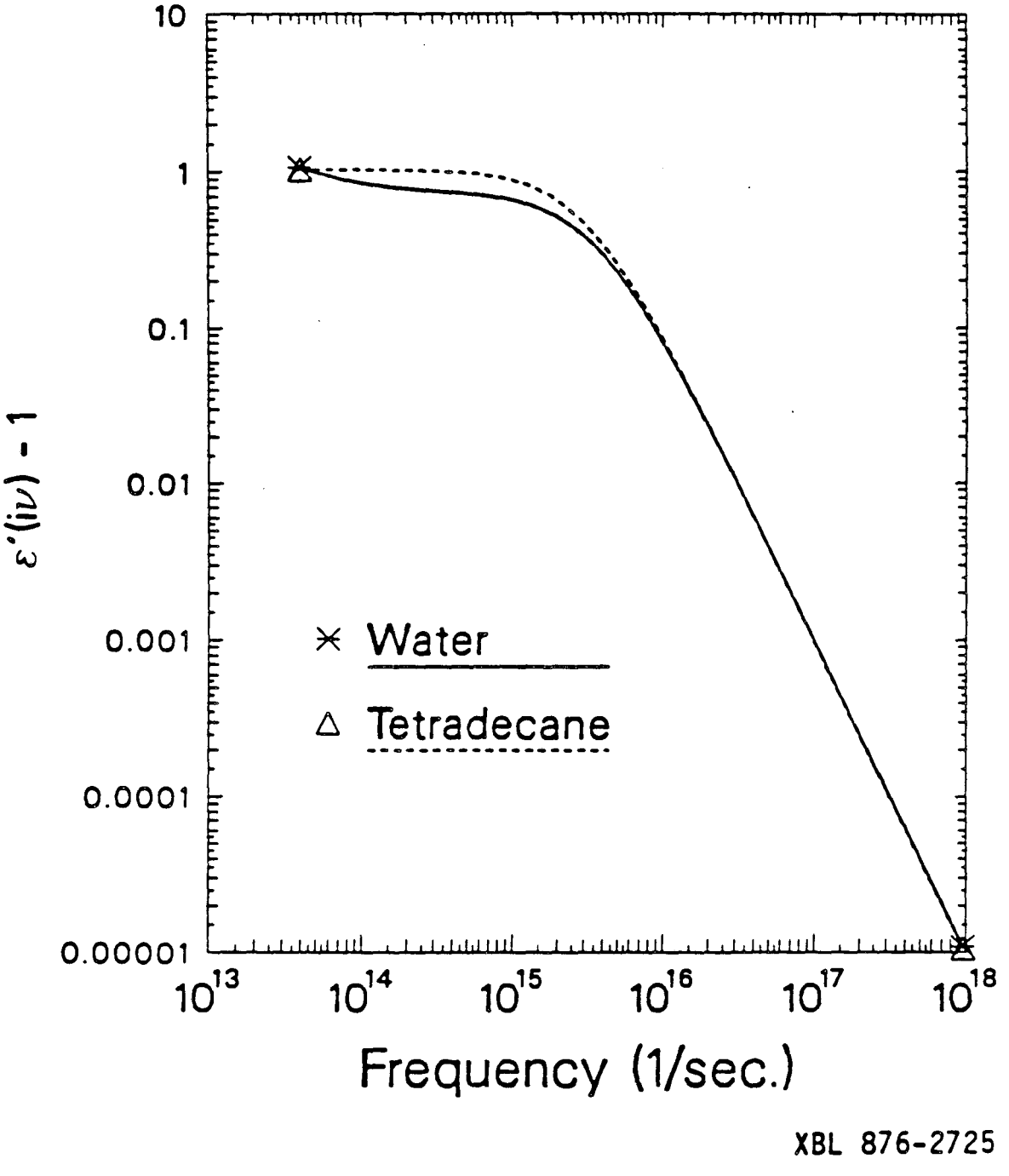


**Figure 4-8:** Real part of the dielectric function evaluated at imaginary frequencies minus one, $\epsilon'(i\nu) - 1$, for water and tetradecane as calculated by the method of Parsegian.

dielectric function.

Because the correction for the presence of a dissolved salt is made to $\epsilon'(i\nu) - 1$, when $\epsilon'(i\nu)$ is reconstructed, all the salient features will remain, *i.e.*, $\epsilon'(i\nu)$ will be taken to equal the dielectric constant at $\nu = 0$, $\epsilon'(i\nu)$ approaches one as frequency approaches infinity, and $\epsilon'(i\nu)$ only decreases as frequency increases. The Hamaker constants calculated using equation 4-14 for various metal/electrolyte/vapor systems are presented in table 4-4.

Using this same method for constructing dielectric functions for new materials, it is possible to explore the range of possible Hamaker constants as calculated from equation 4-14. In essence the dielectric functions for water and for platinum were used as base cases. Then as for the dissolved salts, the dielectric functions were increased uniformly and the Hamaker constant for the metal/liquid/vapor system was calculated. The results are shown in figure 4-10. The x axis of figure 4-10 is the value of the liquid dielectric function at a wavelength of 6000 angstroms. Each curve represents a substrate having a dielectric function similar to that of platinum but increased in the same manner as described for dissolved salts. The value of the dielectric function at 6000 angstroms is given in the legend. The top-most curve is generated when the dielectric function for platinum is used. Each successive curve results from increasing the substrate dielectric function. We see that over the range of a 500% increase in both the water and platinum dielectric functions, a range which encompasses most real materials, there is only a six fold increase in the value of the Hamaker constant. We may thus conclude that the value of the

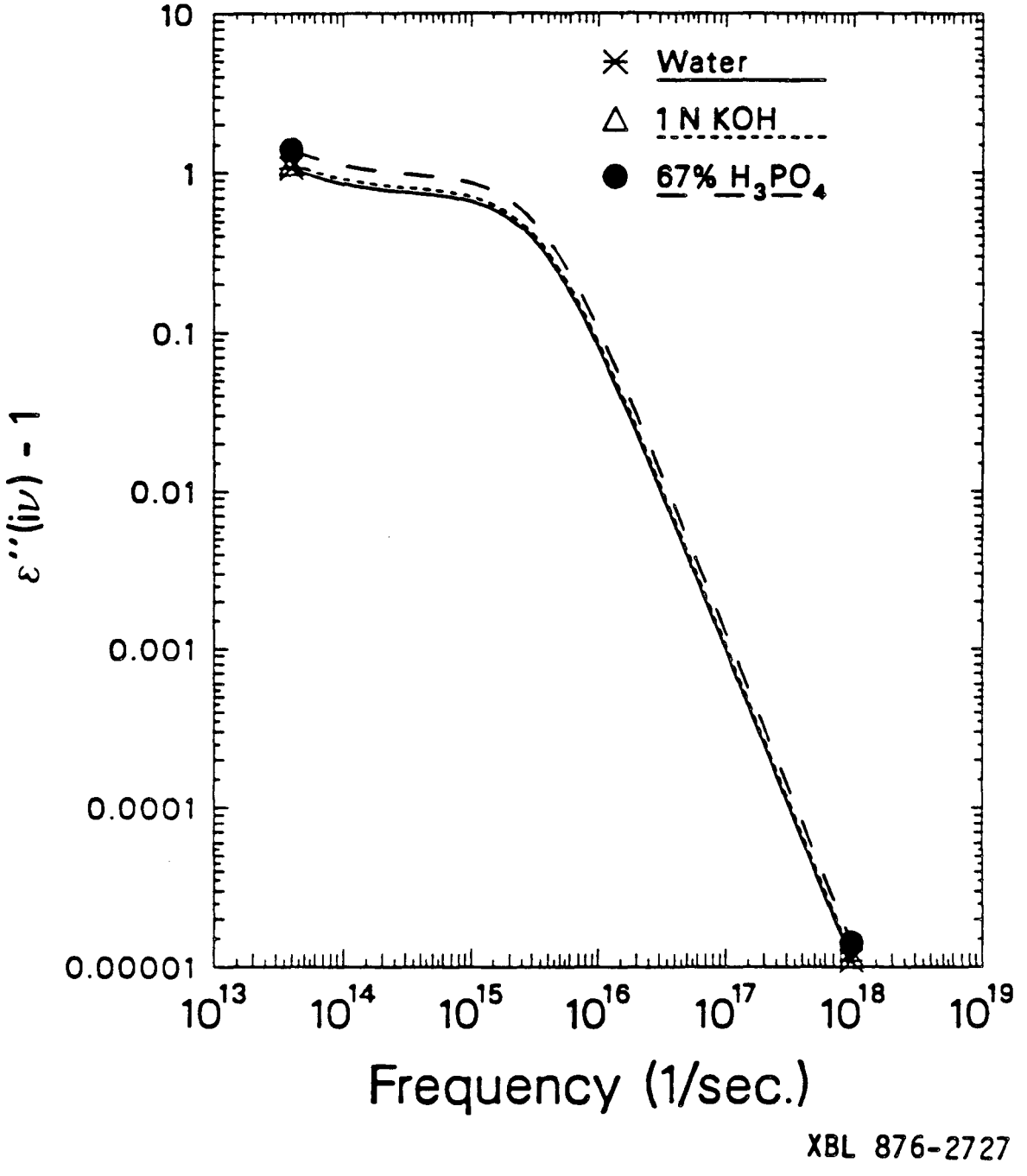


**Figure 4-9:** Real part of the dielectric function evaluated at imaginary frequencies minus one, $\epsilon'(i\nu) - 1$, for water, 1 M KOH, and 67 weight % $H_3PO$ (10.3 moles/liter).

Table 4-4: Calculated Hamaker Constants for Metal/Electrolyte Systems

| **Hamaker Constant; Calculated** | |
|---|---|
| System | Value |
| Gold / 1 M KOH / Vacuum | $-1.3 \times 10^{-12}$ ergs |
| Platinum / 1 M KOH / Vacuum | $-1.4 \times 10^{-12}$ ergs |
| Platinum / 1 M $H_3PO_4$ / Vacuum | $-1.7 \times 10^{-12}$ ergs |
| Platinum / 67% $H_3PO_4$ / Vacuum | $-2.2 \times 10^{-12}$ ergs |

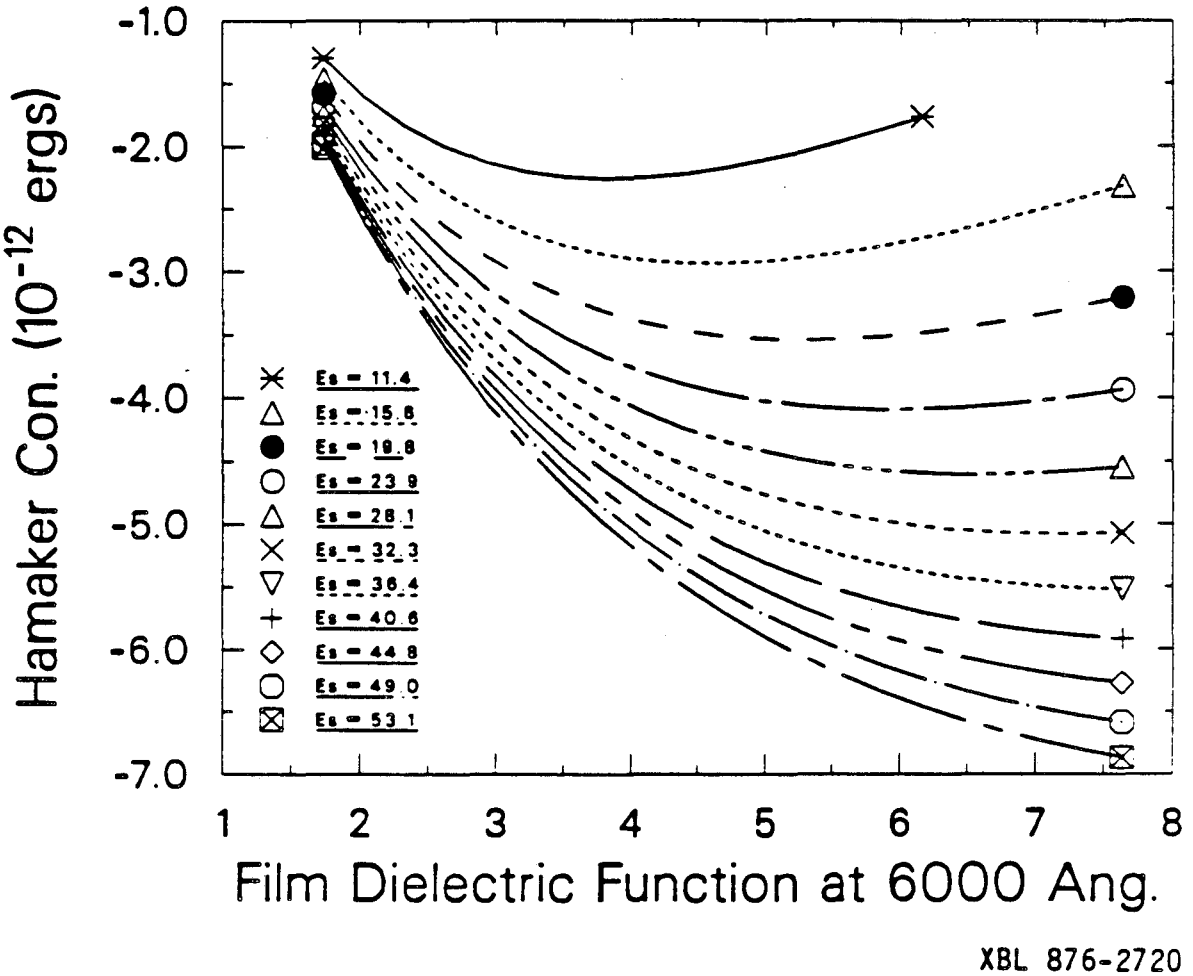


**Figure 4-10:** Dependence of the Hamaker constant on the magnitude of the film and solid dielectric functions.

Hamaker constant as calculated from equation 4-14 will lie in the range of -1.0 to $-6.0 \times 10^{-12}$ ergs for most metal/aqueous electrolyte/vapor systems.

### 4.6. Predicted Film Profiles

In this section, the shape of a supermeniscus film stabilized by repulsive van der Waals interactions will be derived. Therefore, for the purpose of this section, we shall consider the disjoining pressure, $\Pi$, to result purely from van der Waals interactions.

As was discussed in section 3.4, the capillary pressure, $P_{Ca}$, inside a supermeniscus film will be reduced from atmospheric pressure by the hydrostatic pressure.

$$P_{Ca} = 1 - \rho g h \tag{4-19}$$

Also, for no net force to be exerted on the liquid/vapor interface, the total pressure within the film, $\Pi + P_{Ca}$, must equal atmospheric pressure. Hence,

$$\Pi = 1 - P_{Ca} = \rho g h \ . \tag{4-20}$$

Equation 4-20 defines the disjoining pressure as a function of height, h, for a thin film to exist on a vertical surface without draining.

The disjoining pressure resulting from van der Waals interaction may be found by differentiating the interaction energy with respect to the distance of separation. The interaction energy per unit area of two planar surfaces, $U_{Surf.-Surf.}$ was given in table 2-2 as:

$$U_{Surf.-Surf.} = -\frac{A}{12\,\pi\,\delta^2}\ , \tag{4-21}$$

where the separation distance, D, is now represented by $\delta$. The sign convention has been that a positive Hamaker constant denotes a negative interaction energy which leads to an attractive force between the surfaces. However, a positive disjoining pressure is defined as the repulsive force necessary to maintain the thin film in mechanical equilibrium. Therefore, the disjoining pressure is defined as the negative differential of the interaction energy per unit area with separation distance.

$$\Pi = -\frac{dU_{Surf.-Surf.}}{d\delta} \tag{4-22}$$

Substituting equation 4-21 into equation 4-22 and differentiating, gives the van der Waals contribution to the disjoining pressure.

$$\Pi = -\frac{A}{6\,\pi\,\delta^3} \tag{4-23}$$

Setting equations 4-23 and 4-20 equal, and solving for the film thickness delta gives an equation for the film profile, delta as a function of height above the bulk liquid level, h:

$$\delta = -\left(\frac{A}{6\,\pi\,\rho\,g\,h}\right)^{1/3} \tag{4-24}$$

We see that equation 4-24 is only meaningful when the Hamaker constant is less than zero, *i.e.*, the disjoining pressure and hence the repulsive force between the surfaces is positive. Plots of equation 4-24 for various predicted and calculated

Hamaker constants appear in chapter 6. The presentation of graphical results are being delayed in order to simplify the discussion of results and conclusions and to eliminate unnecessary repetition of figures.

### 4.7. Retarded Interactions Between Surfaces

In section 2.7, retardation effects were described for molecules separated by large distances. We will now discuss these effects as they relate to interactions between surfaces. As with intermolecular interactions, retardation effects between surfaces will result in interaction energies that fall off more quickly with distance of separation than do non-retarded interactions.

The potential of interaction between surfaces separated by a distance large enough that retardation effects are important can be determined by the same integration technique used in section 2.8. Now, C which contained the coefficients to the Keesom, Debye, and London potentials will only contain the coefficient for the retarded London Potential.

$$C = \frac{23\ h_P\ c}{8\ \pi^2}\ \frac{\alpha_{o1}\ \alpha_{o2}}{4\ \pi\ \epsilon_o} \tag{4-25}$$

Proceeding as for the interaction of one molecule with a block of material (see figure 2-1) but realizing that the intermolecular interaction potential is given by equation 4-26 the interaction potential of 1 molecule with a surface is given by equation 4-27.

$$U_{rL} = -\frac{C}{r^7} \tag{4-26}$$

$$U_{molec.-surf.} = -\frac{\pi C N_\rho}{10 D^4} \tag{4-27}$$

If the molecule involved in this interaction is part of another surface then equation 4-27 may be used as the starting point for another integration. Assuming the surfaces are made up of the same material, each plane of body 2 will contribute $N_\rho dz$ interactions. The differential interaction potential will be given by;

$$dU = -\frac{\pi C N_\rho^2}{10 ( D + z )^4} dz \tag{4-28}$$

Upon integration from zero to infinity the surface-surface interaction potential may be found.

$$U_{surf.-surf.} = -\frac{\pi C N_\rho^2}{30 D^3} \tag{4-29}$$

This interaction potential is dependent on the inverse third power of the separation distance as opposed to the non-retarded London surface-surface potential which is proportional to the inverse square of the separation distance, see equation 2-22.

## 4.8. The Retarded Hamaker Constant

As with non-retarded interactions, the energy of interaction may be written in terms of a Hamaker constant. However, in the case of retarded interactions, the Hamaker constant is no longer independent of film thickness. Before discussing how this arises, let us first define the retarded Hamaker constant.

To distinguish a non-retarded Hamaker constant from a retarded one, the retarded Hamaker constant will be represented by the symbol $A^R$. Using the same definition as was used in section 2.7, see equation 2-23, and substituting into equation 4-29, the interaction energy per unit area for two surfaces is given by;

$$U_{Surf.-Surf.} = -\frac{A^R}{30\,\pi\,D^3} \quad . \tag{4-30}$$

The first characteristic of the retarded Hamaker constant that is observed from equation 4-30 is that the units of $A^R$ are energy-length, whereas the units of the non-retarded Hamaker constant are energy. Therefore a direct comparison of the two values is meaningless. The van der Waals contribution to the disjoining pressure when retardation effects are important may be found by differentiating the interaction energy with respect to the distance of separation.

$$\Pi = -\frac{dU_{Surf.-Surf.}}{dD} = -\frac{A^R}{10\,\pi\,D^4} \tag{4-31}$$

The fact that the retarded Hamaker constant is no longer independent of film thickness was first discussed by Dzyaloshinskii, et al. (1961). This effect arises from the film thickness becoming of the same order as the wavelength of the frequencies responsible for the dispersion energy. As the film thickness increases, more and more of the high frequency contributions are dampened out by shielding effects. This may be accounted for by eliminating the high frequency contributions from the summation in equation 4-14, *i.e.*, establish a cut-off frequency above which no contribution is made to the total van der Waals

interaction. Israelachvili (1974) gives the cut-off frequency, $\nu_{co}$, as a function of film thickness:

$$\nu_{co} = \frac{c}{\delta} \tag{4-32}$$

where c is the speed of light.

We may now evaluate at what thicknesses retardation effects become important. Referring back to figure 4-4, we see that above $3 \times 10^{16}$ inverse seconds there is virtually no contribution to the dispersion energy. Substituting $3 \times 10^{16}$ into equation 4-32 and solving for $\delta$ we find that for films between zero and 100 angstroms thick, we may expect that retardation effects are not important. As the film thickness increases, retardation effects will increase until $\delta = 10\mu m$, $\omega_{co} = 3 \times 10^{13}$ inverse seconds, where all dispersion effects are completely dampened.

This does not mean that the van der Waals interaction for thicknesses larger than $10\mu m$ is zero. The zero frequency contribution to the van der Waals interaction is not affected by shielding. Israelachvilli (1974) gives the limiting surface/surface interaction energy as:

$$U_{Surf.-Surf.} = -\frac{23\ h_P\ c}{960\ \pi^3\ \delta^3 \sqrt{\epsilon_{3o}}} \left( \frac{\epsilon_{1o} - \epsilon_{3o}}{\epsilon_{1o} + \epsilon_{3o}} \right) \left( \frac{\epsilon_{2o} - \epsilon_{3o}}{\epsilon_{2o} + \epsilon_{3o}} \right) \tag{4-33}$$

where $\epsilon_{1o}$, $\epsilon_{2o}$, and $\epsilon_{3o}$ are the dielectric constants of the three phases. Substituting equation 4-30 and solving for the retarded Hamaker constant,

$$A^R = \frac{23\ h_P\ c}{32\ \pi^2 \sqrt{\epsilon_{3o}}} \left( \frac{\epsilon_{1o} - \epsilon_{3o}}{\epsilon_{1o} + \epsilon_{3o}} \right) \left( \frac{\epsilon_{2o} - \epsilon_{3o}}{\epsilon_{2o} + \epsilon_{3o}} \right) \tag{4-34}$$

Equation 4-34 gives the retarded Hamaker constant at separation distances large enough that the cut-off frequency is less than $3 \times 10^{13}$ inverse seconds, *i.e.*, at distances of separation greater than 10 $\mu$m.

The retarded Hamaker constant for conditions where all dispersion frequencies are important, *i.e.*, separation distances less than 100 angstroms, may be found by matching the non-retarded and retarded Hamaker constants at 100 angstroms separation. This results in the following relation between the constants as a function of the maximum frequency, $\omega_{max}$, for which there is a contribution to the Hamaker constant.

$$A^R = \frac{5\ A\ c}{3\ \omega_{max}} \tag{4-35}$$

The exact way in which the retarded constant depends on the distance of separation is extremely complicated. The numerical calculation using the full expression which may be found in Dzyaloshinskii, et al. (1961) or Mahanty and Ninham (1976) would be cumbersome and computationally expensive. For the purpose of this work it will be assumed that the relative importance of each frequency for the retarded constant is similar to that for the non-retarded constant. Therefore, we will use figure 4-4 to predict the decrease in the retarded constant.

For the platinum/water/vapor system the limiting value of the retarded constant at large film thickness is $1.6 \times 10^{-18}$ erg-cm. As the film thickness

decreases below 10 $\mu$m the cut-off frequency increases above $\nu_1$, $3 \times 10^{13}$ inverse seconds and dispersion begins to contribute to the retarded constant. The total dispersion contribution will increase until the thickness has decreased to 100 angstroms at which point the highest frequency above which there is no further contribution to the dispersion energy. We may also expected that the non-retarded constant will apply for thicknesses less than 100 angstroms, and the lower thickness limit of the retarded constant may be found from equation 4-35. For the platinum/water/vapor system, the lower thickness limit of the retarded constant is found to be $2.2 \times 10^{-18}$ erg-cm. The variation of the retarded constant with film thickness for this system is shown in figure 4-11.

The retardation effect begins to reduce the value of the retarded constant at a distance of separation of about 100 angstroms. The value of the retarded constant falls as thickness increases until the thickness exceeds about 10,000 angstroms. Beyond this thickness, the retarded constant does not change. Starting at 100 where the constant is at its largest, and increasing the film thickness three orders of magnitude to 10 micrometers, the retarded constant decreases by a factor of about two thirds. This is largely due to the fact that the $n=0$ term ($\nu=0$) is not affected by retardation effects and for the platinum/water/vapor system, the dielectric permittivities at zero frequencies are very large. Thus after shielding of all dispersion interactions there is still an appreciable non-shielded component remaining.

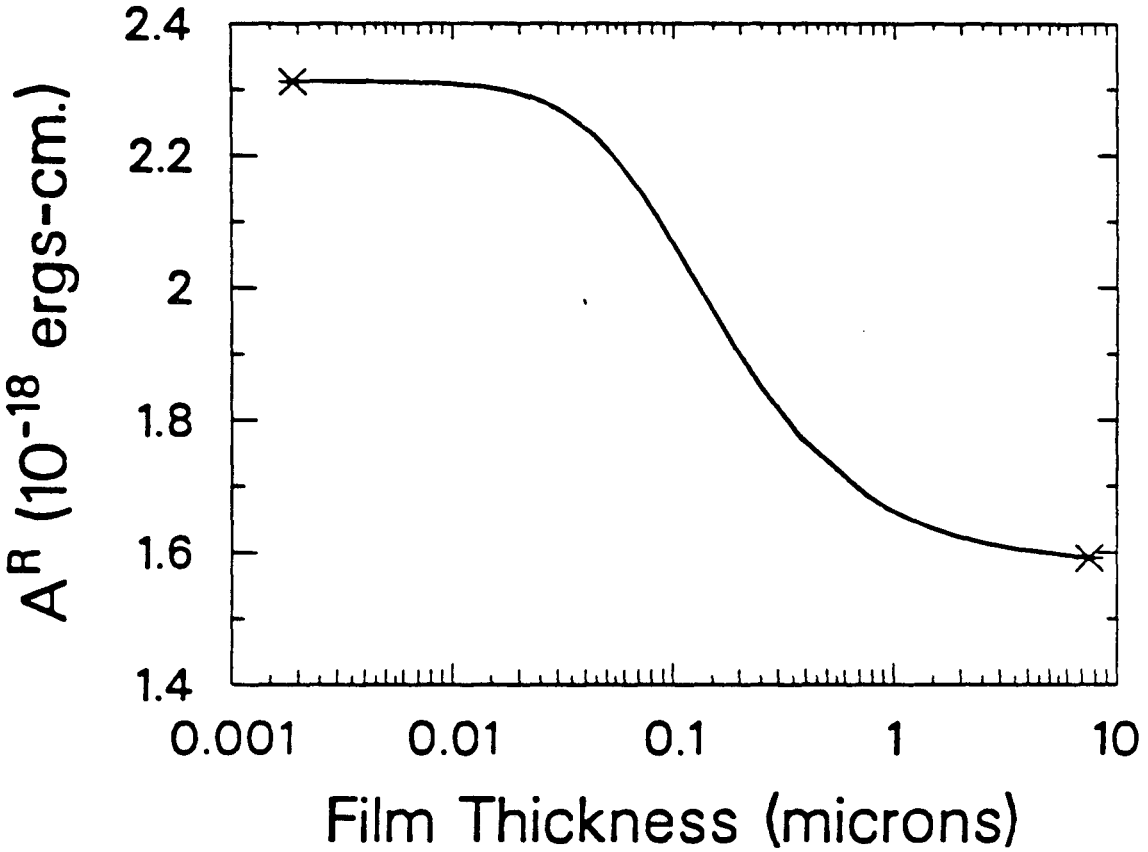


XBL 867-2721

**Figure 4-11:** The retarded Hamaker constant as a function of film thickness for the platinum / 1 M KOH / vapor system.

# Chapter 5

# Experimental Technique, Setup, and Procedure

## 5.1. Introduction

The optical technique used in this study for the measurement of film thicknesses is white-light multiple-beam interference. The technique was developed by Rolf H. Muller and subsequently was in collaboration with Turney (1971), Brown (1973) and Sand (1975). Turney initially considered white-light multiple-beam interference. He determined color series, charts relating color to film thickness, and measured draining film profiles of electrolytes on metals. Brown tested the white-light multiple-beam interference model by comparing the model predictions to observations of vapor deposited solid films of known thickness. Sand calculated the optimum angle of incidence from which to observe interference colors and he predicted color series for both solid and liquid film systems. Since the technique is only used as a measuring device in this work, only the basic ideas underlying its principle and application will be covered here. Little of what is covered in section 5.2 is referenced directly. The development of equations such as the Drude equation or the Fresnel reflection coefficients may be found in the theses by Turney (1970), Brown (1973), and Sand (1975), or in an optics textbook. Any results specific to a single source however, will be referenced in the usual manner.

The experimental set up and procedure will also be discussed in this chapter. This will include the optical bench and the thin film cell. The physical properties of the liquids and solids used in this study will also be described.

## 5.2. White-Light Multiple-Beam Interference

Optical interference techniques provide a means of measuring the thickness of thin transparent films on the surfaces of solids. Interference techniques are non-invasive, *i.e.*, nothing comes in physical contact with the system or disturbs the system in any other way. These techniques can also measure thicknesses over a large surface area simultaneously. With the use of photography, an instantaneous record of film thickness over a large area may be made.

Optical interference in a transparent film on an absorbing substrate results from the interaction of light reflecting from the top surface of the film with that light reflecting from the bottom surface of the film. As figure 5-1 shows, interference in thin films occurs from the interaction of several beams all of which will have differing optical paths. The optical path is the distance traveled by a particular light beam. The optical path length is the product of the geometric distance traveled and the refractive index of the medium. Because the propagating waves, $\hat{w}_1$ through $\hat{w}_4$ (see figure 5-1) all have optical paths of different lengths, a phase shift will be established between each of these waves. The phase shift cLauses interference between the waves, and the amplitude of the resultant beam may be found by summing the amplitudes of the input beams at constant wavelength.

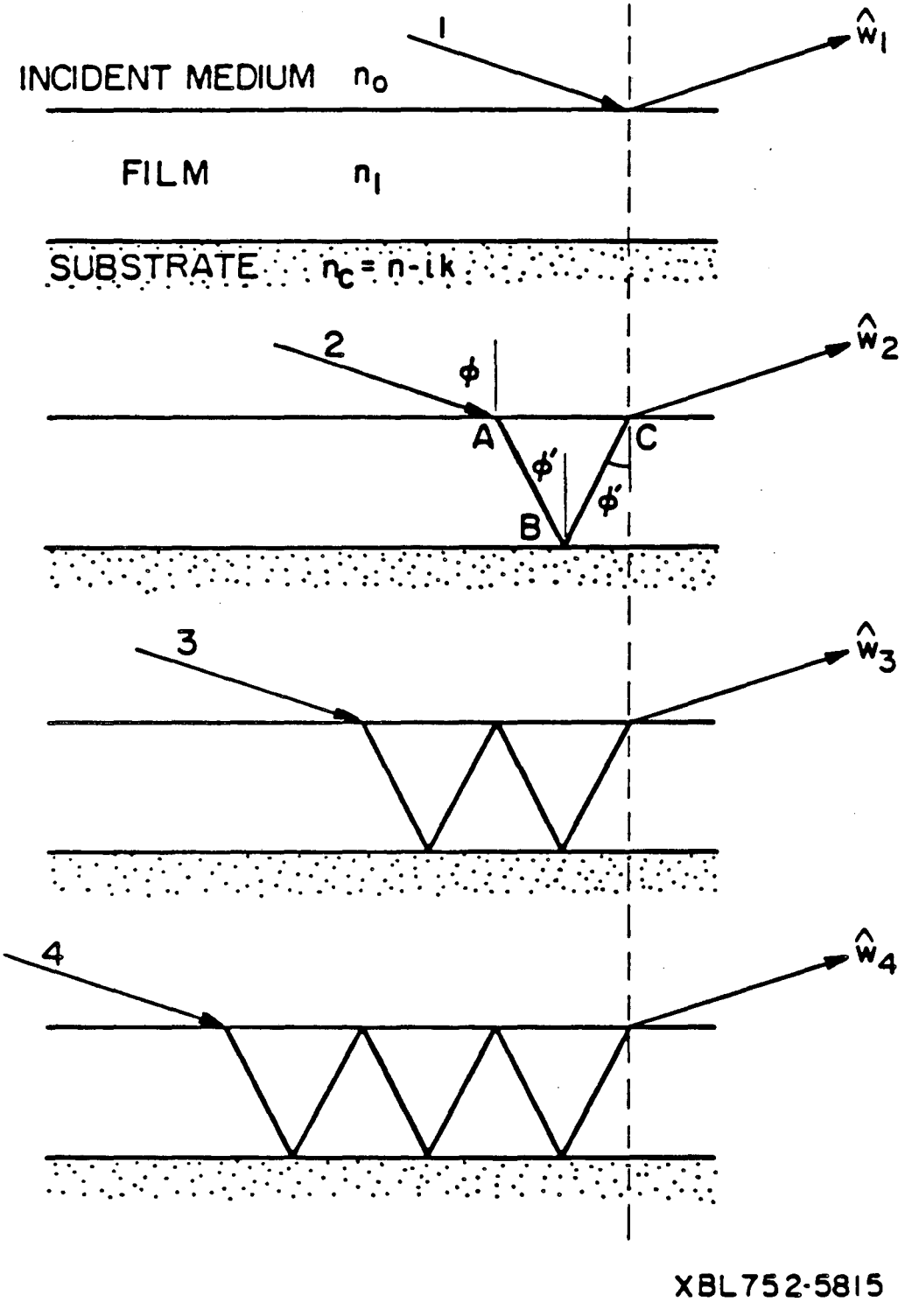


**Figure 5-1:** Schematic of thin-film multiple-beam interference. The reflected wave is the resultant of an infinite number of interfering waves. The first four ($\hat{w}_1$, $\hat{w}_2$, $\hat{w}_3$, $\hat{w}_4$) of which are shown (Sand (1975)).

If, at the angle of incidence (defined to be the angle which incoming beam makes with the surface normal) the wavelength of the light and the thickness of the film are such that the path difference between the two beams is an odd multiple of one half of the wavelength, then destructive interference will result. For the case of destructive interference the resultant beam will have a small amplitude for this wavelength. If the path difference is an even multiple of one half of the wavelength, then constructive interference will occur and the reflected beam will have a large amplitude for this frequency.

White-light is made up of many wavelengths. Therefore, for a given optical path difference some wavelengths will constructively interfere and others will destructively interfere. Those that constructively interfere increase their relative contribution to the reflected beam while those that destructively interfere decrease their relative contribution. The resulting reflected beam will have a spectral distribution different from that of the incident beam and will display color. The wavelengths for which constructive and destructive interference occur are a function of among other things the film thickness. Therefore, for a tapered film the wavelengths for which constructive and destructive interference occurs will change from one end of the film to the other, and thus the color of the reflected beam will change from one end of the film to the other.

The intensity of the reflected and transmitted beams shown in figure 5-1 is dependent on the angle of incidence, polarization state of the light source, the thickness of the film, and the index of refraction of the three phases forming the surfaces of the thin film, *i.e.*, the incident medium, the film, and the substrate

(see figure 5-1). The angle of incidence and the polarization state of the incident light may easily be controlled. The spectral composition of the beam resulting from the sum of the multiple-beams emerging from the surface can be determined for any film thickness given the index of refraction as a function of frequency for the three phases.

We shall only consider linearly polarized light, and will make the following designations. S-polarized light is light whose electric field vector oscillates perpendicular to the plane of incidence. P-polarized light is light whose electric field vector oscillates in the plane of incidence, see figure 5-2. The amplitude reflection coefficient of any surface is defined as the ratio of the amplitude of the reflected light to that of the incident light.

$$r = \frac{E'}{E} \tag{5-1}$$

The s and p-reflection coefficients may be calculated from the angle of incidence and the complex indices of refraction of the materials on either side of the interface using the Fresnel equations.

Upon reflection of light from a surface, there is also an associated phase change in that light. For s-polarized light reflecting from a non-absorbing surface the phase change is always 180° for an external reflection and 0° for an internal reflection. For an external reflection of p-polarized light the phase change is 0° from 0° angle of incidence to Brewster's angle and 180° above Brewster's angle. For an internal reflection, the phase change for p-polarized light is 180° below Brewster's angle and 0° above. The reflection coefficient and

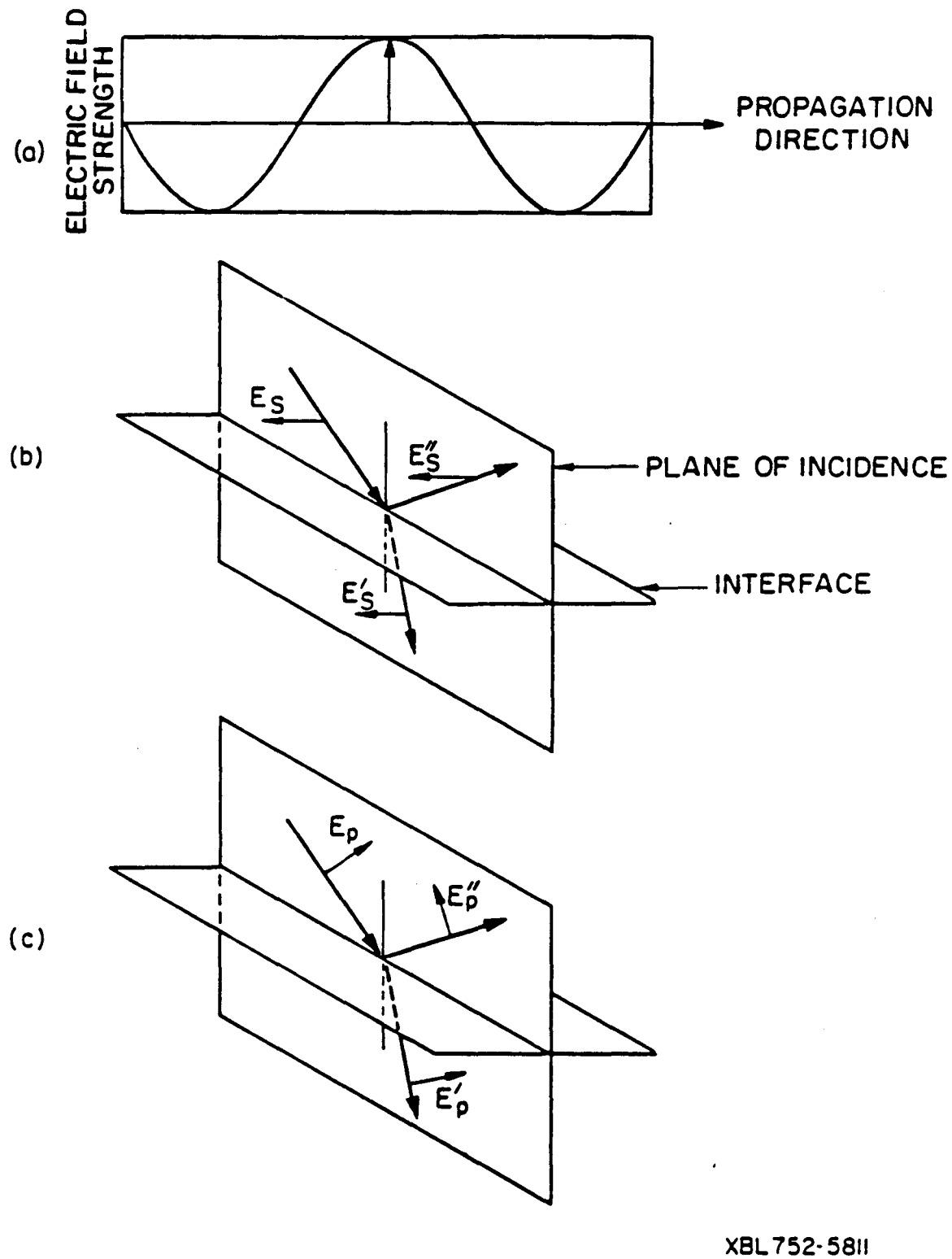


**Figure 5-2:** (a) Electric field strength of linearly polarized light at a fixed time. (b) Positive electric field vectors for incident, reflected, and refracted light for s-polarized light. (c) Same as b, but for p-polarized light (Sand (1975)).

phase change upon reflection for an external reflection, the only one necessary to consider in this work, are shown in figure 5-3. The phase changes upon reflection from absorbing surfaces are much more complicated. These have been calculated, and the exact form has been given by Mowat and Muller (1966). Figure 5-3 shows the reflection coefficient and phase change on reflection for an internal reflection from a substrate having $\hat{n} = 2.07 - i4.40$ with a film having $n = 1.35$.

Now that both reflection coefficients and phase changes due to reflection are known, the complex reflection coefficients, $\hat{r}_1$ and $\hat{r}_2$, may be defined:

$$\hat{r}_1 = \frac{E'_1}{E_1} e^{-i\delta_1} = r_1 e^{-i\delta_1} \tag{5-2}$$

$$\hat{r}_2 = \frac{E'_2}{E_2} e^{-i\delta_2} = r_2 e^{-i\delta_2} \tag{5-3}$$

where the subscripts 1 and 2 denote on which surface the reflection is occurring, 1 is the top surface of the film and 2 is the substrate, see figure 5-4, r denotes the appropriate reflection coefficient from the Fresnel equations, and $\delta$ denotes the appropriate phase change on reflection.

The summation of all beams emerging from the film surface can be shown to be represented by a converging series (Sand, 1975). The sum of this series is given by equation 5-4.

$$\hat{w} = \sum_{n=1}^{\infty} \hat{w} = r_1 e^{i\delta_1} + \frac{(1-r_1^2) r_2 e^{-i(\delta-\delta_2)}}{1+r_2 r_1 e^{-i(\delta+\delta_1-\delta_2)}} \tag{5-4}$$

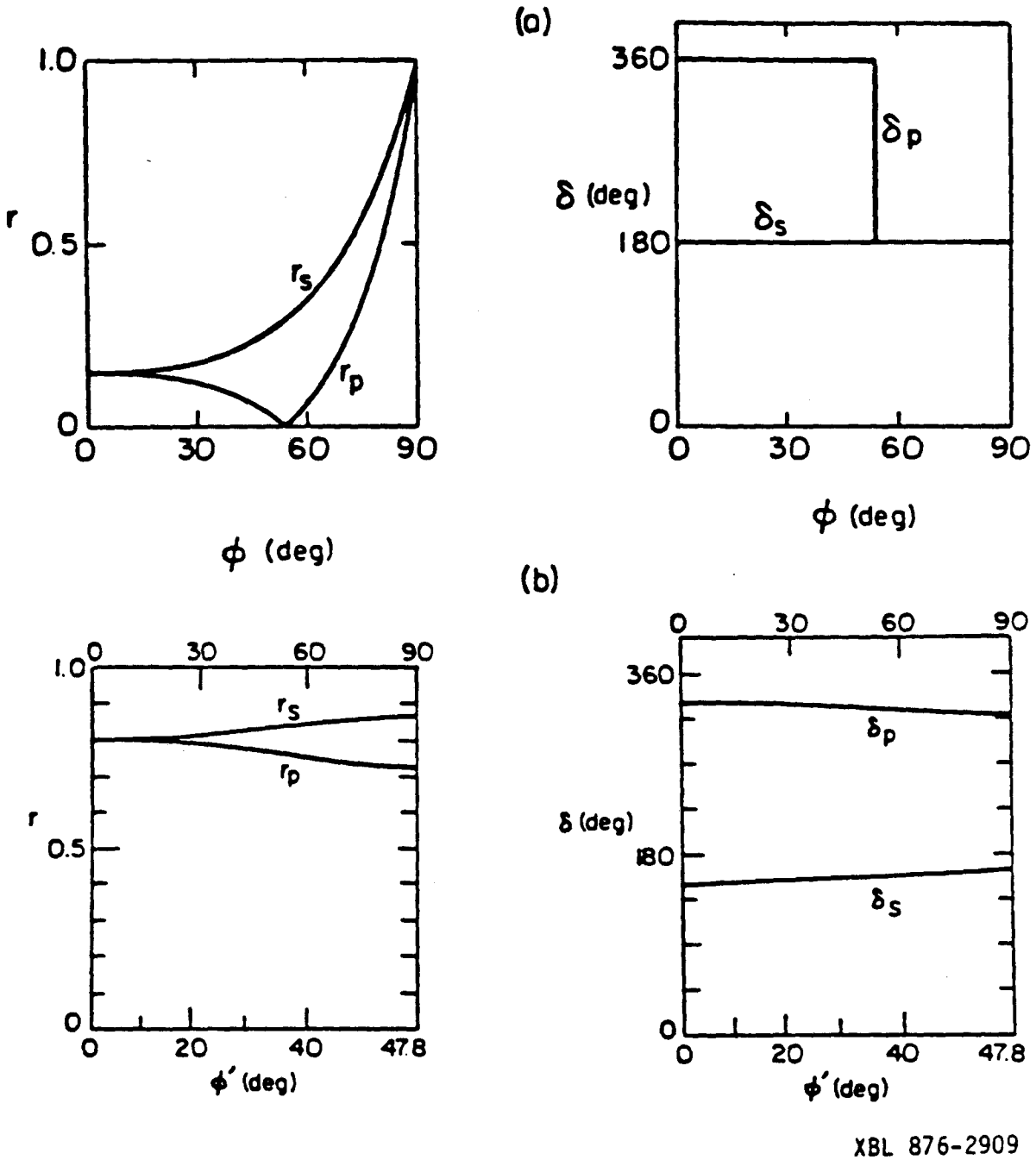


**Figure 5-3:** s- and p-reflection coefficients, r, and phase change upon reflection, $\delta$, for (a) an external reflection from a non-absorbing surface and (b) an external reflection from an absorbing surface (incident medium n = 1.35, substrate $\hat{n} = 2.07 - i\,4.40$).

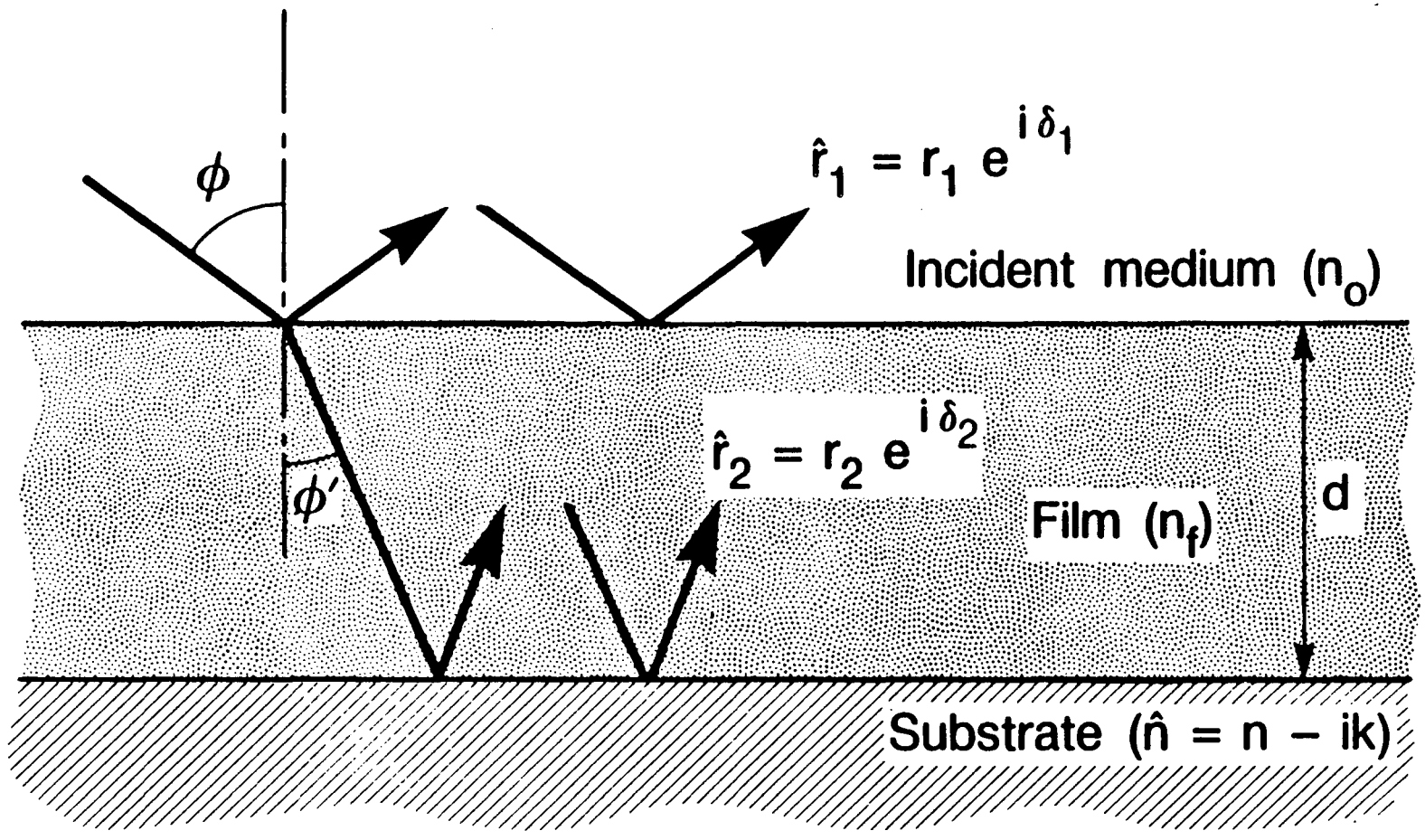


XBL 785-873 A

**Figure 5-4:** Geometry of reflection in thin films and definition of complex reflection coefficients and subscripts

where $r_1$ and $r_2$ are the amplitude reflection coefficients the top film surface and the substrate surface respectively, $\delta_1$ and $\delta_2$ are the phase changes on reflection from these surfaces, and $\delta$ is the phase shift due to the difference in optical path length which will be explained below. When the two terms in equation 5-4 are written over a common denominator and equations 5-1 and 5-2 are substituted, the equation reduces to the Drude equation:

$$\hat{w} = \frac{\hat{r}_1 + \hat{r}_2 e^{-i\delta}}{1 + \hat{r}_2 \hat{r}_1 e^{-i\delta}} \tag{5-5}$$

The phase shift, $\delta$ is defined as the phase shift resulting from the optical path difference for one passage through the film, see figure 5-5. The optical path difference is defined as;

$$\Delta S = \overline{ABC} - \overline{DC} \tag{5-6}$$

Snell's law, equation 5-7 relates the incident angle, $\phi$, to the refracted angle, $\phi'$;

$$n_0 \sin\phi = n_1 \sin\phi' \ , \tag{5-7}$$

where $n_0$ and $n_1$ are the refractive indices of the incident medium and the film respectively, see figure 5-5. It should be noted that in figure 5-3 the refractive index of the film is referred to as $n_f$, but everywhere else in this thesis it will be referred to as $n_1$. Using Snell's law and appropriate trigonometric identities, the optical path difference may be written;

$$\Delta S = 2 n_1 d \cos\phi' \ , \tag{5-8}$$

where d is the film thickness. The phase shift due to the optical path difference

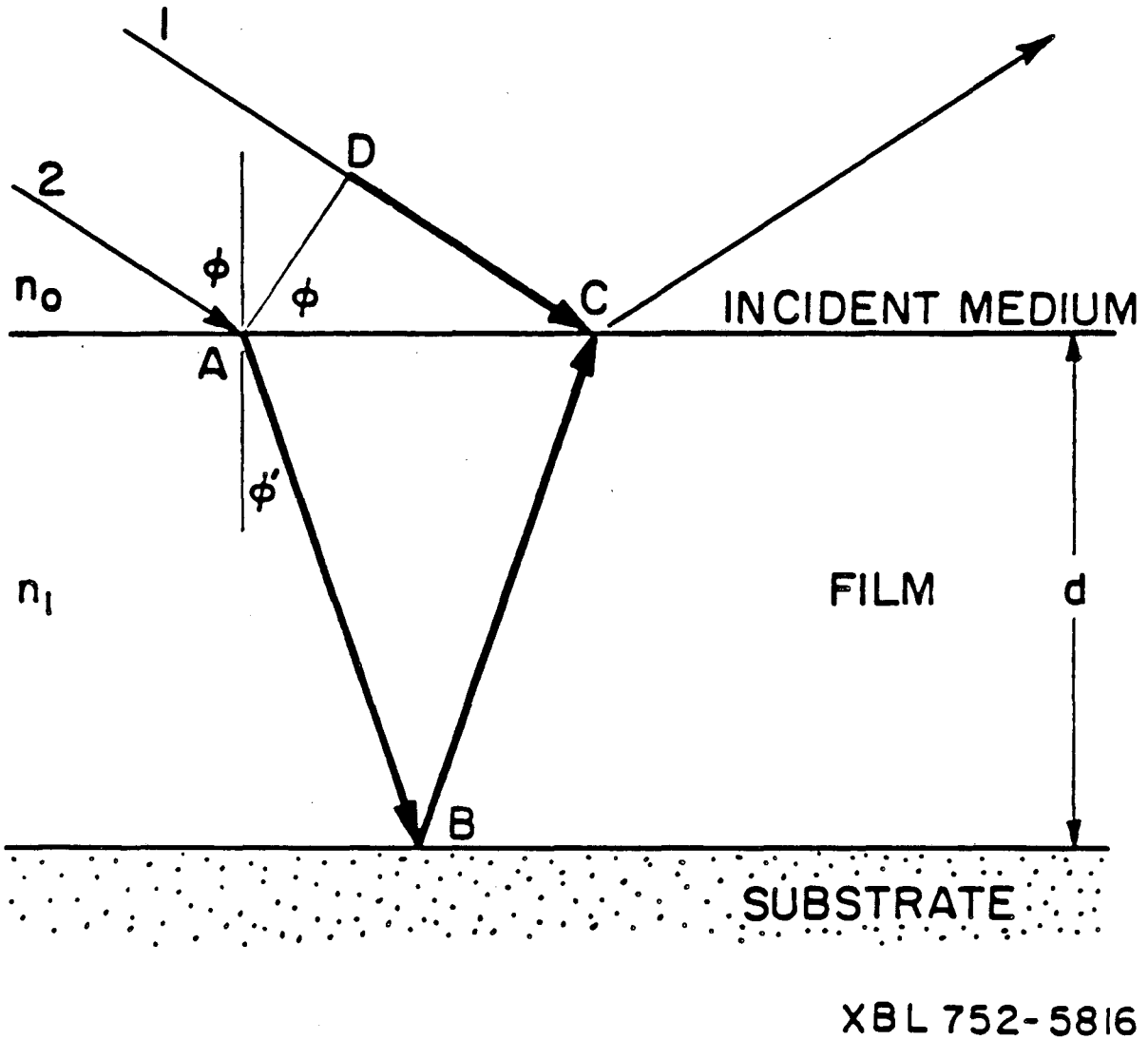


**Figure 5-5:** Geometry for the definition of the optical path difference, $\Delta S = \overline{ABC} - \overline{DC}$, after one internal reflection.

may now be defined for any given wavelength of light, $\lambda$.

$$\delta = \frac{2\pi\Delta S}{\lambda} = \frac{4\pi n_1 d \cos\phi'}{\lambda} \tag{5-9}$$

Up to this point, equation 5-9 is the only equation where an explicit wavelength dependence appears. However, if the index of refraction of any one of the incident medium, the film, or the substrate is wavelength dependent, the reflection coefficient and the phase shift due to reflection which involve that material will also be wavelength dependent. For proper treatment, these dependencies should be accounted for when calculating the spectral composition of a reflected beam from a white-light source. However, Sand (1975) showed that these effects are minimal.

One other aspect of white-light multiple-beam interference must be considered. That is the effect of the angle of incidence on the visibility of the color of the reflected beam. If the angle of incidence is such that either the beam reflected from the surface of the film, or the beam reflected from the surface of the substrate is much more intense than the other, the effect of interference on the resultant reflected beam will be minimal and the color visibility will be poor. An optimal angle of incidence exists for which the interference fringe visibility is maximized. The optimal angle of incidence is dependent on reflection coefficients and therefore indices of refraction. Details concerning the calculation of the optimum angle of incidence for a polychromatic light source is contained in the thesis by Sand (1975) and for a monochromatic light source in Muller and Sand (1980).

Using programs written by Sand, the optimum angle of incidence for a film having an index of refraction of 1.33 on platinum where $\hat{n} = 2.10 - i3.67$ at 5390 angstroms was determined to be 75° and 81° for s and p-polarized light respectively. The color series for s and p-polarized light at 75° and 81° angle of incidence was computed. The results for film thicknesses of zero to one micrometer are shown in figure 5-6. The color names appearing in figure 5-6 are derived according to the 1931 C.I.E. chromaticity diagram from definitions from Wright (1964) as modified by Sand (1975).

Figure 5-6 is representative of the color series used to determine film thicknesses in this work. The series of colors, red-purple-blue-green-yellow-orange, is seen to repeat itself as film thickness is increased. This occurs because the optical path difference in thicker films becomes multiples of half wavelengths. This causes the spectral composition in the reflected beam to produce similar stimulation to the human eye as that for other film thicknesses. Therefore color orders are used to express where on the color series the observed color lies. As color order increases, the color purity in general will decrease even if the observation is being made at the optimum angle of incidence.

Figure 5-6 also shows the difference between s and p-polarized interference colors. By observing interference colors with the naked eye, an observed color of a known color series places the film thickness within a range as defined in figure 5-6. If a transition between to colors of a known interference order is observed, the thickness may be determined much more precisely. We see that color transitions occur at different thicknesses for s and p-polarized light. Therefore, by

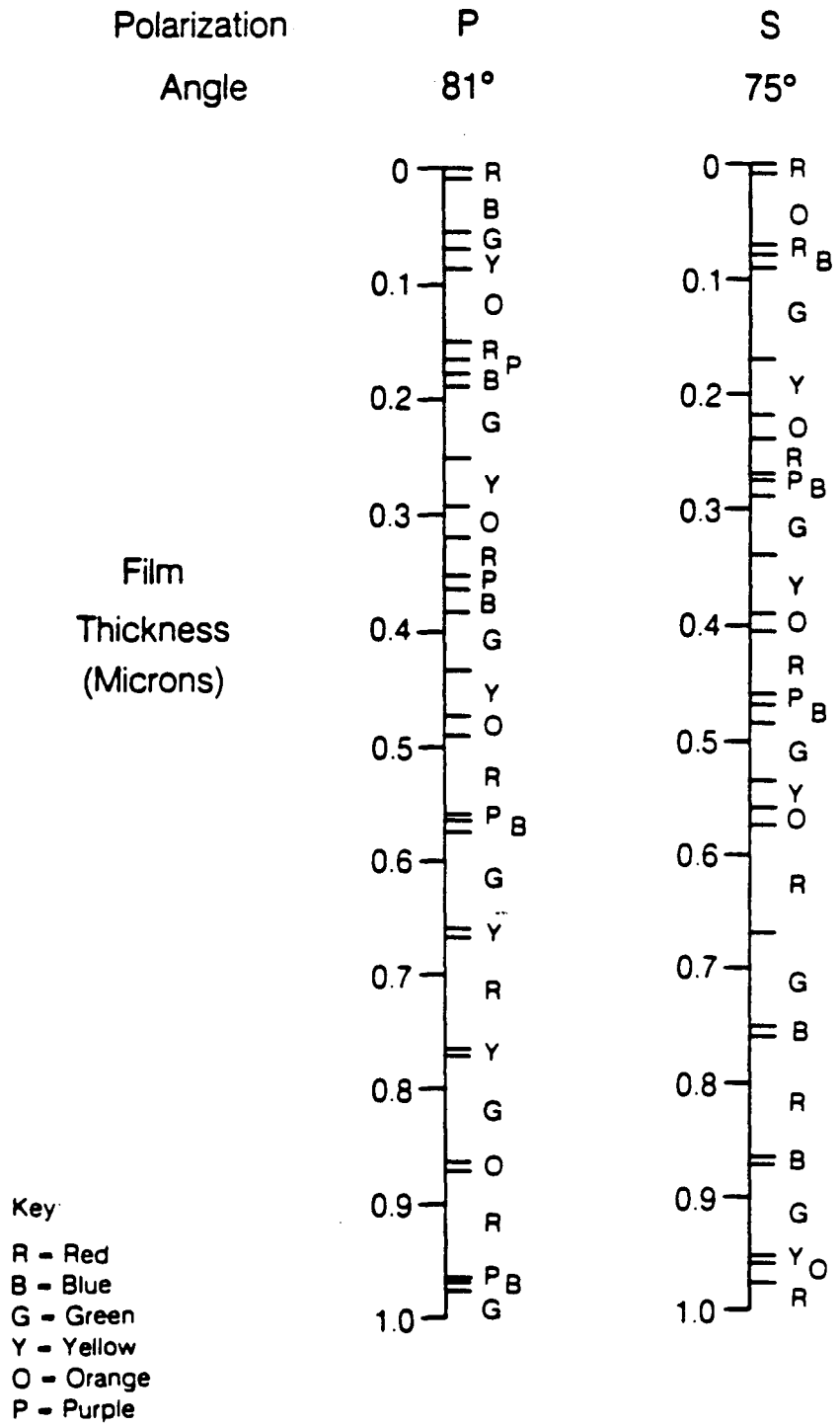


XBL 876-9704

**Figure 5-6:** Color series between 0 and 1 micrometers film thickness for s- and p-polarized light for a dilute aqueous film, n = 1.35 on a platinum substrate (optical properties listed in table 6-1).

observing both the s and p interference colors, approximately twice the number of thickness measurements may be made.

### 5.3. Ellipsometric Measurements

A wavelength scanning ellipsometer was used to verify white-light multiple-beam interference thickness determinations. The Drude equation (eqn. 5-5) when applied to pure p or s-polarized incident light may be resolved into a complex reflection coefficient specific to that polarization:

$$\hat{r}_s = \frac{\hat{r}_{1,s} + \hat{r}_{2,s}e^{-i\delta}}{1 + \hat{r}_{2,s}\hat{r}_{1,s}e^{-i\delta}} = r_s e^{i\delta_s} \tag{5-10}$$

$$\hat{r}_p = \frac{\hat{r}_{1,p} + \hat{r}_{2,p}e^{-i\delta}}{1 + \hat{r}_{2,p}\hat{r}_{1,p}e^{-i\delta}} = r_p e^{i\delta_p} \tag{5-11}$$

The ratio of $\hat{r}_p$ to $\hat{r}_s$ defines two parameters $\Delta$ and $\Psi$.

$$\frac{\hat{r}_p}{\hat{r}_s} = \frac{r_p}{r_s} e^{i(\delta_p - \delta_s)} = \tan\Psi \, e^{i\Delta} \tag{5-12}$$

where $\tan\Psi$ is the relative amplitude attenuation, and $\Delta$ is the relative phase shift between the p and s-polarizations upon reflection from a film covered surface. Film thicknesses may be determined by measuring $\Delta$ and $\Psi$ along with the complex refractive index of the film and substrate (Muller, 1973).

### 5.4. The Optical Bench

The optical bench used for the observation of interference colors is shown schematically in figure 5-7. This figure is a view from above of the optical bench. The schematic shows that light from two point sources is collimated and

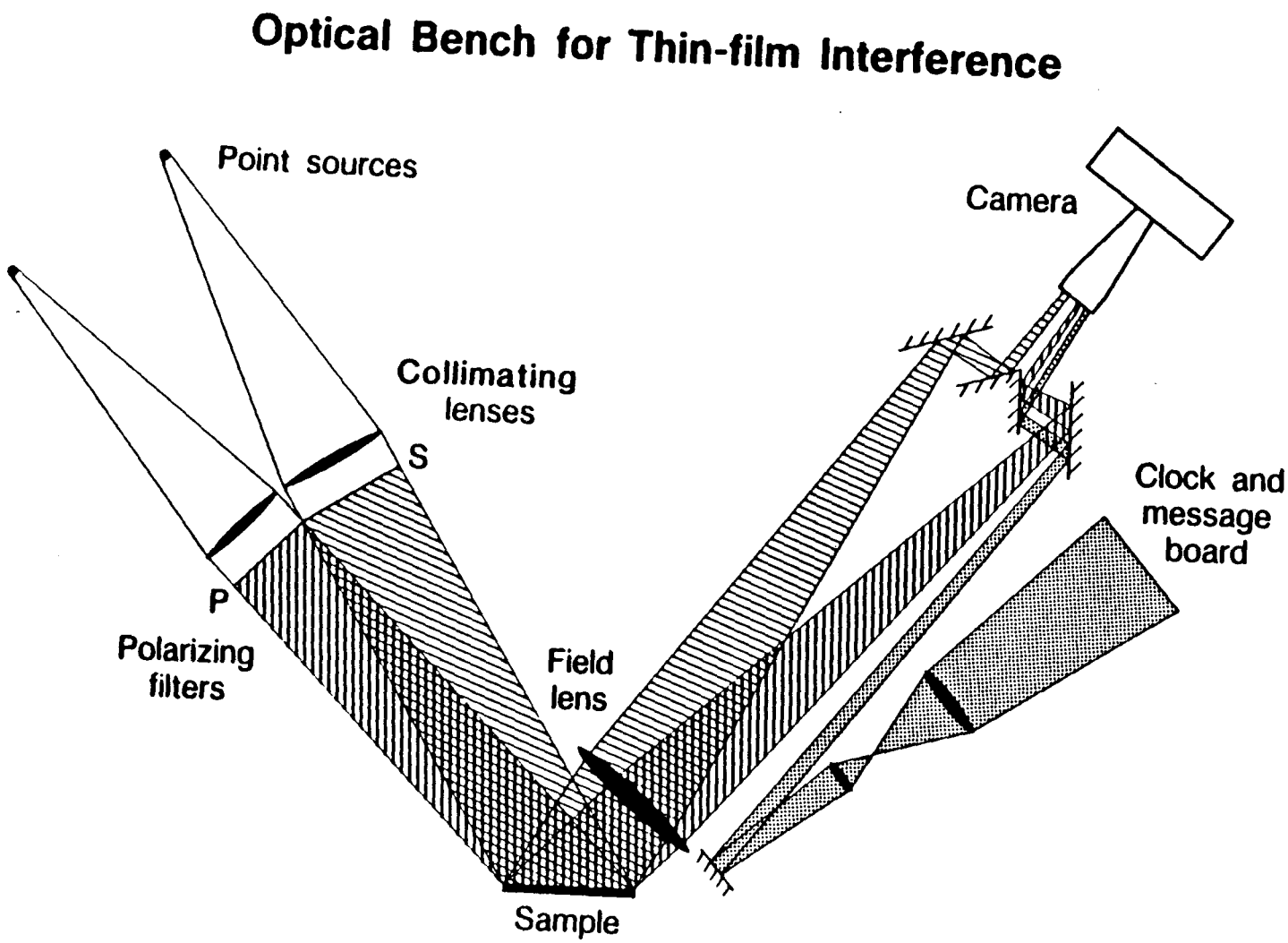


**Figure 5-7:** Top view schematic diagram of the optical bench for the observation of thin film interference colors.

then polarized, one s and the other p. These beams converge onto the sample on which a thin film exists. The reflected beams are collected by the field lens and focused into the lens of a Bolex 16 mm movie camera. Simultaneously the image of a clock and message board are directed into the lens of the camera.

Figure 5-8 is a photograph of the optical bench. Two tungsten microscope lamps, in the top left of the photo, separated by 6° are the light sources. These are focused on ground glass diffusers and 2 mm diameter irises behind the diffusers approximate point sources. The light beams after being collimated and polarized impinge on the sample surface which is in a cell that sits within the plywood constant temperature box seen in the center of the photograph. Windows on either side of the box permit the passage of light. The temperature within this box is controlled to within 0.05° C by an model 5C5-220 controller Oven Industries, Mechanicsburg, PA. A field lens collects the reflected light and a system of mirrors directs the light into the lens of a Bolex 16 mm camera at the right of the photograph. The camera and lamps are controlled by an interval timer so that time-lapse movies may be made of a draining film. A clock and message board, associated optics, and illumination lamps, also controlled by the interval timer, are hidden behind the camera.

Other equipment used include a Gamma Scientific high efficiency dual monochrometer, a model 700 and a model 2020 Gamma Scientific photometer, and a home made ratiometer which are on the cart at the left of the photo. These were used to record the ratio of intensities of reflected to incident beams as a function of wavelength. Also, shown beneath the optical bench are an

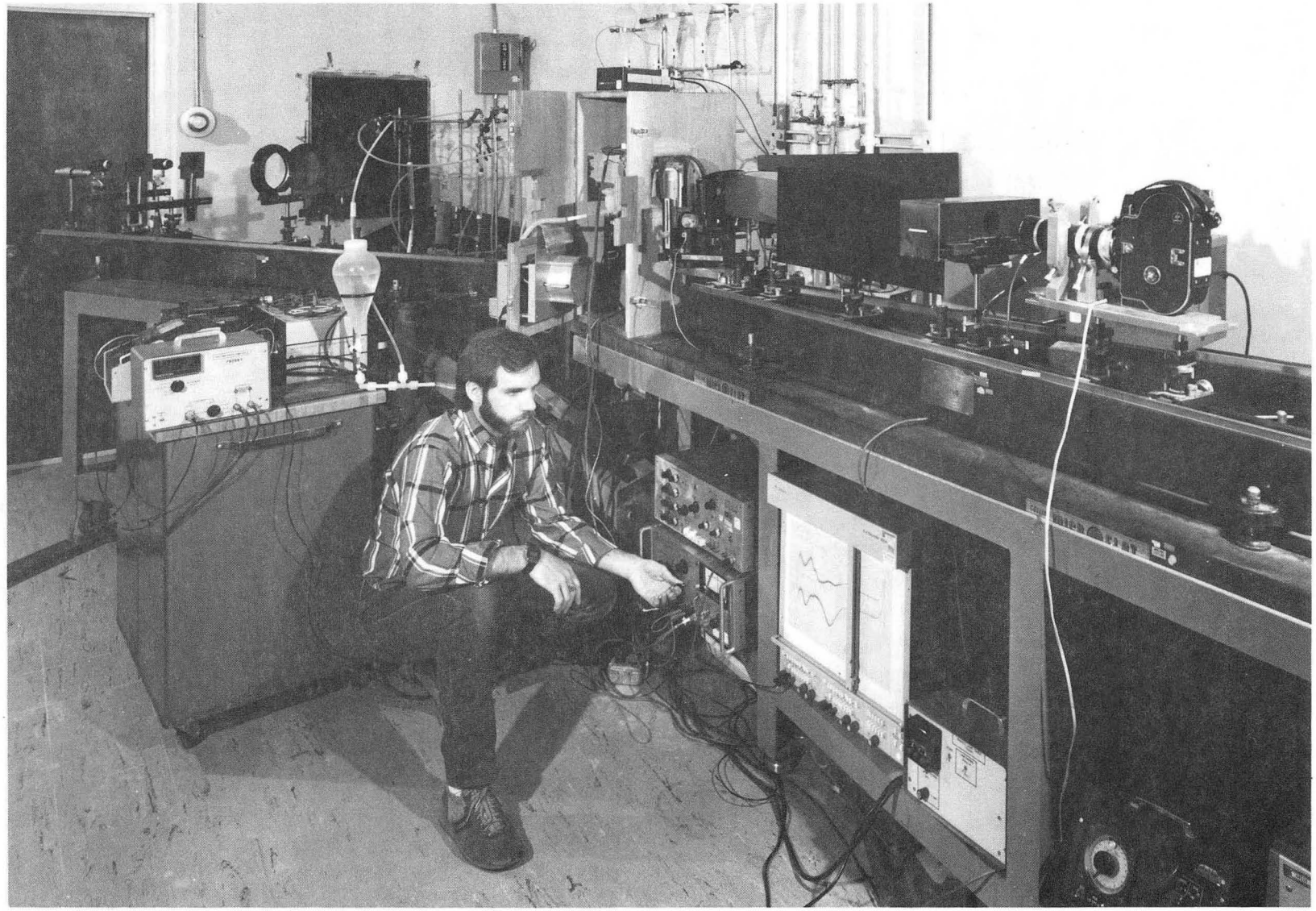

**Figure 5-8:** Photograph of the optical bench and related instruments.

CBB 864-3068

EG&G model 175 programmer, an EG&G model 371 potentiostat, and a Gould 3054 x-y plotter. These were used to do cyclic voltammetry on the metal surface prior to the drainage of electrolyte from the surface. Cyclic voltammetry is used as an indication of the cleanliness of the metal surface and electrolyte.

### 5.5. Liquid Film Cell, Substrates, and Electrolytes

Two different cells were used in this work. The smaller cell, see the cross-section schematic in figure 5-9, was made of polypropylene, and was constructed to house a 10 cm tall 4 cm wide metal plate from which liquid is drained. The larger cell is shown in two schematics. Figure 5-10 is a cross-section schematic showing the arrangement of the substrate, reference electrode, sparge, and counter electrodes. Figure 5-11 is a composite top view. Half of it is a normal top view while the other half is a cross-section. This figure shows the shape of the weir and the means of clamping the windows to the cell. This large cell was made of TFE Teflon, and was constructed to house a 10 cm tall 10 cm wide metal plate. The only other difference between the two is that the smaller cell has a separate compartment for a counter electrode whereas the larger cell has a single compartment in which both the substrate and counter electrode are placed. Figure 5-12 is a photograph of the large liquid film cell.

The metal substrate from which liquid is drained is mounted vertically at the back of the cell. Backstops insure that the substrate is mounted vertically and a platinum pin holds the substrate in place. This pin also serves as an electrical connection to the substrate. There are six ports in the top of the cell. These ports allow for electrical connection to the substrate, electrical connection

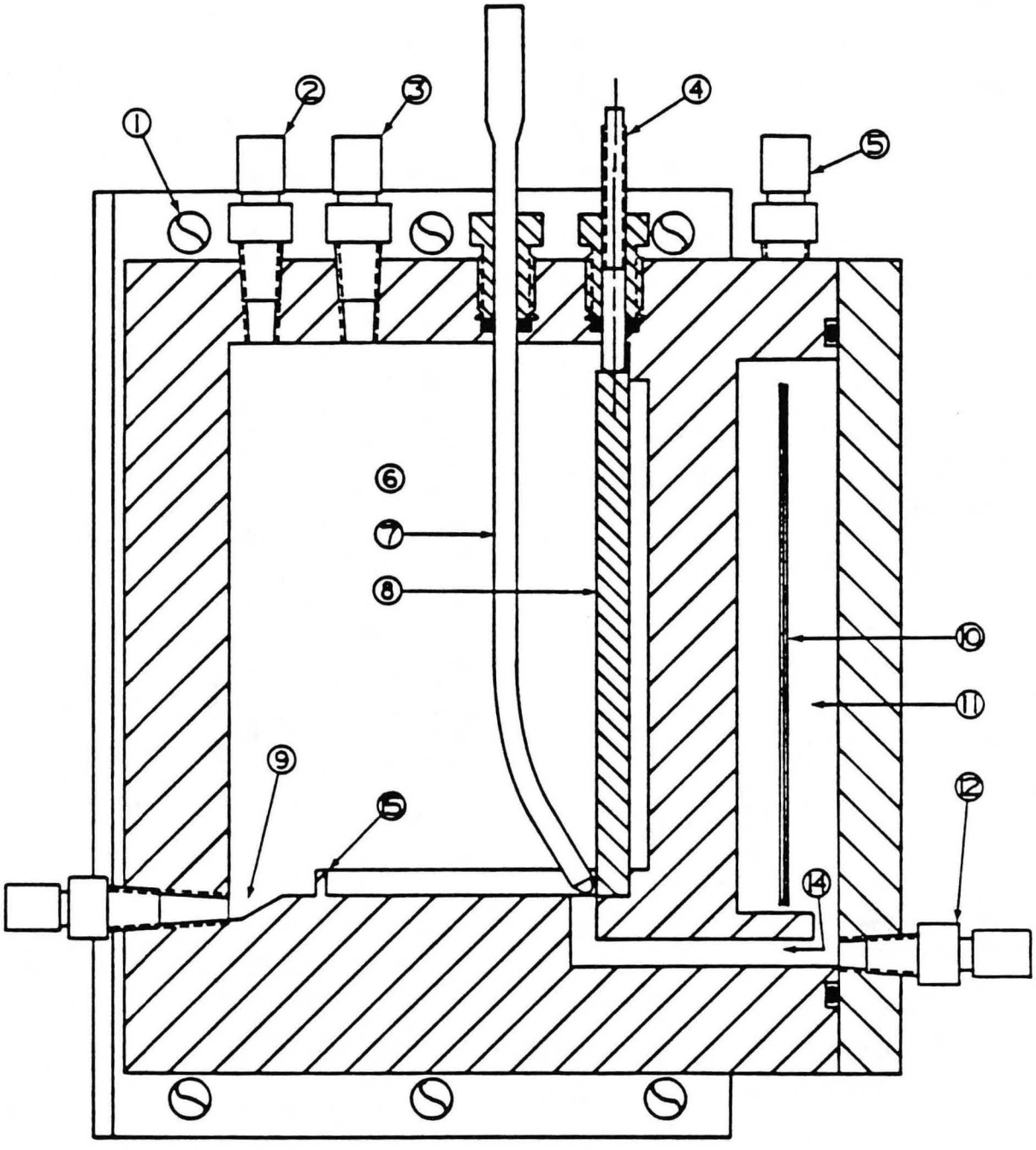


XBL 711-6409

**Figure 5-9:** Cross section schematic of the small liquid film cell: 1. bolt for clamping windows, 2. gas inlet, 3. gas outlet, 4. electrical contact, 5. gas outlet for counter-electrode chamber, 6. main chamber, 7. luggin capillary for reference electrode, 8. metal substrate, 9. electrolyte outlet, 10. Counter electrode, 11. counter electrode chamber, 12. electrolyte inlet, 14.passage between chambers, 15. weir.

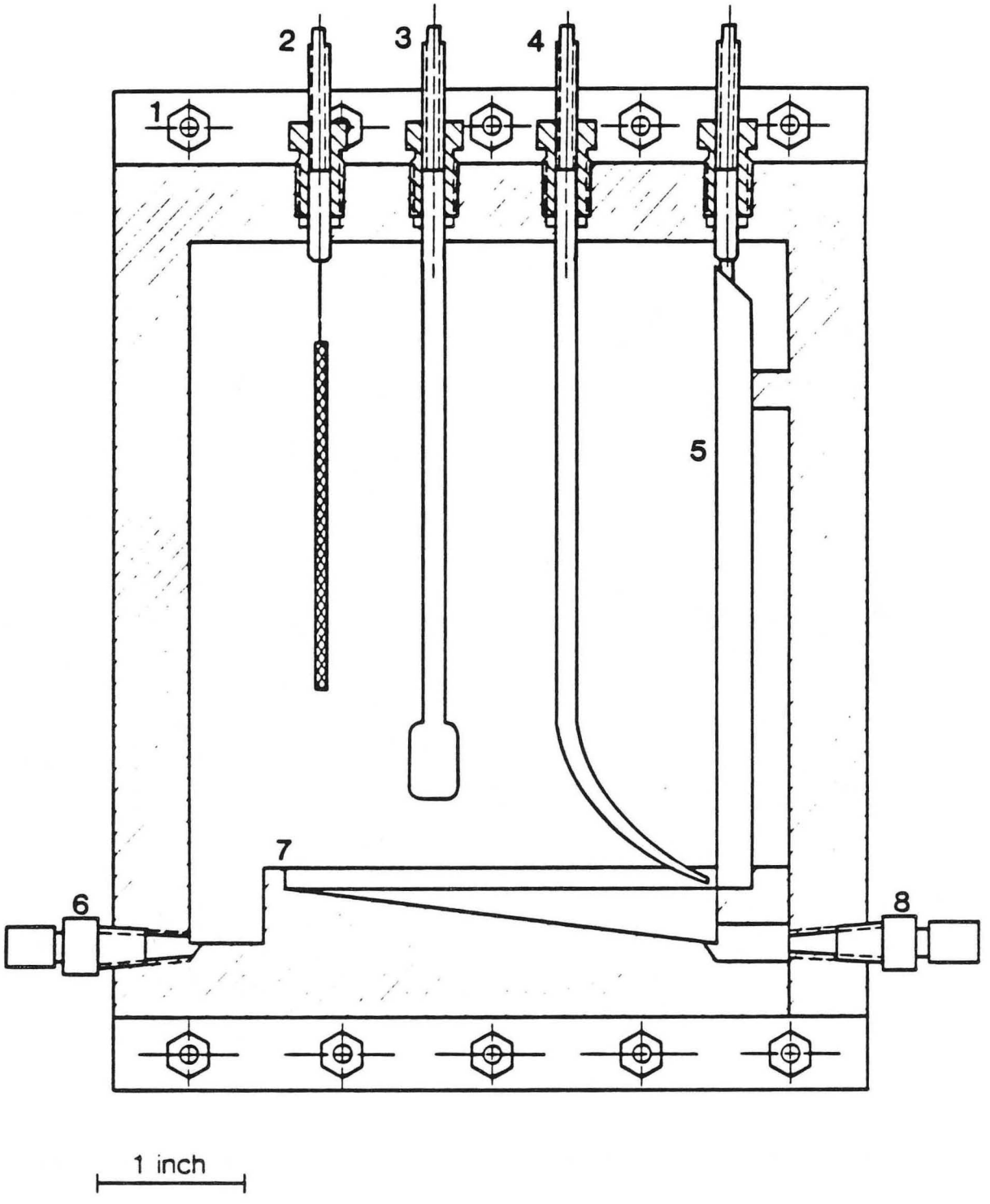


XBL 876-10207

**Figure 5-10:** Cross section schematic of the large liquid film cell: 1. bolt for clamping windows, 2. counter electrode, 3. gas sparge, 4. luggin capillary for reference electrode, 5. metal substrate, 6. electrolyte inlet/outlet, 7. weir, 8. auxiliary electrolyte inlet/outlet.

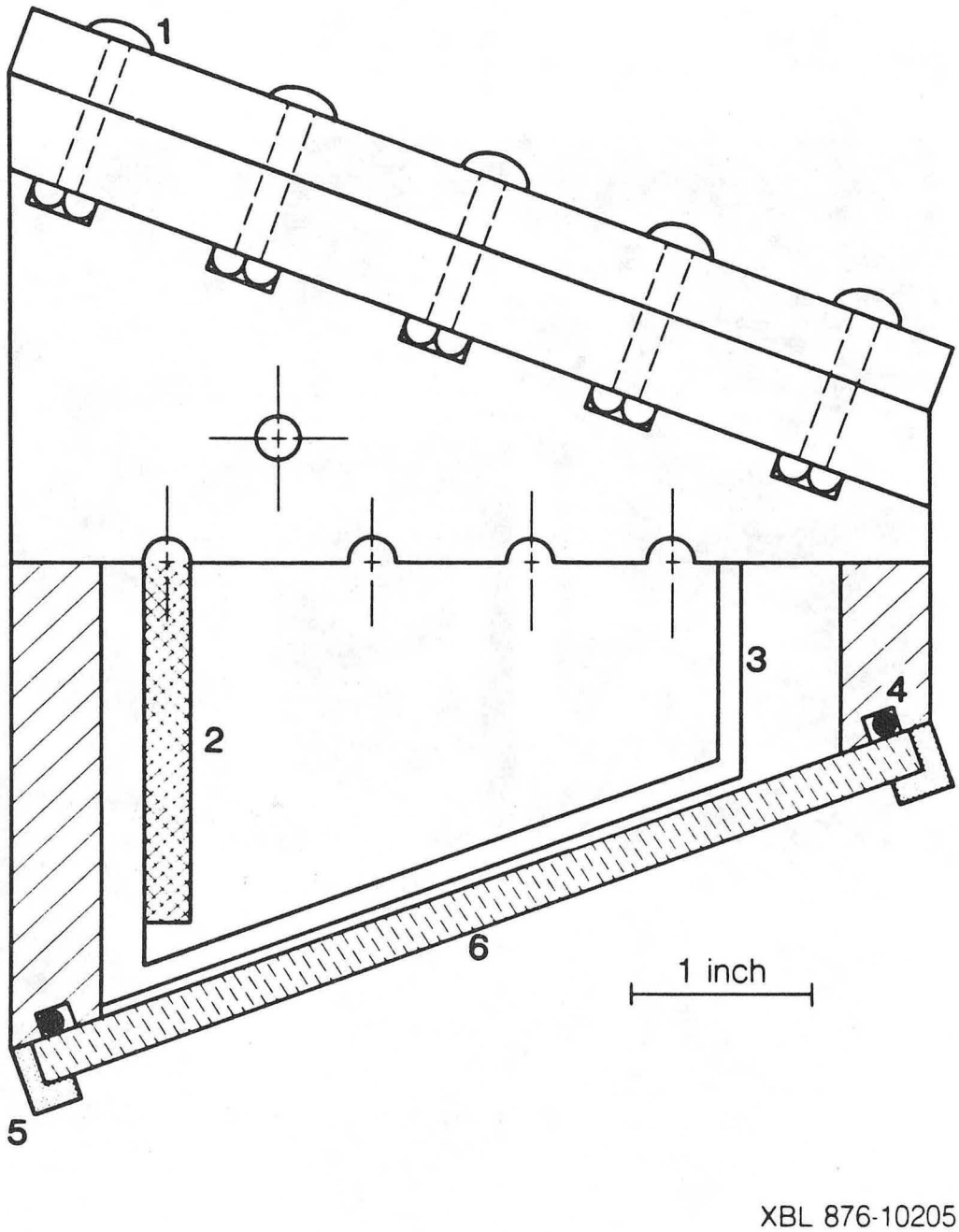


**Figure 5-11:** Top view schematic (top half is normal view, bottom half is cross section) of the large liquid film cell: 1. bolt for clamping windows, 2. metal substrate, 3. weir, 4. Teflon gasket, 5. stainless steel frame for holding window, 6. window.

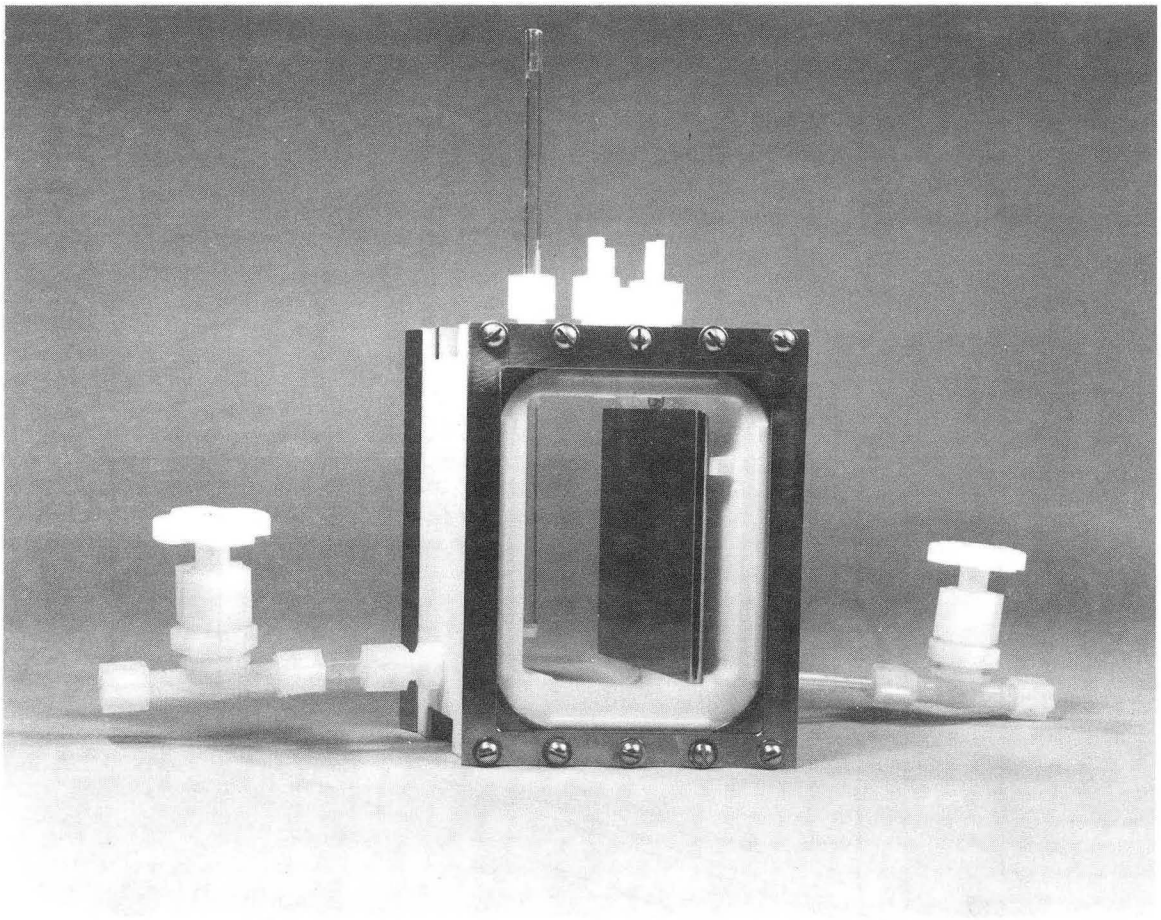

XBB 862-1007

**Figure 5-12:** Photograph of the large liquid film cell.

to a counter electrode, a luggin capillary for a reference electrode, and gas inlet and outlet. A filter or vapor lock was placed on the gas outlet to prevent dust and other airborne contaminants from entering the cell. There are also ports at the front and back of the cell to allow for liquid introduction and removal. All of the port connections are made via FEP Teflon fittings, (Galtek), having pipe threads that screw into the cell body and compression fittings that attach to tubing leading to the outside. A weir at the bottom of the cell maintains a pool of liquid in contact with the bottom of the substrate when liquid is removed through the right hand valve, and a sloped bottom permits total liquid removal through the left hand valve. Two glass windows mounted on either side of the cell permit light to reach the substrate for the observation of interference colors. The seal between the glass and cell body is made with FEP Teflon coated silicon cored composite gaskets, (Bay Seal, Hayward, CA). The windows are held in place by 316 LVM stainless steel frames which bolt through the cell body. For clarification see the schematics and photograph in figures 5-10 through 5-12.

Four metal substrates were used in this work. Two of these are for the small cell. One is 10.5 cm tall 4 cm wide and 0.4 cm thick. It is made of platinum and its back and sides are Kynar coated to prevent wetting on these surfaces and to provide electrical insulation. The other electrode for the small cell is a 20 mil thick 10.5 cm by 4 cm gold sheet bonded to a 0.4 cm thick 316 LVM stainless steel plate of identical area. The back and sides of the stainless steel are also Kynar coated. The other two substrates used are both for the large cell. Both of these substrates are platinum and both have the dimensions of 10.5 cm

tall 10 cm wide and 0.4 cm thick. Neither substrate was Kynar coated. The difference between the two was that the edges of one are square cut where as the sides of the other are rounded, see figure 5-13. All four substrates have the top edge cut into a point, see figure 5-13. This was done to prevent droplets of liquid from adhering to the top edge of the substrate. All substrates are polished to optical flatness. The specifications called for less than 200 angstroms local roughness and less than two wavelengths of surface-roll over the entire surface. The platinum substrate having rounded sides had both the front and back surfaces optically polished and the sides were polished by hand as best as possible. this was done in order to approximate an infinitely wide surface.

Electrolytes were all made up from ultra pure chemicals except for phosphoric acid which was purified in this laboratory, (procedure is listed below). The water used in aqueous electrolytes was in most cases ultra pure water, (Harleco, American Scientific Products, Sunnyvale, CA), specified to be of greater than 10 MΩ/cm specific resistance and virtually particulate free. The maximum particulate size is 0.04 $\mu$m. High-temperature-oxygen-purged deionized doubly-distilled water from an in house source was was used for a few early experiments. This was discontinued because of concern over possible contamination from silicone grease used on the glass joints of the distillation apparatus. Ultra pure potassium hydroxide, sodium perchlorate, and potassium chloride were all purchased from Alfa Products "Puratronics", electronic grade, line of chemicals. Pure, 99%, tetradecane was also purchased from Alfa Products.

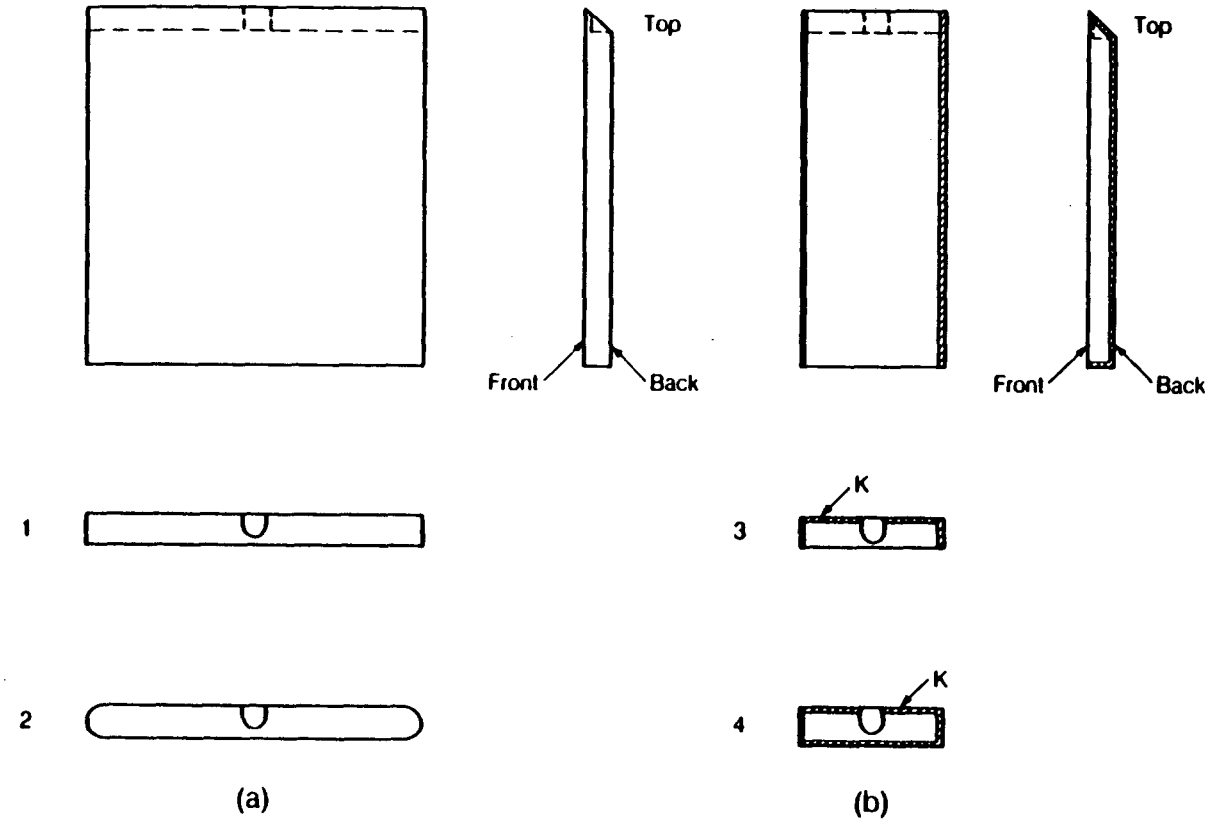


XBL 876-10206

**Figure 5-13:** Schematic of metallic substrate shapes: (a) 100 $cm^2$ bare platinum substrate optically polished only on the front surface, (b) 100 $cm^2$ bare platinum substrate optically polished on both the front and back sides, with rounded sides and tilted top polished by hand, (c) 40 $cm^2$ platinum substrate, front side optically polished all other surfaces Kynar coated, (b) 40 $cm^2$ gold substrate, front side optically polished all other surfaces Kynar coated.

Phosphoric acid solutions were made up from phosphoric acid that was purified in house as per the method of Ferrier, et al. (1975). Two parts Baker reagent grade 85% ortho phosphoric acid and one part 30% hydrogen peroxide were combined in a covered FEP Teflon beaker. This solution was maintained at 40 °C until spontaneous dissociation of the hydrogen peroxide had ceased, approximately 24 hours. The temperature was then increased to 150 °C until all remaining hydrogen peroxide had decomposed and the acid was reconcentrated to 85%. This concentrated solution was then diluted to the proper concentration using Harleco ultra pure water.

All liquids were stored in FEP Teflon containers. Some solutions were used without filtration and others were filtered. If a solution was reused it was always filtered. The filter system is a series of three in-line FEP Teflon filters containing Teflon filter discs. The maximum pore sizes of the three filters are 20, 5, and 1 micron. The filters are linked by Teflon tubing in order of decreasing pore size and the solution was pulled through the filters by vacuum.

All aqueous solutions were preelectrolyzed for a minimum of 24 hours prior to use. The electrodes used were large surface area 90% platinum, 10% rhodium 80 mesh screen. Preelectrolysis was performed in a FEP Teflon separatory funnel and a nitrogen sparge was placed at the bottom of the funnel to provide an inert atmosphere and for stirring. A filter was placed between the top of the vessel and the vent to prevent dust from getting into the solution. The total current between the two electrodes during preelectrolysis was controlled at 50 mA.

## 5.6. Surface Preparation and Procedure

After assembling the cell with the appropriate substrate in place an extensive cleaning procedure was undertaken to insure that a clean, reduced surface was obtained. The first step was to oxidize any organic materials present in the cell. This was achieved by introducing 100 ml quantities of red fuming nitric acid into the cell and then shake and swirl the cell such that all surfaces came into contact with the acid. This "washing" with acid was repeated several times. The acid was then rinsed from the cell with several washings of ultra pure water. The cell was then filled with a 10% hydrogen peroxide solution. The hydrogen peroxide dissociated vigorously when it came in contact with either platinum or gold. This provided both mechanical scrubbing by the roiling nature of the dissociating hydrogen peroxide and also provided further oxidative cleaning. This step was allowed to continue until all the hydrogen peroxide had decomposed, approximately four hours. Once again the cell was rinsed many times with Harleco ultra pure water following the peroxide treatment.

The cell was then placed into the constant temperature box and brought to the experimental temperature which was 30 °C throughout this work. The reason for using a temperature above room temperature was that the controller could only add heat to the system, therefore to insure a stable temperature the inside of the temperature controller box had to be maintained above room temperature. At this time Teflon tubing was connected to the cell which would allow for gas phase control and for electrolyte inlet and outlet. See figure 5-14 for a schematic of the configuration of equipment at this point in the procedure.

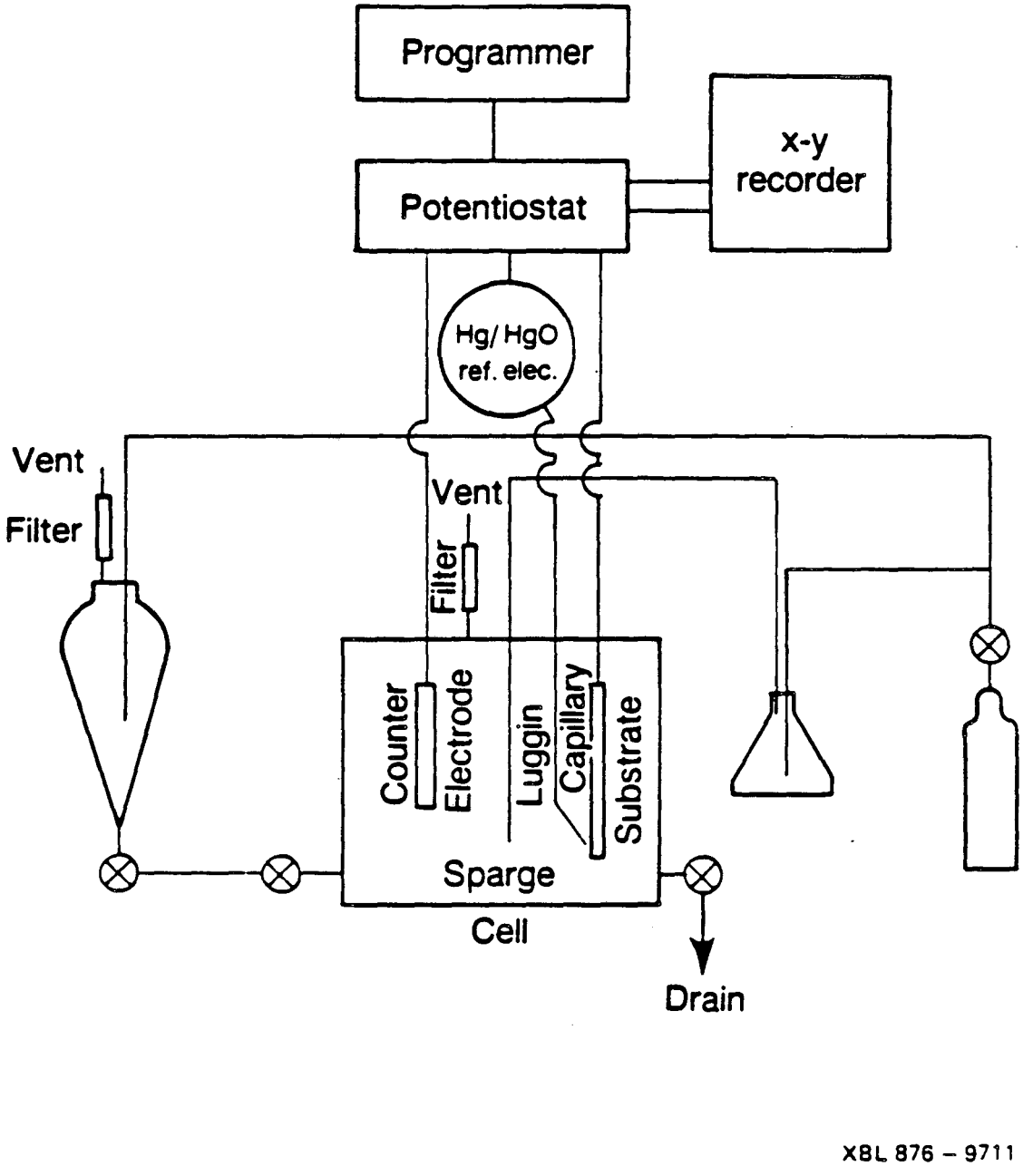


**Figure 5-14:** Schematic of liquid film cell and associated equipment.

Electrolyte was added to the cell and a blanket of 99.999% nitrogen saturated with vapor from electrolyte of the same concentration as in the cell was maintained over the electrolyte.

A reducing potential was then placed on the metal substrate. Current of 0.1 to 5 amps was passed between the substrate surface and a high surface area 90% platinum 10% rhodium 80 mesh screen for various periods of time. Current was passed until hydrogen generation from the substrate surface was uniform and all bubbles were of the same size.

At this point cyclic voltammetry was performed on the surface to see if it behaved as a clean reduced surface and whether the solution was free of contaminants. Figure 5-15 is a typical cyclic voltammogram. The figure is for 1 M KOH on platinum and the potentials are relative to a mercury mercuric oxide reference electrode. Indications of a clean surface and electrolyte are shown in figure 5-15. The three hydrogen peaks are all present on both anodic and cathodic sweeps and these are very nearly reversible. Also, there is a long flat plateau preceeding oxygen evolution and following a slight hump at 0.1 V, anodic sweep between 0.2 and 0.6 V. The only indication of contamination is seen in the small hump appearing on the anodic sweep at -0.4 to -0.2 V. This is most likely due to very low level organic contamination of the potassium hydroxide solution. Despite a significant effort. this hump was never completely eliminated from the KOH voltammogram. It is considered to be caused by one of the most difficult impurities to remove.

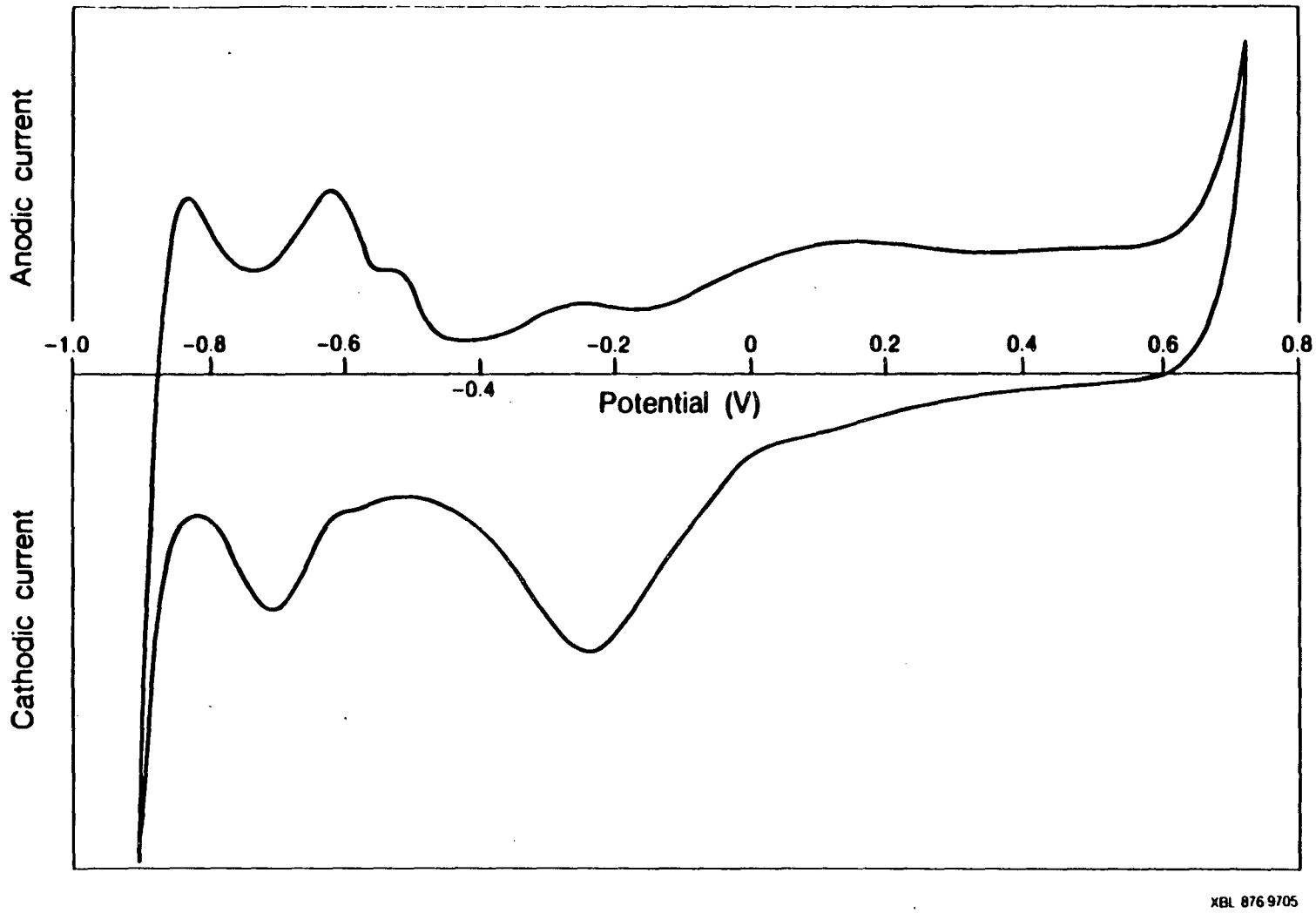


**Figure 5-15:** Cyclic voltammogram of 1 M KOH on the 100 $cm^2$ platinum substrate with rounded edges: potential relative to mercury/mercuric oxide reference electrode and the sweep rate was 50 mV/sec.

After ensuring that the surface and electrolyte are clean, steps were taken to begin an experiment. The clock was set, the interval timer started, and at the appropriate time, the right hand valve (see figure 5-16) was opened and the electrolyte replaced by pure nitrogen saturated with vapor from solution of the same concentration as is in the cell. After the electrolyte has drained from the cell the nitrogen gas flow was turned off and all valves were closed. The weir at the bottom of the cell has retained a small pool of electrolyte in contact with the bottom of the substrate and there was now a thin film of electrolyte draining from the surface.

The experiments involving tetradecane were done in the same way as just described up to the point of adding the liquid to be studied to the cell. At this point, a preelectrolyzed phosphoric acid solution is introduced into the cell. Hydrogen is then evolved from the substrate to ensure that the surface is in a reduced state. The phosphoric acid solution was then removed and the cell was rinse many times with Harleco ultra pure water. The temperature of the cell was then raised to 60 °C and dry nitrogen was blown through the cell to evaporate any water within the cell. Upon drying if there was any evidence of salts or other deposits in the cell the procedure was repeated. If the cell appeared clean and dry, the tetradecane was added and temperature equilibrium was established at 30 °C. From this point the drainage proceeded as stated above.

Two experiments were done with potassium chloride added to the electrolyte. One was 1 M KOH with KCl, and the other was 1N $H_3PO_4$ with KCl. First an experiment was done with the electrolyte without the KCl added to

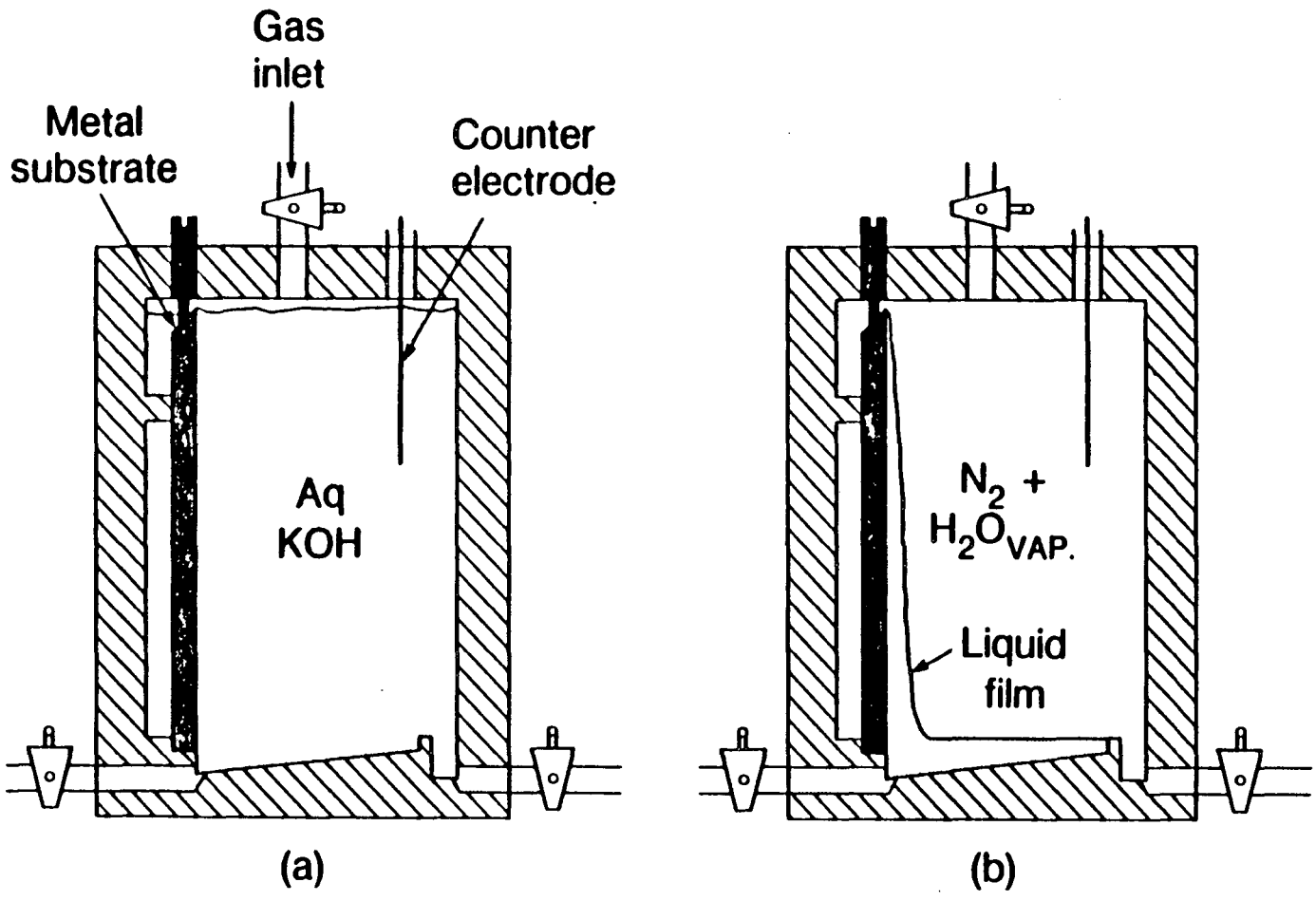


XBL 8611-9959 A

**Figure 5-16:** Schematic of the liquid film cell before and after the liquid level was lowered: (a) filled, (b) drained. KOH is shown as the liquid phase.

establish a base film profile to compare to the profile after KCl was added. The experiment without KCl was done according to the method described above. at the conclusion of the experiment without KCl, a concentrated solution of KCl was added to the separatory funnel shown in figure 5-14 which contained the very same electrolyte used in the previous experiment. A nitrogen sparge provided mixing. The addition of KCl was made such that the final concentration of KCl would be 0.1 M but the addition would not appreciably change the concentration of KOH or $H_3PO_4$ as the case may be. This new solution with KCl was then added to the cell and an experiment was started according to the regular procedure.

# Chapter 6

# Results and Discussion

## 6.1. General Observations

There were surprisingly small differences observed in film behavior for the various systems studied. The observed film thicknesses after long drainage times varied at most by a factor slightly larger than two. The shapes of profiles were nearly identical. These observations are for solutes which are known to specifically adsorb on metallic substrates as well as for those that do not.

The differences between the various substrates used in this study were also not large. Gold tended to give rise to films that were not quite as thick as those on platinum under similar conditions. The various sized platinum substrates gave similar results. Though no differences could be discerned in the thickness of the films along the vertical centerline of the substrate, the distribution of film thicknesses across the substrate depended on the width of the substrate.

The observed film thicknesses for all substrates, gold as well as platinum, were always thinner at the edge of the substrate than at the vertical centerline, *i.e.*, at any given height along the substrate, the film was thinnest at the edge of the substrate and thickest at the center. This observation may be attributed to edge effects. Comparing the various platinum substrates, the square cut 10 cm. wide plate did not show as dramatic a change in film thickness across the substrate surface. Likewise the 10 cm. wide platinum plate with rounded edges

exhibited very uniform thicknesses at any given height. Occasionally films on this plate had shown a thicker film at the edge of the substrate than in the center. Since the edges of this substrate were polished by hand, they were probably rougher than the front surface, causing the edges to drain more slowly.

A standard procedure had to be developed so that measurements of film thickness could be made in the most objective and consistent manner. Since color bands tended to have at least a small curvature, thicknesses were always determined along the vertical centerline of the substrate. Determination of film profiles at long times were generally made at one day intervals, and compared with one another, to be certain that drainage of the film had indeed stopped.

The largest experimental difficulty encountered in this work was one of cleanliness. The least bit of hydrophobic material adsorbed on the substrate surface will cause "holes" to form in an aqueous film. Holes are small regions of the surface which are not wetted by the film. Also, any dust or other particulate matter which finds its way to the surface can cause aberrations in the color bands. The problem of keeping these contaminants out of the system was compounded by the size of the substrate and the volume of electrolyte required to immerse the surface. The surface area was either 40 or 100 $cm^2$ depending on the substrate used, and the volume of electrolyte was either 600 ml or 925 ml depending the cell used.

Any time dewetting problems occurred, one of two steps were taken. Preelectrolysis of the electrolyte was repeated in an external container, and then after returning the electrolyte to the cell, hydrogen was vigorously evolved from

the substrate before attempting another experiment. A more thorough cleaning procedure consisted of repeating the cleaning procedure described in chapter 5 from the point of addition of red fuming nitric acid to the cell. To correct the problem of particulate matter interfering with the film, one of several steps was taken. These steps varied from refiltering the electrolyte to recleaning the cell, or for more severe cases, the cell was completely disassembled, and all windows and gaskets were replaced before starting the cleaning procedure (see chapter 5).

### 6.2. Transient Profiles

Immediately after an experiment was started, *i.e.*, the liquid level in the cell was lowered as is described in chapter 5, the liquid film which adhered to the surface of the substrate was very thick. This film was thicker at the bottom than at the top and its thickness decreased with time. This behavior was observed universally for all the liquid films studied in this work. Figures 6-1, 6-2, and 6-3 show several profiles at different times for the platinum/1 M KOH/vapor, gold/1 M KOH/vapor, and platinum/1 M $H_3PO_4$/vapor systems.

At short times, these films are relatively thick. The curvature is negative, *i.e.*, the shape of the profile is concave down. A negative curvature is what is expected from Jeffrey's equation for drainage from vertical flat plates (see equation 2-5). As time increases, these films become thinner and eventually, the curvature changes sign. Although no profiles are shown for very long times, in all cases these were indistinguishable from the last profile shown. In other words in figures 6-1 through 6-3 the profile for the longest elapsed time shown was a

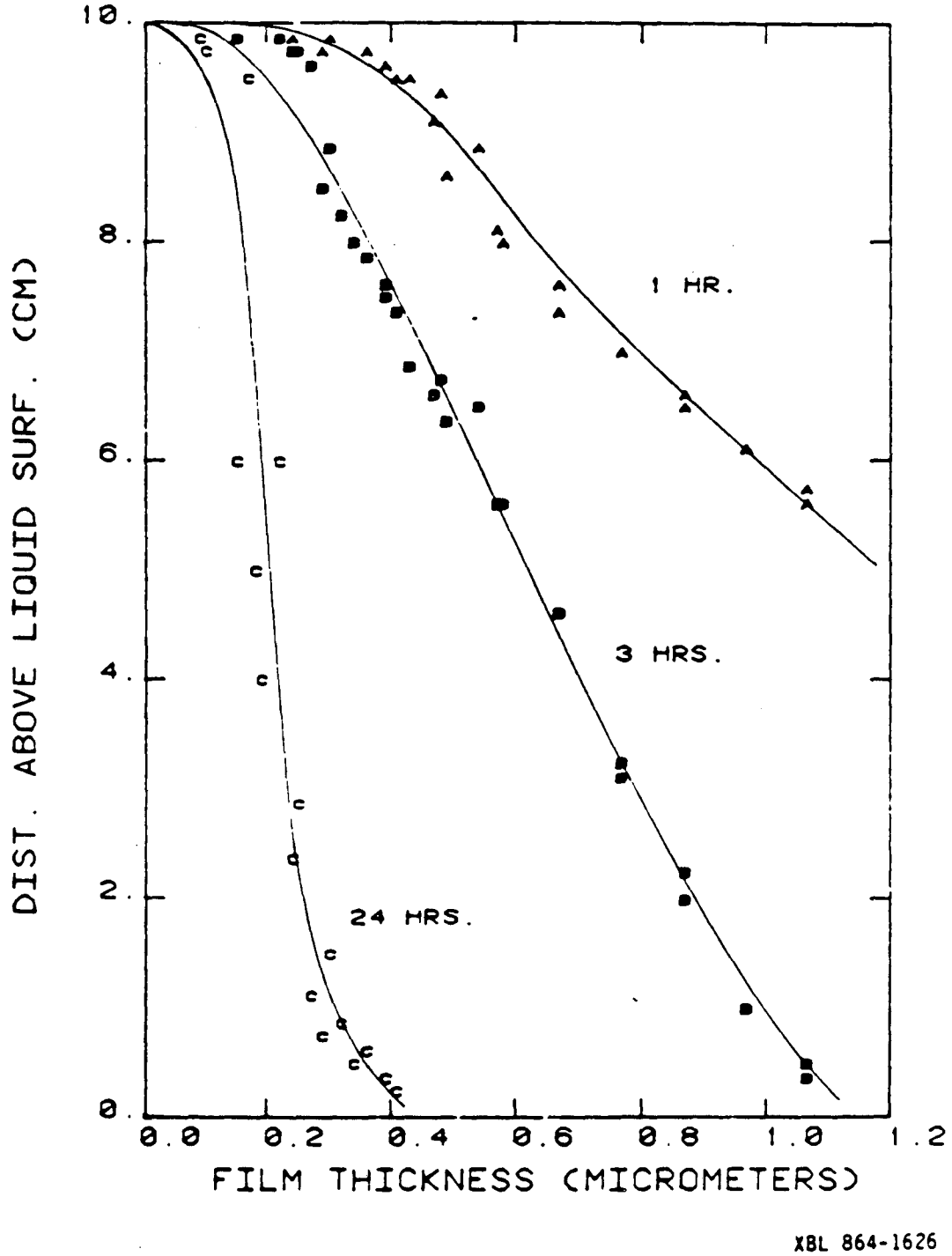


**Figure 6-1:** Film profiles at 1, 3, and 24 hours after the liquid level was lowered for 1 M KOH on the 40 $cm^2$ platinum substrate.

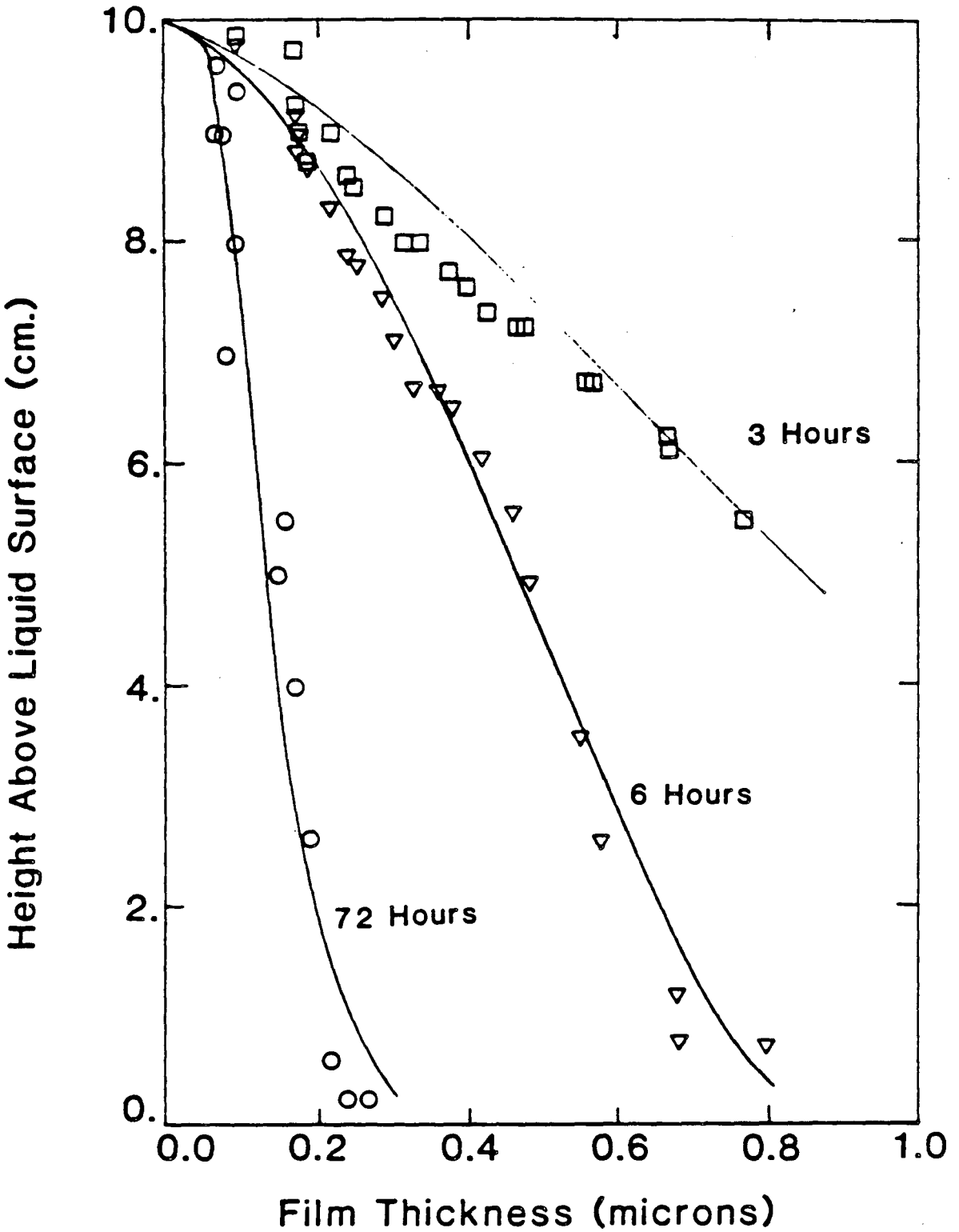


XBL 876-2935

**Figure 6-2:** Film profiles at 3, 6, and 72 hours after the liquid level was lowered for 1 M KOH on the 40 $cm^2$ gold substrate.

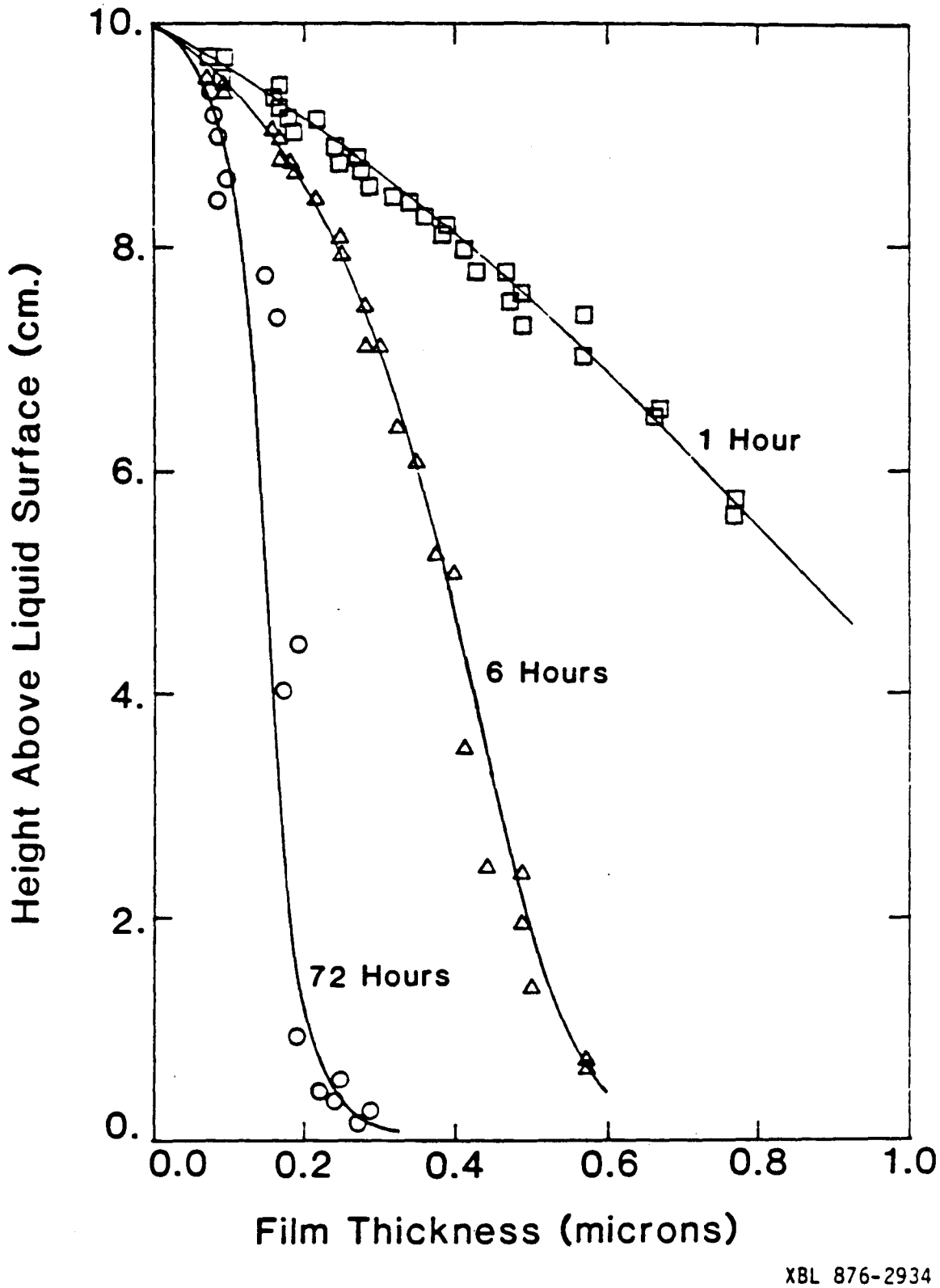


**Figure 6-3:** Film profiles at 1, 6, and 24 hours after the liquid level was lowered for 1 M $H_3PO_4$ on the 100 $cm^2$ platinum substrate with suqare edges.

steady state profile.

A better means of showing the long time behavior of these films is to plot the film thickness at a given height as a function of the inverse square root of time. For a film which is draining according to Jeffrey's equation, plotting the data according to this scheme would result in a straight line. The data for 1 M KOH on Platinum and for 3 M KOH on platinum have been plotted in this fashion and are shown in figures 6-4 and 6-5 respectively. The continuous lines shown in these graphs are predictions based on Jeffrey's equation for the conditions specified in the figure captions.

Figures 6-4 and 6-5 show that for short times these films do indeed drain according to Jeffrey's equation. However, at some time on the order of one day, the thickness at a given height deviates from that expected and eventually the entire profile becomes time invariant. For 1 M KOH on platinum, the film remained unchanged for up to 30 days at which time the experiment was terminated. Other experiments have been continued for up to 60 days without observing any change in the film profile.

### 6.3. Ellipsometric and Intensity Measurements

As was discussed in chapter 5, through ellipsometry two parameters, $\Delta$ and $\Psi$, are determined. Because the ellipsometer used in this study is a wavelength scanning ellipsometer, the values of $\Delta$ and $\Psi$ may be determined as functions of wavelength. Knowing the optical properties of the film and substrate, the wavelength dependence of $\Delta$ and $\Psi$ may be predicted for a given angle of

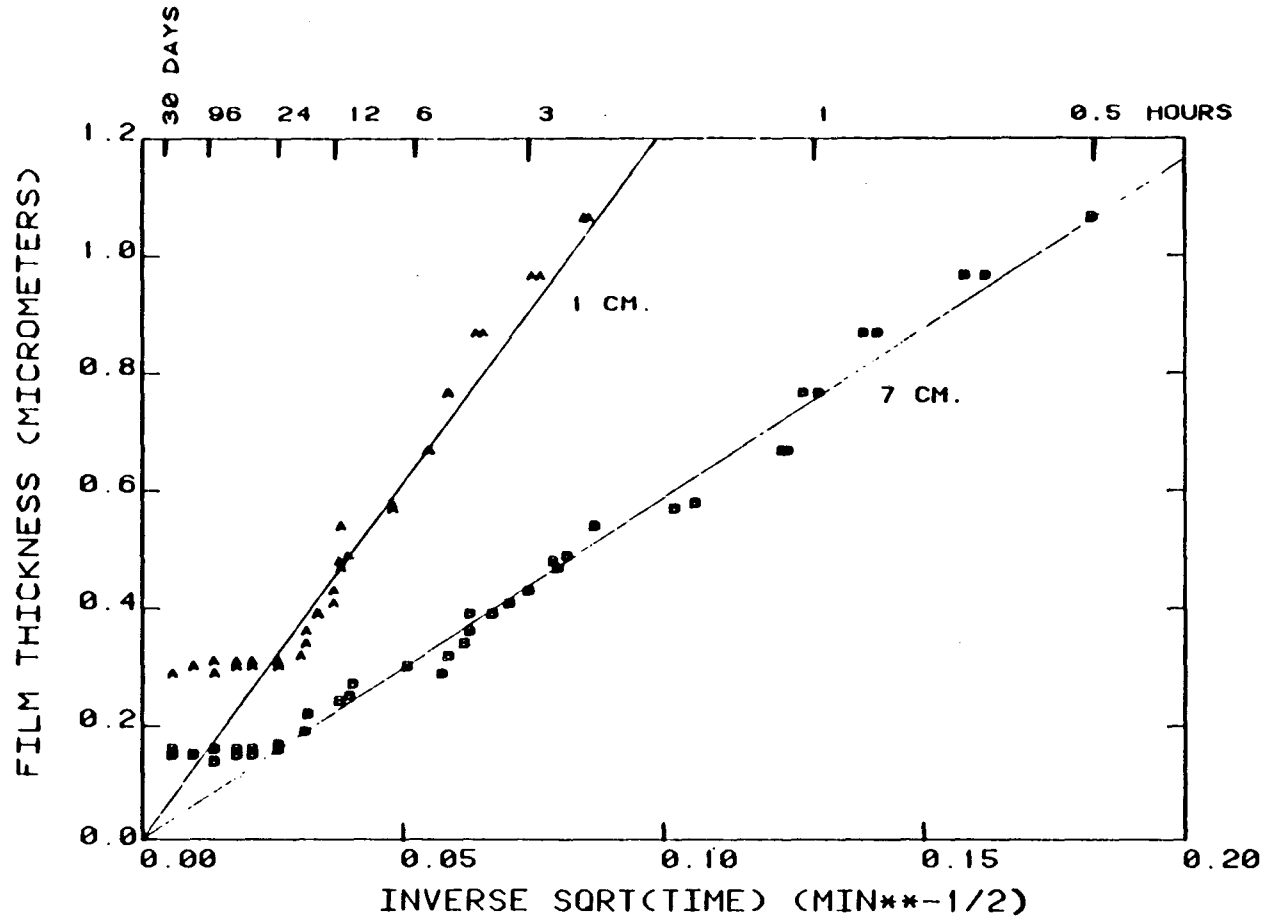


XBL 864-1627

**Figure 6-4:** Drainage of 1 M KOH from the 40 $cm^2$ platinum substrate, observed at 7 and 1 cm above the bulk liquid level. The lines shown are calculated from Jeffrey's equation, eqn. 2-5, with $\rho = 1.04$ $gm/cm^3$ and $\mu = 1.0$ centipoise.

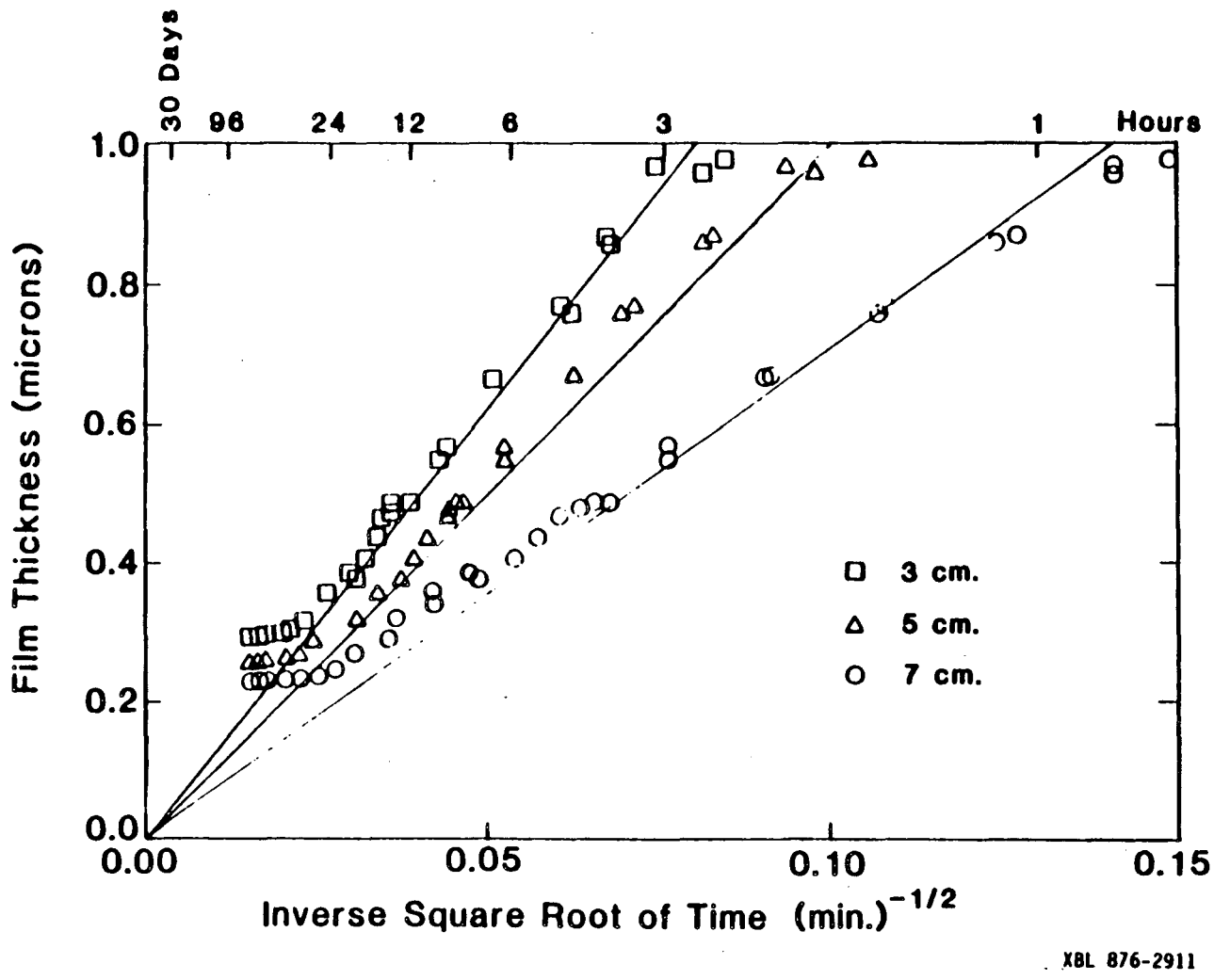


**Figure 6-5:** Drainage of 3 M KOH from the 100 $cm^2$ platinum substrate with rounded edges, observed at 7, 5, and 1 cm above the bulk liquid level. The lines shown are calculated from Jeffrey's equation, eqn. 2-5, with $\rho = 1.10$ $gm/cm^3$ and $\mu = 1.0$ centipoise.

incidence and film thickness. Therefore, the film thickness may be determined by finding the predicted $\Delta$ and $\Psi$ values that best agree with the measured values.

The value of $\Psi$, the ratio of the amplitudes of p- to s-polarized reflected light, was measured at four different heights above the bulk liquid level for a 67 weight % $H_3PO_4$ film on platinum five days following the drainage of liquid from the cell. It was not possible to collect values for both $\Delta$ and $\Psi$ with automatic nulling because large changes in these values occurred over small ranges of wavelength causing the electronics of the ellipsometer to go out of range. To keep the measurements within range, frequent adjustment of the polarizer and analyzer settings would be required. By this method, meant short spectral segments are generated which can be joined to create the entire spectra. In light of this laborious and cumbersome process, it was decided only to collect data for the calculation of $\Psi$. This was done by independently measuring the intensities of the s- and p-polarizations and then taking their ratio as a function of wavelength. For this purpose, the photomultiplier tube current was measured since the current response is linear with light intensity. Values of $\Psi$ were collected for wavelengths of light in the visible range, between 3700 and 7100 angstroms. Measured spectra of $\Psi$ at 9, 7, 5, and 3 cm above the bulk liquid level for 67 weight % $H_3PO_4$ are shown respectively in figures 6-6(a) through 6-6(d).

Predicted values of $\Psi$ were calculated using computer programs written by Mike Armstrong and Robert Crocker of this laboratory. The wavelength

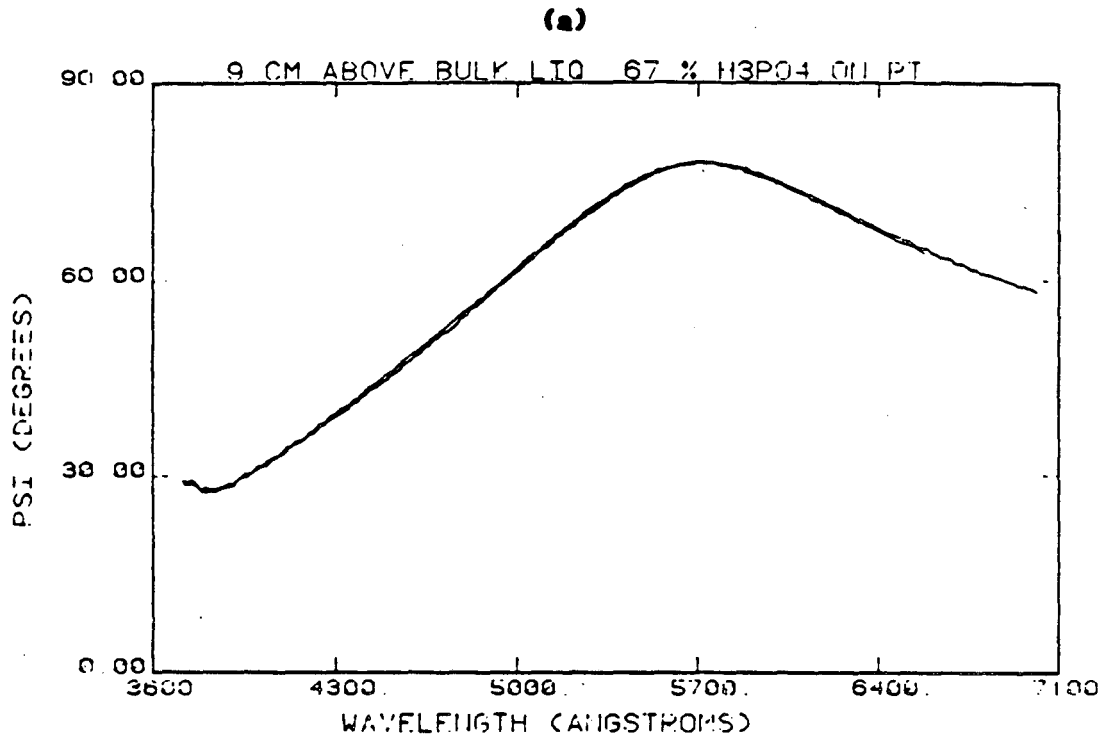


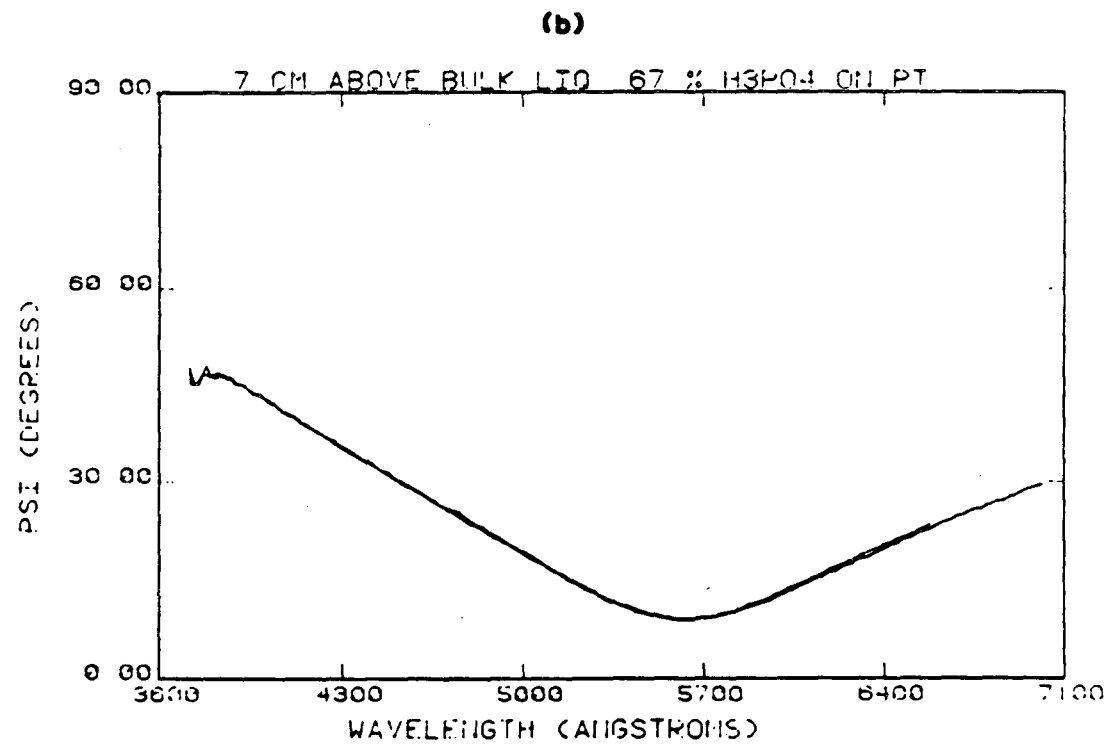


XBL 876-2980

**Figure 6-6(a) & (b):** Measured Ψ spectra for 67 weight % $H_3PO_4$ on the 100 $cm^2$ platinum substrate with square edges five days after the liquid level was lowered at (a) 9 and (b) 7 cm above the bulk liquid level.

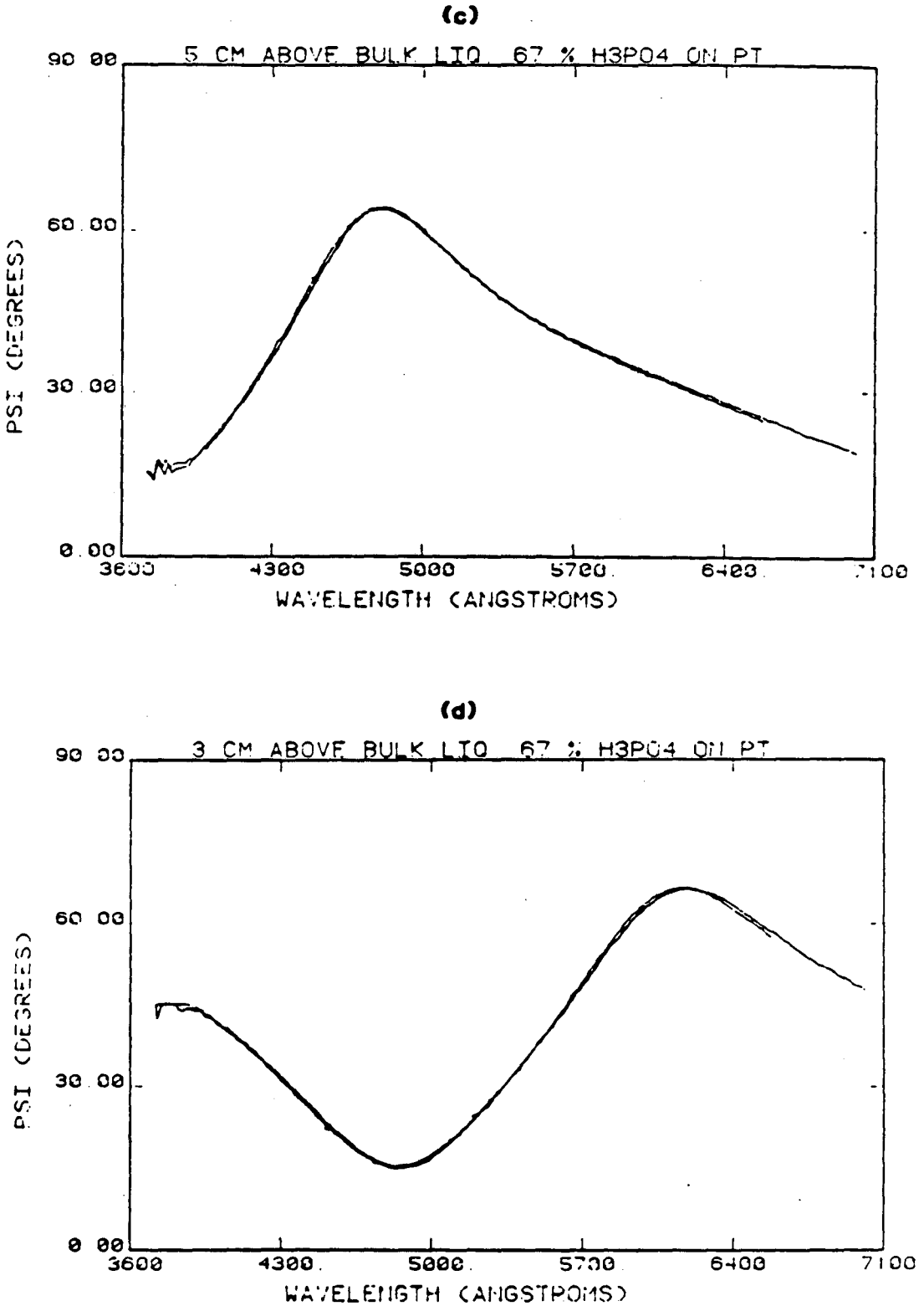


XBL 876-2981

**Figure 6-6(c) & (d):** Measured Ψ spectra for 67 weight % $H_3PO_4$ on the 100 $cm^2$ platinum substrate with square edges five days after the liquid level was lowered at (a) 5 and (b) 3 cm above the bulk liquid level.

dependent complex index of refraction for platinum was calculated from data in Palik (1985) and are displayed in table 6-1. For the index of refraction of 67 % $H_3PO_4$ a value of 1.41 was used, as predicted from Edwards, et al. (1964). The index of refraction for the film was assumed to be constant over the visible spectrum.

The value of $\Psi$ was predicted as a function of film thickness ranging between zero and one micron. Each predicted $\Psi$ spectrum was compared to the measured one and the sum of squares error, $\Sigma$, over 400 wavelengths in each spectrum was calculated. Figure 6-7a through 6-7d show the sum of squares error of the predicted and measured $\Psi$ spectra as a function of film thickness for 9, 7, 5, and 3 cm above the level of the bulk liquid. Each of these error curves exhibit a film thickness for which the error is minimized. These curves show several minima, however, in all cases, there is one which is deeper and sharper than the others.

The thickness determined by the smallest sum of squares error may be compared to the film thickness derived from interference color measurements. This was done for the 67 weight % $H_3PO_4$ film on platinum. As shown in figure 6-8 the agreement is excellent. This film was rather thick and although five days had passed since the lowering of the liquid level, this film had not yet reached an equilibrium profile. This is illustrated in figure 6-9 which compares the film thickness derived from interference colors after five days to that after nine days. Figure 6-9 shows that for heights above the liquid surface less than about seven cm. the measurements after nine days are consistently lower than those after

Table 6-1: Index of Refraction, n, and Extinction Coefficient, k, Data for Platinum in the Visible Range (Palik, 1985)

| $\hat{n} = n - ik$ | | |
|---|---|---|
| Wavelength, Å | n | k |
| 3647 | 1.62 | 2.62 |
| 3757 | 1.65 | 2.69 |
| 3874 | 1.68 | 2.76 |
| 3999 | 1.72 | 2.84 |
| 4133 | 1.75 | 2.92 |
| 4275 | 1.79 | 3.01 |
| 4428 | 1.83 | 3.10 |
| 4592 | 1.87 | 3.20 |
| 4769 | 1.91 | 3.30 |
| 4959 | 1.96 | 3.42 |
| 5166 | 2.03 | 3.54 |
| 5390 | 2.10 | 3.67 |
| 5636 | 2.17 | 3.77 |
| 5904 | 2.23 | 3.92 |
| 6199 | 2.30 | 4.07 |
| 6525 | 2.38 | 4.26 |
| 6888 | 2.51 | 4.43 |
| 7293 | 2.63 | 4.63 |

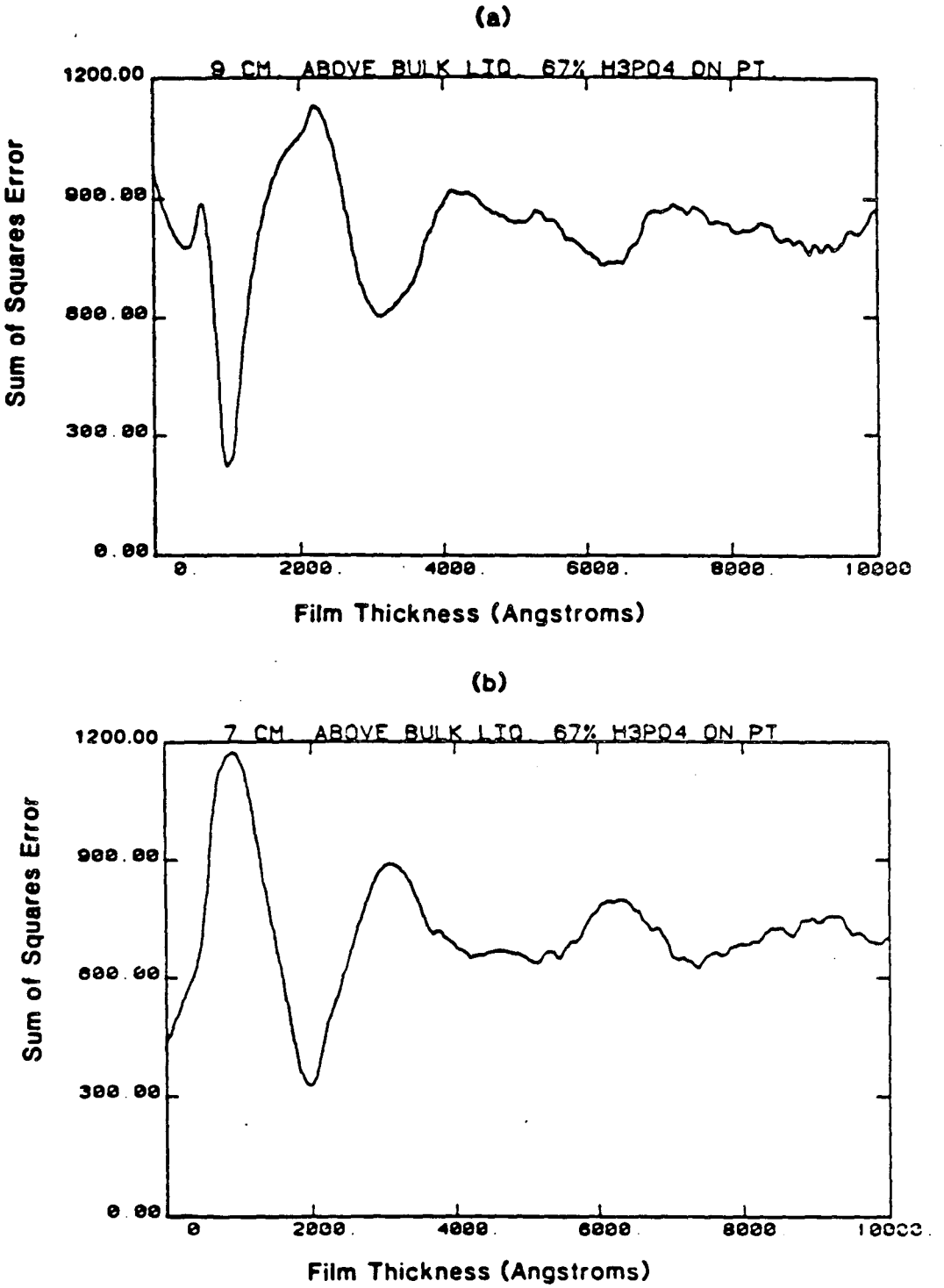


**Figure 6-7(a) & (b):** The sum of squares error between the measured and predicted $\Psi$ spectra vs. assumed film thickness for the predicted $\Psi$. The measured $\psi$ are for 67 weight % $H_3PO_4$ on the 100 $cm^2$ platinum substrate with square edges five days after the liquid level was lowered at (a) 9 and (b) 7 cm above the bulk liquid level.

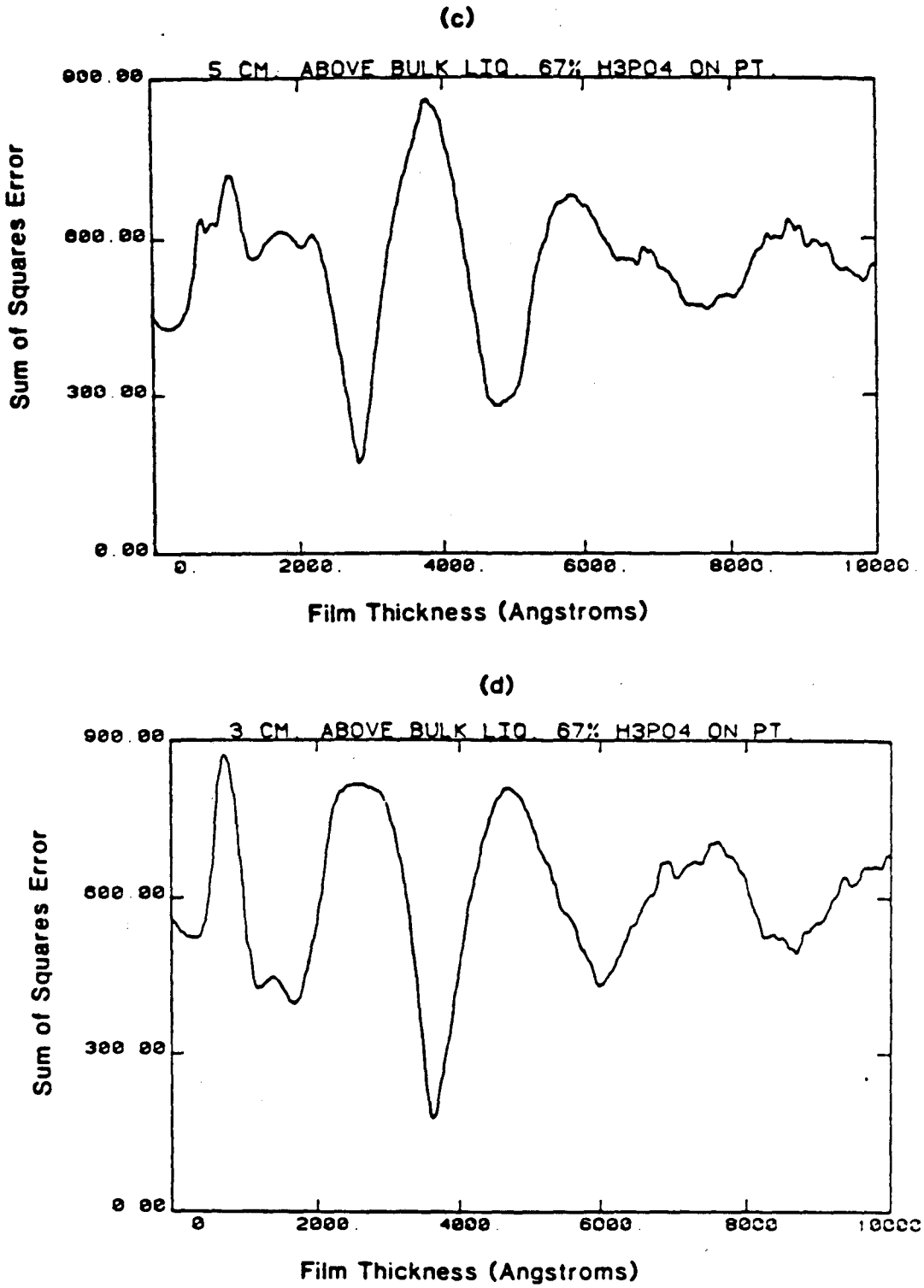


**Figure 6-7(c) & (d):** The sum of squares error between the measured and predicted $\Psi$ spectra vs. assumed film thickness for the predicted $\Psi$. The measured $\psi$ are for 67 weight % $H_3PO_4$ on the 100 $cm^2$ platinum substrate with square edges five days after the liquid level was lowered at (a) 9 and (b) 7 cm above the bulk liquid level.

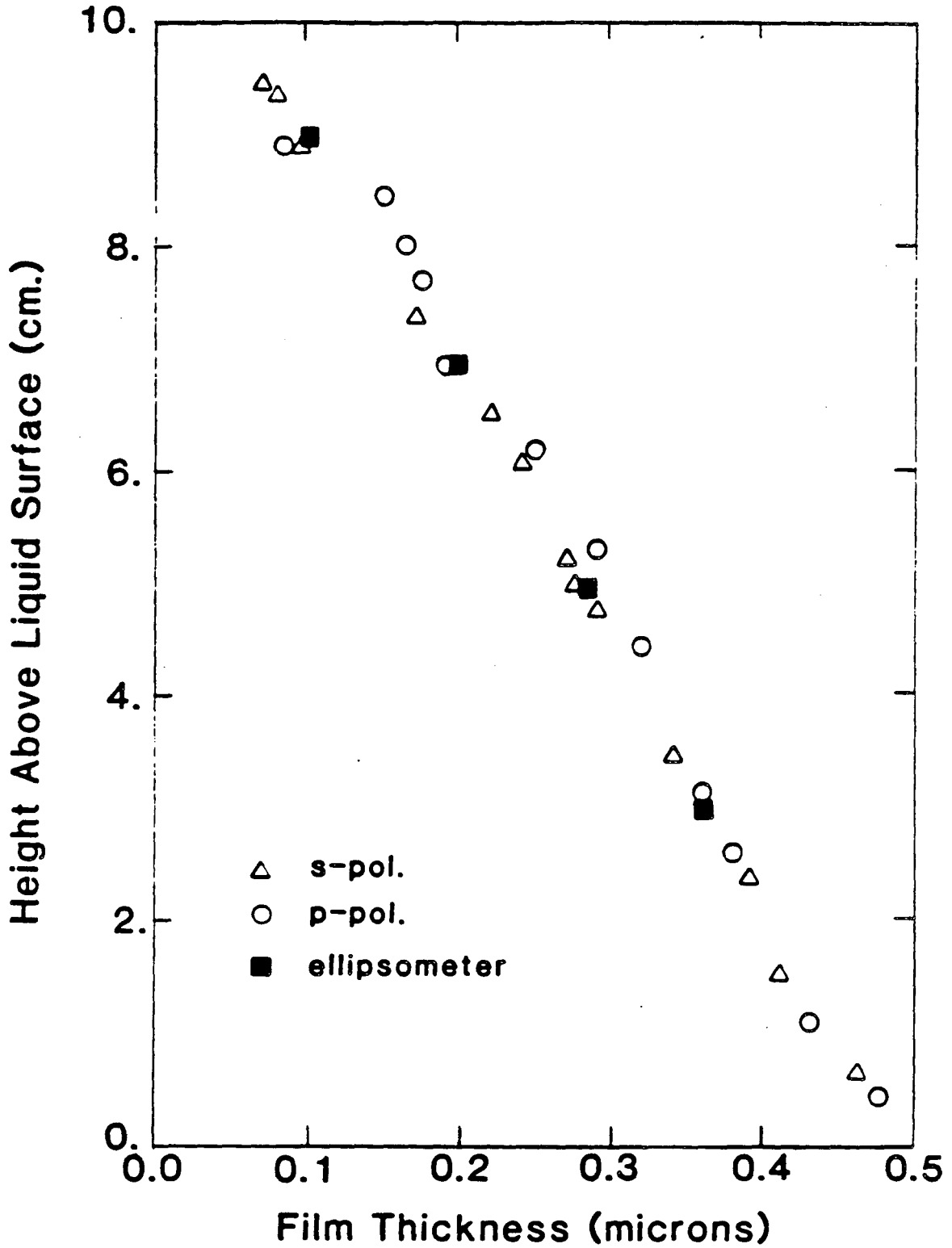


XBL 876-2910

**Figure 6-8:** Comparison of film profiles derived from the measurement of $\Psi$ and from interference colors for 67 weight % $H_3PO_4$ on the 100 $cm^2$ platinum substrate with square edges five days after the liquid level was lowered.

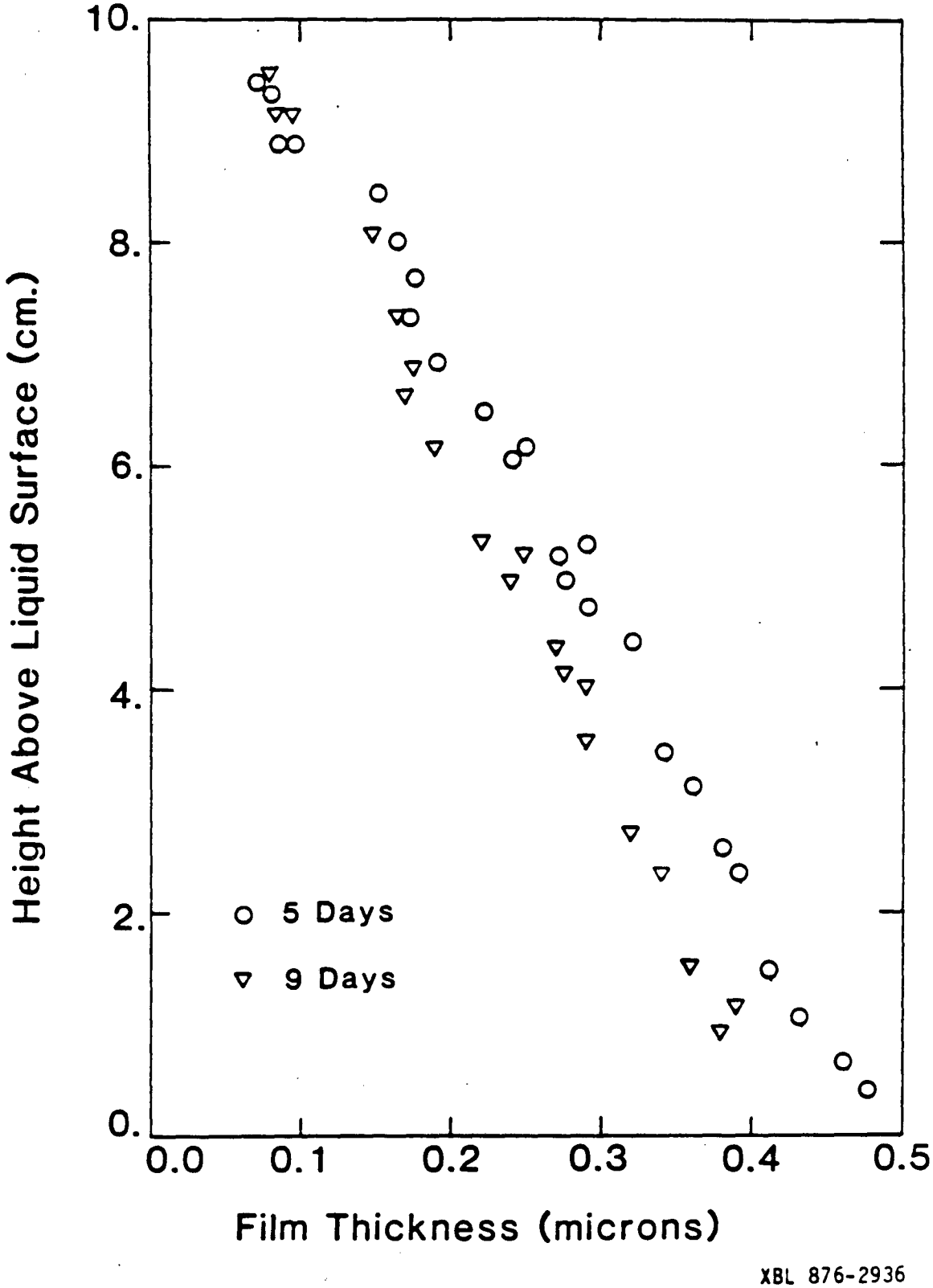


**Figure 6-9:** Comparison of film profiles derived from interference colors for 67 weight % $H_3PO_4$ on the 100 $cm^2$ platinum substrate with square edges at five and nine days after the liquid level was lowered.

five days. Even after nine days, this film does not appear to have achieved an equilibrium profile. Unfortunately, this film was draining so slowly that the day to day change in the film profile was not discernable and the experiment was terminated at the end of 9 days. The reason high concentration phosphoric acid films require such a long time to achieve time-invariant profiles most probably results from the high viscosity (12 times that for water for 67 weight % $H_3PO_4$).

Because of the thickness change from top to bottom of this film it provides an excellent opportunity to illustrate the utility of measuring the intensity of reflected to incident light for each polarization. These measurements may be used to determine which interference order is being observed and therefore assist in determining where on the color chart, see figure 5-5, a particular color lies. Figures 6-10a through 6-10d show the ratio of the reflected intensity to the incident intensity for s and p-polarized light at 9, 7, 5, and 3 cm above the bulk liquid level for 67 weight % $H_3PO_4$ on platinum five days after the liquid level was lowered. At 9 cm. above the bulk liquid level both the s and p-polarizations show very broad maxima or minima and only one of these occurs for each polarization. As we move down to 7, 5, and 3 cm above the bulk liquid level the wavelength at which a maximum or minimum occurs shifts toward longer wavelengths indicating an increasing film thickness. New maxima or minima belonging to the next interference order appear at short wavelengths and for 5 and 3 cm above the bulk liquid level dual maxima appear. Summarizing, at 9 cm we observe a first order interference for both s and p-polarizations. At 7 cm the s-polarization is just beginning to show second order interference. At 5 cm

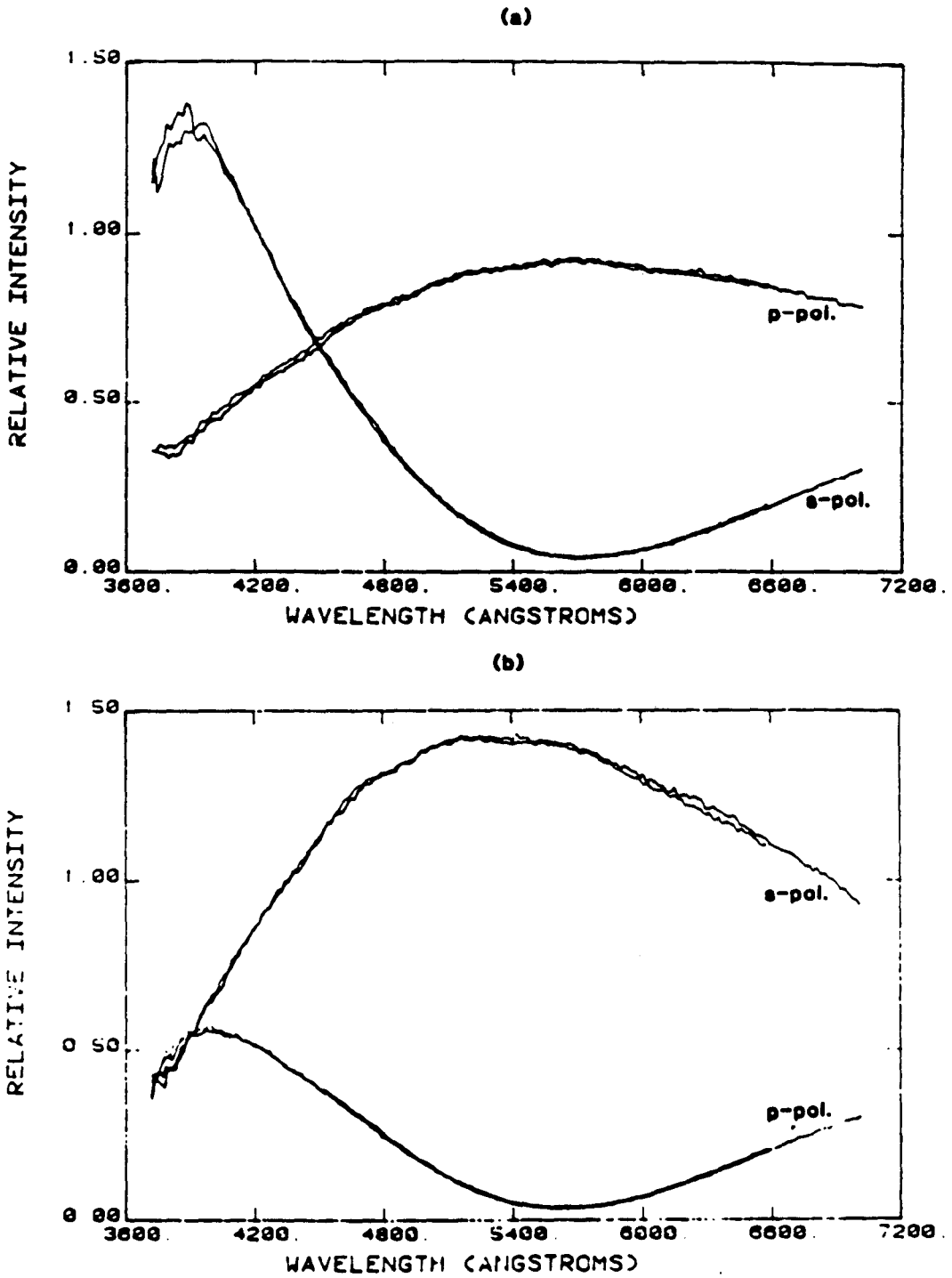


XBL 876-2942

**Figure 6-10(a) & (b):** Relative intensity measurements for s- and p-polarized light reflected from the substrate in the presence of a film to that without the film: for 67 weight % $H_3PO_4$ on the 100 $cm^2$ platinum substrate with square edges five days after the liquid level was lowered at (a) 9 and (b) 7 cm above the bulk liquid level. The dual tracing represents a forward and backward scan of wavelength.

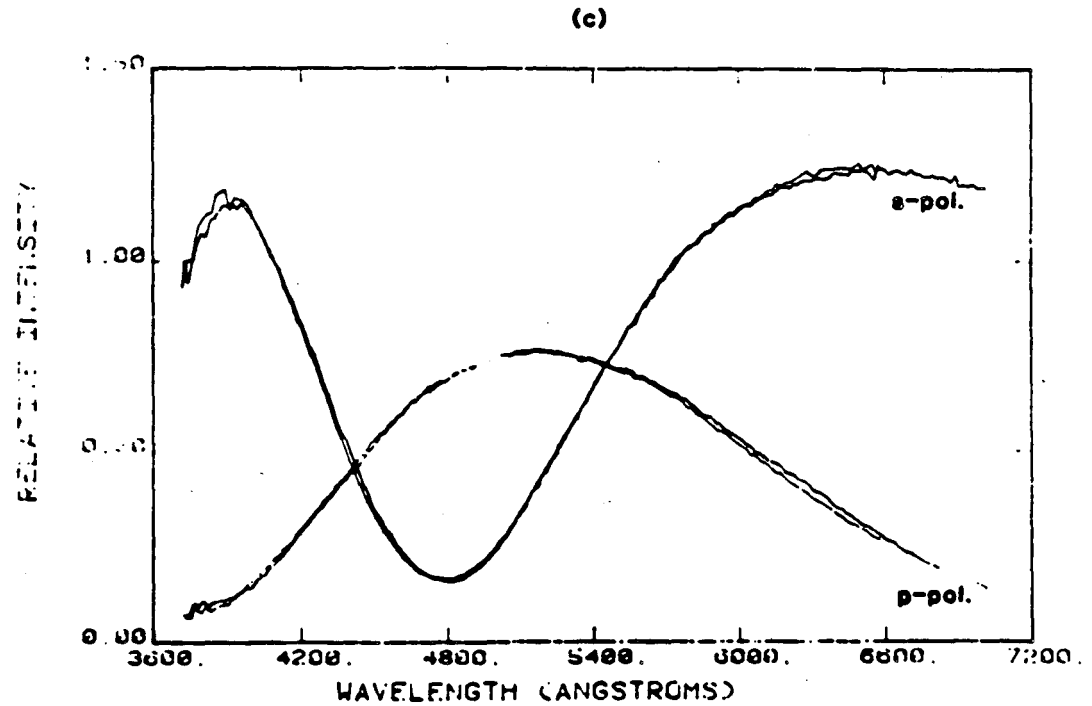


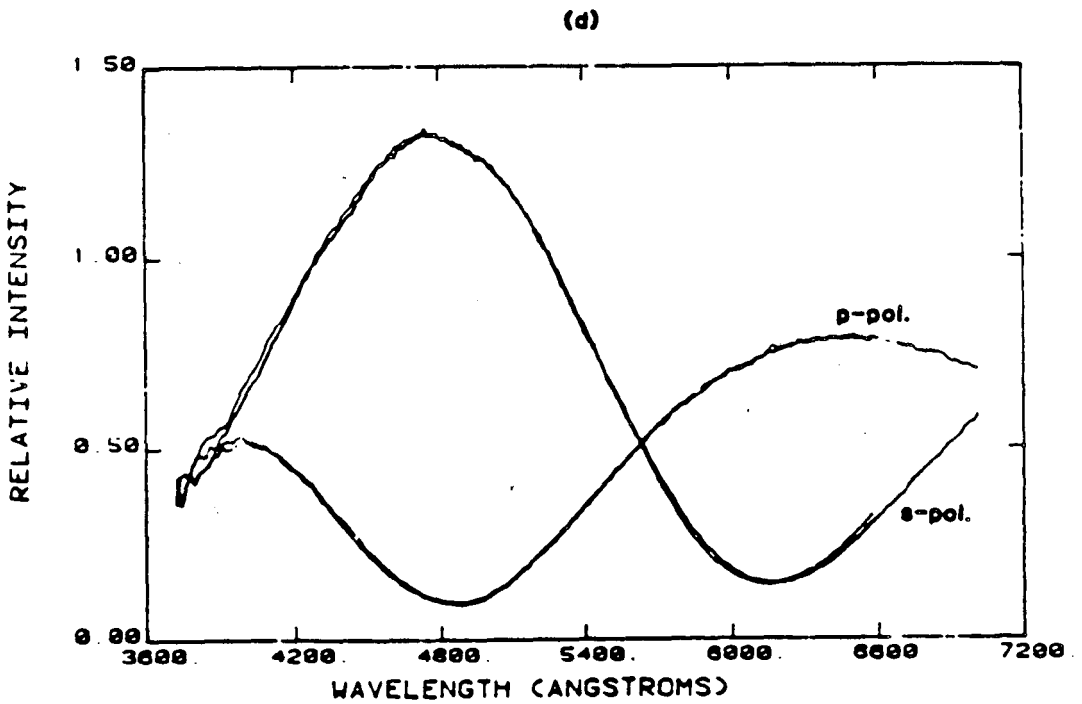


XBL 876-2941

**Figure 6-10(c) & (d):** Relative intensity measurements for s- and p-polarized light reflected from the substrate in the presence of a film to that without the film: for 67 weight % $H_3PO_4$ on the 100 $cm^2$ platinum substrate with square edges five days after the liquid level was lowered at (a) 5 and (b) 3 cm above the bulk liquid level.The dual tracing represents a forward and backward scan of wavelength.

both polarizations are in the second order. At 3 cm the p-polarization is second order while third order interference is just beginning for the s-polarization.

### 6.4. Equilibrium Profiles

Equilibrium profiles for several systems are shown in figures 6-11 through 6-15. At this time the solid curves included in these figures should be ignored. The significance of these curves will be discussed below.

The most remarkable feature of these figures is their similarity with one another. The profile of the films was found to be best fitted by a power law function of the form $\delta = bh^a$, where delta is the film thickness, h is the distance above the bulk liquid, and a and b are fitted parameters. Table 6-2 gives the values of the power, a, and the correlation factor, $r^2$, determined by the sum of least squares error.

Note that the system 1 M $H_3PO_4$ on platinum is not included in this table. The reason for this omission is that the correlation factor was so low that little meaning could be assigned to any reported value of a. All of the systems reported in table 6-2 are fitted relatively well by curves for which the film thickness varies with the inverse cube root of height above the bulk liquid surface. The correlation factors are not extremely high which merely reflects the degree of scatter in the data.

The effect of concentration on the equilibrium film thickness at 5 cm above the bulk liquid level for KOH on platinum, KOH on gold, and $NaClO_4$ on platinum are shown in figure 6-16. The equilibrium film thickness is observed to

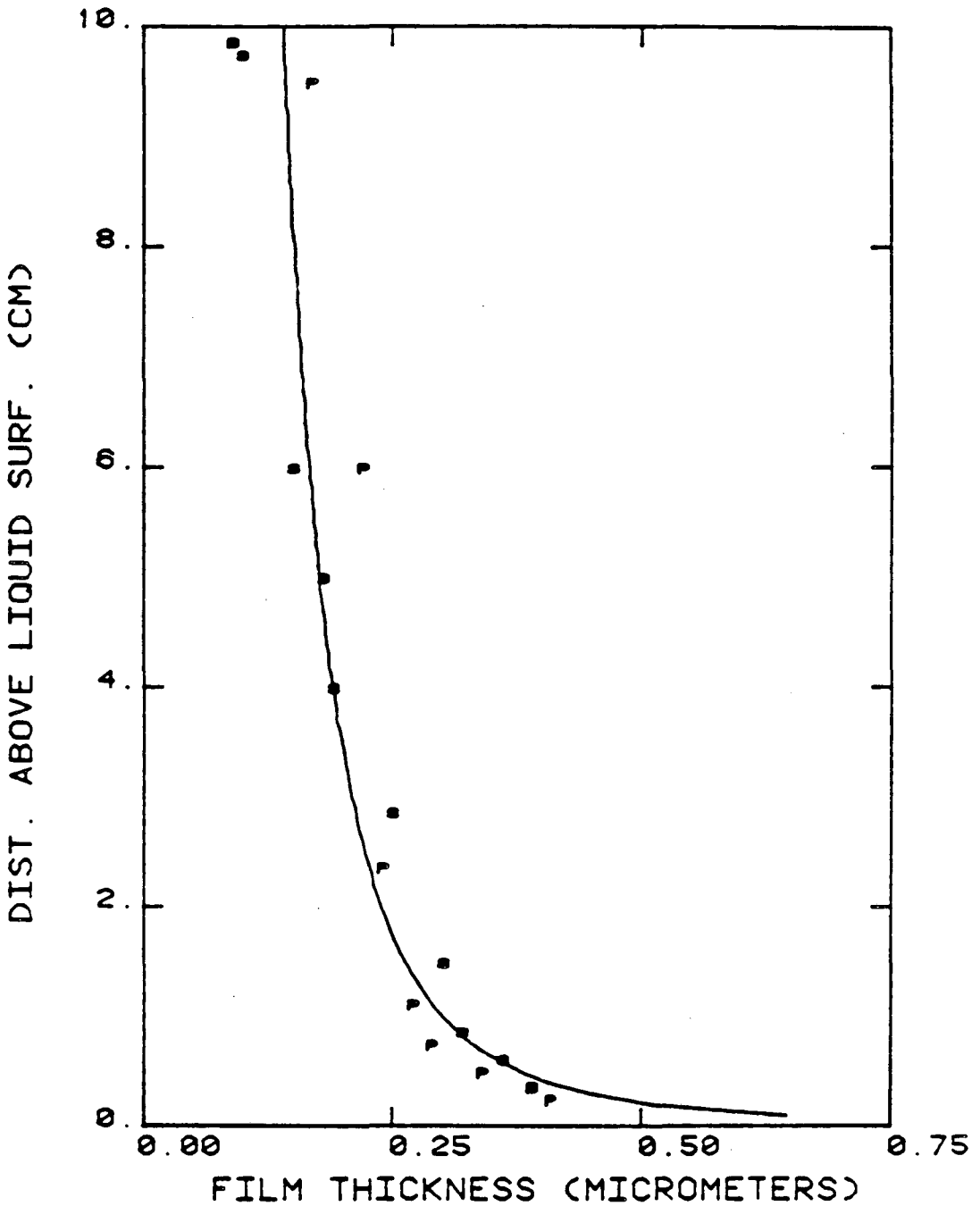


XBL 864-1629

**Figure 6-11:** Equilibrium profile for 1 M KOH on the 40 $cm^2$ platinum substrate 24 hours after the liquid level was lowered (data points P and S are derived from interference colors of p- and s-polarized light). The solid curve is given by equation 4-24 with a Hamaker constant of $-1.0 \times 10^{-11}$ ergs.

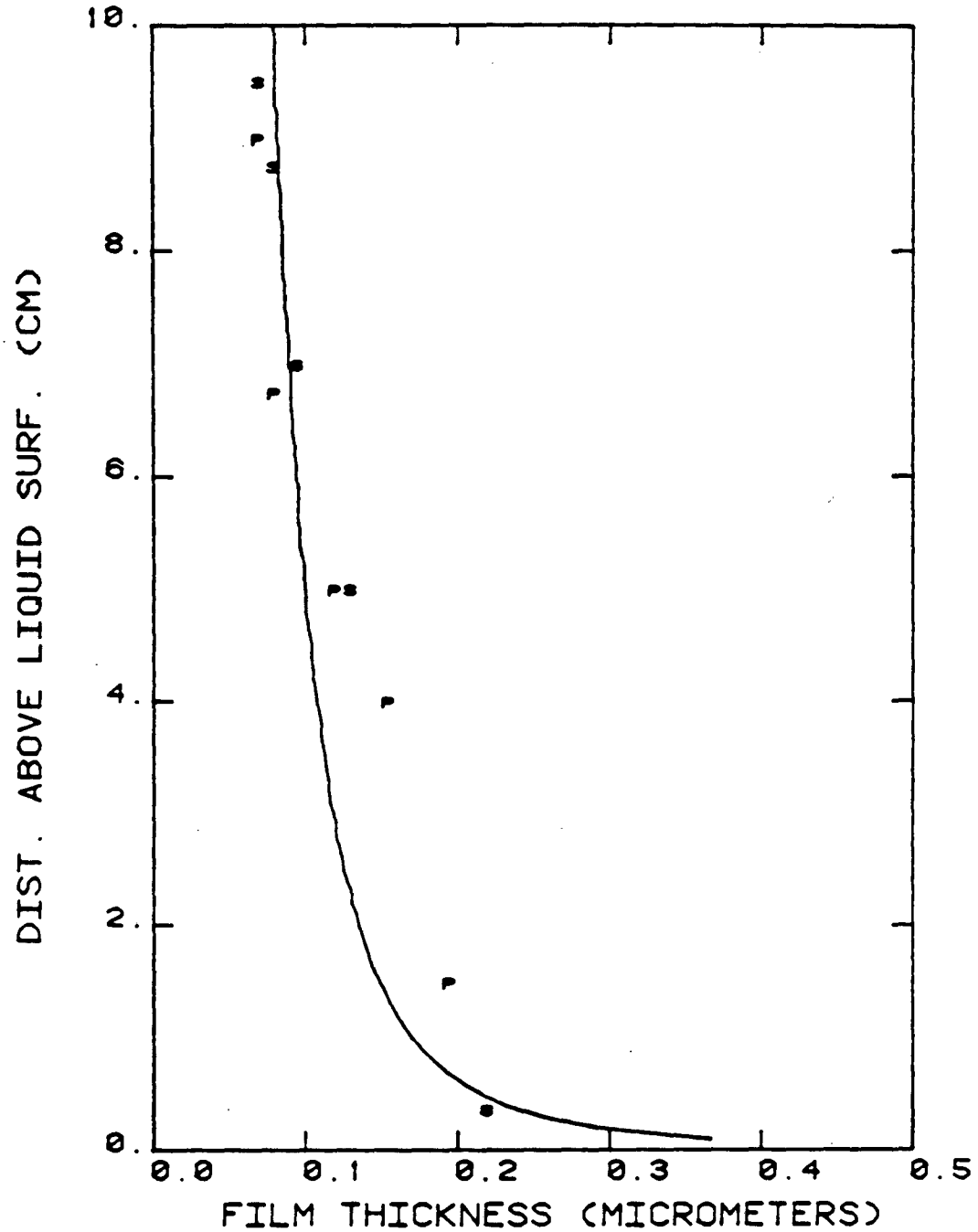


XBL 864-1630

**Figure 6-12:** Equilibrium profile for 1 M KOH on the 40 $cm^2$ gold substrate 48 hours after the liquid level was lowered (data points P and S are derived from interference colors of p- and s-polarized light). The solid curve is given by equation 4-24 with a Hamaker constant of $-1.96 \times 10^{-12}$ ergs.

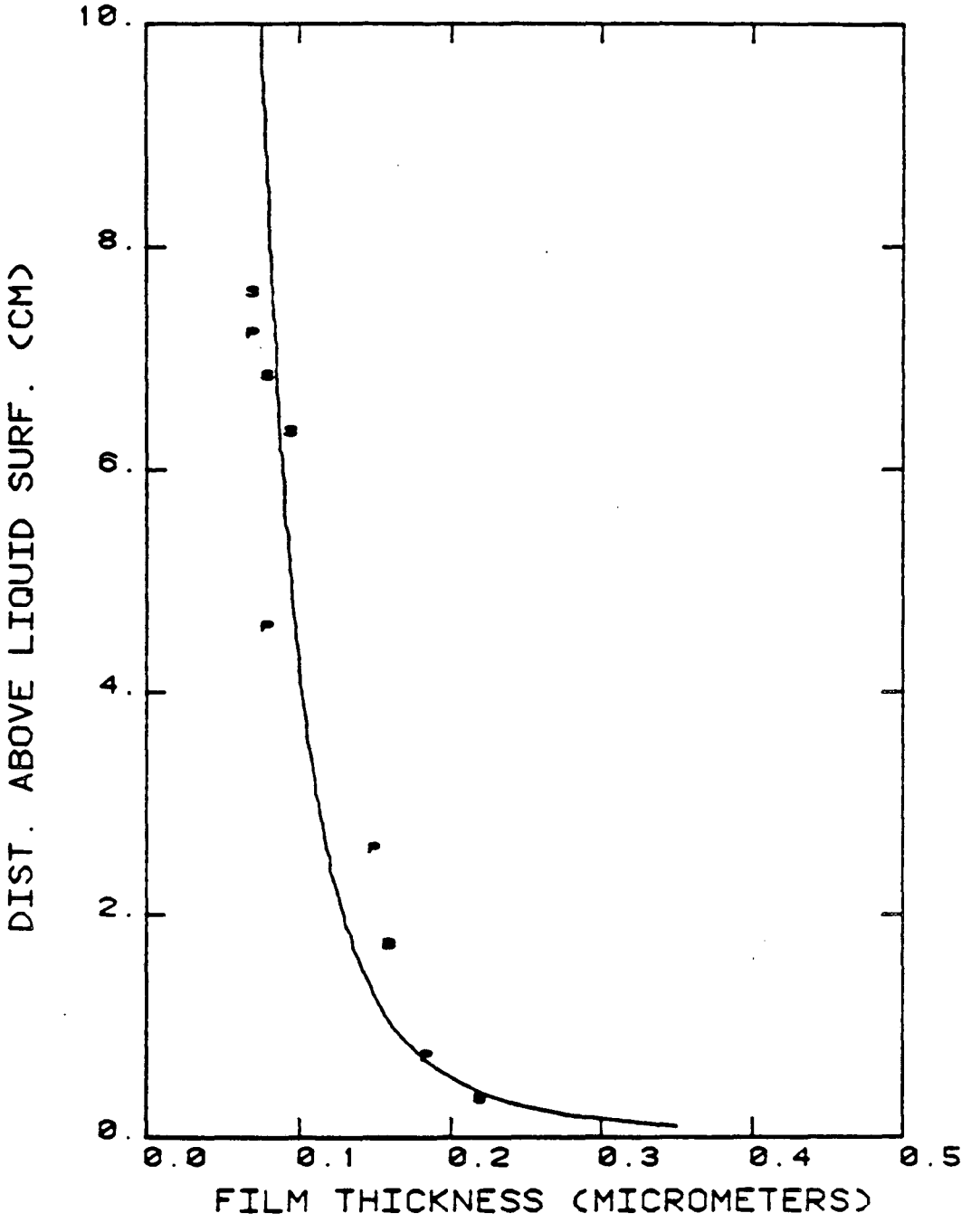


XBL 864-1631

**Figure 6-13:** Equilibrium profile for 1 M $NaClO_4$ on the 100 $cm^2$ platinum substrate with rounded edges 96 hours after the liquid level was lowered (data points P and S are derived from interference colors of p- and s-polarized light). The solid curve is given by equation 4-24 with a Hamaker constant of $-1.6 \times 10^{-12}$ ergs.

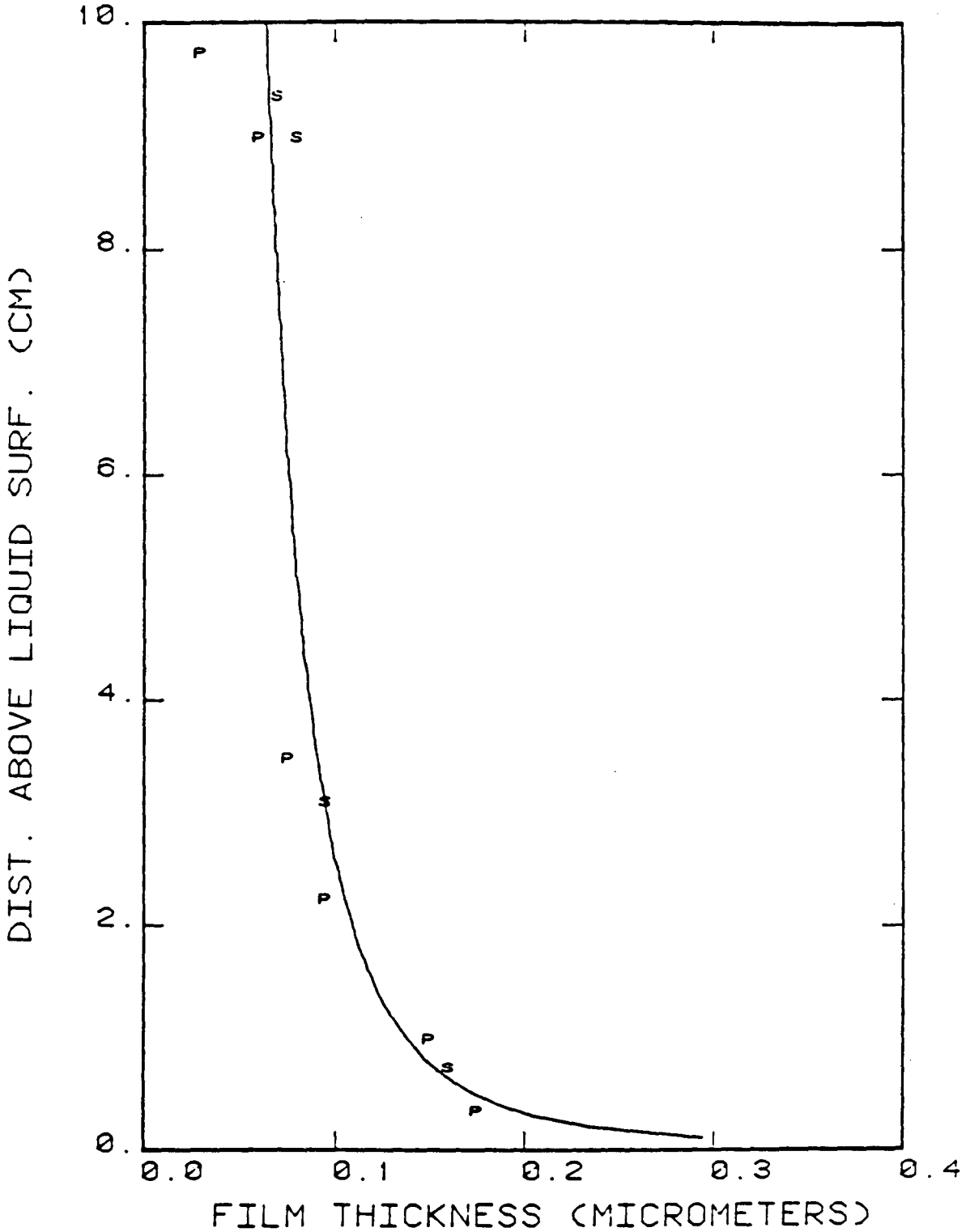


XBL 876-2946

**Figure 6-14:** Equilibrium profile for 0.01 M KOH on the 40 $cm^2$ platinum substrate 72 hours after the liquid level was lowered (data points P and S are derived from interference colors of p- and s-polarized light). The solid curve is given by equation 4-24 with a Hamaker constant of $-1.0 \times 10^{-12}$ ergs.

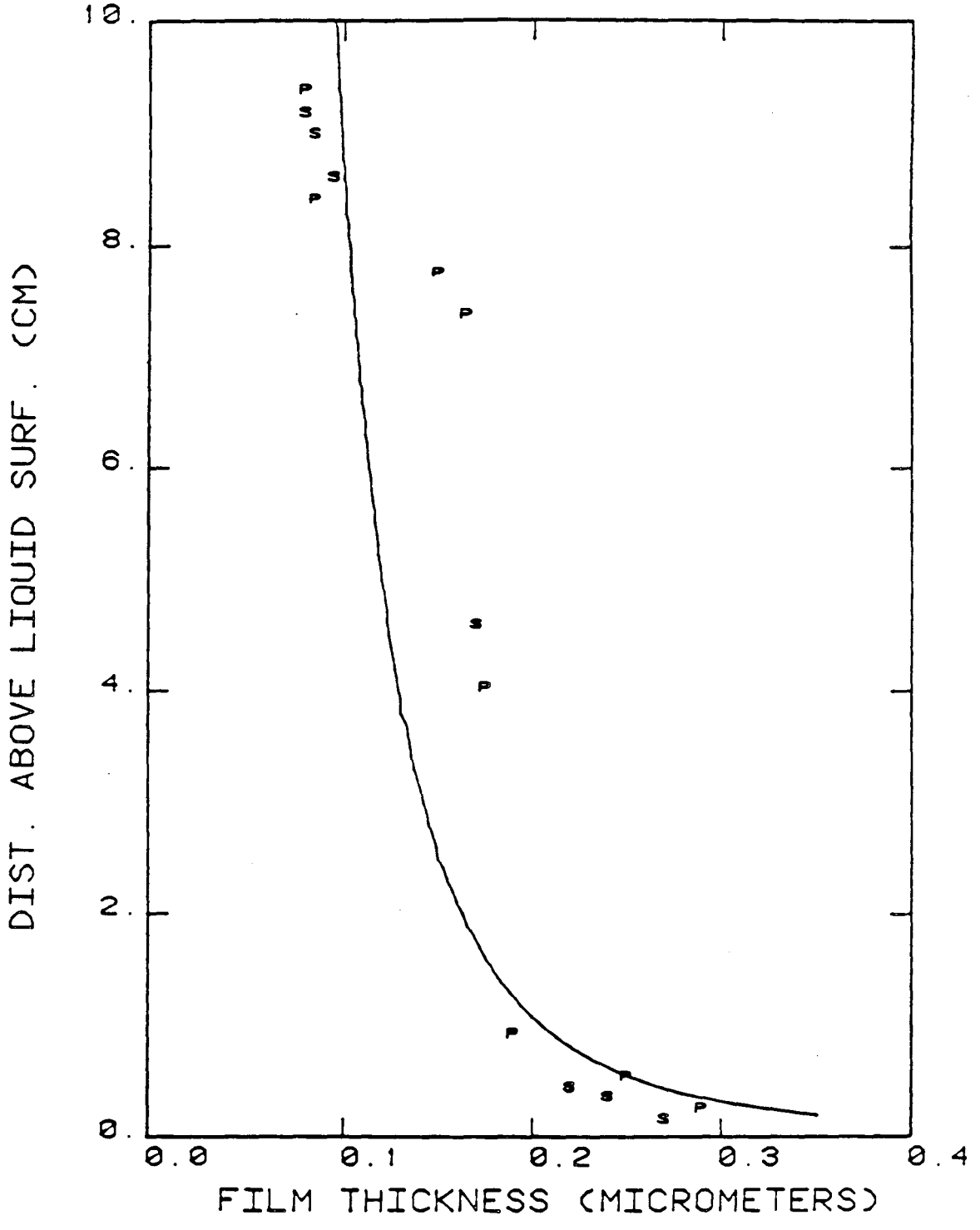


XBL 876-2945

**Figure 6-15:** Equilibrium profile for 1 M $H_3PO_4$ on the 100 $cm^2$ platinum substrate with square edges 72 hours after the liquid level was lowered (data points P and S are derived from interference colors of p- and s-polarized light). The solid curve is given by equation 4-24 with a Hamaker constant of $-3.4 \times 10^{-11}$ ergs.

Table 6-2 Value of the Exponent, a, and the Correlation Factor, $r^2$, from the Method of Least Squares

| **Least Squares Fit to $\delta = b\,h^a$** | | |
|---|---|---|
| System | a | $r^2$ |
| 1 M KOH on platinum | -0.3487 | 0.93 |
| 0.01 M KOH on platinum | -0.390 | 0.88 |
| 1 M $NaClO_4$ on platinum | -0.394 | 0.94 |
| 1 M KOH on gold | -0.307 | 0.89 |

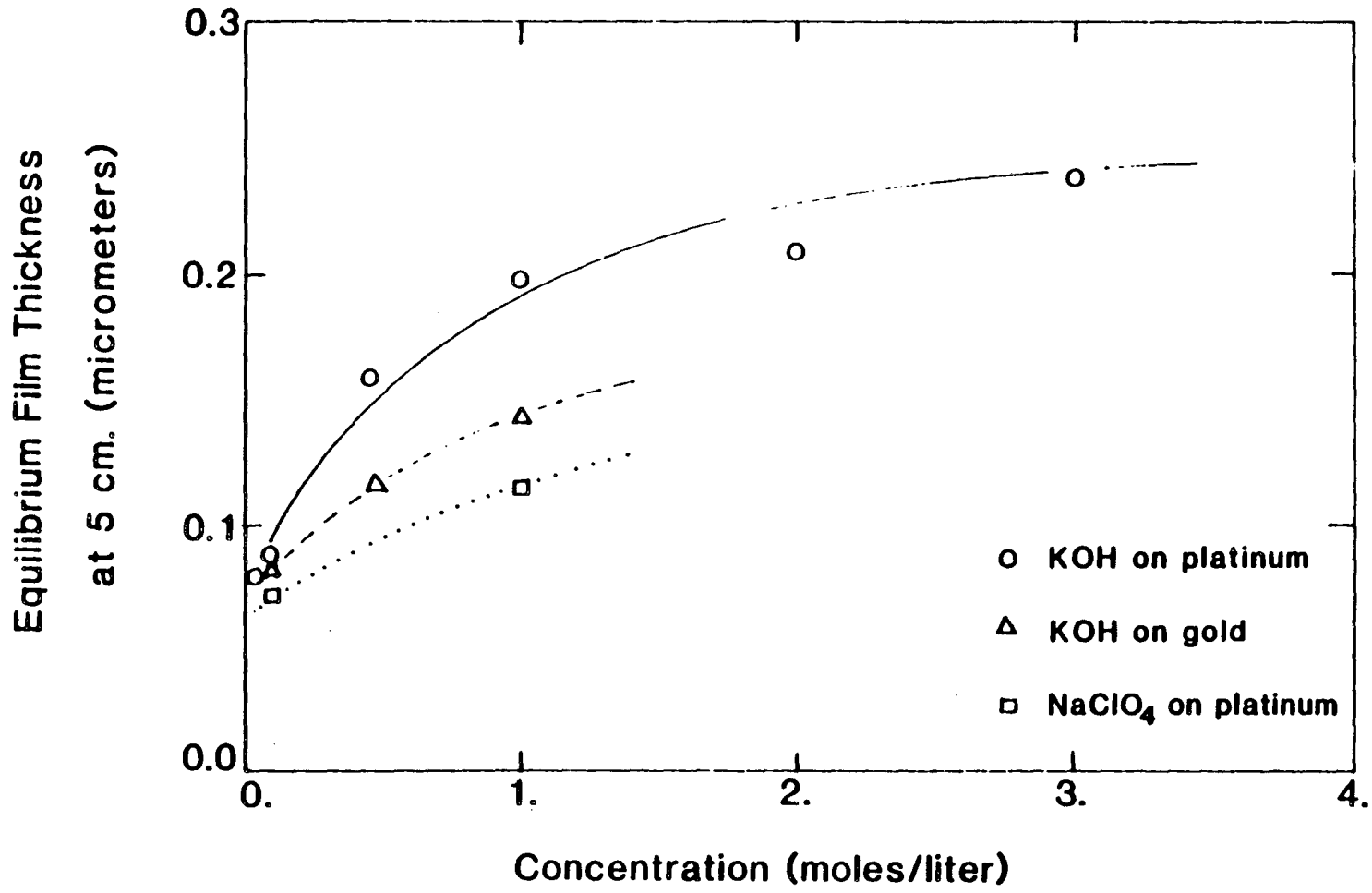


XBL 876-2940

**Figure 6-16:** Effect of concentration on equilibrium film thickness at 5 cm above the bulk liquid level for KOH on platinum, KOH on gold, and $NaClO_4$ on platinum.

increase with increasing concentration for each of these systems.

The information reported in figure 6-16 is sufficient to remove consideration of double layer interaction between the solid/liquid and the liquid/vapor interfaces as a possible mechanism for stabilizing these films. Recalling from section 3.4, predictions made from modeling the interaction of two plain parallel double layers indicate that the interaction would decrease with increasing electrolyte concentration. However, figure 6-16 shows that the observed behavior is the opposite.

In addition to this, the interaction of plane parallel double layers fails to predict the appropriate equilibrium profile shape or the correct magnitude of film thickness. As shown in figure 3-5, double layer interaction predicts that the film thickness at the bottom of the substrate will increase relative to the thickness at the top to a much larger degree than is observed (see figures 6-11 through 6-15). Also, the thickness of the observed profiles is in the range of 0.1 to 0.2 micrometers. The film thickness predicted by double layer interaction, even for extreme parameter values, is at most on the order of 0.03 micrometers. From these observations, double layer interactions may now be eliminated as a possible contributor to the stabilization of these films.

It was shown in chapter 4, section 4.6, that from non-retarded van der Waals interactions it is predicted that the film thickness will be proportional to the inverse third root of height above the bulk liquid level. This functionality is what is experimentally observed. Therefore, it is possible to derive a Hamaker constant, A, which predicts film profiles that agree best with observations. The

results are shown graphically in figures 6-11 through 6-15. The solid curves in these figures are the predicted film profiles which best represent the measurements. Also, table 6-3 lists the Hamaker constants as derived from film profile measurements for most of the systems studied in this work. Hamaker constants predicted using equation 4-12 are also included in table 6-3.

Agreement between experimentally determined Hamaker constants and those calculated from equation 4-12 are very good for dilute electrolytes. Also, experimentally determined Hamaker constants for gold are smaller than for the same electrolyte on platinum. As electrolyte concentration increases the agreement between experiment and theory decreases. Although equation 4-12 does predict that the Hamaker constant will increase with increasing electrolyte concentration, the predicted increase is not as large as that observed.

This discrepancy might be explained by one of the following two reasons. First, the means by which the dielectric function of the electrolytic solution was constructed may lead to prediction of low values. To predict the dielectric function for the electrolyte, the function in the visible range was used to predict an equivalent increase in the function over the entire spectrum. If the dielectric function were actually to increase dramatically in the IR or UV region as a result of increasing the electrolyte concentration the predicted Hamaker constant would be low.

Another possible explanation is that Israelachvilli (1972) showed that the assumptions made in arriving at equation 4-12 could for some systems predict low values of the Hamaker constant. Specifically, he showed that for the

Table 6-3: Hamaker Constant, A: Predicted from Film Profile Measurements; and Calculated from Equation 4-14

| Comparison of Hamaker Constants | | |
|---|---|---|
| System | A (from film profile) | A (calculated) |
| 3 M KOH on platinum | $-2.1 \times 10^{-11}$ ergs | $-1.6 \times 10^{-12}$ ergs |
| 2 M KOH on platinum | $-1.7 \times 10^{-11}$ ergs | $-1.5 \times 10^{-12}$ ergs |
| 1 M KOH on platinum | $-1.0 \times 10^{-11}$ ergs | $-1.4 \times 10^{-11}$ ergs |
| 0.5 M KOH on platinum | $-8.2 \times 10^{-12}$ ergs | $-1.2 \times 10^{-12}$ ergs |
| 0.01 M KOH on platinum | $-1.0 \times 10^{-12}$ ergs | $-1.1 \times 10^{-12}$ ergs |
| 1 M $NaClO_4$ on platinum | $-2.0 \times 10^{-12}$ ergs | - |
| 0.1 M $NaClO_4$ on platinum | $-1.1 \times 10^{-12}$ ergs | - |
| 1 M $H_3PO_4$ on platinum | $-3.4 \times 10^{-11}$ ergs | $-2.3 \times 10^{-12}$ ergs |
| 1 M KOH on gold | $-2.0 \times 10^{-12}$ ergs | $-1.3 \times 10^{-12}$ ergs |
| 0.5 M KOH on gold | $-1.4 \times 10^{-12}$ ergs | $-1.1 \times 10^{-12}$ ergs |
| 0.1 M KOH on gold | $-0.9 \times 10^{-12}$ ergs | $-1.0 \times 10^{-12}$ ergs |

metal/vacuum/metal system, the Hamaker constant predicted by equation 4-12 is roughly 1/3 of the value predicted by rigorously evaluating the full Lifshitz expression. Lifshitz (1956) also points out that higher order terms that are dropped from the full expression during simplification can become significant as the number of free carriers, conduction electrons, increases, especially for thicknesses less than 0.6 micrometers. It may be surmised that upon increasing the concentration of ionic species in solution and therefore the conductivity of the electrolytic solution, the relative importance of the higher order terms may increase and therefore dropping these terms results in a low predicted value of the Hamaker constant.

Some comment should be made about retarded van der Waals interactions. As was shown in section 4.8, for film thicknesses greater than 0.01 micrometers, retardation effects should begin to be important. Retardation effects cause a shift from inverse cube root dependence of film thickness on height to inverse fourth root. Also, as film thickness increases, high frequencies are cut off and will no longer contribute to the total van der Waals interaction. Therefore the value of the retarded Hamaker constant is thickness dependent.

Using the 1 M KOH on platinum system as a typical case, figure 6-17 compares an inverse cube root and inverse fourth root function to the experimental equilibrium profile for this system. Figure 6-17 clearly shows that the data are better represented by a function which is dependent on the inverse cube root in height rather than inverse fourth root. Assuming for a moment that inverse fourth root dependence is correct, the retarded Hamaker constant which

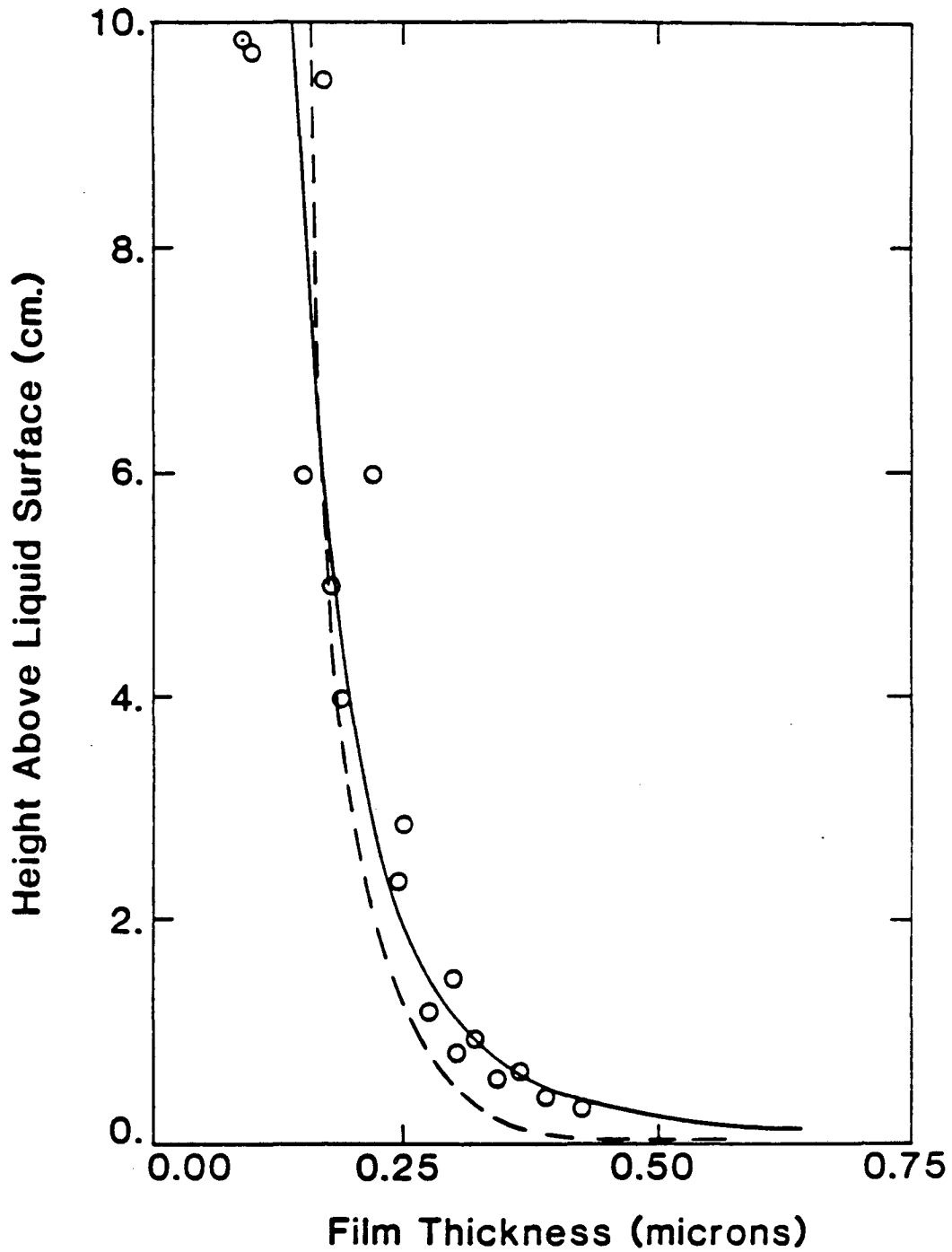


XBL 876-2939

**Figure 6-17:** Comparrison of non-retarded and retarded predicted film profile functionality to a measured profile for 1 M KOH on the 100 $cm^2$ platinum substrate with square edges. Non-retarded interaction profile (solid curve) is calculated from equation 4-24 with $A = -1.0 \times 10^{-12}$ ergs. Retarded interaction profile (dashed curve) is calculated from equation 4-31 with $A^R = -1.9 \times 10^{-16}$ erg-cm.

provides the curve that best represents the data is $-2.0 \times 10^{-16}$ ergs-cm as compared to the calculated retarded Hamaker constant which is $-1.9 \times 10^{-18}$ ergs-cm (see figure 4-11).

It is clear that a model based on non-retarded van der Waals interactions predict the magnitude and functionality of the experimental observations better than a model based on retarded interactions. At this time it is not clear why this is the case. An in depth analysis has not been performed., but the following might explain this observation. The systems that previously have been studied and for which the retarded interactions have been verified are all of the form: body 1 interacting with body 2 through medium 3. The important interaction therefore is that of body 1 with body 2 which are separated by a minimum distance which is the film thickness. However, the systems of this study are fundamentally different. We are considering the interaction of a film with the substrate on which the film resides. Therefore, the important interaction is the substrate with the medium which is separated at most by the thickness of the film. Because a significant portion of the film lies right next to the substrate, a thicker film may be necessary before retardation effects become important.

### 6.5. The Effect of Specific Adsorption

Several systems were chosen specifically to evaluate the importance of specifically adsorbing and non-adsorbing ionic species in solution. Sodium perchlorate, $NaClO_4$, represents a non-adsorbing compound. In other words, neither the anion nor the cation specifically adsorbs to metallic surfaces (Delahay,

1965). Therefore, $NaClO_4$ solutions were chosen to evaluate whether non-adsorbing electrolytes would result in a film. The results for 1 M $NaClO_4$ on platinum are shown in figure 6-13. Less concentrated solutions were also evaluated as shown in figure 6-16. Clearly, specific adsorption is not required for the formation of equilibrium films. In general, the $NaClO_4$ films on platinum are thinner than KOH films on platinum. If the conductivity of the electrolyte is important as was suggested above, this could also explain the difference in the experimental observations described here.

Another means of evaluating the importance of specific adsorption is to observe a system in the absence of a strong adsorber, then add the adsorber to the same electrolyte and observe the effect on the film thickness. This was done for two systems: 1 M KOH on platinum and 1 M $H_3PO_4$ on platinum. Potassium chloride was added in both cases as the chloride ion represents a strong specific adsorber (Delahay, 1965). The procedure used was described at the end of chapter 5.

The film profiles after two days are shown in figure 6-18 for 1 M KOH on platinum before and after the addition of KCl. No detectable difference is seen between the two profiles. Similar results are also shown for 1 M $H_3PO_4$ on platinum in figure 6-19. In figure 6-19 the profile with KCl might be slightly higher than that without, however, the difference is not large enough to be conclusive. In general, it may be concluded that the energy of interaction results from bulk interactions since drastically affecting the structure of the interface has little or

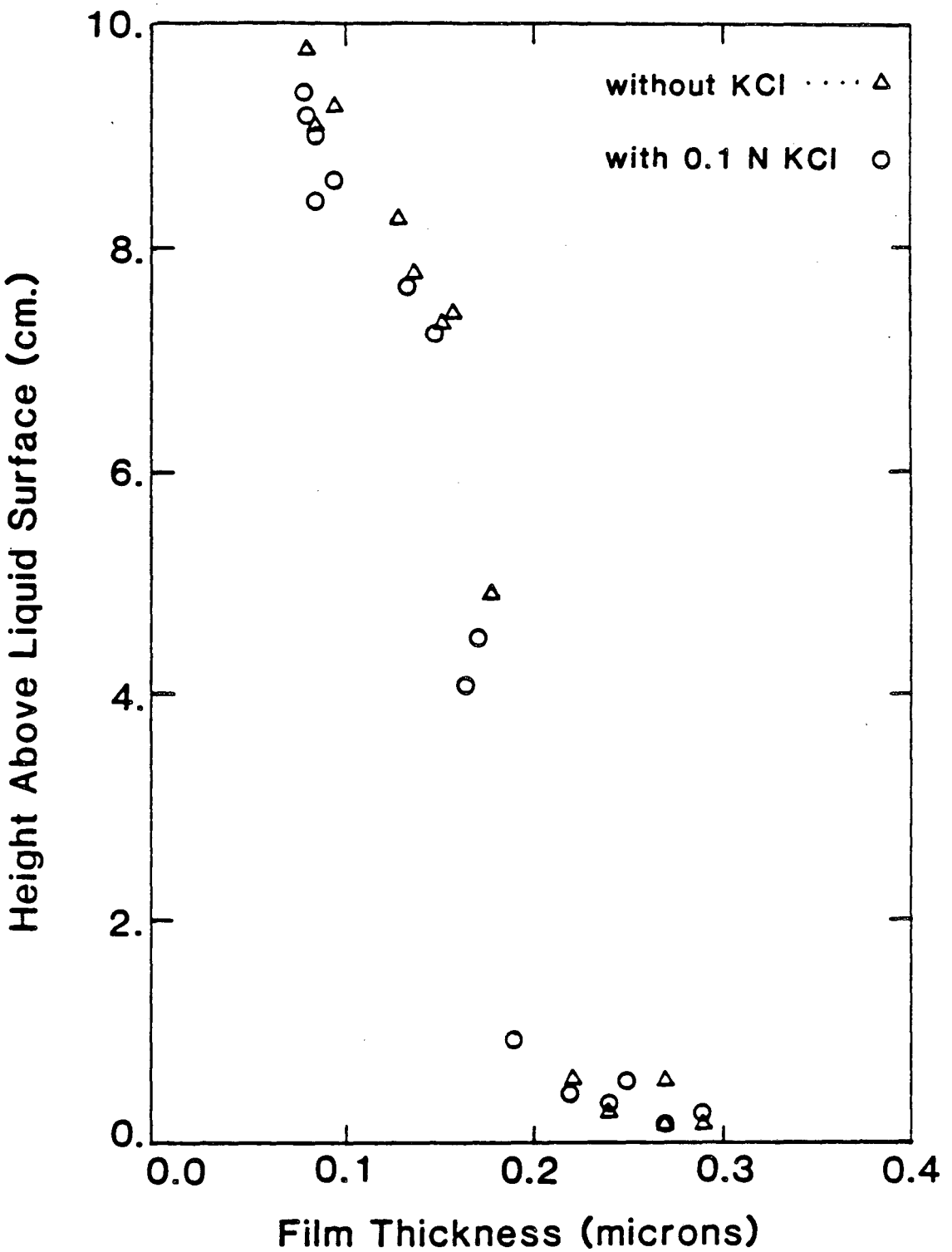


XBL 876-2938

**Figure 6-18:** Effect of strong specific adsorption on equilibrium film profile: 1 M KOH with and witout 0.1 M KCl on the 100 $cm^2$ platinum substrate with square edges both profiles measured two days after liquid level was lowered.

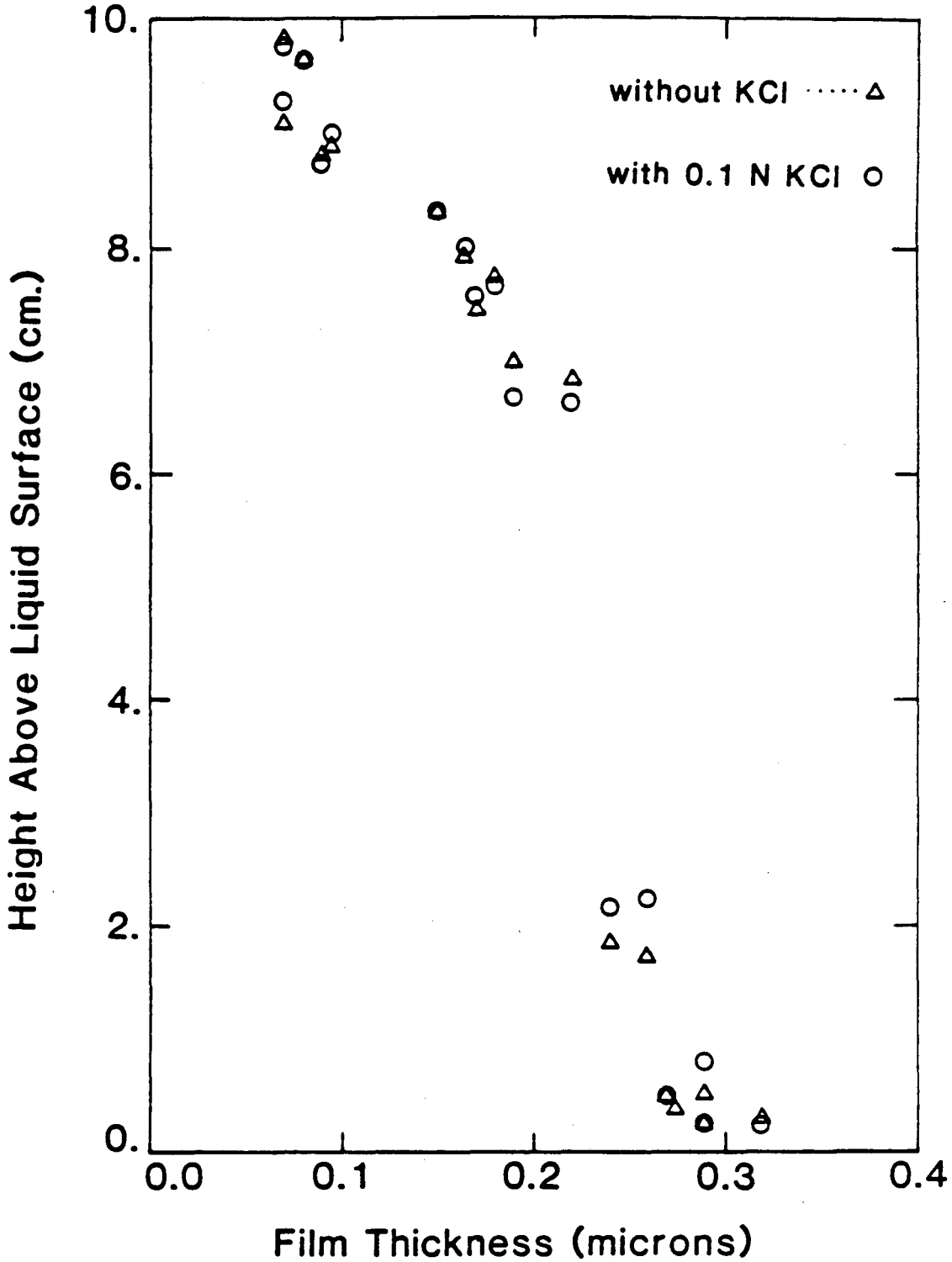


XBL 876-2937

**Figure 6-19:** Effect of strong specific adsorption on equilibrium film profile: 1 M $H_3PO_4$ with and witout 0.1 M KCl on the 100 $cm^2$ platinum substrate with square edges both profiles measured two days after liquid level was lowered.

no influence on the resulting film thickness.

### 6.6. Tetradecane

Three experiments were performed using pure tetradecane instead of an electrolyte. All three of these experiments suffered to various degrees from dewetting problems. These problems are most likely due to the presence of small quantities of polar material; either adsorbed water or salt deposited during the cleaning procedure. Because the film was not uniform, it is difficult to show the data in the form of an equilibrium profile as has been done for other systems. However, it is worthwhile to note some general observations.

The initial drainage of tetradecane resembled the drainage of electrolyte solutions. Holes did not appear in the film until about 15 hours after the liquid level had been lowered. These holes, although severely disrupting the color bands, did not cause the film to completely dewet the surface and the film was observed to be steady and time-invariant for up to six days at which point the experiment was terminated. The observed film thickness was on the order of 0.2 micrometers or slightly less over most of the wetted surface. The film is thicker than would be expected from equation 4-24 where the Hamaker constant, as calculated from equation 4-14, is $-1.48 \times 10^{-12}$ ergs. However, the portions of the surface which are dewetted could be severely affecting the equilibrium profile. If, at the point of transition between a wetting and non wetting region, the surface angle the film makes with the substrate is around 90° or greater, the curvature of the film surface so produced will severely effect the equilibrium thickness.

Although precise information cannot be derived from these experiments the implications are still quite important. First, a repulsive force between the metal/organic interface and the organic/vapor interface is observed, *i.e.*, the Hamaker constant is negative as is predicted from van der Waals interactions. In spite of severe dewetting problems encountered, tetradecane films on platinum were observed to be stable for long periods of time. The film thickness of tetradecane on platinum is within a factor of 2 of that for aqueous systems.

### 6.7. Summary of Conclusions

Aqueous electrolytes draining from vertically oriented metallic substrates initially thin according to a viscous drainage equation. At long times the profiles of these films deviate from that expected from viscous drainage and become time-invariant, the thickness being in the range of 0.1 to 0.2 micrometers. Since the system is contained within a closed isothermal cell, no means of sustaining a vapor pressure, temperature, or concentration gradient can be determined that would cause a dynamic steady-state to support the observed films.

An equilibrium film model based on the interaction of the double layer at the solid/liquid and liquid/vapor interfaces predicts that the equilibrium film thickness should be on the order of 0.03 micrometers. Also, this model predicts that the equilibrium film thickness will decrease with increasing electrolyte concentration. Experimental observations are in conflict with both these predictions.

Finally, an equilibrium film model based on non-retarded van der Waals interactions was developed. This model is based on the Lifshitz general theory of van der Waals interactions. The predicted film thickness is found to be proportional to the inverse cube root of the distance above the bulk liquid level. The proportionality constant is characterized by the Hamaker constant of the three phase metal/electrolyte/vapor system. This Hamaker constant can be derived from the dielectric functions of the substrate and electrolyte. The dielectric functions are determined by the method of Parsegian and Weiss (1981) for the electrolytic solution or, from spectral absorption data and the Kramers-Kronig transformation for metals. This model does predict the observed profile shape with the film thickness being proportional to the inverse cube root of height above the bulk liquid level. For dilute electrolytes, this model also predicts the observed film thickness. However, for increasing electrolyte concentration the observed profiles become thicker than those predicted. This may result from higher order terms, dropped during simplification of the Lifshitz theory, becoming important as the concentration of the electrolyte is increased.

It is peculiar that no indication of retardation effects are encountered. Though the Lifshitz theory predicts that for film thicknesses greater than 0.01 micrometers such effects should become important. This would result in the film thickness shifting to be proportional to the inverse fourth root of height, and also, the retarded Hamaker constant would decrease with increasing film thickness. That this behavior is not observed is perhaps due to the intimate proximity of the substrate and film. Other geometries studied to date have been

concerned with interacting bodies that are separated by *at least* the film thickness: in the present geometry, the interacting bodies are separated by *at most* the film thickness.

It was also shown that adsorption of ionic species at the metal/liquid interface does not affect the equilibrium film thickness. Therefore, the energy of interaction may be solely attributed to the bulk properties of the substrate and film. This conclusion lends credence to the van der Waals interaction model.

Films formed by an organic liquid, tetradecane, were also investigated. Although a uniform, undisturbed film was not achieved, a film of thickness on the order of 0.2 micrometers remained invariant from one to six days after the liquid level had been lowered. The observed film thickness was about double that expected from the Lifshitz theory. However, because of the dewetting problems encountered, the thickness of the tetradecane layer could not be determined accurately.

# Appendix A

# Notation

*Roman*

| | |
|---|---|
| a | effective radius of a molecule |
| A | Hamaker constant (ergs) |
| $A^R$ | retarded Hamaker constant (erg-cm) |
| B | ratio of parameters defined by equation 3-4 |
| C | Sum of coefficients of the Debye, Keesom, and London potentials |
| c | speed of light |
| [c] | concentration (moles/liter) |
| D | the distance between two bodies |
| $D^*$ | diffusion coefficient of vapor through the gas phase |
| d | film thickness |
| E | energy (chapter 4) |
| E | Amplitude of the electric field vector for incident light (chapter 5) |
| E′ | Amplitude of the electric field vector for reflected light (chapter 5) |
| $E_{pot}$ | potential energy (chapter 3) |
| $E_{surf}$ | surface energy (chapter 3) |
| $E_{tot}$ | total energy (chapter 3) |
| $e_-$ | the charge on an electron |
| $F_1$ | ratio of dielectric functions given by equation 2-16 |

| | |
|---|---|
| $F_2$ | ratio of dielectric functions given by equation 2-17 |
| $f_j$ | fitted parameter for the calculation of the dielectric function |
| $G_1$ | ratio of dielectric functions given by equation 2-25 |
| $G_2$ | ratio of dielectric functions given by equation 2-26 |
| $g$ | the gravitational constant |
| $g_j$ | fitted parameter for the calculation of the dielectric function |
| $H$ | the height of meniscus rise (cm) |
| $h$ | vertical direction coordinate |
| $h_j$ | fitted parameter for the calculation of the dielectric function |
| $h_P$ | Plank's constant |
| $I$ | ionization potential |
| $i$ | square root of minus one |
| $j$ | integer counter |
| $K$ | group of positive valued parameters that depend on the geometry of the system |
| $k$ | imaginary part of the complex refractive index, the extinction coefficient |
| $k_B$ | Boltzman's constant |
| $L$ | total length of a draining film |
| $M_W$ | molecular weight |
| $m_e$ | mass of an electron |
| $N_{Ca}$ | capillary number, defined by equation 2-9 |
| $N_{ce}$ | number density of conduction electrons |

| | |
|---|---|
| $N_{Re}$ | Reynold's number, defined by equation 2-4 |
| $N_\rho$ | atomic number density |
| n | integer counter |
| n | real part of the refractive index |
| $\hat{n}$ | complex index of refraction |
| P | pressure |
| $P_{Ca}$ | capillary pressure, defined by equation 3-11 |
| $P_{DL}$ | pressure caused by the interaction of two diffuse double layers |
| $P_n$ | normal component of pressure acting from within on the surface of a film |
| $P_o$ | bulk Laplacian pressure |
| Q | volumetric flow rate |
| R | gas constant |
| r | distance of separation between two molecules (chapters 2 and 4) |
| r | amplitude reflection coefficient, defined by equation 5-1 |
| $\hat{r}$ | complex reflection coefficient, defined by equation 5-2 |
| t | time |
| T | absolute temperature |
| U | energy of interaction |
| $V_w$ | velocity at which the bulk liquid level is withdrawn |
| v | fluid velocity |
| $v_a$ | valence of a 1:1 electrolyte |
| w | width of a film |

| | |
|---|---|
| $\hat{w}$ | reflected electro-magnetic waves |
| x | direction coordinate |
| y | direction coordinate |
| $y_m$ | minimum dimensionless potential within a thin film |
| $y_1$ | dimensionless potential at the metal/liquid interface |
| $y_2$ | dimensionless potential at the liquid/vapor interface |
| $y'$ | differential of y with respect to x |
| $y''$ | second differential of y with respect to x |
| z | direction coordinate |

*Greek*

| | |
|---|---|
| $\alpha$ | polarizability of a molecule |
| $\Gamma_1$ | ratio defined by equation 3-18 |
| $\Gamma_2$ | ratio defined by equation 3-19 |
| $\gamma$ | surface tension |
| $\gamma$ | activity coefficient, Equation 2-17 |
| $\Delta$ | the relative phase shift between p- to s-polarized light upon reflection form a surface |
| $\Delta S$ | optical path difference |
| $\delta$ | film thickness |
| $\delta$ | phase shift (Chapter 5) |
| $\hat{\epsilon}$ | complex dielectric function |
| $\epsilon'$ | real part of the dielectric function |

| | |
|---|---|
| $\epsilon''$ | imaginary part of the dielectric function, absorption spectrum |
| $\epsilon_o$ | electric permittivity of free space |
| 1/kappa | the Debye length |
| $\lambda$ | wavelength of light |
| $\mu$ | fluid viscosity |
| $\mu_1$ | dipole moment of molecule 1 |
| $\mu_2$ | dipole moment of molecule 2 |
| $\nu$ | frequency |
| $\nu_{co}$ | cut off frequency |
| $\nu_I$ | ionization frequency |
| $\nu_k$ | kinematic viscosity |
| $\nu_{rot}$ | average rotational relaxation frequency |
| $\rho$ | density |
| $\Phi$ | flux of vapor through the gas phase (chapter 3) |
| $\Phi$ | angle of incidence of a light beam with a surface |
| $\Phi'$ | refracted angle of light with a surface |
| $\Psi$ | electrical potential |
| $\Psi$ | relative amplitude attenuation of p- to s-polarized light reflected from a surface (chapters 5 and 6) |
| $\tau_{xh}$ | shear stress at x directed in the h direction |
| $\tau$ | relaxation time for a Lorentzian oscillator |
| $\tau_h$ | relaxation time for high frequency limiting behavior |
| $\tau_l$ | relaxation time for low frequency limiting behavior |

| | |
|---|---|
| $\theta$ | the angle an inclined plate makes with the horizontal |
| $\omega$ | frequency |
| $\omega_h$ | frequency where absorption data is matched to high frequency limiting behavior |
| $\omega_j$ | fitted parameter for the calculation of the dielectric function |
| $\omega_l$ | frequency where absorption data is matched to low frequency limiting behavior |
| $\omega_p$ | plasma frequency |
| $\Pi$ | the disjoining pressure |
| $\xi$ | dimensionless distance, defined by equation 3-16 |
| $\xi_\delta$ | dimensionless distance of separation between two interfaces |

# Appendix B

## The Surface Profile of Minimum Total Energy

As was shown in chapter 3, section 3.2, the total energy of a liquid film wetting a solid to a distance H above the bulk liquid level (see figure 3-1) is the sum of the potential energy expended lifting the liquid film plus the surface energy expended creating the new surface. These energies are given by:

$$E_{pot} = \rho g w \int_0^H y x \, dx \tag{B-1}$$

$$E_{surf} = \gamma w \int_0^H \sqrt{1 + y'^2} \, dx \tag{B-2}$$

where $\rho$ is the liquid density, g the gravitational constant, w the width of the film, H is the total height the film rises above the bulk liquid level, $\gamma$ is the liquid/vapor surface tension, and $y'$ is the derivative of y with respect to x. The total energy, $E_t$, is the sum of equations B-1 and B-2.

$$\frac{E_t}{w} = \frac{E_{surf}}{w} + \frac{E_{pot}}{w} = \int_0^H [\, \gamma(1+y')^{1/2} + \rho g y x \,] dx \tag{B-3}$$

For simplicity, we set the integrand of equation B-3 equal to F. Thus,

$$\frac{E_t}{w} = \int_0^H F \, dx \tag{B-4}$$

The calculus of variations may be used to find the function, F, which minimizes the total energy given in equation B-4. If F is the minimum function

already, then any perturbation in its shape will lead to an increase in energy. Therefore, the condition:

$$\delta \frac{E_t}{w} = 0 = \int_0^H \delta F \, dx \tag{B-5}$$

will provide the function, F, which minimizes the energy. The quantity $\delta F$ is defined as:

$$\delta F = \left[ \frac{\partial F}{\partial y} - \frac{d}{dx} \frac{\partial F}{\partial y'} \right] \delta y \tag{B-6}$$

which results from a basic analysis of the method of variational calculus. The integral in equation B-4 may now be written as:

$$\delta \frac{E_t}{w} = 0 = \int_0^H \left[ \frac{\partial F}{\partial y} - \frac{d}{dx} \frac{\partial F}{\partial y'} \right] \delta y \, dx \tag{B-7}$$

The trivial solution of this equation is that $\delta y = 0$ which will not be permitted. Therefore, to ensure that the integral is always zero, the quantity enclosed by the square brackets in equation B-7 must be equal to zero. Therefore,

$$\frac{\partial F}{\partial y} = \frac{d}{dx} \frac{\partial F}{\partial y'} \tag{B-8}$$

The partial differentials described above may be taken for the desired system, resulting in:

$$\frac{\partial F}{\partial y} = \rho g x \tag{B-9}$$

$$\frac{\partial F}{\partial y'} = \frac{\gamma y'}{(1 + y'^2)^{1/2}} \tag{B-10}$$

$$\frac{d}{dx}\frac{\partial F}{\partial y'} = \gamma \frac{y''(1+y'^2)^{1/2} - y'\dfrac{y'y''}{(1+y'^2)^{1/2}}}{1 + y'^2} \tag{B-11}$$

Equating equations B-9 and B-11 and simplifying results in:

$$\frac{y''}{(1+y'^2)^{3/2}} = \frac{\rho g}{\gamma} x \tag{B-12}$$

This may be integrated once resulting in:

$$\frac{y'}{(1+y'^2)^{1/2}} = \frac{\rho g}{2\gamma} x^2 + C \tag{B-13}$$

The integration constant, C, may be evaluated from the limiting slope at $x = 0$. This limit will have one of two values depending on the contact angle of the liquid with the solid. Referring to figure 3-1, notice that if the contact angle is less than 90°, then the geometry as shown in the figure is correct and as x decreases from H to 0, the value of y will steadily increase until at $x = 0$, $y = \infty$. Therefore, $y'$, the slope of the curve, approaches $-\infty$, as x approaches 0. However, if the contact angle is greater than 90°, *i.e.*, the liquid does not wet the solid, then the geometry is opposite that shown in figure 3-1, and the liquid will make contact with the solid at a negative value of x. For this situation, as x is increased toward $x = 0$, y will increase to $\infty$, therefore, $y'$, the slope, will approach $+\infty$, as x approaches 0.

The limit of the left hand side of equation B-13 will be $-1$ as $y'$ approaches $-\infty$, and $+1$ as $y'$ approaches $+\infty$. Therefore, C will equal $-1$ for contact angles less than 90° (liquids that wet the solid), and C will be $+1$ for contact angles greater than 90° (liquids that do not wet the solid).

Equation B-14 may now be simplified. For this purpose we will define the following group of parameters as such:

$$B = \frac{\rho g}{2 \gamma} \tag{B-15}$$

After simplification we find that:

$$y' = \pm \frac{B x^2 - 1}{(2B)^{1/2} x (1 - \frac{B}{2} x^2)^{1/2}} \tag{B-16}$$

The positive sign is chosen when the liquid wets the solid, and the negative sign is chosen when the liquid does not wet the solid.

In either case, the maximum meniscus rise or maximum meniscus depression may be found when we realize that equation B-16 must not be permitted to change sign. If this were permitted, the film thickness would increase with increasing height for the wetting case, or in the non-wetting case the air film thickness between the solid and the liquid would increase with decreasing height, both situations are physically impossible. Therefore, the value of x is limited by the numerator of equation B-16 because the numerator will change sign if x becomes too large. The limit on x is given by:

$$\frac{\rho g}{2 \gamma} x^2 - 1 \leq 0 \tag{B-17}$$

or, solving for the magnitude of x;

$$x_{max} = H = \left(\frac{2 \gamma}{\rho g}\right)^{1/2} \tag{B-18}$$

The profile shape of a perfectly wetting liquid (0° contact angle) or a perfectly

non-wetting liquid (180° contact angle) may now be numerically solved for by using the point $y = 0$, at $x = H$ in a Runge-Kutta or some other initial value integration routine.

The meniscus shape for other contact angles may also be found by this method. From the contact angle, the slope at the point of contact ($y = 0$) may be found. This may be used in equation B-13 with the appropriate value of C to find the value of x at $y = 0$. This pair of values is then used as the starting point for the initial value integration routine.

# Appendix C

## Program for the Calculation of the Hamaker Constant

The following program was used to calculate the Hamaker constants of metal/liquid/vapor three phase systems. The dielectric function of the metal is calculated from its absorption spectra using the Kramers-Kronig transformation. Low and high frequency limiting behavior functions are used to extend the available data. The liquid dielectric function is calculated using the method and data of Parsegian and Weiss, 1981. A sample data file is included following the program.

## Program HAMAKER

```
      program hamaker
c
c     ---
c     this program performs the following functions:
c     1)  fits absorption spectra using a least square
c         bspline routine from the nag math library
c         see nag routine e02baf.
c     2)  evaluates the dielectric function for imaginary
c         frequencies.  this is accomplished using one of
c         the kramers-kronig transformations.
c       a) the integral which is evaluated from 0 to infinity
c          is broken into three parts.
c       b) two of these, the high and low frequency limits,
c          are evaluated analytically.
c       c) the third part is integrate numerically using
c          the nag library routines d01ahf and e02bbf.
c     3)  uses the dielectric function to calculate the
c         hamaker constant for a substrate/water/air system.
c
c     ---
c     declaration of variables for routines e02baf and e02bbf
c     ---
c
      integer m,ncap,ncap2,ncap3,ncap7,j,ifail,r
      real*8  ss,xarg,fit,res,x(500),y(500),w(500),c(50),
     x        work1(500),work2(4,50),k(50),title(7)
c
c     ---
c     declaration of variables for routine d01ahf
c     ---
c
      real*8    a,b,relacc,relerr,ans
      integer   npts,nlimit
      external  f1
c
c     ---
c     declaration of variables for evaluation of z
c     ---
c
      real*8    kb,h,evtfrq,t,z,echrge,dz,az,pi
      integer*4  ncount,nquit
```

```
c
c           ---
c           declaration of variables for e1l and e1h
c           ---
c
          real*8 gaml,gamh,wl,wh,wp,e1low,e1high,e1
c
c           ---
c           declaration of variables for calculation
c           of the hamaker constant
c           ---
c
          integer i2,k1
          real*8 w2(3,20)
          real*8 e2s,e2,d,sum,totsum,a1,ap,alwp,af
          real*8 con,alw,dalw,dadlz,a2,b1
c
c           ---
c           declaration of common blocks
c           ---
c
          common / zz / ncap7,k,c,az,z
          common / epsilon / gaml,gamh,wp,wl,wh,pi
c
c           ---
c           reading data for least squares spline fit
c           ---
c
          open (unit=1,name='splineptepp.dat',status='old')
          open (unit=2,name='kktrans.dat',status='new',
     x            carriagecontrol='list')
          open (unit=3,name='hamaker.dat',status='new',
     x           carriagecontrol='list')
          read (1,1000) title
          write (2,1001) (title(i),i=1,7)
          write (3,1001) (title(i),i=1,7)
   20     read (1,1002) m
          write (2,1001)
          read (1,1003) ncap
          ncap2=ncap+2
          ncap3=ncap+3
          ncap7=ncap+7
          if (ncap.eq.1) goto 40
          read (1,1004) (k(j),j=5,ncap3)
   40     do 80 r=1,m
              read (1,1005) x(r),y(r)
              w(r)=1.
```

```
   80     continue
c
c          ---
c          calling the least squares spline fitting routine
c          ---
c
          ifail=1
          call e02baf(m,ncap7,x,y,w,k,work1,work2,c,ss,ifail)
          if (ifail.ne.0) goto 360
c
c          ---
c          writing spline fit coefficients to kktrans.dat
c          ---
c
          write (2,1014)
          do 140 j=1,ncap7
             write (2,1007) j,k(j),c(j)
  140     continue
          write (2,1003)
          write (2,1008) ss
          write (2,1007)
c
c          ---
c          spline portion of program is complete.
c          this is the beginning of the integration portion.
c          ---
c
c          ---
c          read coefficients for the calculation of the dielectric
c          function for water.
c          ---
c
          read (1,1002) i2
          do 160 j=1,i2
             read(1,1016) w2(1,j),w2(2,j),w2(3,j)
  160     continue
          write (2,1013)
          write (3,1015)
c
c          ---
c          constants for the evaluation of z, the (imaginary) frequency
c          at which the kramers-kronig transformation is to be evaluated
c          ---
c
          pi=3.141592654
```

```
      kb=1.380662e-23              ! boltzman's constant
      h=6.626176e-34               ! plank's constant
      evtfrq=2.417971e+14          ! conversion for ev to frequency
      echrge=1.60219e-19           ! charge on an electron
      t=303.
      ncount=-1
      e2s=1.000                    !setting e2s larger than 1 causes
      e2s=dlog10(e2s)              !a uniform shift in the dielectric
                                   !function of water (thus accounting
                                   !for increase due to electrolyte)
      dz=2.*pi*kb*t*evtfrq/echrge
c
c      ---
c      constants for low and high frequency limits of k-k trans.
c      ---
c
      gaml=1.e+16          ! low frequency damping coefficient
      gamh=2.8184e+17      ! high frequency damping coefficient
      wp=3.13586e+16       ! plasma frequency
      wl=2.45e+13          ! low frequency integration limit
      wh=4.8e+17           ! high frequency integration limit
c
c      ---
c      constants for integration routine d01ahf
c      ---
c
      relacc=1.0e-5
      nlimit=10000
      a=wl
      b=wh
c
c      ---
c      loop for stepping through all values of z.
c      integration routine d01ahf is called once for each
c      value of z and that frequency's contribution to
c      the total hamaker constant is calculated.
c      ---
c
      nquit=800            !maximum no. of terms to be evaluated
      totsum=0.
      ap=0.
      alwp=0.
      af=-9.591e-13        !for calculation of % increase in
                           !running sum, a/af (must know answer)
  310 ncount=ncount+1
          z=dz*(dfloat(ncount))
```

```
c
c               ---
c               there are special considerations for ncount=0 term
c               ---
c
                if (ncount) 180,170,180
  170           con=1./2.
                e1=1.e13
                e2=80.
                goto 190
  180           con=1.
c
c               ---
c               call integration routine to evaluate dielectric
c               function from k-k transformation.
c               ---
c
                az=dlog10(z)
                ifail=0
                ans=d01ahf (a,b,relacc,npts,relerr,f1,nlimit,ifail)
                e1low=e1l(z)
                e1high=e1h(z)
                e1=e1low+ans+e1high+1.
                if (ifail.eq.0) goto 320
                goto 340
  320           continue
c
c               ---
c               evaluation of the dielectric function for water using
c               pashley's method and data
c               ---
c
                e2=dielec(w2,z/evtfrq,i2)
                e2=1.+10.**(e2s+dlog10(e2-1.))
c
c               ---
c               evaluation of this (z) frequency's contribution to
c               the total hamaker constant.
c               ---
c
  190           sum=0
                j=0
  200           j=j+1
                  b1=float(j)
                  d=(con/b1**3)*(((e1-e2)/(e1+e2))*((1.-e2)/(1.+e2)))**
     x                (int(b1))
                  sum=sum-abs(d)
```

```
                if ((abs(d/sum))-.0000001) 220,220,210
  210         goto 200
  220         totsum=totsum+sum
c_________to prevent output of intermediate results comment these out!
              if (ncount) 230,240,230
  240         alw=0                      !intermediate results for
              dalw=15.                   !every tenth frequency
              goto 250                   !evaluation are written
  230         alw=az                     !hamaker.dat
              dalw=alw-alwp
  250         a1=(3./2.)*kb*t*totsum
              dadlz=1.e12*abs((a1-ap)/dalw)
              alwp=alw
              ap=a1
              a2=(3./2.)*kb*t*sum
              k1=ncount/10
              if (ncount-1) 290,260,290
  290         if ((float(ncount)/10.)-k1) 270,260,270
  260         write (3,1017) float(ncount),alw,a2/af,dadlz,e1,e2,a1
c^_________^
              if (ncount-nquit) 270,280,280
  270       goto 310
  280       continue
            a1=(3./2.)*kb*t*totsum
            write (3,1004) a1            !write final hamaker constant
            close (unit=1)               !value to hamaker.dat
            close (unit=2)
            close (unit=3)
  330       goto 2000
  340       write (2,1011) ifail
            goto 2000
  350       write (2,1012) if10
            goto 2000
  360       write (2,1009) ifail
            goto 2000
 1000       format (1x,7a4)
 1001       format (2x,7a4)
 1002       format (1x,i4)
 1003       format (2(1x,i4))
 1004       format (2x,e13.6)
 1005       format (2x,e13.6,3x,e13.6)
 1006       format (2x,e13.6,4(1x,',',1x,e13.6))
 1007       format (2x,i7,2(1x,e13.6))
 1008       format (2x,'ss=',e13.6)
 1009       format (2x,i7,2x,'you blew it on e02baf')
 1010       format (2x,i7,2x,'you blew it on e02bbf')
 1011       format (2x,i7,2x,'you blew it on d01ahf')
```

```
1012      format (2x,i7,2x,'you blew it during the function call')
1013      format (2x,'the following numbers are from the integraion')
1014      format (2x,'these are the splinefit knots and coefficients')
1015      format (4x,'ncount',5x,'log(z)',6x,'a2/af',3x,'da/dlog(z)',
     x            5x,'e1',9x,'e2',9x,'a')
1016      format (2x,f7.3,2(1x,f7.3))
1017      format (2x,e10.3,6(1x,e10.3))
2000      stop
          end


          double precision function f1(x)                          f1
          common / zz / ncap7,k,c,az,z
          integer ncap7
          real*8 k(50),c(50),az,z
          real*8 x,fit,ax,ex,efit,ez
          ax=dlog10(x)
          ex=x/1.e+10
          ez=z/1.e+10
          if10=0
          call e02bbf (ncap7,k,c,ax,fit,if10)
          efit=(10**fit)/1.e+10
          if (if10.ne.0) stop
          f1=(ex*efit)/(ex*ex+ez*ez)
          return
          end


          double precision function e1l(z)                         e1l
          common / epsilon / gaml,gamh,wp,wl,wh,pi
          real*8 gaml,egaml,wp,ewp,z,ez,wl,gamh,wh,pi
          egaml=gaml/1.e+10
          ewp=wp/1.e+10
          ez=z/1.e+10
          e1l=(datan2(wl,z))*((ewp*ewp)/(egaml*ez))
          return
          end


          double precision function e1h(z)                         e1h
          common / epsilon / gaml,gamh,wp,wl,wh,pi
          real*8 gamh,egamh,wp,ewp,z,ez,wh,ewh,gaml,wl,pi
          real*8 e1h1,e1h2,e1h3
          egamh=gamh/1.e+10
          ewp=wp/1.e+10
          ez=z/1.e+10
          ewh=wh/1.e+10
```

```
      elh1=(ewp*ewp*egamh)/(ez*ez*ewh)
      elh2=(ewp*ewp*egamh)/(ez*ez*ez)
      elh3=(datan2(wh,z))-(pi/2.)
      elh=elh1+(elh2*elh3)
      return
      end
```

*dielec*

```
      double precision function dielec(w,ev,i)
      real*8 w(3,20)
      real*8 ev,term,sum
      sum=0
      do 20 ic=1,i
         term=w(1,ic)/(w(2,ic)**2+ev**2+ev*w(3,ic))
         sum=sum+term
20    continue
      dielec=sum+1.
      return
      end
```

INPUT **DATA FILE** SPLINEFITEPP.DAT

```
310                    !no. of x-y data pairs

17                     !no. + 1 of internal knots

0.135592E+02           !internal knots   log(frequency)
0.138603E+02
0.139852E+02
0.140821E+02
0.141613E+02
0.142283E+02
0.144044E+02
0.150064E+02
0.158044E+02
0.160141E+02
0.160697E+02
0.160963E+02
0.163918E+02
0.165593E+02
0.166864E+02
0.170012E+02
```

```
0.133832E+02 ,  0.307191E+01        !x-y data pairs
0.134971E+02 ,  0.286177E+01        !log (ν), log (ε'' )
0.135592E+02 ,  0.270794E+01        !data from Palik, 1985
0.136136E+02 ,  0.256683E+01
0.136842E+02 ,  0.245209E+01
0.137256E+02 ,  0.235280E+01
0.137811E+02 ,  0.226093E+01
0.138303E+02 ,  0.217637E+01
0.138603E+02 ,  0.210383E+01
0.138883E+02 ,  0.202688E+01
0.139272E+02 ,  0.195362E+01
0.139629E+02 ,  0.187938E+01
0.139852E+02 ,  0.180664E+01
0.140166E+02 ,  0.177925E+01
0.140364E+02 ,  0.175142E+01
0.140553E+02 ,  0.175165E+01
0.140821E+02 ,  0.178026E+01
0.140992E+02 ,  0.180373E+01
0.141235E+02 ,  0.181559E+01
0.141390E+02 ,  0.182589E+01
0.141613E+02 ,  0.184045E+01
0.141825E+02 ,  0.185465E+01
0.141961E+02 ,  0.186644E+01
0.142157E+02 ,  0.188186E+01
0.142283E+02 ,  0.189209E+01
0.142465E+02 ,  0.189660E+01
0.142582E+02 ,  0.189322E+01
0.142697E+02 ,  0.188420E+01
0.142863E+02 ,  0.187370E+01
0.142970E+02 ,  0.186024E+01
0.143126E+02 ,  0.184818E+01
0.143276E+02 ,  0.183410E+01
0.143374E+02 ,  0.181903E+01
0.143609E+02 ,  0.178483E+01
0.143832E+02 ,  0.175028E+01
0.144044E+02 ,  0.171522E+01
0.144246E+02 ,  0.168280E+01
0.144439E+02 ,  0.165314E+01
0.144623E+02 ,  0.162358E+01
0.144971E+02 ,  0.156719E+01
0.145293E+02 ,  0.151830E+01
0.145593E+02 ,  0.147142E+01
0.145873E+02 ,  0.142678E+01
0.146136E+02 ,  0.138657E+01
0.146384E+02 ,  0.134711E+01
0.146619E+02 ,  0.130702E+01
0.146842E+02 ,  0.127235E+01
```

```
0.147054E+02 ,  0.124262E+01        !x-y data pairs
0.147256E+02 ,  0.121383E+01        !continued
0.147449E+02 ,  0.118792E+01
0.147634E+02 ,  0.115753E+01
0.147811E+02 ,  0.112731E+01
0.147981E+02 ,  0.110058E+01
0.148145E+02 ,  0.107802E+01
0.148303E+02 ,  0.105484E+01
0.148456E+02 ,  0.103245E+01
0.148603E+02 ,  0.100945E+01
0.148745E+02 ,  0.989877E+00
0.148883E+02 ,  0.967248E+00
0.149017E+02 ,  0.948266E+00
0.149146E+02 ,  0.928846E+00
0.149272E+02 ,  0.911690E+00
0.149395E+02 ,  0.894139E+00
0.149514E+02 ,  0.877970E+00
0.149629E+02 ,  0.860470E+00
0.149742E+02 ,  0.845495E+00
0.149852E+02 ,  0.826399E+00
0.150064E+02 ,  0.792812E+00
0.150266E+02 ,  0.765996E+00
0.150459E+02 ,  0.734079E+00
0.150644E+02 ,  0.708081E+00
0.150821E+02 ,  0.680082E+00
0.150992E+02 ,  0.657285E+00
0.151156E+02 ,  0.641395E+00
0.151314E+02 ,  0.622090E+00
0.151466E+02 ,  0.601886E+00
0.151540E+02 ,  0.593087E+00
0.151613E+02 ,  0.587037E+00
0.151685E+02 ,  0.571289E+00
0.151755E+02 ,  0.551986E+00
0.151865E+02 ,  0.525563E+00
0.151978E+02 ,  0.528505E+00
0.152094E+02 ,  0.534331E+00
0.152213E+02 ,  0.543224E+00
0.152335E+02 ,  0.555288E+00
0.152461E+02 ,  0.560576E+00
0.152590E+02 ,  0.554077E+00
0.152724E+02 ,  0.551743E+00
0.152862E+02 ,  0.529841E+00
0.153005E+02 ,  0.529045E+00
0.153063E+02 ,  0.529045E+00
0.153122E+02 ,  0.529045E+00
0.153182E+02 ,  0.526081E+00
0.153242E+02 ,  0.526081E+00
```

```
0.153304E+02 ,  0.523096E+00        !x-y data pairs
0.153366E+02 ,  0.513271E+00        !continued
0.153430E+02 ,  0.513271E+00
0.153494E+02 ,  0.517064E+00
0.153560E+02 ,  0.517064E+00
0.153626E+02 ,  0.520824E+00
0.153693E+02 ,  0.521504E+00
0.153762E+02 ,  0.515344E+00
0.153831E+02 ,  0.509633E+00
0.153901E+02 ,  0.503246E+00
0.153973E+02 ,  0.489790E+00
0.154048E+02 ,  0.475671E+00
0.154121E+02 ,  0.461318E+00
0.154198E+02 ,  0.450157E+00
0.154273E+02 ,  0.435366E+00
0.154351E+02 ,  0.423835E+00
0.154431E+02 ,  0.415641E+00
0.154514E+02 ,  0.407968E+00
0.154594E+02 ,  0.395990E+00
0.154681E+02 ,  0.391711E+00
0.154766E+02 ,  0.368246E+00
0.154853E+02 ,  0.350128E+00
0.154944E+02 ,  0.350628E+00
0.155034E+02 ,  0.348694E+00
0.155129E+02 ,  0.336228E+00
0.155224E+02 ,  0.325483E+00
0.155321E+02 ,  0.313623E+00
0.155421E+02 ,  0.304008E+00
0.155522E+02 ,  0.292300E+00
0.155627E+02 ,  0.281951E+00
0.155735E+02 ,  0.271972E+00
0.155846E+02 ,  0.259833E+00
0.155956E+02 ,  0.248022E+00
0.156072E+02 ,  0.234441E+00
0.156192E+02 ,  0.226012E+00
0.156314E+02 ,  0.230847E+00
0.156377E+02 ,  0.232356E+00
0.156440E+02 ,  0.237825E+00
0.156506E+02 ,  0.236998E+00
0.156571E+02 ,  0.228395E+00
0.156635E+02 ,  0.236184E+00
0.156703E+02 ,  0.234191E+00
0.156772E+02 ,  0.227648E+00
0.156842E+02 ,  0.217437E+00
0.156913E+02 ,  0.208277E+00
0.156983E+02 ,  0.194919E+00
0.157056E+02 ,  0.181398E+00
```

```
0.157132E+02 ,  0.165428E+00        !x-y data pairs
0.157206E+02 ,  0.140203E+00        !continued
0.157283E+02 ,  0.120528E+00
0.157361E+02 ,  0.101778E+00
0.157441E+02 ,  0.852192E-01
0.157522E+02 ,  0.711011E-01
0.157605E+02 ,  0.543564E-01
0.157689E+02 ,  0.359058E-01
0.157776E+02 ,  0.779899E-02
0.157863E+02 , -0.146202E-01
0.157953E+02 , -0.283680E-01
0.158044E+02 , -0.393114E-01
0.158137E+02 , -0.484507E-01
0.158233E+02 , -0.586774E-01
0.158331E+02 , -0.777542E-01
0.158430E+02 , -0.272678E-01
0.158533E+02 , -0.901691E-01
0.158637E+02 , -0.903167E-01
0.158745E+02 , -0.120862E+00
0.158855E+02 , -0.168963E+00
0.158968E+02 , -0.227149E+00
0.159083E+02 , -0.255413E+00
0.159202E+02 , -0.277722E+00
0.159324E+02 , -0.296365E+00
0.159451E+02 , -0.320710E+00
0.159580E+02 , -0.344259E+00
0.159714E+02 , -0.372864E+00
0.159852E+02 , -0.402950E+00
0.159994E+02 , -0.434459E+00
0.160141E+02 , -0.459771E+00
0.160294E+02 , -0.487924E+00
0.160452E+02 , -0.514279E+00
0.160616E+02 , -0.543355E+00
0.160697E+02 , -0.562554E+00
0.160963E+02 , -0.417534E+00
0.161148E+02 , -0.467806E+00
0.161341E+02 , -0.504678E+00
0.161543E+02 , -0.546455E+00
0.161755E+02 , -0.592133E+00
0.161978E+02 , -0.640457E+00
0.162213E+02 , -0.691700E+00
0.162461E+02 , -0.752483E+00
0.162724E+02 , -0.814107E+00
0.163005E+02 , -0.876965E+00
0.163832E+02 , -0.112500E+01
0.163918E+02 , -0.115733E+01
0.164002E+02 , -0.118787E+01
```

```
0.164125E+02 , -0.123253E+01        !x-y data pairs
0.164246E+02 , -0.126940E+01        !continued
0.164324E+02 , -0.129292E+01
0.164439E+02 , -0.132597E+01
0.164550E+02 , -0.135290E+01
0.164660E+02 , -0.138197E+01
0.164766E+02 , -0.140497E+01
0.164870E+02 , -0.141857E+01
0.164971E+02 , -0.143286E+01
0.165070E+02 , -0.144551E+01
0.165167E+02 , -0.145627E+01
0.165293E+02 , -0.145980E+01
0.165385E+02 , -0.146387E+01
0.165505E+02 , -0.146782E+01
0.165593E+02 , -0.146963E+01
0.165707E+02 , -0.147391E+01
0.165818E+02 , -0.147572E+01
0.165927E+02 , -0.147761E+01
0.166033E+02 , -0.147707E+01
0.166136E+02 , -0.147659E+01
0.166237E+02 , -0.147615E+01
0.166336E+02 , -0.147579E+01
0.166432E+02 , -0.147549E+01
0.166550E+02 , -0.147765E+01
0.166642E+02 , -0.147743E+01
0.166754E+02 , -0.147726E+01
0.166864E+02 , -0.147965E+01
0.166970E+02 , -0.148999E+01
0.167074E+02 , -0.149783E+01
0.167176E+02 , -0.150582E+01
0.167276E+02 , -0.151683E+01
0.167392E+02 , -0.152519E+01
0.167487E+02 , -0.153373E+01
0.167597E+02 , -0.154250E+01
0.167706E+02 , -0.155450E+01
0.167811E+02 , -0.156376E+01
0.167914E+02 , -0.157318E+01
0.168015E+02 , -0.158615E+01
0.168129E+02 , -0.159948E+01
0.168225E+02 , -0.160977E+01
0.168334E+02 , -0.162390E+01
0.168441E+02 , -0.163477E+01
0.168545E+02 , -0.164595E+01
0.168646E+02 , -0.165744E+01
0.168759E+02 , -0.167328E+01
0.168856E+02 , -0.168137E+01
0.168964E+02 , -0.169390E+01
```

```
0.169069E+02 , -0.170766E+01          !x-y data pairs
0.169172E+02 , -0.171917E+01          !continued
0.169285E+02 , -0.173238E+01
0.169383E+02 , -0.174364E+01
0.169490E+02 , -0.175570E+01
0.169595E+02 , -0.176810E+01
0.169697E+02 , -0.177987E+01
0.169809E+02 , -0.179463E+01
0.169917E+02 , -0.181554E+01
0.170012E+02 , -0.183452E+01
0.170126E+02 , -0.185683E+01
0.170226E+02 , -0.187579E+01
0.170335E+02 , -0.189698E+01
0.170440E+02 , -0.191854E+01
0.170543E+02 , -0.193972E+01
0.170644E+02 , -0.196043E+01
0.170751E+02 , -0.198301E+01
0.170849E+02 , -0.200419E+01
0.170958E+02 , -0.202553E+01
0.171066E+02 , -0.204417E+01
0.171172E+02 , -0.205183E+01
0.171275E+02 , -0.206063E+01
0.171383E+02 , -0.208097E+01
0.171488E+02 , -0.210336E+01
0.171591E+02 , -0.212581E+01
0.171699E+02 , -0.215070E+01
0.171804E+02 , -0.217328E+01
0.171907E+02 , -0.219709E+01
0.172014E+02 , -0.222512E+01
0.172118E+02 , -0.225050E+01
0.172220E+02 , -0.227581E+01
0.172326E+02 , -0.230094E+01
0.172435E+02 , -0.232395E+01
0.172536E+02 , -0.234448E+01
0.172640E+02 , -0.236603E+01
0.172747E+02 , -0.238870E+01
0.172852E+02 , -0.241703E+01
0.172959E+02 , -0.244745E+01
0.173064E+02 , -0.247496E+01
0.173167E+02 , -0.250432E+01
0.173272E+02 , -0.253284E+01
0.173379E+02 , -0.256336E+01
0.173484E+02 , -0.259295E+01
0.173586E+02 , -0.262088E+01
0.173690E+02 , -0.265072E+01
0.173797E+02 , -0.268298E+01
0.173901E+02 , -0.271220E+01
```

```
0.174006E+02 , -0.274328E+01          !x-y data pairs
0.174113E+02 , -0.277547E+01          !continued
0.174218E+02 , -0.280660E+01
0.174320E+02 , -0.283714E+01
0.174427E+02 , -0.286902E+01
0.174532E+02 , -0.290032E+01
0.174638E+02 , -0.293181E+01
0.174741E+02 , -0.296257E+01
0.174846E+02 , -0.299396E+01
0.174951E+02 , -0.302549E+01
0.175057E+02 , -0.305799E+01
0.175161E+02 , -0.309098E+01
0.175268E+02 , -0.312205E+01
0.175373E+02 , -0.315428E+01
0.175475E+02 , -0.318509E+01
0.175581E+02 , -0.321681E+01
0.175687E+02 , -0.324949E+01
0.175791E+02 , -0.328067E+01
0.175897E+02 , -0.331336E+01
0.176001E+02 , -0.334679E+01
0.176105E+02 , -0.337882E+01
0.176212E+02 , -0.341117E+01
0.176316E+02 , -0.344370E+01
0.176420E+02 , -0.347625E+01
0.176527E+02 , -0.351145E+01
0.176631E+02 , -0.354363E+01
0.176736E+02 , -0.357512E+01
0.176842E+02 , -0.360906E+01

11          !no. of terms for water dielectric function

 0.001    0.021    0.015        !f_j    ω_j    g_j
 0.004    0.069    0.038        !data for water from
 0.001    0.092    0.028        !Parsegian and Weiss, 1981
 0.006    0.200    0.025
 0.014    0.420    0.056
 2.700    8.300    0.510
 5.700   10.000    0.880
12.000   11.400    1.540
26.300   13.000    2.050
33.800   14.900    2.960
92.800   18.500    6.260
```

# Bibliography


F. Abeles (ed.), Optical Properties of Solids. Elsevier, New York, pp. 93-162, 1972.

A.W. Adamson, Physical Chemistry of Surfaces. 4th ed., Wiley, New York, pp. 185-257, 1982.

S. Banarjee, E. Rhodes and D.S. Scott, *Chem. Eng. Sci.*, **22**, 43 (1967).

A.J. Bard and L.R. Faulkner, Electrochemical Methods Fundamentals and Applications. Wiley, New York, pp. 488-552, 1980.

F. Bashforth and J.C. Adams, An Attempt to Test the theory of Capillary Action, Cambridge, New York, 1883.

T.B. Benjamin, *J. Fluid Mech.*, **2**, 554 (1957).

D.N. Bennion and C.W. Tobias, *J. Electrochem. Soc.*, **113**, 589 (1966).

A.M. Binnie, *J. Fluid Mech.*, **2**, 551 (1957).

J. Bond and M.B. Donald, *Chem. Eng. Sci.*, **22**, 237 (1967).

P.L.T. Brian, *A.I.Ch.E. J.*, **17**, 765 (1971).

P.L.T. Brian, J.E. Vivian and D.C. Matiatos, *A.I.Ch.E. J.*, **13**, 28 (1967).

C.R. Brown, Interferometry of Solid Thin Films. M.S. Thesis, Univ. Ca., Lawrence Berkeley Laboratory, Berkeley, California, LBL-2264, 1973.

H.G.B. Casimir and D. Polder, *Phys. Rev.*, **73**, 360 (1948).

C.J. Coakley and D. Tabor, *J. Phys. D*, **11**, L77 (1978).

P. Delahay, Double Layer and Electrode Kinetics. Interscience, New York, pp. 1-150, 1965.

C.D. Denson, *Ind. Eng. Chem. Fund.*, **9**, 443 (1970).

B.V. Derjagin and N.V. Churaev, *J. Colloid Sci.*, **66**, 389 (1978).

B.V. Derjagin and L. Landau, *Acta Physicochimica URSS*, **14**, 633 (1941).

B.V. Derjagin and M. Kussakov, *Acta Physicochimica URSS*, **10**, 25 (1939a).

B.V. Derjagin and M. Kussakov, *Acta Physicochimica URSS*, **10**, 153 (1939b).

O.F. Devereux and P.L. de Bruyn, Interaction of Plane-Parallel Double Layers. M.I.T. Press, Cambridge, MA, pp. 1-49, 1964.

I.E. Dzyaloshinskii, E.M. Lifshitz and L.P. Pitaevskii, *Adv. Physics*, **10**, 165 (1961).

O.W. Edwards, R.L. Dunn and J.D. Hatfield, *J. Chem. Eng. Data*, **1**, 508 (1964).

R.E. Emmert and R.L. Pigford, *Chem. Eng. Sci.*, **2**, 87 (1954).

D. Ferrier, K. Kinoshita, J. McHardy, and P. Stonehart, *J. Electroanal. Chem.*, **61**, 233 (1975).

G.D. Fulford, in Advances in Chemical Engineering. T.B. Drew, J.W. Hooper, and T. Vermeulen, eds., **5**, 151-236, Academic Press, New York (1964).

D.C. Grahame, *Chem. Revs.*, **41**, 441 (1947).

P. Groenveld, *Chem. Eng. Sci.*, **25**, 1267 (1970).

P. Groenveld, *A.I.Ch.E. J.*, **17**, 489 (1971).

W.A. Gross, et al., Fluid Film Lubrication. Wiley, New York, 1980.

H.C. Hamaker, *Physica* **4**, 1058 (1937).

S. Hartland and R.W. Hartley, Axisymmetric Fluid-Liquid Interfaces. Elsevier, New York, 256-348, 1976.

P.C. Hiemenz, Principles of Colloid and Surface Chemistry. Dekker, Inc., New York, pp. 352-452,

D.B. Hough and L.R. White, *Adv. Col. Int. Sci.*, **14**, 3 (1980).

J.N. Israelachvili, *Proc. Roy. Soc. Lond. A*, **331**, 39 (1972).

J.N. Israelachvili, *Q. Rev. Biophys.*, **6**, 341 (1974).

J.N. Israelachvili, Intermolecular and Surfaces Forces. Academic Press, New York, pp. 36-160, 1985.

J.N. Israelachvili and D. Tabor, *Proc. Roy. Soc. Lond. A*, **331**, 19 (1972).

J.N. Israelachvili and D. Tabor, *Prog. Surf. Membr. Sci.*, **7**, 1 (1973).

J.D. Jackson, Classical Electrodynamics, 2nd ed., Wiley, New York, pp. 306-13, 1975.

H. Jeffreys, *Proc. Camb. Phil. Soc.*, **26**, 204 (1930).

L.D. Landau and E.M. Lifshitz, Statistical Physics, 3rd ed., Pergamon, New York, pp. 377-84, 1980.

I. Langmuir, *J. Chem. Phys.*, **6**, 893 (1938).

V.G. Levich, Physico-Chemical Hydrodynamics. Prentice-Hall, Englewood Cliffs, NJ, pp. 591-698, 1962.

E.M. Liftshitz, *Soviet Physics JETP*, **2**, 73 (1956).

J. Llopis, in Modern Aspects of Electrochemistry. **9**, J.O'M Bockris and B.E. Conway (eds.) Plenum, New York, pp. 91-158, 1976.

V. Ludviksson and E.N. Lightfoot, *A.I.Ch.E. J.*, **14**, 620 (1968).

J. Mahanty and B.W. Ninham, Dispersion Forces, Academic Press, New York, pp. 1-63, 1976.

G. Marrucci, *Chem. Eng. Sci.*, **24**, 975 (1969).

A.D. McLachlan, *Proc. Roy. Soc. Lond. A*, **271**, 387 (1963a).

A.D. McLachlan, *Mol. Phys.*, **6**, 423 (1963b).

A.D. McLachlan, *Discuss. Faraday Soc.*, **40**, 239 (1965).

D.F. Moore, *Wear*, **8**, 245 (1965).

J.R. Mowat and R.H. Muller, "Reflection of Polarized Light from Absorbing Media," Univ. of Calif., Lawrence Berkeley Laboratory, UCRL-11813, 1966.

R.H. Muller, *J. Opt. Soc. Amer.*, **54**, 419 (1964).

R.H. Muller, *J. Electrochem. Soc.*, **113**, 943 (1966).

R.H. Muller, in Advances in Electrochemistry and Electrochemical Engineering. **9**, P. Delahay and C.W. Tobias (eds.), Wiley, New York, pp. 167-226, 1973.

R.H. Muller and M.L. Sand, *J. Opt. Soc.*, **70**, 93 (1980).

J.S. Newman, Electrochemical Systems, Prentice-Hall, Englewood Cliffs, NJ, pp. 140-66, 1973.

W.S. Norman, Absorption, Distillation and Cooling Towers. Wiley, New York, 1961.

W.S. Norman and B.K. Soloman, *Trans. Inst. Chem. Eng.*, **37**, 237 (1959).

W. Nusselt, *Ver. Deut. Ingr. Z.*, **60**, 549, 569 (1916).

J.Th.G. Overbeek, *J. Phys. Chem.*, **64**, 1178 (1960).

E.D. Palik (ed.), Handbook of Optical Constants of Solids. Academic Press: New York, pp. 275-368, 1985.

V.A. Parsegian, in Physical Chemistry: Enriching Topics from Colloid and Surface Chemistry, H. Van Olphen and K.J. Mysels (eds.), IUPAC Comm. 1.6, California, (1975).

V.A. Parsegian and G.H. Weiss, *J. Col. Int. Sci.*, **81**, 285 (1981).

T.N.L. Patterson, *Math. Comp.*, **22**, 847 (1968).

P. Richmond, *Spec. Period. Rep.: Col. Sci.*, D.H. Everett (ed.), London Chem. Soc., **2**, (1975).

E. Ruckenstein and R.K. Jain, *J. Chem. Soc. Faraday Trans.*, **70**, 132 (1974).

A.V. Ruddy and D. Summer-Smith, *Tribology*, **15** (1982).

M. L. Sand, Light Interference in Electrolyte Films on Metals. M.S. Thesis, Univ. Ca., Lawrence Berkeley Laboratory, Berkeley, California, LBL-3589, 1975.

J. Satterly and H. Givens, *Trans, Roy. Soc. Can.*, **27**, 145 (1933).

J. Satterly and E.L. Stuckey, *Trans, Roy. Soc. Can.*, **26**, 131 (1932).

A. Sharma and E. Ruckenstein, *Langmuir*, **2**, 480 (1986).

I. Shibuya, *Rept. Inst. High Speed Mech., Tohoku Univ.*, **1**, 17 (1951).

O. Stern, *Z. Electrochem.*, 30, 508 (1924).

C.V. Sternling and L.E. Scriven, *A.I.Ch.E. J.*, **6**, 514 (1959).

A.Z. Szeri, Tribology: Friction, Lubrication and Wear. McGraw-Hill, San Francisco, 1980.

D. Tabor and R.H.S Winterton, *Proc. Roy. Soc. Lond. A*, **312**, 435 (1969).

J.A. Tallmadge, *J. Phys. Chem.*, **75**, 583 (1971a).

J.A. Tallmadge, *A.I.Ch.E. J.*, **17**, 760 (1971b).

J.A. Tallmadge, K.C. Khilar and C.B. Weinberger, *Ind. Eng. Chem. Fund.*, **19**, 266 (1980).

J.A. Tallmadge and K.C. Lang, *Ind. Eng. Chem. Fund.*, **10**, 648 (1971).

G.F. Teletzke, Thin Liquid Films: Molecular Theory and Hydrodynamic Implications, Ph.D. Thesis, U. of Minnesota, 1983.

J. H. Turney, Profiles of Supermeniscus Electrolyte Films on Partially Submerged Gas Electrodes. M.S. Thesis, Univ. Ca., Lawrence Berkeley Laboratory, Berkeley, California, LBL-171, 1971.

J.J. Van Rossom, *Appl. Sci. Res.*, **A7**, 121 (1958).

E.J.W. Verwey and J.Th.G. Overbeek, Theory of the Stability of Lyophobic Colloids, Elsevir, New York, 1948.

J. Visser, *Advan. Col. Int. Sci.*, **3**, 331 (1972).

A.R. Von Hippel, Dielectric Materials ans Applications, Wiley, New York, 1958.

K.H. Wang, V. Ludviksson and E.N. Lightfoot, *A.I.Ch.E. J.*, **17**, 1402 (1971).

F.G. Will, *J. Electrochem. Soc.*, **110**, 145 (1963).

M.B. Williams and S.H. Davis, *J. Col. Int. Sci.*, **90**, 220 (1982).

F. Wooten, Optical Properties of Solids. Academic Press, New York, pp. 1-84, 1972.

W.D. Wright, The Measurement of Colour, 3rd ed. Adam Hilger, LTD, London, pp. 96-127, 1964.

C.-S. Yih, *Proc. 2nd U.S. Natl. Congr. Appl. Mech. 1954*, Society of Mechanical Engineers, New York, 623 (1955).

C.-S. Yih, *Phys. Fluids*, **6**, 321 (1963).

*LAWRENCE BERKELEY LABORATORY*
*TECHNICAL INFORMATION DEPARTMENT*
*UNIVERSITY OF CALIFORNIA*
*BERKELEY, CALIFORNIA 94720*